

Evaluation and Optimisation of Diamond-Like Carbon for Tribological Applications

Louise Beth Austin

Submitted in accordance with the requirements for the degree of

Doctor of Philosophy

The University of Leeds

School of Mechanical Engineering

September 2014

The candidate confirms that the work submitted is her own, except where work which has formed part of jointly authored publications has been included. The contribution of the candidate and the other authors to this work has been explicitly indicated below. The candidate confirms that appropriate credit has been given within the thesis where reference has been made to the work of others. Transmission electron microscope sample preparation and operation (including EELS) was undertaken by Dr Michael Ward. Assistance with MATLAB for the production of graphs and equations was provided by Gregory De Boer.

This copy has been supplied on the understanding that it is copyright material and that no quotation from the thesis may be published without proper acknowledgement

© 2014 The University of Leeds and Louise Beth Austin

Papers Contributing to this Thesis

“The Impact of the Lubricant Additive Package on the Tribological Performance of Diamond-Like Carbon Coatings in Simulated Cam-Follower Conditions.” Austin, L., Liskiewicz, T., Neville, A., Tietema, R. SVC 2012 Conference Proceedings

“The Influence of Anti-wear Additive ZDDP on Doped and Un-doped Diamond-Like Carbon Coatings.” Austin, L, Liskiewicz, T, Neville, A. (*Pending submission*)

“Tribological Performance and Tribofilm Formation on DLC Films Prepared by PECVD and Microwave Excited Plasma Enhanced CVD under Boundary Lubrication Conditions”. Hongyuan Zhao, Louise Austin, Chun Wang, Tomasz Liskiewicz and Anne Neville. (*Pending submission*)

Acknowledgements

First and foremost, I would like to extend my deepest gratitude to my supervisor, Anne Neville, for her endless guidance and support throughout this thesis. Your insight and numerous anecdotes made the entire process enjoyable, thank you. Also thank you to Tomasz Liskiewicz for co-supervising this project. Thank you to Hauzer who sponsored this PhD and provided much guidance and support throughout.

I would like to thank the technical staff within iFS for their help and support throughout my time at Leeds. To LEMAS, Mike and John for help with electron microscopy. Thank you to Chun, for her assistance and training on much of the equipment within the lab – and for allowing me to use it!

I am indebted to Jackie Kidd and Fiona Slade, without their help this thesis would not have been possible.

I would also like to thank my colleagues and friends at the University of Leeds, for sharing the experience and making my time there thoroughly enjoyable. In no particular order; to James for his endless stream of pranks and heated academic debates; to Rick, for helping me to find the stationary cupboard and introducing me to many good friends; Dave, for being himself; to Joe, for all of the laughs, and rum!; Mike, for being the most stereotypical Yorkshire man I have ever come across, Ben for his love of paninis, and Vio, Laura, Thibaut, Yugal, Shahriar and to everyone in the group who I shared a laugh with, and to Jen, for keeping me somewhat sane throughout the duration!

Finally, I would like to say an eternal thank you to my mother and brother, who have not only put up with me throughout the duration of this thesis, but throughout my life. Without you I would never have believed it to be possible, for your support I am ever grateful.

For Dad

Abstract

Fuel economy and environmental protection have become increasingly important over the last few decades and this has led to the demand for higher efficiency within the automotive sector. Non-ferrous coatings with excellent and unique tribological properties, intended to increase efficiency by lowering friction and wear internally within the car engine are becoming increasingly more prevalent within this sector. Since current lubrication practices are geared towards ferrous materials, it is important to determine the effect that lubricants have on non-traditional coatings.

In this study, three Diamond-Like Carbon (DLC) coatings are assessed for their viability within this application, more specifically for the cam-follower interface. The coatings are an amorphous hydrogenated Diamond-Like Carbon and a silicon doped amorphous hydrogenated Diamond-Like Carbon, both produced at the University of Leeds, using a Hauzer Flexicoat 850 deposition system, and a tungsten doped Diamond-Like Carbon coating from Oerlikon Balzers, type Balanit C*. The coatings are characterised to quantify their hardness, thickness, elastic modulus and sp^2 content before being tribologically tested in group III base oil and fully formulated oil containing the anti-wear additive zinc dialkyldithiophosphate on a pin-on-reciprocating plate tribometer. The three DLCs are tested against a cast iron counter-body and analysed for wear and the presence of a phosphate tribo-film. The nature of growth of the tribo-film is commonly known for ferrous contacts but much uncertainty still remains for DLC lubricated contacts.

The Hauzer Flexicoat 850 system houses within it two microwave sources which aid in the Plasma Enhanced Chemical Vapour Deposition (PECVD) of DLC. This new technology offers potentially improved coatings for tribological coatings and the ability to tailor the coating for a particular lubricant. In this study the microwave PECVD process is tested to determine its viability within a commercial setting, and to discover the effect of different processing parameters on the mechanical properties of the coatings. The parameters of particular interest are the bias voltage, gas ratio and power of the microwave sources. Preliminary tests were undertaken in order to determine the optimum position and other fundamental deposition properties before the full scale tests began.

This study has shown that a-C:H DLC is the most suitable coating of those tested here for implementation into this application. The Si-DLC and W-DLC were not compatible with the lubricants or the system as will be shown. The lubricant additive ZDDP is important in ferrous systems, and it is shown here to be useful within a DLC environment

The microwave DLC coatings have demonstrated good mechanical properties, in particular a high hardness. They have proven to be very promising, and with a substantial reduction in deposition time, demonstrate their potential commercial viability for tribological applications.

Contents

Papers Contributing to this Thesis	iii
Acknowledgements.....	iv
Abstract.....	vi
Contents	viii
List of Figures.....	xiv
List of Tables	xxvi
Nomenclature.....	xxx
Chapter 1	1
Introduction.....	1
1.1. Global Concerns.....	1
1.2. Vehicle Efficiency.....	5
1.3. Objectives.....	6
1.4. Thesis Outline	7
1.5. Thesis Structure.....	9
1.6. Theory of Tribology.....	10
1.7. Theory of Plasma in Coating Processes	11
Chapter 2	17
Literature Review.....	17
2.1. Introduction.....	17
2.2. Tribology of Valve Train Components.....	17
2.3. Current Materials used in the Valve Train.....	21
2.4. Currently Used Surface Treatments	21
2.5. Diamond-Like Carbon	22
2.5.1. Historical Overview	22

2.5.2.	Structure and Bonding Mechanisms	23
2.5.3.	H/E ratio	29
2.5.4.	Adhesion	30
2.5.5.	Deposition Parameters and Typical Properties of DLC Coatings	33
2.5.6.	Tribochemistry of DLC	40
2.6.	Surface Preparation	45
2.7.	Deposition Techniques	47
2.7.1.	Physical Vapour Deposition by Magnetron Sputtering	47
2.7.2.	Arc Deposition	48
2.7.3.	High Power Impulse Magnetron Sputtering	52
2.7.4.	Plasma Enhanced Chemical Vapour Deposition.....	54
2.7.5.	Microwave Plasma Enhanced Chemical Vapour Deposition	55
2.7.6.	Coating Growth.....	59
2.7.7.	Summary	61
Chapter 3	65
Experimental Methodology	65
3.1.	Introduction	65
3.2.	The Hauzer Flexicoat 850 System at the University of Leeds.....	65
3.3.	Details of the System	65
3.4.	Calo-tester	69
3.5.	Nano Indentation Hardness	70
3.6.	Scanning Electron Microscopy	71
3.7.	Energy Dispersive X-Ray Analysis	72
3.8.	X-Ray Photoelectron Spectroscopy	73
3.9.	TEM and EELS	75

3.10. Pin-on-Reciprocating Plate Tribometer	77
3.11. White light Interferometry	81
3.12. Atomic Force Microscopy.....	82
Chapter 4	84
Results: Tribological Performance of a-C:H, Si-DLC and W-DLC.....	84
4.1. Introduction	84
4.1.1. Substrate and Lubricant Types.....	85
4.1.2. Coating Recipe	85
4.2. a-C:H, Si-DLC and W-DLC Coatings: Mechanical Results.....	87
4.2.1. Thickness	87
4.2.2. Hardness and Elastic Modulus	87
4.2.3. TEM and EELS	89
4.2.4. Scratch Testing.....	91
4.2.5. Tribological Tests.....	94
4.2.6. a-C:H.....	95
4.2.7. Microscope Images of a-C:H Coating Wear.....	100
4.2.8. Microscope Images of Counter-body Wear for a-C:H.....	101
4.2.9. Si-DLC	102
4.2.10. Microscope Images of Si-DLC Coating Wear	107
4.2.11. Microscope Images of Counter-body Wear for Si-DLC.....	108
4.2.12. W-DLC.....	110
4.2.13. Microscope Images of W-DLC Coating Wear.....	113
4.2.14. Microscope Images of Counter-body Wear for W-DLC	114
4.2.15. Counter-body Wear for a-C:H, Si-DLC and W-DLC.....	117
4.2.16. Scanning Electron Microscopy and Energy Dispersive X-ray Analysis	119
4.2.17. White Light Interferometry	122

4.2.18.	Atomic Force Microscopy.....	123
4.2.19.	XPS	125
4.3.	Summary	132
Chapter 5	134
Results: Microwave Plasma Enhanced Chemical Vapour Deposition Using One Microwave Source	134
5.1.	Introduction	134
5.2.	Gas Ratio Tests	136
5.2.1.	Recipe.....	136
5.2.2.	Thickness	139
5.2.3.	Hardness and Elastic Modulus	142
5.2.4.	Scratch Test Results	143
5.2.5.	Summary	144
5.3.	Optimum Time Tests Using One Microwave Source	145
5.3.1.	Recipe.....	145
5.3.2.	Thickness	148
5.3.3.	Scratch Test Results	149
5.3.4.	Summary	149
5.4.	Tests to Determine the Optimal Position of Samples Using One Microwave Source	150
5.4.1.	Recipe.....	151
5.4.2.	Thickness	153
5.4.3.	Summary	156
5.5.	Microwave PECVD Two Variable Matrix Using One Microwave Source.....	157
5.5.1.	Test Matrix	157
5.5.2.	Recipe.....	158
5.5.3.	Thickness	160

5.5.4.	Hardness and Elastic Modulus	161
5.5.5.	Semi-Empirical Equations Relating Bias Voltage and Gas Ratio to Hardness and Elastic Modulus	163
5.5.6.	Summary	166
Chapter 6	168
Results: Microwave Plasma Enhanced Chemical Vapour Deposition Using Two Microwave Sources		168
6.1.	Introduction	168
6.2.	Tests to Determine the Optimal Position of Samples Using Two Microwave Sources	168
6.2.1.	Test Recipe for the Optimal Sample Position Test Using Two Microwave Sources.....	169
6.2.2.	Thickness of the samples prepared in the position test using two microwave sources	171
6.2.3.	Summary	173
6.3.	Microwave Power Experiments 1000 W versus 1200 W	173
6.3.1.	Microwave Power experiments conducted at 1000 W.....	174
6.3.2.	Microwave Power experiments conducted at 1200 W.....	175
6.3.3.	Thickness	176
6.3.4.	Summary	177
6.4.	Bias Scan.....	177
6.4.1.	Recipe.....	178
6.4.2.	Hardness and Elastic Modulus	181
6.4.3.	Summary	182
6.5.	Bias Scan – Smaller Increments.....	182
6.5.1.	Hardness and Elastic Modulus	183
6.5.2.	Scratch Testing.....	185
6.5.3.	Current Densities of the Diamond-Like Carbon Deposition Process	186

6.5.4.	Summary	187
Chapter 7	188
Discussion	188
7.1.	Plasma Enhanced Chemical Vapour Deposition Diamond-Like Carbon Coatings, Including Tungsten and Silicon Dopants	188
7.1.1.	Tribochemical Interactions.....	189
7.1.2.	a-C:H.....	190
7.1.3.	Si-DLC	193
7.1.4.	Friction	193
7.1.5.	Friction and Wear.....	194
7.1.6.	Critical Load and Wear	196
7.2.	Microwave Plasma Enhanced Chemical Vapour Deposition Diamond-Like Carbon Coatings	199
7.2.1.	Thickness of Microwave PECVD Coatings with Variation in Position on Substrate Holder Created with One and Two Microwave Sources.....	199
7.2.2.	The Effect of Bias Voltage on Thickness, Hardness and Elastic Modulus of DLC Coatings Made with One and Two Microwave Sources.....	200
7.2.3.	Comparison of the Coatings Created at the University of Leeds to Those Found in the Literature	203
Chapter 8	205
Conclusions	205
8.1.	Conclusions.....	205
8.2.	Future work	208
References	209

List of Figures

Figure 1-1: Records of changes in atmospheric composition of: CO ₂ , CH ₄ , N ₂ O.: direct atmospheric sources over past few decades, previous data derived from ice core samples from Antarctica [3].....	2
Figure 1-2: Variations of the Earth's surface temperature over the past 1000 years [3].....	3
Figure 1-3: Greenhouse gas emissions by main source in Europe, 2007 [4].....	4
Figure 1-4: Energy distribution in a typical passenger car. Adapted from [8] and [7]6	
Figure 1-5: Aurora Australis. Picture taken from the ISS. Courtesy of NASA	12
Figure 1-6: Glow discharge regime [17].....	15
Figure 2-1: (a) Cross-section through a V6 engine with a valve train mechanism of centre pivot rocker arm or centre pivot rocker with a lifter with commonly coated parts highlighted in grey:. (b) piston (c) tappet (d) camshaft (e) piston and gudgeon (f) valve stem and head (g) rocker arm [8, 19]	18
Figure 2-2: Typical P-V values of commonly coated engine components. Adapted from [20]	19
Figure 2-3: Comparison of friction torque vs speed for phosphate, TiN, CVD DLC and PVD DLC coated shims against camshaft [21].....	20

Figure 2-4: Comparison of torque vs time for uncoated steel tappet, WC/C-a-C:H and a-C:H coating [22].....	20
Figure 2-5: a. Tetrahedrally arranged C atoms and b. Graphitically arranged C atoms	24
Figure 2-6: Ternary phase diagram for DLC coatings [18]	25
Figure 2-7: Deposition rate of DLC vs ionisation potentials of different hydrocarbon gases used in processing [18].....	28
Figure 2-8: H, E, W_e and H/E ratio of Al-O-N coatings and their resistance to cracking using a diamond indenter. [74].....	30
Figure 2-9: Structure of ZDDP as proposed by Bell <i>et al.</i> [113].....	41
Figure 2-10: Composition of ZDDP tribo-film as proposed by Martin et al.[115] ..	43
Figure 2-11: Pad-like formation of ZDDP derived tribo-film on ferrous materials [109].....	43
Figure 2-12: Schematic of sputtering PVD process	48
Figure 2-13: Mechanism of PVD by arc deposition	50
Figure 2-14: Physical line of sight deposition [138].....	51
Figure 2-15: Schematic of IBM non-line of site cathodic arc deposition system [139]	52
Figure 2-16: Common engine components coated using DLC, including piston rings, shims and valve lifters.....	54

Figure 2-17: Image of microwave plasma generators on the Hauzer Flexicoat 850 deposition system.....	57
Figure 2-18: Hauzer example of in-line Magnetron sputtering	59
Figure 2-19: Deposition mechanisms of DLC deposited by plasma chemical vapour deposition, presented in [11] in chapter 1, by Robertson.....	60
Figure 3-1: Hauzer Flexicoat 850 system schematic	66
Figure 3-2: Hauzer Flexicoat 850 Deposition System	66
Figure 3-3: Image of the front of the Hauzer Flexicoat 850 System chamber with door open.....	67
Figure 3-4: Microwave source antenna and reflector a. image, b. schematic diagram	68
Figure 3-5: Image of the substrate table for the Hauzer Flexicoat 850 deposition system.....	68
Figure 3-6: (a) Calo-tester schematic, (b) Calo-tester.....	69
Figure 3-7: Example of a nano indentation curve from the sample produced within the microwave bias scan matrix at 210 V	70
Figure 3-8: Mechanisms of Energy Dispersive X-ray Analysis	73
Figure 3-9: Diagram of sample prepared by focused ion beam etching	75
Figure 3-10: Focused ion beam etched sample ready for input into TEM.....	76

Figure 3-11: Low loss region of EELS spectrum of a-C:H	76
Figure 3-12: Core loss region of EEL spectrum of a-C:H	77
Figure 3-13: Spherical contact and semi-elliptical pressure distribution.....	78
Figure 3-14: Pin on reciprocating plate tribometer	79
Figure 3-15: Biceri pin on reciprocating plate tribometer schematic	80
Figure 3-16: Modified Stribeck curve with lubrication regimes and their associated application. [32]	80
Figure 3-17: Schematic of the AFM showing the basic mechanisms within the equipment.....	82
Figure 3-18: Typical AFM image of diamond-like carbon.....	83
Figure 4-1: Schematic of the composition of a. a-C:H, b. Si-DLC and c. W-DLC coatings	86
Figure 4-2 TEM images of a. a-C:H, b. Si-DLC and W-DLC.....	89
Figure 4-3: Fitted EELS spectra for a-C:H	90
Figure 4-4: sp^2 % of a-C:H, Si-DLC and W-DLC	91
Figure 4-5: Scratch test images of a. a-C:H, b. Si-DLC, c. W-DLC with L_{c2} value indicated with arrows.	93
Figure 4-6: Critical loads from scratch test of a-C:H, Si-DLC and W-DLC	94

Figure 4-7: Example of error bars for friction plot of a-C:H after six hours testing in fully formulated oil	96
Figure 4-8: Coefficient of friction of a-C:H in base oil (BO) and fully formulated oil + ZDDP (FF) tested for six hours on pin on reciprocating plate tribometer.....	96
Figure 4-9: Coefficient of friction of a-C:H in base oil and fully formulated oil tested for twelve hours on pin on reciprocating plate tribometer	96
Figure 4-10: Coefficient of friction of a-C:H in base oil and fully formulated oil tested for twenty hours on pin on reciprocating plate tribometer	97
Figure 4-11: Steady state friction results for a-C:H. (BO = base oil, FF = fully formulated oil + ZDDP).....	98
Figure 4-12: Wear volume of a-C:H plate after tribological testing in base oil (BO) and fully formulated oil + ZDDP (FF).....	99
Figure 4-13: a-C:H Wear rate after tribological testing in base oil (BO) and fully formulated oil + ZDDP (FF)	99
Figure 4-14: Wear images of a-C:H after tribo-testing in the pin-on-reciprocating plate rig: a. in base oil after six hours, b. in base oil after 20 hours, c. in fully formulated oil + ZDDP after six hours and d. in fully formulated oil +ZDDP after 20 hours.....	100
Figure 4-15: Microscope images of counter-body after tribometer testing against a-C:H.....	101

Figure 4-16: Coefficient of friction of Si-DLC in base oil and fully formulated oil tested for six hours on pin on reciprocating plate tribometer	103
Figure 4-17: Coefficient of friction of Si-DLC in base oil and fully formulated oil tested for twelve hours on pin on reciprocating plate tribometer.....	103
Figure 4-18: Coefficient of friction of Si-DLC in base oil and fully formulated oil tested for twenty hours on pin on reciprocating plate tribometer	103
Figure 4-19: Steady state friction results for Si-DLC after tribological testing in base oil (BO) and fully formulated oil + ZDDP (FF)	104
Figure 4-20: Wear volume of Si-DLC after tribological testing in base oil (BO) and fully formulated oil + ZDDP (FF).....	106
Figure 4-21: Wear rate of Si-DLC after tribological testing in base oil (BO) and fully formulated oil (FF).....	107
Figure 4-22: Wear images of Si-DLC plate	108
Figure 4-23: Microscope images of counter-body after tribometer testing against Si-DLC.....	109
Figure 4-24: Coefficient of friction of W-DLC in base oil and fully formulated oil tested for six hours on pin on reciprocating plate tribometer	111
Figure 4-25: Coefficient of friction of W-DLC in base oil and fully formulated oil tested for twelve hours on pin on reciprocating plate tribometer.....	111

Figure 4-26: Coefficient of friction of W-DLC in base oil and fully formulated oil tested for twenty hours on pin on reciprocating plate tribometer	111
Figure 4-27: Steady state friction of W-DLC after tribological testing in base oil (BO) and fully formulated oil (FF)	112
Figure 4-28: Wear Volume of W-DLC after tribological tests in base oil (BO) and fully formulated oil + ZDDP (FF).....	113
Figure 4-29: Wear Rate for W-DLC after tribological tests in base oil (BO) and fully formulated oil + ZDDP (FF)	113
Figure 4-30: Wear images of W-DLC plate.....	114
Figure 4-31: Microscope images of counter-body after tribometer testing against W-DLC.....	115
Figure 4-32: Pin wear of a-C:H, Si-DLC and W-DLC after tribo-testing against DLC	117
Figure 4-33: Wear rate for cast iron counter-body for a-C:H, Si-DLC and W-DLC after six and 20 hours sliding in base oil and fully formulated oil + ZDDP (FF oil)	118
Figure 4-34: SEM image and EDX analysis for a-C:H after pin on reciprocating plate test in fully formulated oil + ZDDP for twenty hours	120
Figure 4-35: SEM image and EDX analysis for Si-DLC after pin on reciprocating plate test in fully formulated oil + ZDDP for twenty hours	121

Figure 4-36: SEM image and EDX analysis for W-DLC after pin on reciprocating plate test in fully formulated oil + ZDDP for twenty hours 122

Figure 4-37: White light interferometry images for a. a-C:H, b. Si-DLC and c. W-DLC after testing on pin on reciprocating plate tribometer for twenty hours in fully formulated oil + ZDDP showing the wear tracks of three selected samples 123

Figure 4-38: AFM images of a. a-C:H and b. Si-DLC prior to tribological testing 124

Figure 4-39: AFM Images of a-C:H and Si-DLC after six and twenty hours on the tribometer using fully formulated oil + ZDDP 124

Figure 4-40: XPS survey scan of a. cast iron pin and b. a-C:H after six hours and c. Cast iron pin and d. a-C:H after twenty hours on tribometer in fully formulated oil. 126

Figure 4-41: Chemical species present at the cast iron counter-body surface after twenty hours tribometer testing..... 130

Figure 4-42: Chemical species present at DLC surface after twenty hours tribometer testing 131

Figure 5-1: Position of the samples on the substrate holders in the deposition chamber for microwave gas ratio experiments. 137

Figure 5-2: Trend showing the bias current for samples in the DLC deposition process in the gas ratio matrix tested at 100 V bias voltage for 33 minutes 138

Figure 5-3: Temperature of the substrate table during the microwave deposition process of the gas ratio samples 139

Figure 5-4: Thickness of gas ratio experiments – whole coating including interlayers	140
Figure 5-5: Images of the coatings made in the gas ratio series of experiments after calo testing to measure the thickness. (Where there is an x in place of an image, no coating was deposited onto the substrate and no calo test was done).	141
Figure 5-6: Critical load values from scratch testing of the DLC coatings produced in the gas ratio matrix.....	143
Figure 5-7: Scratch test imaged taken from critical load experiments using 0 – 60 N gradual loading on DLC coatings produced in the gas ratio matrix	144
Figure 5-8: Bias current for optimum time tests with Cr interlayer.....	147
Figure 5-9: Bias current for optimum time tests with Cr + WC interlayer	147
Figure 5-10: Scratch test results of the samples tested to determine correct duration in the microwave step.....	149
Figure 5-11: Trend of the C ₂ H ₂ flow, Ar flow, bias voltage, microwave power and reflected power of the tests to determine the optimum position of the substrates using one microwave source.	152
Figure 5-12: Bias current trend of the tests conducted to determine the optimum position of the substrates using one microwave source	153
Figure 5-13: Thickness of the DLC layer produced when determining the optimal position for the substrates when using one microwave source	156

Figure 5-14: Bias currents of the tests conducted in the two variable matrix.....	159
Figure 5-15: Temperature of the microwave deposition process for tests conducted in the two variable matrix	160
Figure 5-16: Thickness contour graph of two variable test matrix (entire coating)	161
Figure 5-17: Hardness of the microwave DLC coatings as a function of gas ratio and bias voltage.....	162
Figure 5-18: Elastic Modulus of the microwave DLC coatings as a function of gas ratio and bias voltage	162
Figure 5-19: Least squares regression fit to hardness data for Matrix	164
Figure 5-20: Least squares regression fit to elastic modulus data for the two variable matrix series of experiments	165
Figure 6-1: Energy distribution of a. one and b. two microwave sources	169
Figure 6-2: Trend of the deposition parameters: C ₂ H ₂ flow, Ar flow, bias voltage, microwave power and reflected power for the position test using two microwave sources experiments	170
Figure 6-3: Position test using two sources bias current versus time	171
Figure 6-4: Microwave power 1000 W power trend.....	175
Figure 6-5: Microwave power 1000 W power bias current	175
Figure 6-6: Microwave power 1200 W power trend.....	176

Figure 6-7: Microwave power 1200 W power bias current trend.....	176
Figure 6-8: Bias current trends for the experiments conducted for bias scan matrix	179
Figure 6-9: Maximum temperature reached during the final microwave step in each process within the bias scan variable matrix.....	180
Figure 6-10: Thickness of the DLC made in the bias scan matrix of experiments.	180
Figure 6-11: Hardness for microwave DLC deposited from -50 - -300 bias voltage	181
Figure 6-12: Elastic modulus for samples created in bias scan matrix.....	182
Figure 6-13: Hardness of DLC coatings from the matrix: bias scan, smaller increments	184
Figure 6-14: Elastic modulus of DLC coatings from the matrix: bias scan, smaller increments	184
Figure 6-15: Scratch test images of samples produced using -250 V and -220 V bias, scratch tested using a maximum load of 60 and 120 N respectively.	185
Figure 6-16: Current densities of the Diamond-Like Carbon deposition process across a selection of samples.....	186
Figure 7-1: Transfer of tribo-film from cast iron pin to DLC surface	192

Figure 7-2: Coefficient of friction as a function of wear rate for a-C:H and Si-DLC after six and twenty hours testing. BO = Base oil, FF = fully formulated oil + ZDDP 195

Figure 7-3: Wear rate as a function of coating hardness of a-C:H and Si-DLC. BO = base oil. FF = fully formulated oil + ZDDP. Including literature values from Vengudusamy *et al.* [95] and de Barros’Bouchet [97] 196

Figure 7-4: Critical load versus H/E ratio for the samples created during the course of this thesis. 197

Figure 7-5: Wear rate as a function of critical load for a-C:H, Si-DLC and W-DLC after twenty hours testing 198

Figure 7-6: Thickness of DLC made using one and two microwave sources in different positions along the substrate holder. 200

Figure 7-7: Variation of the thickness of microwave DLC coatings produced using one and two microwave sources with respect to bias voltage..... 201

Figure 7-8: Variation of the hardness of microwave DLC coatings produced using one and two microwave sources with respect to bias voltage..... 202

Figure 7-9: Variation of the elastic modulus of microwave DLC coatings produced using one and two microwave sources with respect to bias voltage 203

List of Tables

Table 1-1: Euro 5 legislation, petrol vehicles from 2011 [5].....	4
Table 1-2: Euro 5 legislation, diesel vehicles from 2011 [5].....	4
Table 1-3: Euro 6 legislation, diesel vehicles from 2015 [5].....	5
Table 1-4: Comparison of ionisation percentage in different deposition techniques [18].....	16
Table 2-1: Typical tribological conditions of a cam/follower [24].....	20
Table 2-2: Typical DLC film properties adapted from [19]	25
Table 2-3: Examples of critical load values taken from scratch testing of different types of coating	32
Table 2-4: Properties of ta-C from the literature (FC – Filtered cathodic arc deposition, AI – Arc Ion plating)	34
Table 2-5: Properties of a-C:H from the literature (M – Magnetron sputtering, PE – PECVD)	36
Table 2-6 Properties of a-C:H deposited using microwave PECVD (MP).....	37
Table 2-7: Properties of tungsten doped DLC from the literature (PE – PECVD, M – Magnetron sputtering).....	38

Table 2-8: Properties of silicon doped DLC as in the literature (PE – PECVD, M – Magnetron sputtering).....	39
Table 4-1: Recipe for a-C:H and Si-DLC. (Pre-deposition cleaning and processes, interlayer deposition and final DLC layer)	86
Table 4-2: Thickness of a-C:H, Si-DLC and W-DLC	87
Table 4-3: Tabulated hardness and Young's modulus of a-C:H, Si-DLC and W-DLC	88
Table 4-4: Classification of scratch test results [184].....	92
Table 4-5: Summary of wear tests of a-C:H, Si-DLC, W-DLC and counter-body	119
Table 4-6: XPS elemental quantifications of cast iron counter-body and a-C:H in fully formulated oil + ZDDP after twenty hours.....	127
Table 4-7: Binding energies, chemical composition and concentration of the XPS analysis carried out on a-C:H and the cast iron counter-body after six hours testing	128
Table 4-8: Binding energies, chemical composition and concentration of the XPS analysis carried out on a-C:H and the cast iron counter-body after twenty hours testing	129
Table 5-1: Processing parameters for gas ratio experiments	137
Table 5-2: Hardness of samples tested in gas ratio experiments	142

Table 5-3: Recipe for thickness versus time tests for DLC deposited with a Cr interlayer	145
Table 5-4: Recipe for thickness versus time test for DLC deposited with a Cr + WC interlayer.	146
Table 5-5: Thickness of the DLC samples created with a Cr and Cr + W-DLC interlayers determined using a calo-tester.....	148
Table 5-6: Recipe for the tests to determine optimum position of samples in the deposition chamber using one microwave source.....	151
Table 5-7: Positional thickness test results including microscope images, one microwave source – entire coating thickness.....	154
Table 5-8: Test matrix.....	158
Table 5-9: Recipe for microwave two variable matrix using one source	159
Table 5-10: Microwave two variable matrix using one source, hardness and elastic modulus.....	161
Table 5-11: Constant values for equation 5-1	163
Table 5-12: Constant values for equation 5-2.....	164
Table 5-13: Accuracy values for the hardness and elastic modulus fit determined from least squares regression data fit to empirical data.	166
Table 6-1: Recipe for position test using two microwave sources.....	170
Table 6-2: Position test using two microwave sources – entire coating	172

Table 6-3: Position test using two microwave sources – DLC coating only	172
Table 6-4: Processing parameters of 1000 and 1200 W power variables	174
Table 6-5: Thickness of samples tested with 1000 and 1200 W microwave power	177
Table 6-6: Deposition recipe for Microwave DLC: Bias Matrix	178
Table 6-7: Hardness and elastic modulus of samples deposited with bias voltages from -210 - -240 V	183
Table 7-1: A selection of coating properties from the literature	204

Nomenclature

μ	Friction Coefficient
a-C:H	Amorphous Hydrogenated Carbon
AFM	Atomic Force Microscope
BE	Binding Energy (eV)
DLC	Diamond-Like Carbon
E	Elastic Modulus (Pa)
E'	Effective Elastic Modulus (Pa)
ECR	Electron Cyclotron Resonance
EDX	Energy Dispersive X-ray
EELS	Energy Electron Loss Spectroscopy
F	Force (N)
H	Hardness (Pa)
$h\nu$	Photon Energy (eV)
iFS	Institute of Functional Surfaces
k	Dimensional wear coefficient ($\text{m}^3\text{N}^{-1}\text{m}^{-1}$)
K	Spring constant
KE	Kinetic Energy (J)
LEMAS	Leeds Electron Microscopy and Spectroscopy Centre
M	Microwave Plasma Enhanced Chemical Vapour Deposition
PECVD	Plasma Enhanced Chemical Vapour Deposition
p_{\max}	Maximum Hertzian Contact Pressure
p_{\min}	Minimum Hertzian Contact Pressure
PVD	Physical Vapour Deposition

R	Effective Radius (m)
$R_{x/y}$	Radius in x/y Direction (m)
Si-DLC	Silicon Doped Diamond-Like Carbon
ta-C	Tetrahedral Amorphous Carbon
TEM	Transmission Electron Microscopy
w	Load (N)
W-DLC	Tungsten Doped Diamond-Like Carbon
XPS	X-ray Photoelectron Spectroscopy
ZDDP	Zinc Dialkyldithiophosphate
λ	Lambda Ratio

Chapter 1

Introduction

1.1. Global Concerns

Over the past few decades, global warming has become increasingly prevalent. It is a huge concern amongst the government, academics and the general population. It has been sensationalised, downplayed and rationalised, but the global consensus on the matter is that action must be taken to prevent further rises in the Earth's temperature as a result of global warming and any further consequences of this. Action is being taken in various different forms, for example, the use of 'greener fuels' (solar power, wind energy, nuclear generation), widespread recycling and the limiting of emissions on a global scale. Surface engineering is having an impact in the reduction of emissions. It is being recognised as a major player in the fight against global warming as the demand for functional surfaces increases [1].

Global warming is a term used to describe the effect that human activity has on the climate and specifically refers to the generation of large amounts of greenhouse gases (including CO₂, NO_x, CFCs (chlorofluorocarbons) and methane) produced by the burning of fossil fuels (oil, gas and coal). The rapidity and magnitude of global industrialisation contributes a huge amount of greenhouse gases to the atmosphere, around 7 billion tonnes of carbon dioxide per annum alone [2]. These greenhouse

gases have a negative effect on the Earth and its atmosphere by their ability to absorb infrared radiation and to destroy vital atmospheric components such as O_3 . This alters the radiation balance of the Earth and as a result of this the temperature rises to restore this balance [2]. The rising temperature of the Earth can be directly correlated with the rising concentration of greenhouse gases in the atmosphere [3], Figure 1-1 and Figure 1-2 illustrate this correlation. Figure 1-1 shows the rise in greenhouse gas emission over the past 1000 years, which can be directly compared to the rising temperature over this time period shown in Figure 1-2.

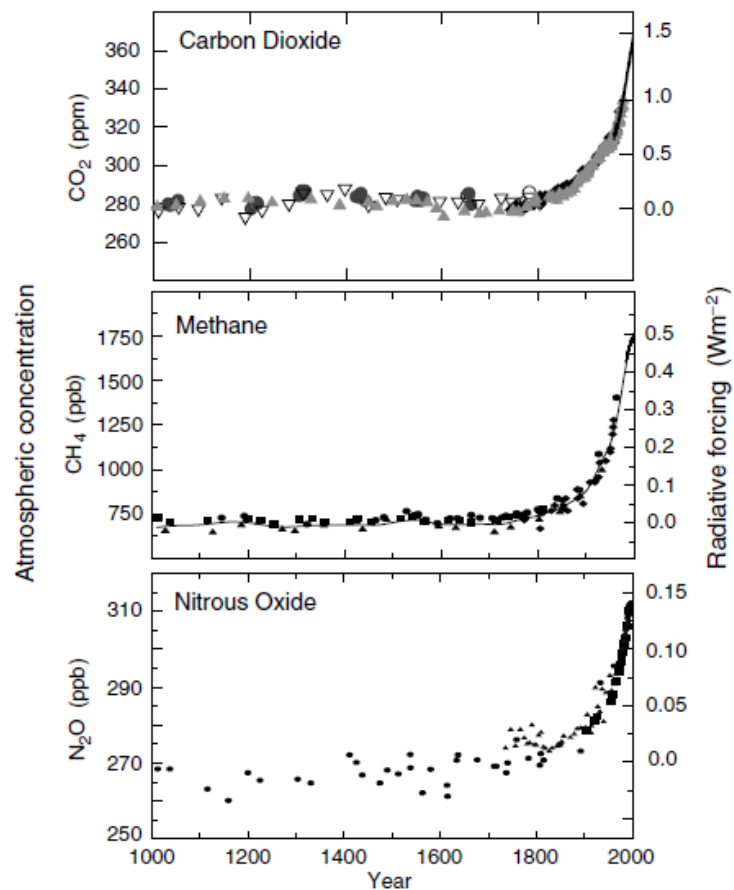


Figure 1-1: Records of changes in atmospheric composition of: CO_2 , CH_4 , N_2O .: direct atmospheric sources over past few decades, previous data derived from ice core samples from Antarctica [3]

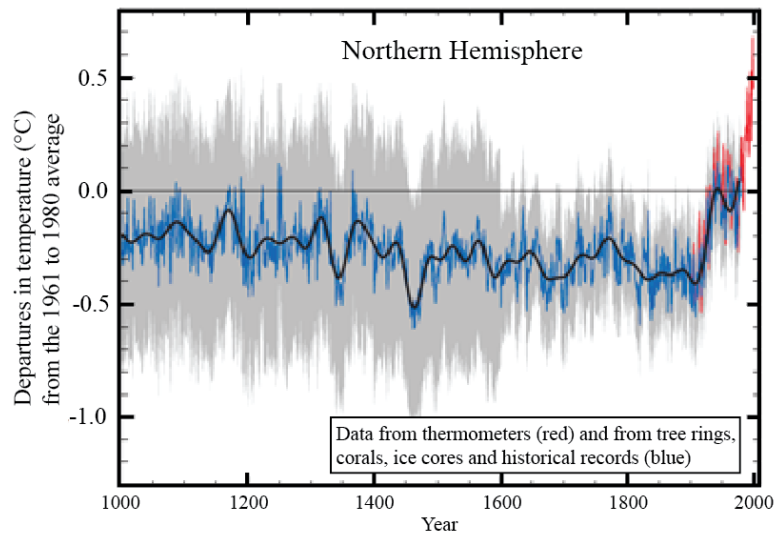


Figure 1-2: Variations of the Earth’s surface temperature over the past 1000 years

[3]

As a result of this correlation, the European Union (amongst other nations and organising bodies) in recent years has introduced targets on the gases emitted by industry. Figure 1-3 shows the greenhouse gas emissions across Europe for the year 2007 by their main source. As can be seen here, the sectors releasing the majority of greenhouse gases into the atmosphere are energy production (26%) and road transportation (17%); this is a large contribution by road vehicles and the European Union has imposed legislation in order to decrease this.

The current European legislation for the reduction of pollutant emissions from light vehicles came into force in 2009 and was gradually introduced from 2011, rising to the full legislative effects in 2015. It is known as the ‘Euro 5 standard’, preceding the ‘Euro 6 standard’ which will come into force from 2015. These standards are outlined for both petrol and diesel vehicles in Table 1-1, Table 1-2 and Table 1-3. Carbon dioxide is not mentioned directly since this is a product of the combustion of the hydrocarbon gases and is controlled via the reduction of these.

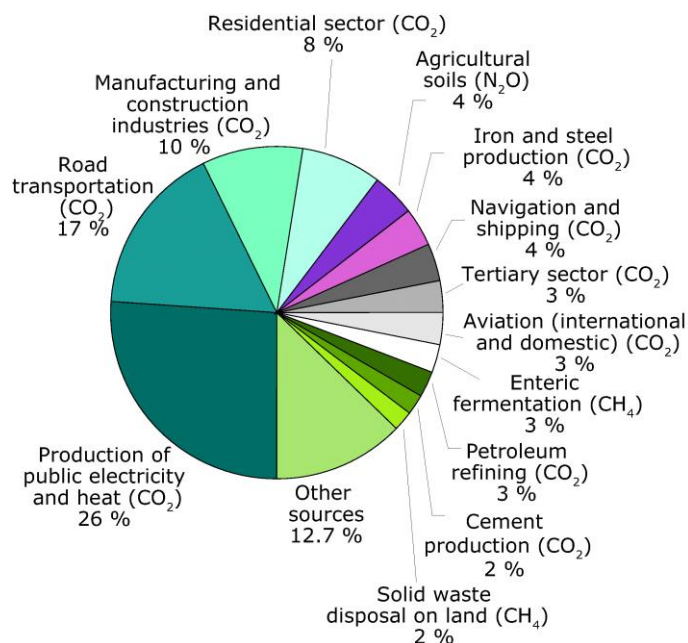


Figure 1-3: Greenhouse gas emissions by main source in Europe, 2007 [4]

Table 1-1: Euro 5 legislation, petrol vehicles from 2011 [5]

Pollutant emission	Limit	Compared with previous legislation
Carbon Monoxide	1000 mg/km	Same
Non-methane hydrocarbons	68 mg/km	New
Total hydrocarbons	100 mg/km	Same
Nitrogen oxides	60 mg/km	25% reduction on Euro 4
Particulates	5 mg/km	New

Table 1-2: Euro 5 legislation, diesel vehicles from 2011 [5]

Pollutant emission	Limit	Compared with previous legislation
Carbon Monoxide	500 mg/km	Same
Nitrogen oxides	180 mg/km	20% reduction on Euro 4
Combined hydrocarbons and nitrogen oxides	230 mg/km	20% reduction on Euro 4
Particulates	5 mg/km	80% reduction on Euro 4

Table 1-3: Euro 6 legislation, diesel vehicles from 2015 [5]

Pollutant emission	Limit	Compared with previous legislation
Carbon Monoxide	500 mg/km	Same
Nitrogen oxides	80	55% reduction on Euro 5
Combined hydrocarbons and nitrogen oxides	170 mg/km	26% reduction on Euro 5
Particulates	2.5 mg/km	50% reduction on Euro 5

Diesel engines will experience the highest impact from Euro legislation over the next few years, (the legislation for petrol passenger vehicles remains the same for Euro 6), though the legislation is tough on both types of vehicle. The legislation has had a major impact on car manufacturers and on public attitudes toward car emissions; car manufacturers are now focusing their sights on a more environmentally friendly vehicle, as is required by the legislation and by the increasing demands of the consumer for more efficient vehicles [6]. The regulations have driven research, design and development of passenger cars towards a greener future.

1.2. Vehicle Efficiency

The efficiency of the internal combustion engine can be improved by looking at the surfaces of those components most susceptible to high levels of friction and wear; of particular interest in this study are components in the valve train and the piston assembly. Modifying these surfaces can reduce the effects of friction and wear on these components and decreases the overall mechanical loss experienced by the engine. There is a significant amount of energy lost this way as shown in Figure 1-4.

Friction is accountable for around 33% of the total mechanical loss experienced in the engine. Research in surface engineering and tribology will help to achieve a drop in harmful emissions released by vehicles and can help automotive manufacturers to reach the emissions targets outlined above. It is estimated that by taking advantage of new technology for friction reduction such as coatings and surface texturizing, friction losses could be reduced by as much as 61% in the long term [7]. The advancement of technology in the field of surface coatings has led to very thin coatings which have been shown to reduce friction by 10 – 50% in lubricated contacts [7].

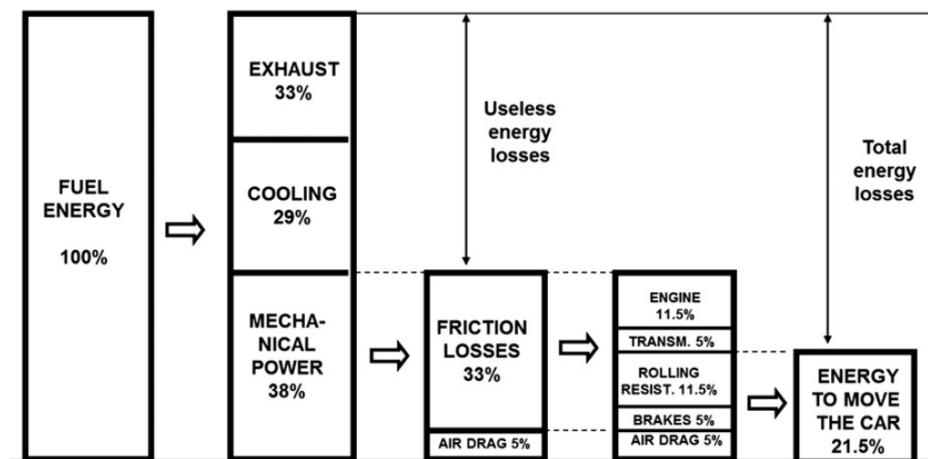


Figure 1-4: Energy distribution in a typical passenger car. Adapted from [8] and [7]

1.3. Objectives

In this study, Diamond-Like Carbon coatings are produced using plasma enhanced chemical vapour deposition, and microwave plasma enhanced chemical vapour deposition and some DLC acquired from commercial sources. The main objectives of this thesis are as follows:

Phase one: tribochemical evaluation of the tribochemistry of DLC

- To gain familiarity with the processing operations and to develop competency with regards to operating the coating deposition system at the University of Leeds.
- Create coatings in conjunction with Hauzer Techno Coating, namely a-C:H and Si-DLC.
- Compare the properties of a-C: H DLC, Si-DLC and the acquired W-DLC.
- Determine the effect of the lubricant additive ZDDP has on the coatings by comparing tribological testing with base oil.

Phase two: evaluation of microwave plasma as a coating production process.

- Configure and determine the optimal parameters necessary to optimally operate the microwave sources on the system.
- To use these sources to develop DLC coatings comparable properties to current PECVD DLC coatings.
- To determine the maximum hardness reachable using the microwave sources.

1.4. Thesis Outline

- Chapter One: An outline of the purpose of this thesis and some basic theories of tribology and plasma theory are discussed
- Chapter Two: A comprehensive review of the current literature, including methods of depositing DLC, different types, properties of existing coatings and tribochemistry of DLC.

- Chapter Three: An overview of the experimental methods used within this thesis.
- Chapter Four: PECVD deposited coatings are deposited and tested mechanically, tribologically and characterized fully.
- Chapter Five: The microwave PECVD system is used with one microwave source in order to deposit coatings. The testing within this chapter begins with preliminary testing and ends with a two variable matrix and concludes with an empirical equation useful for users.
- Chapter Six: The microwave PECVD system is again used to deposit DLC coatings and both sources are used. Preliminary testing begins the chapter, and the effect of varying the bias voltage to find the hardest possible coating concludes it.
- Chapter Seven: A comprehensive discussion surrounding the tribochemical interactions with the PECVD DLC is presented here, alongside further discussion concerning the effect of the deposition parameters on the final coating in the microwave PECVD processed
- Chapter Eight: Main conclusions and suggestions for future work are provided here.

1.5. Thesis Structure

Introduction				
Objectives				
Theory of Tribology and Coating Processes				
<hr/> Literature Review <hr/>				
<hr/> Experimental Methodology <hr/>				
Results				
PECVD			Microwave PECVD	
<i>a-C:H</i>	<i>Si-DLC</i>	<i>W-DLC</i>	<i>One Source</i>	<i>Two Sources</i>
<i>(Created at Leeds)</i>		<i>(Oerlikon Balzers)</i>	<i>(Created at Leeds)</i>	
<i>Mechanical Characterisation</i>			<i>Gas Ratio Tests</i>	<i>Optimum Position Tests</i>
<i>Tribological Tests</i>			<i>Optimum Time Tests</i>	<i>Optimum Power Tests</i>
<i>Tribochemical Characterisation</i>		<i>Discontinued</i>	<i>Optimum Position Tests</i>	<i>Bias Scan Matrix</i>
<i>XPS</i>	<i>Discontinued</i>	<i>Discontinued</i>	<i>Two Variable Matrix and Empirical Equations</i>	
<i>Mechanical Characterisation</i>				
Discussion				
<i>PECVD</i>			<i>Microwave PECVD</i>	
<i>Comparison</i>				
Conclusion				
Further Work				

1.6. Theory of Tribology

Tribology is defined as the science of friction, wear and the lubrication of interacting surfaces under relative motion [9, 10]. This makes the field of automotive engine design perfectly suited for the application of tribological theory and practice. Tribology has the ability to maximise efficiency in many different applications by reducing the friction and wear and by increasing the durability of the surfaces of these systems. Within an engine, this translates to the reduction of the fuel consumption of the vehicle overall, and a reduction in emissions. The main influencing factors within a tribological system are:

- Physical and mechanical properties – of the surfaces in particular. Many advanced surface engineering methods are used to enhance the surfaces of components (e.g. coatings, hardening, carburizing, texturing, and polishing). This is generally to reduce the friction of the surface and to prevent wear.
- Lubricants – the viscosity of lubricants is ever under scrutiny and differs all over the world in a car engine. The nature of lubricants with regards to legislation is tending towards lower viscosity oils. The reactivity of a lubricant (and its additives) is also an important factor – extreme pressure/corrosion inhibitors/friction modifiers etc. are added to engine lubricant and have different interactions with differently treated surfaces
- Operating conditions – within a car engine environment, of main concern are the temperature of the system, speed, pressure, sliding/rolling contacts, humidity etc. [9].

This study will concentrate on the surfaces of the valve train components, and pay particular attention to the development of DLC coatings.

1.7. Theory of Plasma in Coating Processes

The Hauzer Flexicoat 850 system at the University of Leeds employs PVD, PECVD and microwave PECVD deposition techniques. The deposition techniques employed within this project rely heavily on the use of plasma for a more dense, homogenous and uniform structure of the finished coatings. Enhancing the processes using plasma increases the deposition rate and overall efficiency, thus a fundamental understanding of plasma is necessary and highlighted in this section.

The plasma primarily increases deposition rate of the process and a separate plasma source can be used to etch the substrates before deposition. During deposition the plasma provides an ionized transport medium through which the target material may travel. Using plasma within a CVD process allows the average temperature to be lowered and thus new materials can be deposited and deposited on (for example, polymers may be coated). The deposition of DLC in particular benefits from this reduction in temperature, allowing harder structures to form at $< 400^{\circ}\text{C}$ rather than at the usual CVD operating temperatures which cause the sp^3 structure of DLC to collapse $> 400^{\circ}\text{C}$ [11].

A plasma is a quasi-neutral, ionized gas consisting of negatively charged electrons and positively charged ions [12]. Plasma is often referred to as the fourth state of matter and it is theorized that over 90% of the universe consists of plasma [12, 13]. Plasma exists within the universe as interstellar gas, stellar atmospheres, stars, and assists in the formation of planetary radiation belts, the sun, solar winds and flares.

On Earth, plasma is not formed under normal conditions due to the high temperatures and low pressures required for plasma to be sustained. Plasma is found on Earth only when such extreme conditions exist, it is seen as lightning, which is triggered by an electrical discharge occurring in atmospheric gas, which is ionized and greatly heated.

The recombination rate¹ is very high (due to insufficient pressures and temperatures on Earth) and as such the lightning exists for a very short period of time. Other natural phenomena of plasma on earth are the Aurora shown in Figure 1-5, which occur due to highly energised electrons and ions colliding with the atmosphere.



Figure 1-5: Aurora Australis. Picture taken from the ISS. Courtesy of NASA

The Earth is surrounded by a thick plasma known as the ionosphere at around 100 km above the Earth's surface, and above this is the magnetosphere, which is a layer of magnetised plasma [12]. Plasma existing on earth is mainly man made plasmas such as fluorescent tubes, fusion plasmas and electric arcs.

¹ The recombination rate is the process by which positive ions combine with negative ions or electrons to create neutral species.

The overall charge in a plasma is said to be neutral since the number of ions and electrons is approximately equal. Small deviations can occur on a local scale but these fluctuations are corrected by large electric fields produced within the plasma to establish charge neutrality [12]. Within a stable structured system such as a solid, the ionisation energies of atoms are much larger than their thermal energy, which allows it to remain stable. When the thermal energy is increased the material changes state from a solid to a liquid to a gas as the atoms become more loosely bonded. When the gas phase is heated above 10000 K or close to the atomic ionisation energy of the material, the individual atoms of the gas begin to decompose into a collection of electrons and ions, and a plasma state is established; this is a gradual process [14].

Plasma can also be generated by passing a potential difference across a cathode and an anode; this sustains the plasma and prevents its collapse by sustaining electron and ion energies. The particles released by the intense heating of a gas (electrons and ions) are not bound by each other but are strongly affected by the overall electromagnetic field of the plasma [13]. The plasma is dominated by these collective effects, known as long range coulomb interaction forces, which are of greater significance than short range forces and interactions between single particles.

Commonly used within a lab environment, a gas discharge plasma is generated by introducing a neutral gas such as argon into an evacuated chamber containing a cathode and an anode, a voltage is then applied across the electrodes (of 100s of V) . The free electrons in the neutral gas existing due to cosmic rays or background radiation become excited by the electric field produced by the potential difference across the anode and cathode and are accelerated towards the anode. The electrons

gain energy and collide with Ar atoms and ionize them. Equation 1.1 explains the reaction that takes place here.



An avalanche effect is created whereby the two free electrons have enough energy to bombard further Ar atoms and ionize them. In the PVD process, the Ar^{+} ions are attracted to the cathode (target) and collide with the target atoms with enough energy to release a target atom and another electron which will go on to further ionize the gas, the target atoms are then attracted to the negatively biased substrates and deposit. A similar process occurs within PECVD and microwave PECVD; in this case the gas used is a mixture of argon and acetylene. The gases are ionised in the same way; a high potential difference is generated across the deposition chamber, the positive ion species then deposit on the negatively biased substrates. This continues and leads to a cascade of ionising collisions, which generates a high current density, and allows the plasma to become stable and self-sustaining. The avalanche of ionisation is balanced by the recombination of lower energy ions and electrons which is the reason a ‘glow’ is seen, it is a result of photon emission during the recombination of an ion and an electron. Due to the recombination, the system experiences a voltage drop and the discharge enters the ‘normal glow’ region of the glow discharge regime, shown in Figure 1-6. If the voltage is increased, the discharge enters into the ‘abnormal glow’ region, where sputtering and etching takes place. The plasma density here reaches the desired level of $10^{15} \text{ m}^{-3} - 10^{19} \text{ m}^{-3}$. Decreasing the voltage at this point, and increasing the current density allows

thermionic emission of electrons which is used in cathodic arc deposition techniques, where the current density is much higher [13, 15, 16].

The plasma used in most processing environments is known as a cold plasma. The individual species are at very different temperatures: electrons can be a few eV, or over 10,000 K, whereas the larger ions are much heavier and slow moving and so are at a much lower temperature. This gives us a reasonably low average temperature and prevents a glow to arc transition (thus avoiding thermal evaporation of the cathode and eventual melting).

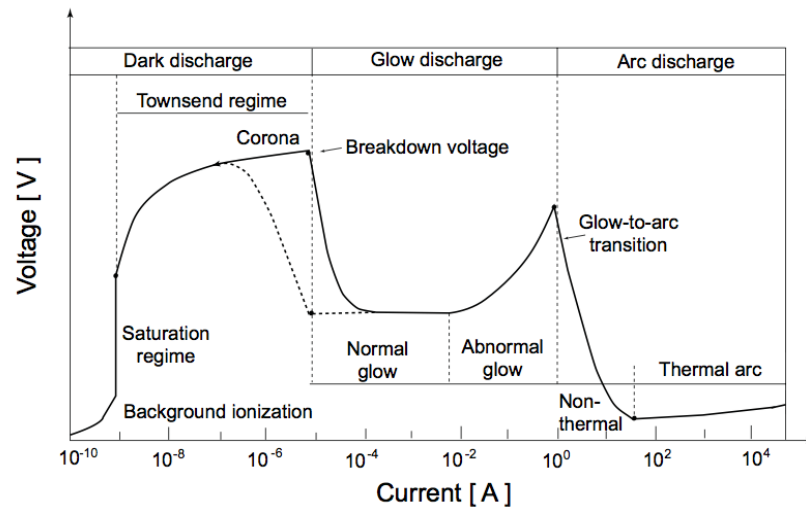


Figure 1-6: Glow discharge regime [17].

In the case of microwave PECVD, microwaves are used to increase the ionisation density (or rate) of the plasma and therefore depositing species. Table 1-4 presents a comparison between different processes involving plasma and their ionisation rate. As can be seen here, the ionisation rate for microwave PECVD is two orders of magnitude higher than that of traditional PECVD, which gives it a distinct advantage over this process in the form of a much higher deposition rate. This is due

to the quasi-parallel beam generated by the microwave system; this is described later in 2.7.6

Table 1-4: Comparison of ionisation percentage in different deposition techniques [18]

Process	Ionisation percentage
PECVD	0.01%
ECR	1 – 5%
Microwave PECVD	~ 10%
Core of Sun	100%

Chapter 2

Literature Review

2.1. Introduction

In this study the main objective is to develop Diamond-Like Carbon coatings with architectures that can withstand the pressures (650 MPa Hertzian contact pressure) and temperatures (100°C) found in a cam-follower interface using novel deposition techniques. A Hauzer Techno Coating 850 Flexicoat system has been recently commissioned at the University of Leeds, which will be used to create the coatings. The system incorporates a variety of Plasma Enhanced Physical and Chemical Vapour Deposition techniques, which are explained in this chapter.

2.2. Tribology of Valve Train Components

The modern valve train system within a passenger vehicle engine includes valves, valve springs, valve spring retainers, valve keys, rocker arms, piston rods, tappets and a cam shaft as can be seen in Figure 2-1. The valve train is mainly concerned with turning the rotary motion of the cam shaft into linear motion; this controls the fluid flow into and out of the combustion chamber. There are three common designs of the valve train; sleeve valve, rotary valve, and the most popular design, the poppet valve which is used by most major vehicle manufacturers [8]. There are many interfaces within the valve train that have potential to cause tribological

problems: valve guides, valve stem guides, valve seats, lifter guides, piston rings, pivots and bearings, the typical values of pressure and velocity are outlined for these component in Figure 2-2.

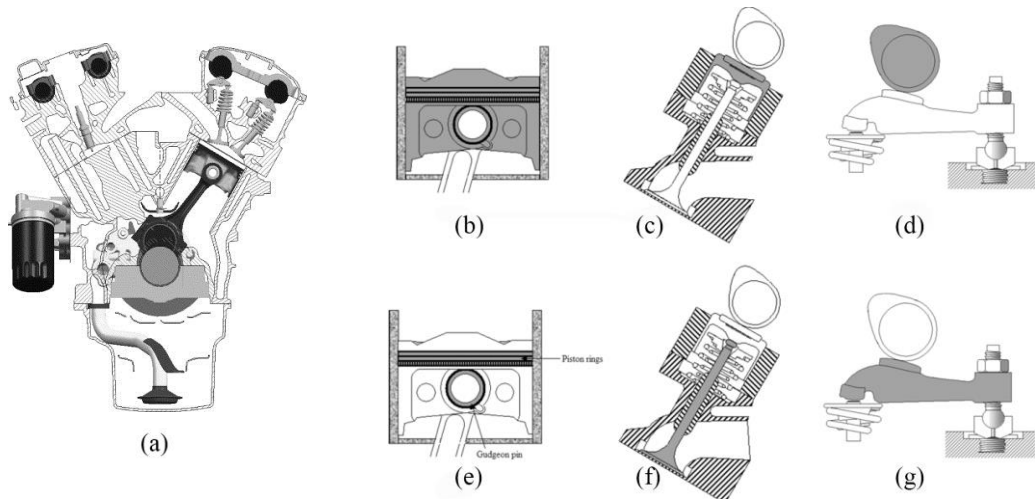


Figure 2-1: (a) Cross-section through a V6 engine with a valve train mechanism of centre pivot rocker arm or centre pivot rocker with a lifter with commonly coated parts highlighted in grey. (b) piston (c) tappet (d) camshaft (e) piston and gudgeon (f) valve stem and head (g) rocker arm [8, 19]

The most crucial interface in the valve train is the cam/tappet interface. This interface is notoriously difficult to lubricate, it experiences friction and wear problems arising from high pressures and high temperatures (100 - 500°C) [8]. Different surface treatments such as coatings, alternative materials and lubricant additives are currently being researched in an attempt to combat this issue.

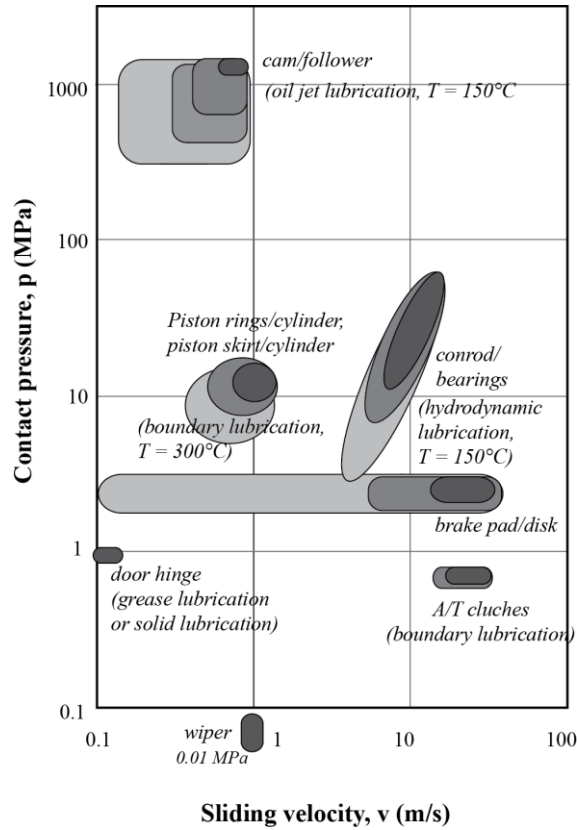


Figure 2-2: Typical P-V values of commonly coated engine components. Adapted from [20]

The application focused upon in this thesis is the cam/follower interface; the tribological conditions experienced here are presented in Table 2-1. Various studies have been undertaken with regards to coatings on a cam/follower interface. Notably, Yasuda *et al.* [21] used ion-plated DLC on steel shims, lubricated using fully formulated oils and observed a 45% reduction in friction when compared with a traditional phosphate coated shim. However, Lawes *et al.* [22] found that there was no significant difference when using DLC coated shims or the conventional steel shims. Nissan [23] have reported successful use of DLC on cam/tappet interfaces and claim a 40% reduction in friction, showing that there is great potential in this area.

Table 2-1: Typical tribological conditions of a cam/follower [24]

Property	Value
Maximum Temperature	150°C
Maximum Hertzian contact pressure	600 MPa
Lubrication regime	Boundary
Tribological condition	Rolling/sliding

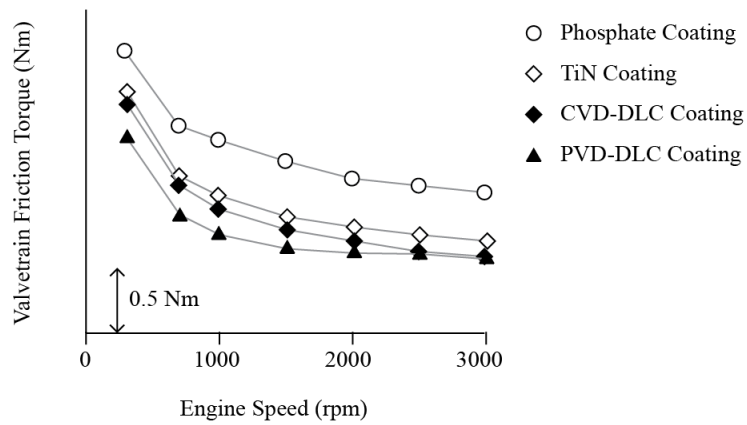


Figure 2-3: Comparison of friction torque vs speed for phosphate, TiN, CVD DLC and PVD DLC coated shims against camshaft [21]

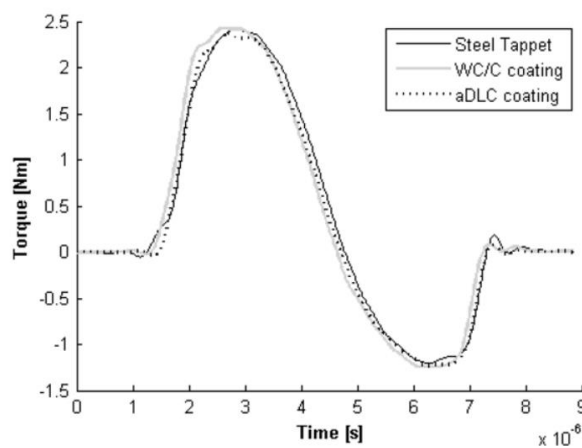


Figure 2-4: Comparison of torque vs time for uncoated steel tappet, WC/C-a-C:H and a-C:H coating [22]

2.3. Current Materials used in the Valve Train

The cam shaft itself is traditionally made from varying forms of cast iron with hardened cam lobes. The types of cast iron commonly used for this application are grey cast iron [25], chilled cast iron and nodular cast iron [20, 26]. Cast iron is used due to its low cost and its ready availability.

The cam follower or shim is commonly made from chilled cast iron with recent advances seeing the introduction of aluminium shims resulting in a 40% reduction of friction over traditional cast iron shims [27]. Aluminium requires extra measures such as coatings to avoid galling on the tappet walls.

2.4. Currently Used Surface Treatments

Current cast iron cam shafts and followers are subject to various surface treatments, intended to give the material long life wear resistance and short term running in time. Chemical conversion methods are used such as phosphating, oxidation, tufftriding and carburising [26], these methods change the surface chemistry of the cast iron by introducing different elements (e.g. carbon) to create a metal compound at the surface in order to protect it. Methods can that do not change the chemical composition of the surface of the material also can be used, such as shot peening and metal inert gas welding. Coatings can be applied to the surface for protection, these protect the substrate and donate their properties such as hardness, chemical inertness, low friction and wear resistance, without becoming the bulk material as they are often expensive and not suitable. Methods include: anodising, electroplating, high temperature spraying, weld coatings and more recently, the

introduction of physical and chemical vapour deposition, which has allowed the deposition of metallic and ceramic coatings to become increasingly more popular, with the deposition of chromium nitride, titanium nitride, tungsten carbide and diamond-like carbon all being introduced to engine components [28].

More recently, diamond-like carbon has been used as a low friction and low wear coating for engine components such as diesel fuel injection systems, pump plungers, pistons, piston rings, valve stem and head, and rocker arms. It is seen more commonly due to the recent innovations in technology, making the equipment needed for the deposition more widely available and more commercially viable, and the coatings have become more durable and with more desirable properties such as super low friction [28-30] and compatibility with lubricants [31-33]. The combination of this new technology and the existing problem seen in the cam tappet interface makes for an interesting area of research and potentially a solution to the high levels of friction and wear experienced in this application.

2.5. Diamond-Like Carbon

2.5.1. Historical Overview

Diamond-Like Carbon was first discovered in the 1950s by Schmellenmeier, as noted by Donnet [11]. Despite the novelty and high hardness of these coatings, they were largely ignored until around 20 years later when Aisenberg and Chabot [34] created (and coined the phrase) diamond-like carbon films using a new ion beam deposition technique using negatively biased substrates and carbon electrodes. This DLC was high in hardness and had unique properties such as scratch resistance and were highly corrosion resistant. This sparked an interest in DLC coatings, and

research around this area grew steadily throughout the 1980s; more techniques were developed, some more successful than others. Arc evaporation techniques successfully deposited DLC but with a rather uneven distribution of hardness across the coating [35].

In the mid-1980s, a European and American renaissance took place in the Plasma Enhanced Chemical Vapour Deposition (PECVD) of DLC coatings, having discovered its widespread use in Russia and Japan [36], the challenge was discovered to be in the stabilisation of the sp^3 content, or diamond-like portion of the coatings. During this time, it was correctly predicted that DLC could be potentially useful for magnetic recording media [37, 38]. Subsequently, tribological research using DLC began to take place on a more frequent basis, as was documented in Robertson's review article, which summarised the properties and developed nomenclature for this area [39].

The research taking place into DLC began to focus more on the tribological properties of DLC as huge arrays of potential applications were discovered [40-44]. DLC films with metallic inclusions were made [45], again furthering the range of applications, alongside a mountain of review papers published within the area which built on the work carried out from the mid-80s –90s [39, 46-48], to the early 2000s [18, 49-51] and more recently [11, 52].

2.5.2. Structure and Bonding Mechanisms

Diamond-Like Carbon has an amorphous structure with a network of sp^3 (diamond-like) and sp^2 (graphite-like) bonds which can also include hydrogen and other metallic dopants. The physical, chemical and mechanical properties rely heavily on

the sp^2/sp^3 ratio (this is the graphitic: tetrahedral bonding ratio which dictates the properties of the coating) of the coating and upon the amount of hydrogen and metallic dopants included. DLC coatings often incorporate hydrogen in amounts as little as 2% or as much as 50% [11, 18]. Hydrogen is included to stabilise the structure and this provides additional lubricity to the coating. Too much hydrogen can cause the mechanical properties of the coating to suffer due to the sp^3 bonding being inhibited. The sp^3 (diamond-like) bond is a three dimensional tetrahedral structure as can be seen in Figure 2-5. The carbon atoms are bonded covalently, by the sharing of electron pairs, this donates strong, hard, stiff, diamond-like properties; coatings with hardness up to 90 GPa have been noted [53]. The sp^3 bond in this case can be formed using low temperature deposition conditions ($< 400^\circ\text{C}$ [11]), using high ion energies and is metastable.

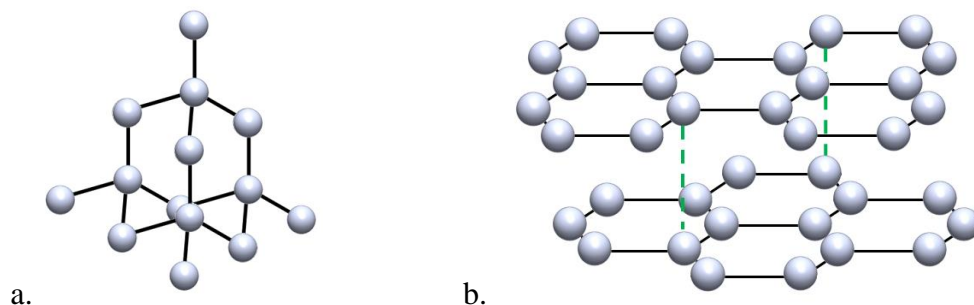


Figure 2-5: a. Tetrahedrally arranged C atoms and b. Graphitically arranged C atoms

The sp^2 bond is a two dimensional graphitic structure, as can be seen in Figure 2-5.b. This bond occurs naturally in graphite and is characterised by its strong intralayer bonding (covalent), yet weak interlayer bonding (Van der Waals). The weak interlayer bonding allows the ‘sheets’ of strongly bonded carbon atoms to slide over one another, this is due to the weak Van der Waals forces (or p bonds) that are formed between the layers. This allows for very low coefficient of friction films to

be produced (as low as 0.001 [50]). Figure 2-6 shows a ternary phase diagram of DLC [18], this shows the ratio of $sp^2:sp^3:H$ that occurs within different coatings and Table 2-2 shows the mechanical properties of different types of DLC. Robertson and O'Reilly [54] suggest that amorphous carbon consists of sp^2 bonded clusters which are interconnected by random networks of sp^3 bonded atoms.

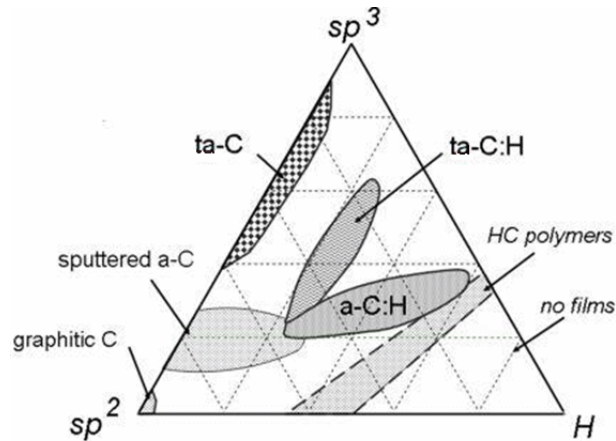


Figure 2-6: Ternary phase diagram for DLC coatings [18]

Table 2-2: Typical DLC film properties adapted from [19]

Type	Hydrogen (%)	sp^3 (%)	Hardness (GPa)	Elastic modulus GPa
Diamond	0	100%	100	1144
Graphite	0	0	0.2	9 – 15
a-C:H (hard)	30 – 40	40	10 – 20	140 – 170
a-C:H (soft)	40 – 50	60	< 10	50
ta-C	0	80 - 88	40 – 90	757 ± 47.5
ta-C:H	30	70	< 50	300 ± 49
W DLC	20	~50	13	100 – 150
Si DLC	15	60 – 84	14 – 25	100 – 175

The term DLC encompasses a broad range of different coatings with varying ratios of $sp^2:sp^3:H$ and therefore a vast range of mechanical properties. Different elements may also be incorporated into the coating, such as Si, W, Ti, and different interlayers can also influence the properties.

It is clear to see that the structure and properties of the coating depend on bond types, but this in turn also relies heavily on the deposition type and parameters. The key parameters within the deposition stages are:

- Ion energy – this is the energy of the depositing ions. This energy has an optimum value of around 100 – 150 eV [11, 55]. This parameter is controlled by the bias voltage.
- Bias voltage – the negative bias voltage placed on the substrates is used to attract the positively ionised species within the chamber in order for them to deposit. The bias has been shown to affect the adhesion, hardness, wear resistance and compressive stresses within the film [56]. By varying the bias voltage, the high compressive stresses that are characteristic of all DLC coatings, can be reduced, alongside the amount of sp^3 bonding [56, 57]. As a consequence of this, some of the key mechanical properties of the coating such as stiffness and hardness are also reduced due to the sp^3 content being decreased [58]. Despite this, a higher bias voltage can promote a more homogenous, dense structure [59], which is important when depositing a functional as opposed to a decorative coating. A compromise must be reached between the two extremes in order to select the correct bias voltage.
- Pressure – the pressure within the deposition chamber is a vital part of the processing. This parameter affects the amount of defects within the coating

and the deposition rate and the stability of the process. An increase in the pressure allows for a higher deposition rate. Choi et al. [60] discovered a 12 fold increase in deposition rate when raising the chamber pressure from 0.3 – 2 Pa; an increase in surface roughness and a decrease in key mechanical properties such as hardness and elastic modulus was also noted. Lower pressures allow the mechanical properties to remain at a desirable level and the inclusion of unwanted impurities are eliminated, but this is at the cost of a lower deposition rate.

- Temperature – the temperature within the chamber and of the substrates is an important factor, especially when depositing DLC. DLC is extremely sensitive to temperatures above 600°C [11] due to the metastable nature of the sp^3 sites within the coating. Above this temperature, these sites collapse into an sp^2 matrix. A cold working plasma can be used in order to decrease the temperature. A decrease in temperature has been shown to increase the sp^2 / sp^3 ratio [61], whilst leaving the properties of various interlayers unaffected.
- Gas Type – The hydrocarbon gas used to deposit DLC can vary. In general, a low hydrogen/carbon ratio gas is chosen in order to minimize hydrogen content within the finished coating, a gas such as acetylene or benzene. Acetylene is commonly used as it has a low ionisation energy and a high deposition rate. Acetylene has $C\equiv C$ bonds meaning that it has a simple dissociation pattern and experiences much less plasma polymerization [11, 18]. The different types of hydrocarbon gases that can be used for this application, their ionisation potentials and deposition rates are presented in Figure 2-7.

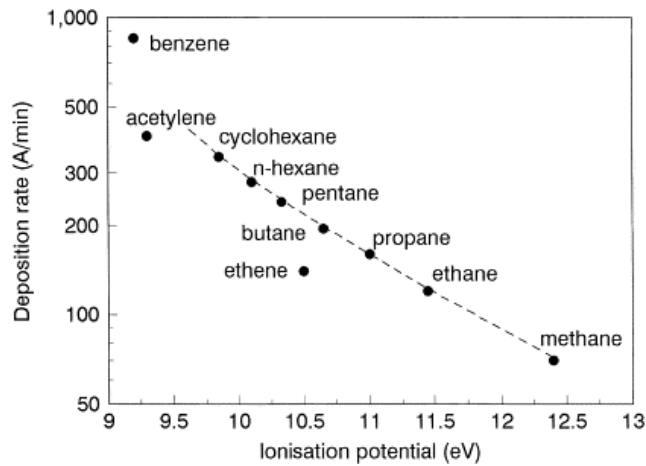


Figure 2-7: Deposition rate of DLC vs ionisation potentials of different hydrocarbon gases used in processing [18]

Other factors such as the substrate material [62, 63], gas type [11] and deposition time can also affect the properties of the coating.

The deposition process and more importantly, the ion energy govern the characteristics of the DLC coating. The sp^3 content in pure a-C relies on a subplantation process, this process occurs when an incoming C ion gains a high enough energy to break through the outer layer of the substrate and gives rise to subsurface growth [11]. This causes localised densification and high stresses, and as such is a metastable phase which can be affected by high temperatures and high pressures. This structure occurs at a C ion energy of around 100 eV, because the structure of sp^3 bonded carbon is metastable, lower ion energies cause sp^2 bonds to form, which stick to the surface rather than sub-planting due to their lower energy; higher energy ion collisions also cause the structure to relax into the lower energy state sp^2 orientation. The growth of a-C:H films is similar to this process but slightly more complex than pure a-C due to the inclusion of H and other radicals (see Figure 2-19) [18]. The ion bombardment causes the abstraction of H while another is

incorporated into the film as an addition to dangling C bonds, and so does not decrease H content. Increasing ion energy causes a decrease in H content and also in sp^3 sites. The sp^3 content however does not decline as fast and therefore a maximum energy can be reached, this is where the hardness and elastic modulus reach a maximum. Bias voltage, plasma energy and microwave energy also affect the ion energy.

2.5.3. H/E ratio

Theories of wear regard the hardness of a coating or material as an important factor [64], however it has been noted in the literature that the elastic modulus of a material must not be ignored when attempting to predict the wear resistance [65-69]. Leyland and Matthews have drawn attention to the importance of the H/E ratio and explored it in great detail [70, 71]. The H/E ratio is included in the plasticity index of a material, this describes the materials ability to deform plastically in the face of an abrasive [70, 72], which in turn has been linked to the elastic strain to failure as a prediction of the coatings wear performance. For hard coatings exhibiting similar H/E ratios, those with lower elastic modulus have been found to outperform those with higher elastic modulus with regards to wear performance [73]. Musil *et al.* have suggested that coatings with high hardness with a H/E ratio of over 0.1 and a low E^* (where $E^* = E/(1-\nu)$) are preferred for wear-resistant applications [73, 74].

Leyland *et al.* [70] agree with this, describing a high H/E ratio as being an indicator of the wear resistance of a coating, with the exception of coatings with ultra-high hardness (> 70 GPa), as these have a high elastic property mismatch between coating and substrate. Diamond has a H/E ratio of 0.1, whereas DLC can have H/E

ratios over 0.16 [18] which suggests excellent wear rates, however this isn't always the case in practice [75-77].

Musil's [74, 78] work has proven the H/E^* ratio including low elastic modulus of a material to be effective as can be seen in Figure 2-8, whereby the coatings with a high hardness and lower E^* demonstrate a resistance to cracking, as is shown in the yellow regions. This experiment was carried out using Al-O-N coatings deposited on Si(100) substrates, where W_e is the elasticity and τ_{O_2} is the length of the oxygen pulse used in the deposition process.

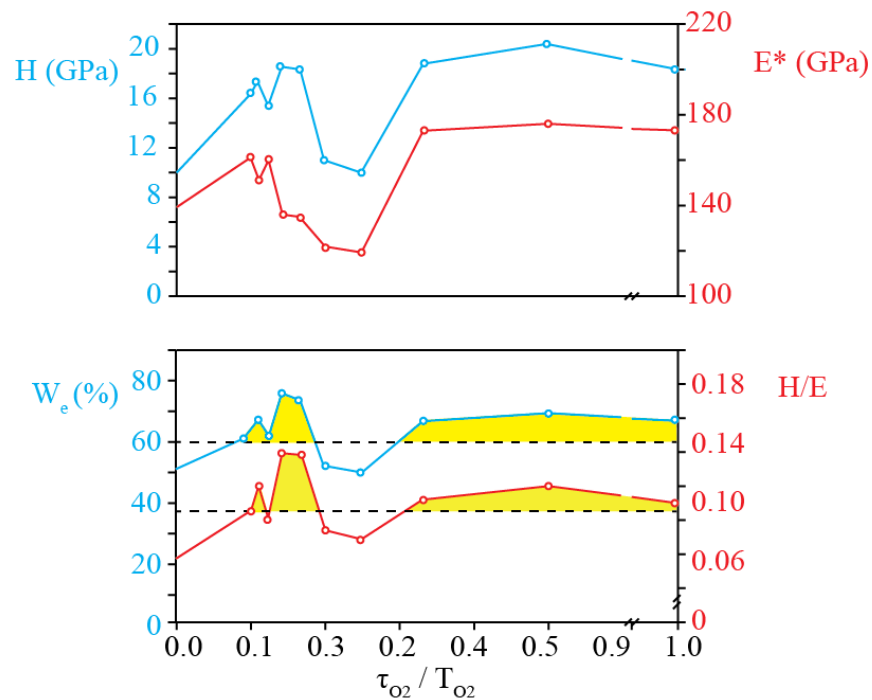


Figure 2-8: H , E , W_e and H/E ratio of Al-O-N coatings and their resistance to cracking using a diamond indenter. [74]

2.5.4. Adhesion

High energy ions bombard the substrate during deposition in order for film growth to occur. This promotes the formation of sp^3 sites and introduces high compressive

stresses into the structure, which are characteristic of DLC coatings [57]. High internal stresses promote poor adhesive properties of the coating to the substrate, especially when subjected to thermal expansion and contraction [79], and where there is thermal and plastic mismatch between the DLC and the substrate [80]. The thickness of a majority of tetrahedral (ta-C) DLC films is limited to around 0.1 – 0.2 μm [81] due to the high internal stresses generated by the deposition process. a-C:H with a mixed ratio of sp^2/sp^3 sites is limited to around 3 μm .

Adhesion is of fundamental importance to the durability and quality of DLC coatings, and as such, the reduction of internal stress has become an important factor in DLC research [11]. Many different methods have been suggested and are currently being used to combat this issue. Methods such as plasma pre-treatment (etching) of the surface, thinner carbon layers, interlayers to act as adhesion promoters which allow a gradual change in thermal expansion coefficient throughout the structure (such as Cr, CrN, TiN, WC, SiC etc). Functional gradient layers have also been developed which introduce carbon gradually before the final DLC layer. These have been found to improve adhesion [62].

Elements can be doped into the coating structure to enhance adhesive properties (such as W, Ti, Mo, WC, Cr, etc.). Whilst improving the internal stress within the structure, they can also aid other mechanical and lubrication properties of the coating [11, 18], the incorporation of tungsten in DLC has been shown to reduce the coefficient of friction of the surface (in fully formulated lubricant) by up to 50% [82]. Examples of the adhesion of coatings tested using a scratch tester can be seen in Table 2-3.

Table 2-3: Examples of critical load values taken from scratch testing of different types of coating

Coating	Critical Load (N)	Substrate	Reference
CrN	4 – 18	Stainless steel/Si wafer	[83]
Ti/TiN	10 – 30	Si wafer	[84]
r.f. PECVD DLC	8 – 15		
PVD/CVD DLC	15 – 30		
Ti-DLC	10 – 35	Cr6 Steel	[85]
W-DLC	8 – 26		
Si-DLC	8 - 20		

The structure, interlayers and dopants included in DLC govern the properties of the finished coating. Subsequently, the recipes and deposition parameters will be compiled using the experienced advice of Hauzer, and knowledge gathered from the literature surrounding this area to create coatings with good friction and wear properties, whilst offering performance required within a cam/tappet environment.

DLC coatings have found many industrial applications such as:

- Bearings (friction reduction) [86-88]
- Razor blades (prolonged life) [88-90]
- Automotive components (for both racing and selected production vehicles) [11, 19, 88, 91]
- Magnetic storage media (improved tribological properties) [87-89, 92]
- Biomedical applications (protection from metallic ion release) [52, 88, 90, 92]

These applications provide us with an important area of research looking toward the advancement of these and more tribological applications.

2.5.5. Deposition Parameters and Typical Properties of DLC Coatings

Typical parameters have been obtained from literature surrounding DLC coatings shown in Table 2-2, the full table of results found from various sources can be found in Table 2-6 Table 2-7 and Table 2-8. The properties of the deposited coatings are expected to fall within the bounds presented in Table 2-2 and meet the criteria found in the literature. Table 2-6 Table 2-7 and Table 2-8 have been compiled using various sources from the literature (as shown) and provide a comparison between differing deposition parameters and end results. As is evident from the tables containing the literature values, there are many parameters which influence the coating. A bias voltage above 100 V has been postulated to lower the sp^3 content of the films, introduce high stresses and has a negative effect on the hardness and wear resistance of the film [56, 58, 93]. However, low bias voltage (50 – 100 V) can produce softer coatings; an optimum value for this must be found for each piece of deposition equipment.

There are some values missing within the table, due to the lack of information in the literature, but enough information is presented to gain a general view of the numbers used within processing and the potential and expectations from DLC coatings.

Table 2-4: Properties of ta-C from the literature (FC – Filtered cathodic arc deposition, AI – Arc Ion plating)

Coating	Method	Bias (V)	Thickness (μm)	E (GPa)	H (GPa)	K_{DLC} (m^3/Nm)	K_{C} (m^3/Nm)	μ	Lubricant	Reference
ta-C	FC	0	0.2		59					[94]
ta-C	FC	-100	0.2		59					[94]
ta-C	FC	-500	0.2		59					[94]
ta-C	FC	-200	0.2		59					[94]
ta-C	FC	-85			52			0.09		[56]
ta-C	FC	-300			35			0.07		[56]
ta-C	AI		0.5	650	65			0.07	PAO	[29]
ta-C	AI		0.5	650	65			0.08	5w-30	[29]
ta-C	AI		0.5	650	65			0.02	PAO + GMO	[29]
ta-C	FC		-			1.60×10^{-17}	1.10×10^{-17}	0.05	API group III Base Oil	[95]

Table 2-4 shows data from the literature concerning ta-C, from which, the following can be summarised:

- ta-C is most commonly deposited using filtered arc and arc ion plating.
- It has a characteristically high hardness and elastic modulus (> 59 GPa in literature reviewed).

- ta-C has a tendency to be considerably thinner than a-C:H deposited using PECVD (commonly around 2 – 3 μm thick as seen in Table 2-5).
- This could possibly be a limitation of the process.
- Has a wide range of friction values, from 0.09 – 0.02. However, super-low friction was found in the presence of a high wt. % of GMO, friction modifier.

Table 2-5 presents data from the literature concerning a-C:H coatings. From this, the following can be surmised:

- a-C:H is most commonly produced using PECVD.
- Has a higher thickness in comparison to ta-C, this could be due to the high residual stress in the ta-C coating being a limitation.
- a-C:H is lower in hardness than ta-C, and also has a lower elastic modulus.
- Both a-C:H, ta-C and the microwave produced a-C:H (from limited data) showed similar coefficients of friction.
- Low wear rates are seen amongst the a-C:H presented here, with values of $10^{-19} \text{ m}^3/\text{Nm}$.

Table 2-5: Properties of a-C:H from the literature (M – Magnetron sputtering, PE – PECVD)

Coating	Method	Thickness (μm)	E (GPa)	H (GPa)	K_{DLC} (m^3/Nm)	K_{C} (m^3/Nm)	μ	Lubricant	Reference
a-C:H	M	3.5	110	8.8	9×10^{-8}		0.15		[96]
a-C:H 20% H	PE	1			2×10^{-18}	NMW	0.09	API group III Base Oil	[95]
a-C:H 20% H	PE	1					0.09	PAO + GMO	[29]
a-C:H 30% H	PE				D	4.4×10^{-19}	0.1	PAO + Secondary ZDDP	[77]
a-C:H 30% H	PE				9.2×10^{-19}	9.5×10^{-19}	0.057	PAO + Moly Dimer + Secondary ZDDP	[77]
a-C:H 50% H	PE	3	130	16		7×10^{-20}	0.045	PAO + MoDTC + ZDDP	[97]
a-C:H 50% H	PE	3	130	16		1×10^{-17}	0.075	PAO	[97]
a-C:H 50% H	PE	3	130	16		1.2×10^{-18}	0.05	PAO + MoDTC + ZDDP	[97]
a-C:H 50% H	PE	3	130	16		7×10^{-18}	0.1	PAO	[97]

Table 2-6 Properties of a-C:H deposited using microwave PECVD (MP)

Coating	Method	Bias (V)	Thickness (μm)	E (GPa)	H (GPa)	μ	Lubricant	Reference
a-C:H	MP	0 – -150		160 - 200	16			[98]
a-C:H	MP	-150			25			[99]
a-C:H	MP	0 – -350			5 - 30			[100]
a-C:H	MP	-375 – -550		174- 186	14 - 16	.7 – 1.5	dry	[101]
a-C:H	MP		1					[102]
a-C:H	MP	-100		132 - 160	15 - 19			[103]
a-C:H	MP	-125 – -250			13 - 25			[104]

From Table 2-6, which is comprised of data from the literature concerning a-C:H created using a microwave PECVD method, the following can be summarised:

- High hardness relative to that found in the a-C:H (Table 2-5) has been shown (> 16 GPa).
- Friction coefficient of 0.7 is comparable to that found in PECVD DLC (Table 2-5) however very high friction values of 1.5 were found but this was in dry sliding conditions where the microwave PECVD coatings are concerned, whereas in the PECVD coating test, friction modifier was used, alongside a lubricant and so the values cannot be compared directly.

- The microwave PECVD DLC coatings have comparable properties to those created using PECVD, whilst having the advantage of a much lower deposition time (~ 15 minutes compared with 2.5 + hours PECVD).

Table 2-7: Properties of tungsten doped DLC from the literature (PE – PECVD, M – Magnetron sputtering)

Coating	Method	Thickness (μm)	E (GPa)	H (HV)	K_{DLC} (m^3/Nm)	K_{C} (m^3/Nm)	μ	Lubricant	Reference
a-C:H:W 15% H	PE	1			4.40×10^{-17}	1.00×10^{-17}	0.06	API group III Base Oil	[95]
a-C:H:W 15% H, 12% W	M		135 ± 5	1183 ± 80	11.2×10^{-17}	0.93×10^{-17}		Base Oil	[105]
					0.11×10^{-17}	0.02×10^{-17}		Base oil + ZDDP	
a-C:H:W 15% H, 14% W	M		140 ± 7	1250 ± 80	0.73×10^{-17}	12.0×10^{-17}		Base Oil	[105]
					1×10^{-17}	8.67×10^{-17}		Base oil + ZDDP	
a-C:H:W 15% H 18% W	M		165 ± 3	1318 ± 35	8.8×10^{-17}	1.04×10^{-17}		Base Oil	[105]
					2.9×10^{-17}	0.5×10^{-17}		Base oil + ZDDP	
a-C:H:W 15% H, 21% W	PE		118 ± 6	1190 ± 60	14.4×10^{-17}	0.85×10^{-17}		Base Oil	[105]
					12.7×10^{-17}	0.72×10^{-17}		Base oil + ZDDP	

Table 2-7 shows data from the literature concerning tungsten doped DLC and the following summary comments can be made:

- A higher sliding wear rate than the PECVD DLC was noted.
- Has a lower hardness relative to the PECVD DLC and Microwave DLC.

Table 2-8: Properties of silicon doped DLC as in the literature (PE – PECVD, M – Magnetron sputtering)

Coating	Method	Thickness (μm)	H	K_{DLC} (m^3/Nm)	K_{C} (m^3/Nm)	μ	Lubricant	Reference
Si DLC	PE	1		2.00×10^{-18}	1.00×10^{-18}	0.01	API group III Base Oil	[95]
Si DLC	M	3.5	1235 $K_{0.1}$			0.08		[10 6]
Si DLC	M	0.6	1761 $K_{0.1}$			0.15		[10 6]
Si DLC	M	1.4	1325 $K_{0.1}$			0.11		[10 6]
Si DLC	M	0.5	1430 $K_{0.1}$			0.12		[10 6]
Si-DLC	M		30 – 40 GPa	$0.6 – 0.9$ $\times 10^{-15}$		0.06 – 0.15	Dry	[10 7]
Si-DLC	M/P E					0.06 – 0.2	Dry	[10 8]

Table 2-8 presents some data from the literature regarding Si-DLC. The following principal points can be made about these data:

- On the whole, the friction coefficient is larger than that seen in a-C:H in Table 2-5.

All of the literature values presented in tables 2-4 – 2-8 have differing friction values which rely on the coating and also on the counter face material, for example, in the case of DLC sliding against DLC this value will be much lower than DLC sliding against a steel counterface [95]. Thus these values are a function of the counterface and sliding conditions, and must be viewed as such.

2.5.6. Tribochemistry of DLC

ZDDP was first used by Lubrizol in 1941 as an antioxidant additive, its anti-wear properties were discovered around 15 years later in 1955, when it was discovered that less wear problems on the cam follower interface where ZDDP was included in the oil, this led to the rapid uptake of ZDDP in engines oil [109]. The mechanism of ZDDP protection of ferrous surfaces is well understood, however, this is not the case when applied to DLC coatings.

2.5.6.1. The Anti-Wear and Extreme Pressure Performance of ZDDP

The anti-wear tribo-film formed by ZDDP also acts as an extreme pressure additive; this property is useful in environments such as the cam/follower interface where the elastohydrodynamic lubrication film breaks down [110] . The physisorption of ZDDP is said to begin at around 50°C, and the chemisorption, or the chemical reaction of the component with the surface (Fe material) at 80°C [111] . ZDDP is said to be more effective on harder surfaces, and that better wear protection is

achieved where there is only a small difference in hardness between the two interacting surfaces [111, 112].

2.5.6.2. The Chemical Composition of a ZDDP Tribo-Film on Ferrous Surfaces.

The tribo-film created by ZDDP is said to consist of varying chain length phosphates, originally proposed by Bell et al. [113] is shown in Figure 2-9. The lower layers of the film here are shown to be iron sulphides and oxides.

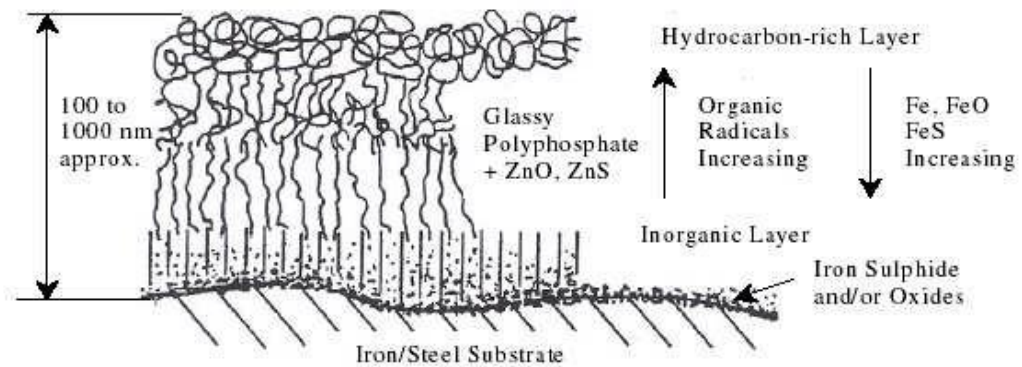


Figure 2-9: Structure of ZDDP as proposed by Bell *et al.* [113]

A three step mechanism for the decomposition of ZDDP and the formation of a protective tribo-film was hypothesised by Yin *et al.* [114].

- ZDDP is physisorbed onto the steel surface.
- Reaction between ZDDP and oxides forms zinc metaphosphate, $Zn(PO_3)_2$ and a small portion of zinc sulphide.
- $FeZnP_2O_7$ forms as pyrophosphate and $FeZn(PO_4)_2$ forms as an orthophosphate.

It was also hypothesised at this time that the final steps in this reaction occur slowly, and that the long chained phosphate forms and due to the interaction of the two surfaces these are broken down into 7short chain polyphosphate.

In contrast to this, Martin *et al* [115] found that, although there was a similar structure, no oxide/sulphide layer existed within the ZDDP tribo-film. A model of formation based on the HSAB (Hard Soft Lewis Acid Base) – which is the theory of stability of compounds and reaction mechanisms: it tells us that hard acids (small species with high charge and are non-polarisable) react faster and form stronger bonds with hard bases and that soft acids (larger species with low charge and are strongly polarisable) react faster and form stronger bonds with soft bases - was formed, highlighting the possibility of iron oxide wear particles being digested and eliminated by the formation of Fe/Zn phosphates. Fe^{3+} is a harder Lewis acid than Zn^{2+} and this exchange is more favourable based on the HSAB principle highlighted above, and since phosphates are hard bases which will preferentially react with hard acids, iron and phosphate will react and form a tribo-film. The composition of the proposed tribo-film by Martin *et al.* is seen in Figure 2-10.

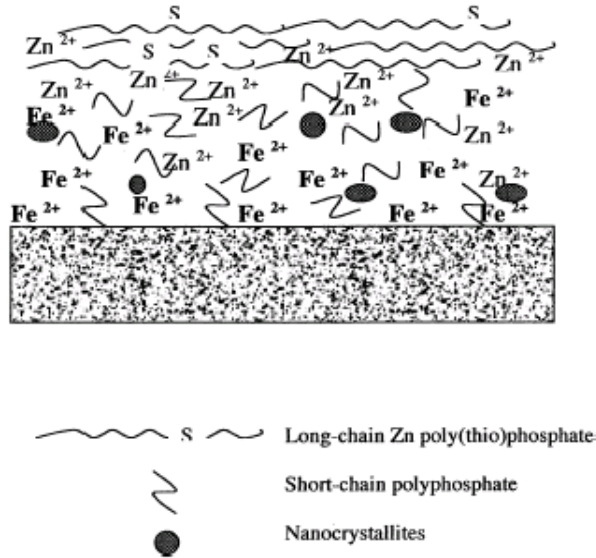


Figure 2-10: Composition of ZDDP tribo-film as proposed by Martin et al.[115]

The structure of ZDDP on a steel substrate is described by Spikes [109] as being a ‘pad-like’ structure shown in Figure 2-11.

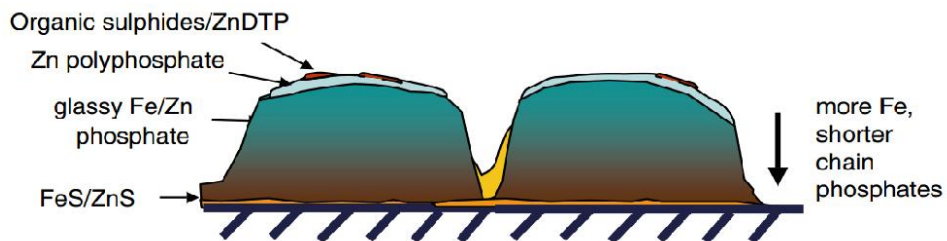


Figure 2-11: Pad-like formation of ZDDP derived tribo-film on ferrous materials [109]

It is this structure that protects the surface of a substrate during sliding and is under much debate as to whether it forms on a DLC interface, due to the inert nature of this coating. For example, the inertness of the DLC was documented by Kano *et al.*, [116] whereas Miyake *et al.* [31], de Barros’ Bouchet *et al.* [97] and Equey *et al.* [117] all found ZDDP tribo-films at DLC/DLC and DLC/steel interfaces.

Haque [77] found that the addition of the anti-wear additive ZDDP and friction modifiers moly dimer and moly trimer were crucial to ensure the protection of hydrogenated diamond-like carbon coatings sliding against cast iron, and found a ZDDP derived tribofilm at the surface of the DLC. He notes that the wear mechanism for the removal of the coatings in certain cases is due to the wear induced graphitisation at the surface of the coating induced by increased pressure, this area then being removed due to the tribological contact conditions. During similar testing, a transfer film consisting of graphitic carbon species was detected on a cast iron counterbody [118], indicating that the friction protection of the lubricant additives was supplemented by the transfer film.

The anti-wear additive ZDDP was found to have a large impact on the performance of the coating when used alone, where the wear mechanism was found by AFM to be that of primarily polishing wear, but when other lubricant additives were added, this performance was compromised. The addition of moly dimer into the system changed the wear mechanism to that of third body abrasion, which resulted in grooving of the coating [118, 119], this was also found to be the case for Mistry *et al.* [120].

Yasuda *et al* [21]. noted that a-C:H experienced high friction values (0.11) whereas non-hydrogenated a-C gave a lower value of 0.07 [116] both in the presence of engine oil 5W-30. They found no tribofilm on the a-C coating, although this was present against the counter-body (steel AISI 52100).

Conflicting views are widely present within the literature as to the tribochemical reactions between DLC coatings and lubricant additive. Since the term DLC

encompasses a wide variety of coatings, it cannot simply be said that DLC forms a tribofilm, since it is clear that the vast array of surface chemistry alters the tribochemical reactions within the lubricant. The additive interactions are therefore wholly dependent on the nature of the tribo-couple, and the optimum performance of the lubricant and surface characterisation will rely on coating-specific investigation.

2.6. Surface Preparation

The substrate surface is one of the most important factors in deposition and film formation; it must be of measurable and reproducible quality, free from surface defects, dirt and grease. The main concern when preparing the surface for any kind of coating (be it PVD, PECVD, Electroplating etc.) are contaminants on the surface. A contaminant can be a particulate species present on the surface, an entire oxide layer formed (usually on more reactive species) or grease left from fingerprints.

The properties of the deposited film depends heavily on the condition of the substrate surface, important factors include:

- Surface roughness [121, 122]
- Contaminants [123, 124]
- Surface composition [125, 126]
- Preferential nucleation sites [127]
- Thermal coefficient [128]

In order to reduce surface contamination, the surface must be cleaned. Pre-treating surfaces is of paramount importance, any residual particles or grease can affect the coating adhesion and properties, creating atomistic displacements, pin holes and

delamination points, all of which can cause the coating to fail. For example, an entire oxide layer on the surface of a substrate may prevent electrical contacts being made, cause low nucleation density and promote the poor adhesion of the film to the surface. Single particulate contamination (or local contamination; grease, fingerprints, dust) can cause poor adhesion of the coating to substrate on a local scale, and also be the cause of pinholes, surface inclusions etc. [129, 130]. Atomically clean surfaces can be achieved but this can be expensive and time consuming (especially when considering possible contamination in the deposition chamber, room etc.) and often unnecessary; usually an acceptable level of contaminants remain on the surface. There are multiple ways to clean a surface to prepare it for coating, a few are outlined below:

Degreasing: The degreasing stage of cleaning removes dirt, soil and grease from the surface using a solvent, an alkaline or a mild acid. The substrate can then be immersed in to a solution, be brushed or sprayed onto the substrate or the solution can be degreased using vapour [129, 131].

Ultrasonic cleaning: Ultrasonic cleaning uses cavitation to clean a surface. High temperatures and very high pressures local to the surface of the substrate, which then erodes the surface and removes contamination [124].

Abrading: Harder surface contamination layers, such as oxide layers can be removed by abrasive techniques, i.e. sand blasting, shot peening, sanding etc [129].

Plasma Etching: Plasma etching uses a high energy plasma in order to remove rather than deposit atomic layers by bombarding the substrate surface. Deposition and ion implantation are avoided by using low energy ions. Etching not only cleans the

surface but also activates the substrate surface and improves adhesion of the coatings, it has been reported that the optimum duration for argon etching for DLC is 15 minutes [126]. The etching achieved with plasma is generally isotropic due to the nature of plasma. Little atomic damage occurs when plasma etching and so this will be used before any coating is applied to the samples.

Metal Ion Etching: Ion etching is a purely physical process, which accelerates metal ions towards the substrate surface. Since this process is very directional, selective etching can be easily achieved with the correct equipment [132]. Atoms are physically knocked from the substrate by the high-energy ions (energies of several hundred eV); this causes severe lattice damage within the upper atomic layers of the substrate, can also cause implantation of the ionized species and due to the high ion energies, heats the substrate to high temperatures which may further damage the structure. A more reactive species can be used during ion beam etching; this is commonly used to achieve the chemical reactivity seen in plasma etching and the physical bombardment of ion beam sputtering to combine the desirable properties of both.

2.7. Deposition Techniques

2.7.1. Physical Vapour Deposition by Magnetron Sputtering

Physical Vapor Deposition (PVD) is an atomistic deposition process whereby coatings are formed by the evaporation or sputtering of atoms from a target in a low pressure environment. The ionized gas (in this instance, argon) atoms collide with the target materials and eject metal ions, these are then attracted to the substrates by a negative bias voltage which is applied to the table, in addition with an array of

permanent magnets and electromagnetic coils. These direct the ionized species towards the substrates ensures a greater efficiency of deposition than the bias voltage alone. This mechanism is illustrated in Figure 2-12.

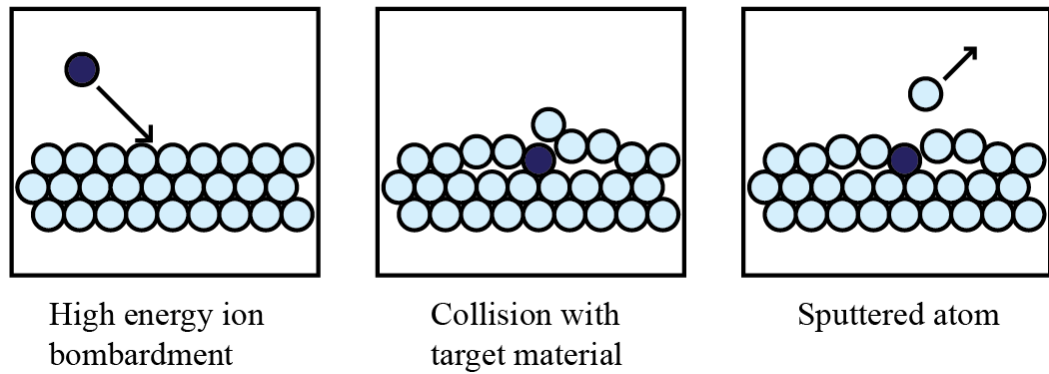


Figure 2-12: Schematic of sputtering PVD process

Target materials can be of any composition; elements, alloys or compounds can all be deposited this way [129]. Alloys and compounds must be of a homogenous structure to achieve uniform deposition on the substrate. Target materials must be as pure as is needed for deposition, in some cases, cost is a bigger issue than performance, in this case lower purities can be used (~96%), however, for highly functional applications, 99.999% pure targets are used [129].

2.7.2. Arc Deposition

Cathodic arc deposition is another method of coating deposition and is employed within many industries. It is a potential rival for microwave enhanced plasma chemical vapour deposition and relies on different deposition mechanisms.

A cathodic arc produces a plasma discharge at a high current density ($>10^{10}$ A/m²) and at a low voltage (10 – 40 V), thus falling in the thermal evaporation region of

the glow discharge regime shown in Figure 1-6. Two electrodes are brought together for a short period and then separated to initiate an arc. A cathode spot² develops on the cathodic electrode due to the high current density ($10^4 - 10^8 \text{Am}^{-2}$) at these locations, the current is concentrated over an area roughly 1 – 10 μm diameter that appears to scan across the cathode, - however a cathode spot is only present at the same location for around 10 ns – 1 μs - and many can be produced. Very high levels of ionisation are achieved and where more cathode spots are present a more dense plasma is generated. The plasma created flows away from the cathode via an explosive emission process and is attracted to the negatively biased substrates; this creates a self-sustaining discharge [133]. Most of the depositing material produced from the arc is in vapour form; however some escapes as larger globules of the material commonly referred to as macro droplets. The macro droplets are expelled from the cathode in molten form and quickly solidify in their path to the substrate. The presence of macro droplets in the finished film can adversely affect the overall properties by introducing internal stresses and delamination points. Filters are used to stop the macro droplets being incorporated into the coating, as can be seen in Figure 2-13. One common solution to this problem is a non-line of sight deposition systems such as Figure 2-15 as used by IBM [134].

² A cathode spot is a region of high current density.

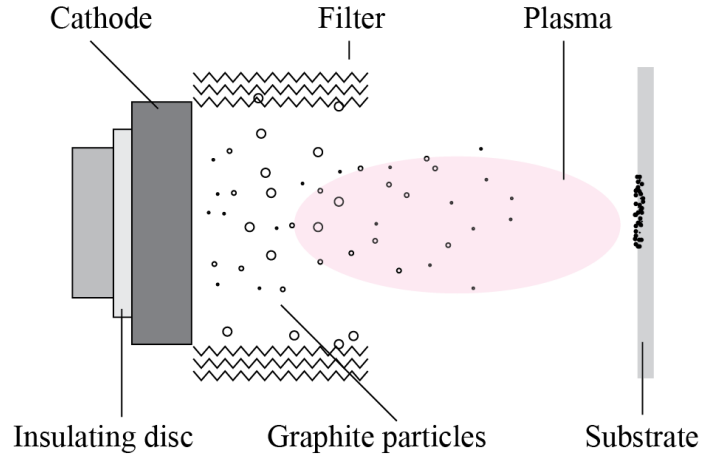


Figure 2-13: Mechanism of PVD by arc deposition

In the case of a metal film, macro droplets can easily be caught on the walls of the chamber which often act as anodes when being filtered, but the DLC is not affected by the electric fields and so the macro droplets generated ‘bounce’ off the filtering duct wall and can be incorporated into the coating, creating highly stressed regions and delamination initiation sites, therefore several different methods have been developed to combat this occurrence.

One solution to this problem has been developed; a T-shaped device with an electrostatic trap developed by Kamiya *et al.* [135], improving on their previous work trapping macro droplets in to an “end pocket” located at one end of the T-junction [136]. They have found that by trapping the droplets this way, a macro droplet concentration in the produced coating over 0.1mm^2 can be reduced from a linear filtered arc deposition system where 3400 droplets were recorded [136], the end pocket concentration was recorded as 40 macro droplets [136], and this number was further reduced when using the electrostatic trap to 15 macro droplets [135] which is a great improvement on both the end pocket and linear results.

Various methods can be used in order to combat the macro droplet incorporation into the final coating [134, 136-139]. Two popular methods are; shielding: this method involves physically blocking the path of the macro droplets in a line of sight system, to prevent the droplets from reaching the substrate, as seen in Figure 2-14 [138]. This method is the simplest to achieve but some macro droplets tend to arrive at the substrate, this also limits the geometry of the substrate significantly [138]. ta-C coatings are produced using this method.

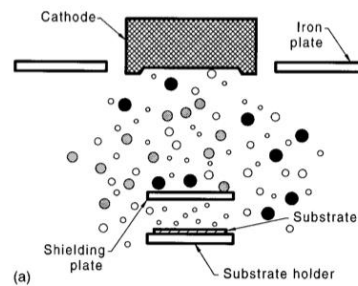


Figure 2-14: Physical line of sight deposition [138]

Non-Line-of-Sight Systems are also a solution to the macro droplet incorporation into DLC coatings; this method is to physically move the target and the substrate so that the deposition is not line of sight. The macro droplets then deposit on the walls of the chamber instead of the substrate, or a magnetic coil system is used to trap the droplets whilst steering the bulk plasma towards the substrate.

IBM have devised a system to deposit ta-C³ onto the surface of compact disks as a protective layer [139]. In this set up the substrate is at 120° to the target as shown in Figure 2-15.

³ Tetrahedral amorphous Carbon

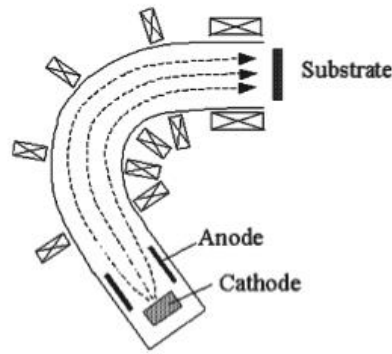


Figure 2-15: Schematic of IBM non-line of sight cathodic arc deposition system [139]

Takikawa et al. [134, 136] have designed some filtered arc mechanisms. The methods are the ‘bent knee’ structures and other non-line of sight methods are all rather large, space consuming systems. More compact systems use a filtered arc system which incorporates a ‘radial arc source’ and the target is at 90° to the substrate, with a large hexagonal ‘honey comb’ structured baffle placed in the path of the plasma to catch the macro droplets emanating from the target.

2.7.3. High Power Impulse Magnetron Sputtering

High Power Impulse Magnetron Sputtering (HiPIMS) is a relatively new technique which is incorporated into the Flexicoat 850 deposition system at the University of Leeds. HiPIMS is a recent advancement in magnetron technology, with the first publication released in 1999 by Kouznetsov [140], building on work carried out by Bugaev [141] and Fetisov [142]. This technique may be used to deposit higher density and more homogenous coating structures and potentially provide better adhesive layers for DLC coatings.

HiPIMS began to make headway with the publication of the much cited Kouznetsov paper of 1999 [140], bringing HiPIMS into the view of researchers after quantifying

the high level of ionisation observed, target utilization and uniformity of the films produced. Since the initial discovery, much research in this area has been concentrated between Sheffield Hallam University [143-145] and Linköping University, Sweden [146].

HiPIMS (High Power Impulse Magnetron Sputtering) is an ionized physical vapour deposition process. In comparison to DCMS (Direct Current Magnetron Sputtering), HiPIMS has a very high rate of ionisation of the sputtered material which is crucial to deposition quality and film characteristics. However HiPIMS has a much lower deposition rate in comparison to DCMS. HiPIMS uses a much higher power density than DCMS; this is delivered in short pulses to prevent melting of the target by keeping the average power density low. A higher power density gives a much higher plasma density, thus more of the target species is ionized and this gives a much denser coating and better thickness uniformity; the plasma density is around $10^{15} - 10^{19} \text{ m}^{-3}$, compared to DCMS at $\sim 10^{15}$ [147].

The high power density ($\sim 3 \text{ kW cm}^{-2}$ [148]) is delivered to the cathode in pulses ranging from 10 – 100 μs , at a frequency of 50 – 200Hz [149] for deposition. Results from Sheffield Hallam University [149] have been promising, in that smooth, defect free surfaces have been observed with excellent repeatability. Sheffield Hallam and Linköping have combined in their research efforts and are currently looking into the possibility of combining standard UBM systems with HiPIMS within the same machine, as the industrial likelihood of adopting HiPIMS in its current state is poor; with a deposition rate of around 25 – 35% that of standard DCMS [150].

2.7.4. Plasma Enhanced Chemical Vapour Deposition

Plasma Enhanced Chemical Vapour Deposition (PECVD) is derived from a much simpler process, Chemical Vapour Deposition (CVD), which involves the deposition of a coating on to heated solid substrates from a chemical vapour reaction of gases [151]. Like PVD, this process is atomistic by nature. CVD allows the deposition of materials onto geometrically complex shapes as it is not a line of sight process, unlike PVD. Thick coatings can be produced using this method and a high deposition rate can be achieved. The gas used during a CVD process and its waste products are often toxic and must be handled correctly, this is a disadvantage of the process and can be costly. CVD generally has a higher deposition rate than PVD, it can be a more economical process and its sensitivity to vacuum conditions are much lower than that of PVD [129, 151].

Plasma Enhanced Chemical Vapour Deposition (PECVD) is a process by which coatings are deposited by an enhanced form of chemical vapour deposition. Chemical vapour deposition is commonly used in the semiconductor, tooling and decorative coatings industry [151], images of components commonly coated using DLC are shown in Figure 2-16.



Figure 2-16: Common engine components coated using DLC, including piston rings, shims and valve lifters

PECVD is a process that is initiated by the introduction of a gas into the deposition chamber (in this study acetylene is used). The gas is then ionised using a large potential difference across the chamber. This is a negative voltage which is applied to the substrate table, known as a bias voltage. The substrate table is electrically isolated from the rest of the deposition chamber, which is grounded. This provides the system with enough energy to ionise the acetylene gas and to attract the positively ionised species to the negatively biased substrates where it is deposited.

The plasma in this instance is a 'cold' working plasma, thus allowing deposition to take place at much lower temperatures than in a conventional system and broadening potential substrate materials, for example, polymers can be coated using this method. Using a plasma in the chamber increases the ionisation density of the gases and therefore the coating deposition rate. During this PhD, a relatively new method will be used in the deposition of DLC coatings; Microwave Plasma Chemical Vapour Deposition (Microwave PECVD). Using microwave energy, the plasma has an even higher ionisation density, this further increases deposition quality and rate. Microwave PECVD will be combined with PVD techniques to create coatings that are durable, adherent, have desirable properties, such as hardness and low friction, and are applicable to automotive applications.

2.7.5. Microwave Plasma Enhanced Chemical Vapour Deposition

One of the main focuses of this study will centre on the novel PECVD technique utilising microwave power to enhance Plasma Enhanced Chemical Vapour Deposition. The microwave head and microwave power supply (Muegge MH2000S

– 212BB and Muegge MX2000D – 110LL, respectively) on the deposition system at the University of Leeds can be seen in Figure 2-17.

Over the past 20 – 30 years, plasma processing in the field of surface coatings has been applied both on a research and an industrial scale. Plasma processing is now commonplace within the coatings industry and methods to improve the quality and deposition rate of processing is of vital commercial importance [150, 152]. Research into the Microwave enhancement of Plasma Enhanced Chemical Vapour Deposition has been carried out over the course of this time. Microwave energy can be used to introduce more energy into the system and therefore a high ionisation density without adversely affecting the end coating. Rossnegal et al. [153] have described different methods of generating and sustaining microwave plasma, from the fundamentals to configuration parameters for sustaining a plasma, mainly concerning an electron cyclotron resonance process (a process used commonly in research areas but rarely in industry). The advantage of using electron cyclotron resonance is that it is able to confine multiply charged ions in an area for a time period that is sufficient for multiple collisions to take place, which therefore leads to a higher ionisation of the gas.

Diamond-Like Carbon can be deposited by Microwave PECVD using a variety of hydrocarbon source gases: C_2H_2 , C_2H_4 , CH_4 , and C_6H_6 . C_2H_2 was chosen in this study due to its high deposition rate and low ionisation potential as shown in Figure 2-7.

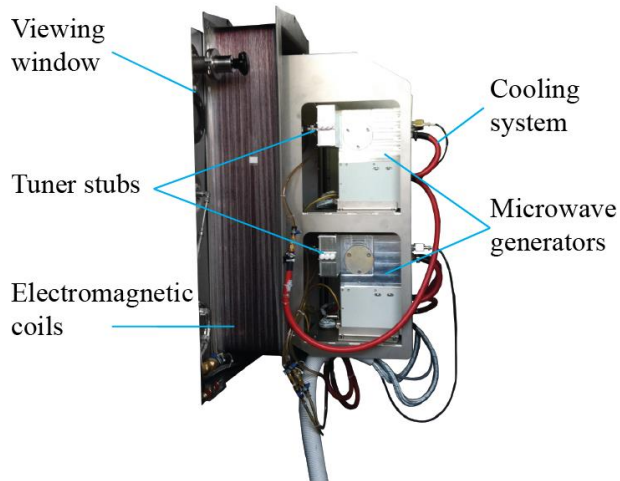


Figure 2-17: Image of microwave plasma generators on the Hauzer Flexicoat 850 deposition system

To ignite the plasma within the system, argon gas is first introduced to the chamber, where a negative voltage is applied to the bias, and the microwave power initiated. This leads to the rapid ignition of the microwave sources, stability of the sources is manually controlled using a set of three impedance stubs which are located on the microwave generator head on the outside of the chamber. Once the Ar plasma is stable, the reactive source gas (in the case of this study: C_2H_2) is introduced into the system, where it becomes ionised. The ionised species is then attracted to the substrates by the applied bias voltage, similarly to PECVD.

The microwave plasma frequency used during these experiments was 2.45 GHz; this differs from the 13.56 MHz radio frequency (r.f) discharges used most commonly for research purposes. To understand why we must look at the electron energy distribution function. This function is able to define the rates of electron elastic collisions and therefore provides electron transport information, also details of the inelastic properties of the plasma such as ionisation, excitation etc. [154]. The distribution of EEDF is for the majority, Maxwellian in microwave plasma, this

allows there to be a higher number of electron – ion pairs formed per unit of delivered energy relative to r.f. plasmas. In addition to this, the microwave plasma is governed by ambipolar diffusion, in which process, in the presence of a concentration gradient within the plasma (i.e. near to the chamber walls), the electrons move at a greater speed than the ions (due to their higher mobility and higher diffusion coefficient). This creates a more positive region within the plasma and as a consequence of this, a restraining electric field develops which serves to equalise the diffusion coefficient of the ions and electrons. The ambipolar diffusion applies to all of the motion within the plasma [16], whereas the r.f. plasma is controlled by mobility; this leads to higher ion flux and dissociation rates within the microwave plasma [155].

The working pressure of the microwave process is 1×10^{-2} mBar. The antenna is made from silver plated brass tube, outer diameter 9.5 mm; inner diameter 4 mm. Overheating of the components is prevented by an air cooling system through the centre of the antenna. The antennas are protected by vacuum sealed quartz tubes surrounded by two ceramic outer tubes. The paraboloidal reflector is double walled and water cooled, made from stainless steel. The reflectors serve to direct the plasma into a quasi-parallel beam.

The Rosnagel et al. [153] review of microwave plasma deposition very much occurred within the developmental stages of the technology, and current systems have proven that research and experimental perseverance has been worthwhile in this area as the true versatility and potential of microwave plasma processing is now being realised [18, 156, 157]. Industry is attracted by recent developments, increasing process chamber size and the potential for up scaling of the technique.

New processing machines include technology for in-line deposition, allowing large scale production to take place, see Figure 2-18 for an example of in-line magnetron sputtering recently developed by Hauzer, and also varying sources which allows for in-situ processes to occur, such as deposition of materials by different means i.e. PVD, PAPVD, CVD, PECVD, FCARC, etching and ion implantation.



Figure 2-18: Hauzer example of in-line Magnetron sputtering

2.7.6. Coating Growth

Coating growth principles using PECVD and Microwave PECVD are explained here. The plasma closest to the growing film consists mainly of ions and neutrals. The effect of the neutral species on the growing film is dependent on the sticking coefficient and type of the individual species [11, 18]:

- Di-radicals - C-C and C-H bonds are invaded by chemically unstable di-radicals (e.g., CH_2); these react with the surface of the film and have a high sticking coefficient.
- Neutrals - The more stable, closed shell neutrals (such as CH_4) have very low sticking coefficients and do not affect the film.
- Mono-radicals – these are incorporated into the surface structure by single dangling bonds. These can be created by atomic H (dissociated from H_2

within the microwave generated plasma) that reacts with surface H bonds. H within the coating structure can also be removed by ion bombardment and by unstable radicals (e.g. CH₃) abstracting the H from the surface bonds and attaching to the dangling bond. CH₃ under normal circumstances has a low sticking coefficient, but in the presence of atomic hydrogen this is raised significantly.

- Carbon and Hydrogen – These species are able to implant within the surface and the growing coating, making a more dense and strong structure. Hydrogen atoms ‘knocked out’ of the coating structure are able to combine with other H atoms to form H₂ and these desorb from the film. Therefore as the ion energy within the process increases, the H content decreases.

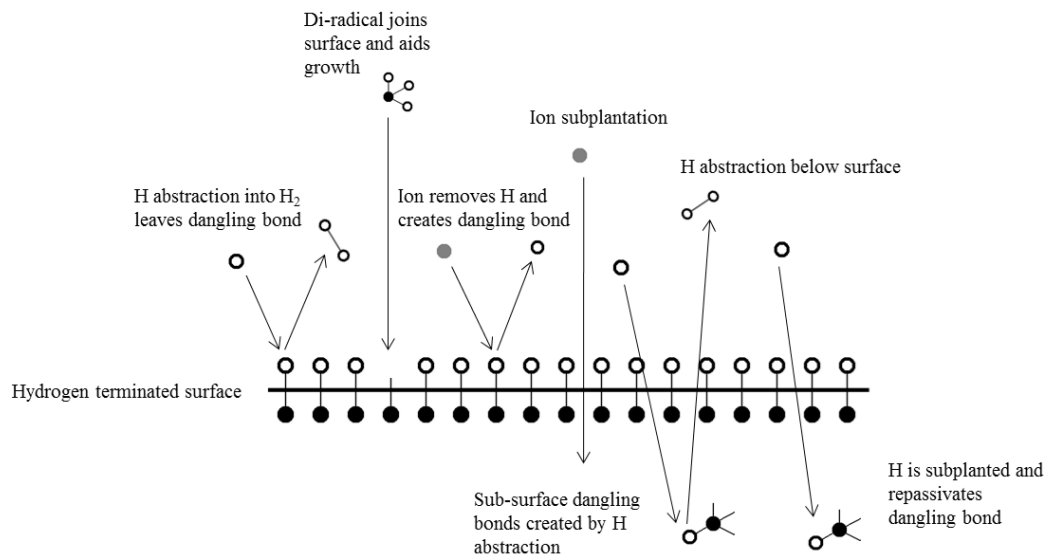


Figure 2-19: Deposition mechanisms of DLC deposited by plasma chemical vapour deposition, presented in [11] in chapter 1, by Robertson

The film then grows on the substrate surface via these mechanisms, a dense microwave enhanced plasma aids this and thus, a high density, homogenous plasma that reaches across the entire deposition chamber must be generated; a half wave

dipole antenna will not achieve this alone and so the equipment is modified by adding a paraboloidal reflector about the antenna with a half wave dipole antenna at its focal point, the resulting microwave emission is said to be a quasi-parallel beam ⁴ [158]. A dense, homogenous plasma can be achieved throughout the processing chamber using this method. Substrates can be placed at distances over 300 mm away from the microwave source, which allows for a wide variety of substrate geometries and for the addition of alternative deposition techniques to the coating system; metallic elements and non-metallic elements can be incorporated into the coating this way, allowing for a multitude of different coatings to be deposited inside a single machine and during a single process.

2.7.7. Summary

As is shown in Table 2-2, Table 2-6, Table 2-7 and Table 2-8, the properties of DLC vary drastically depending on the composition, deposition parameters and the nature of the deposition itself. Filtered Cathodic Arc is commonly used to deposit ta-C, which typically has a very high sp^3 content and does not include hydrogen. This results in high hardness and Young's modulus values. Using a very low bias voltage (85 V) a DLC coating of 50 - 60 GPa hardness is regularly achieved, along with a high sp^3 content (> 80%) [56, 94, 159, 160], with the hardest DLC coating found to be 95 GPa [161]; despite high hardness, these coating proceeded to fail in tribological testing, showing that a coating of high hardness does not necessarily equal a better tribological performance [56]. This could be due to the high amount of

⁴ The beam is not fully parallel due to size restrictions of the reflector and the microwave radiation being emitted from the entire length of the antenna.

internal stress the coating experiences, these types of coatings have very high levels of elastic modulus, reaching 757 GPa in 88% sp³ DLC, and 300 GPa in 70% sp³ DLC [162]. Deposition rates are higher for the filtered arc process, relative to others, with up to 3.6 µm/hour being achieved [163] using this process, and only 1 µm/hour achieved using magnetron sputtering using graphite [164] and up to 1 µm/hour achieved using r.f. PECVD [165]. For the application of the cam/follower interface this level of hardness and internal stress will not be adequate as a robust tribological performance is required.

ta-C DLC coatings can also be deposited using arc ion plating, these coatings have been shown to exhibit ultralow friction coefficients (0.03) when in contact with one another and in the presence of PAO-GMO lubricants [29]. The lubricant used in this study incorporated a high percentage of GMO (~1%) and as such is not entirely representative of a lubricant used within an engine, whilst this data is still useful, these techniques will not be incorporated into this study.

The coatings created using PECVD are most commonly a-C:H due to the nature of the precursor hydrocarbon gas used, they incorporate more sp² and H bonds and thus are softer than the majority tetrahedral ta-C coatings, ranging in hardness from around 10 - 30 GPa [11, 166-168] and elastic modulus from 160 – 190 GPa [11]. This is the process that will be used within this study, due to the wealth of literature and comparable coatings and the interest of the sponsors of this project.

DLC coatings can be deposited using magnetron sputtering, with a carbon cathode. Magnetron sputtered DLC is particularly useful in microelectronics due to a high resistivity [169] and have been shown to have a hardness of up to 40 GPa and elastic

modulus of up to 300 GPa [107, 170]. A relatively new process which amalgamates magnetron sputtering and PECVD is reactive magnetron sputtering, which uses carbon as a magnetron target material and also introduces a hydrocarbon gas (such as acetylene or butane) into the chamber, hardness values for these coatings has been found to be above either magnetron sputtering and PECVD when used alone, and the DLC coatings provide good wear resistance and low friction values, it is a promising technique within this area [171]

Microwave PECVD is a relatively new process and will be used extensively in this study. Gunther et al. highlight the importance of the relationship between microwave power and substrate bias, noting that there is a significant reduction of hardness at higher bias voltages which they attribute to the high energy ion flux present within the deposition stage [156]. However, Patil et al. discuss the possibility of the preferential re-sputtering of weaker bonds during the high flux process which would favour the growth of the stronger sp^3 bonds, thus making the coating harder. Other authors have noted decreasing hardness (and increasing stress) with extremes of both high bias voltages and low bias voltages, [103, 104, 164, 172, 173]. These authors also present a peak at which the highest hardness and stresses exist; it is evident that for each piece of equipment, an optimum point of bias voltage exists. A select few authors conducted their experiments regarding the deposition of DLC at high substrate temperatures ($> 400^\circ\text{C}$) [61, 102], it has been well established in the literature that the sp^3 phase within DLC is metastable and can collapse into the sp^2 structure at around 400°C [164] and thus low deposition temperatures will be used for this study. Methane (CH_4) was used as the source gas in various experiments [99, 101, 102, 173, 174] which contains a high amount of hydrogen and

also has a very high ionisation energy (see Figure 2-7, rendering it quite energy consuming to deposit DLC, also promoting the formation of sp^2 bonds rather than sp^3 bonds in higher quantities than 10% of total flow [174], these studies experienced much lower deposition rates than those conducted using lower ionisation energy source gases, such as acetylene (C_2H_2) [104, 172, 175, 176], which was chosen as the source gas for this study.

Chapter 3

Experimental Methodology

3.1. Introduction

The methods used to characterise the deposited coatings are an integral part of this PhD. A fundamental knowledge of the processes and equipment used for characterisation is crucial in order to correctly utilise and interpret the results. Following from the literature review a detailed description of the methods used is presented here.

3.2. The Hauzer Flexicoat 850 System at the University of Leeds

The Hauzer Flexicoat 850 system was installed and commissioned at the University of Leeds in December 2010. This system will be used for the deposition of DLC coatings in this project. This followed initial Factory Acceptance Testing (FAT) and training at the Hauzer headquarters in Venlo. Training sessions focusing on specific areas of the machine have taken place both at the manufacturing site in Venlo, NL and at the University of Leeds.

3.3. Details of the System

The coating system at the University of Leeds is a Hauzer Flexicoat 850 system, with Microwave, Magnetron, High Power Impulse Magnetron Sputtering (HiPIMS),

Filtered Arc Deposition, Cold Finger and Plasma Etching capabilities. The system is laid out as shown in Figure 3-1. The cold finger capability is an addition which can be fitted adjacent to the plasma source when needed. Figure 3-2 shows the system in the laboratory.

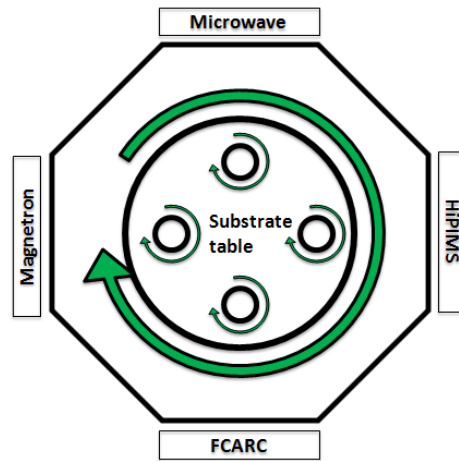


Figure 3-1: Hauzer Flexicoat 850 system schematic



Figure 3-2: Hauzer Flexicoat 850 Deposition System

The front of the system functions both as a door and as a potential housing for another target. The open system is shown in Figure 3-3, the filtered arc deposition

mechanism is also shown here, but this has since been decommissioned and will be replaced by CARC+ technology.

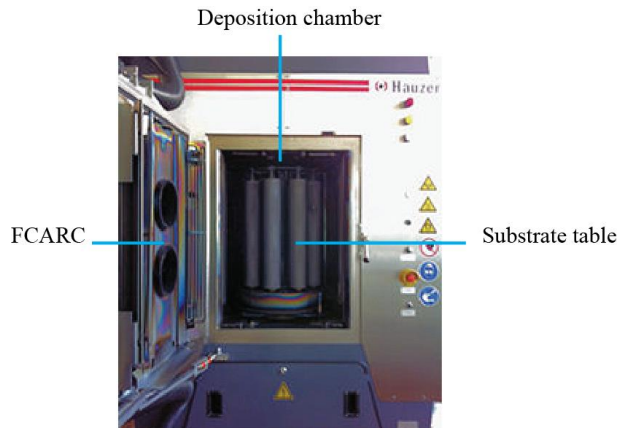


Figure 3-3: Image of the front of the Hauzer Flexicoat 850 System chamber with door open.

Inside the system, on opposing walls are the magnetron sources. One of the sources is equipped with HiPIMS capabilities and one is magnetron only. The final deposition source is located at the back of the chamber; this also has a double function as a door and may be opened in order to clean the microwave sources. This is highly important with regards to the deposition quality; as the paraboloidal microwave reflector becomes coated, it becomes less effective and the coating quality suffers as a result. Figure 3-4 shows the microwave reflector and antenna. The antennae are protected by Boron Silicate ‘sleeves’ as they are delicate and damage easily.

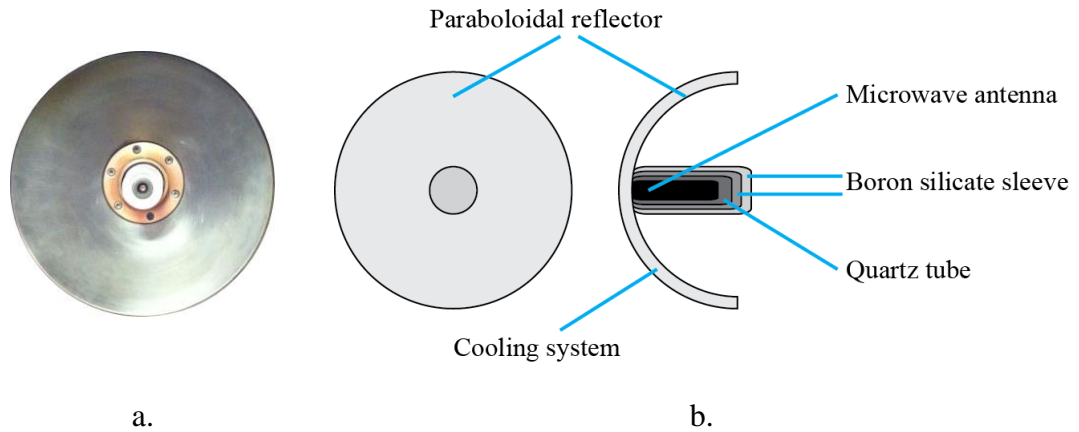


Figure 3-4: Microwave source antenna and reflector a. image, b. schematic diagram

Inside the deposition chamber, the substrates are affixed to cylindrical columns shown in Figure 3-5. These large columns can be replaced by substrate holders. The columns allow for a two fold rotation, whereby the dummies are rotating independently from the table, whereas the holders can achieve a threefold rotation which allows the samples to be rotated separately from the table and dummies.



Figure 3-5: Image of the substrate table for the Hauzer Flexicoat 850 deposition system

The system is controlled using a computer installed toward the rear of the machine using unique software designed by Hauzer. The water systems, control units and power supplies are all located behind the deposition chamber. Chilled water must be

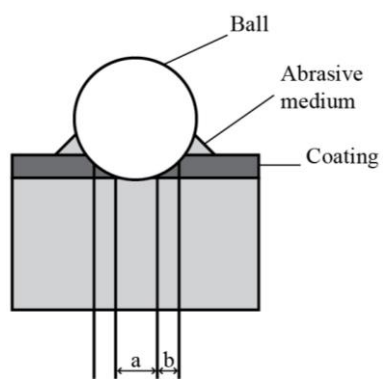
available at all times when using the deposition system due to the need for cooling. All of the sources use this to prevent overheating of the system.

3.4. Calo-tester

A calo-tester is a form of micro scale abrasion testing. The purpose of this test is to provide a quick and simple way of determining the thickness of coatings. A rotating ball is placed against the sample and an abrasive medium is introduced (in this case a 1 μm diamond suspension). A crater is then formed on the coating surface, (shown in Figure 3-6) allowing the thickness of the coating to be gauged using equation 3.1.

$$e = \frac{a \cdot b}{d} \quad 3.1$$

Where e is the coating thickness, a and b are found using a microscope (shown in figure and d is the ball diameter. See Figure 3-6 for schematic. The calo-tester is shown in Figure 3-6.a.



a.



b.

Figure 3-6: (a) Calo-tester schematic, (b) Calo-tester

3.5. Nano Indentation Hardness

The measurement of nano-indentation hardness uses depth sensing rather than the measurement of the indent due to the need for expensive imaging equipment and accuracy concerns, unlike the micro hardness tester which uses an optical microscope and a measuring gauge to determine the hardness from the dimensions of the indent. The difference between nano indentation and micro hardness can be substantial. Qian et al [177] discovered that a nano indentation hardness reading gave on average a 10 – 30% higher value than was found on the micro hardness tester, attributing this to assumptions made regarding the elastic/plastic deformation process, but acknowledging that shortcomings in this area may lead to the ability to qualitatively analyse a materials resistance to deformation.

It is recommended that the tip of the indenter goes no further than 10% of the coatings total thickness [178]. This is to avoid incorporating any substrate or interlayer properties into the end result. An example of the load displacement curve from the nano-indentation test is shown in Figure 3-7.

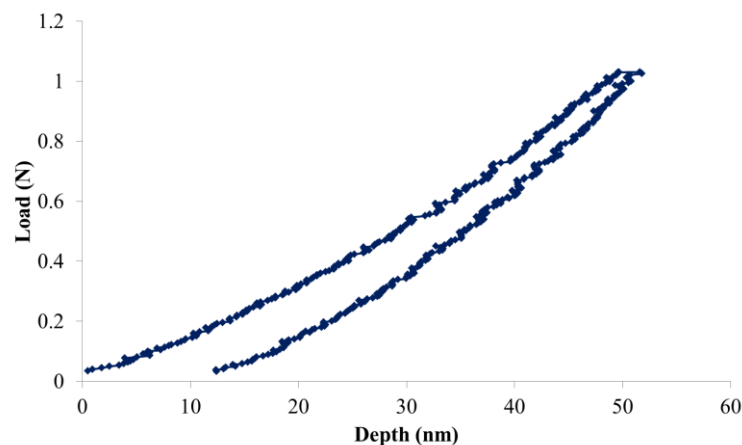


Figure 3-7: Example of a nano indentation curve from the sample produced within the microwave bias scan matrix at 210 V

The nano-test platform was a MicroMaterials indentation platform, and calculates the reduced modulus of the material. In order to calculate the elastic modulus from this, equation 3.2 is used.

$$\frac{1}{E_r} = \frac{(1 - \nu^2)}{E} + \frac{(1 - \nu_i^2)}{E_i} \quad 3.2$$

Where E_r is the reduced modulus, ν_i and E_i are the Poisson's ratio and elastic modulus of the indenter tip, respectively, ν and E are the Poisson's ratio and the Young's modulus of the specimen, respectively.

3.6. Scanning Electron Microscopy

A Philips XL30 Scanning Electron Microscope (SEM) will be used to examine samples at high magnification. The SEM is equipped with an energy dispersive spectrometer. This allows for the elemental compositional analysis of the samples in situ with the SEM. This has been used for the characterisation of functionally graded layers and for chemical analysis of the wear track.

In a typical SEM electrons are emitted from an electron gun. This can be either by thermionic emission (i.e. passing a current through a filament wire for example, tungsten) or by field emission (i.e. a large electric field is created around and dissociates electrons from atoms).

The beam is accelerated through the anode and passes through magnetic condenser lenses, which are used to focus and condense the electron beam. The objective lens focuses the electron beam to a fine point which is then directed over the sample.

Deflector lenses move the beam across the surface where secondary and backscattered electrons are produced (amongst others) and are detected by instruments within the sample chamber. The most commonly used are secondary electron detectors, which detect low energy (< 50 eV) secondary electrons emitted nanometres from the sample surface. An Everhart-Thornley detector is often used, this amplifies the detected electrons and forms the high resolution (up to 0.5nm) image required. The SEM operates under vacuum conditions to prevent molecules interfering with the beam and to prevent the oxidation of the tungsten filament.

3.7. Energy Dispersive X-Ray Analysis

Energy dispersive X-ray (EDX) analysis in the SEM works according to the following principles:

A high energy electron beam reaches the sample surface and interacts with local atoms; inner shell electrons are excited to higher energy states, this creates an electron hole which is filled by an outer shell electron. As shown in Figure 3-8, an X-ray is emitted due to this change in state; the X-ray energy is of equal magnitude to the change in state and corresponds to the specific energy levels within each individual element. This allows us to identify which elements are present; the composition of samples with many different elemental species can be quantified using this method due to the quantity of X-rays being affected by the abundance of the separate elements. Despite being classified as a surface analysis technique, the electrons do penetrate the surface, up to 1 μm depending on the atomic number of the element (the higher the atomic number, the lower the penetration depth) and so quantification represents volume rather than surface area.

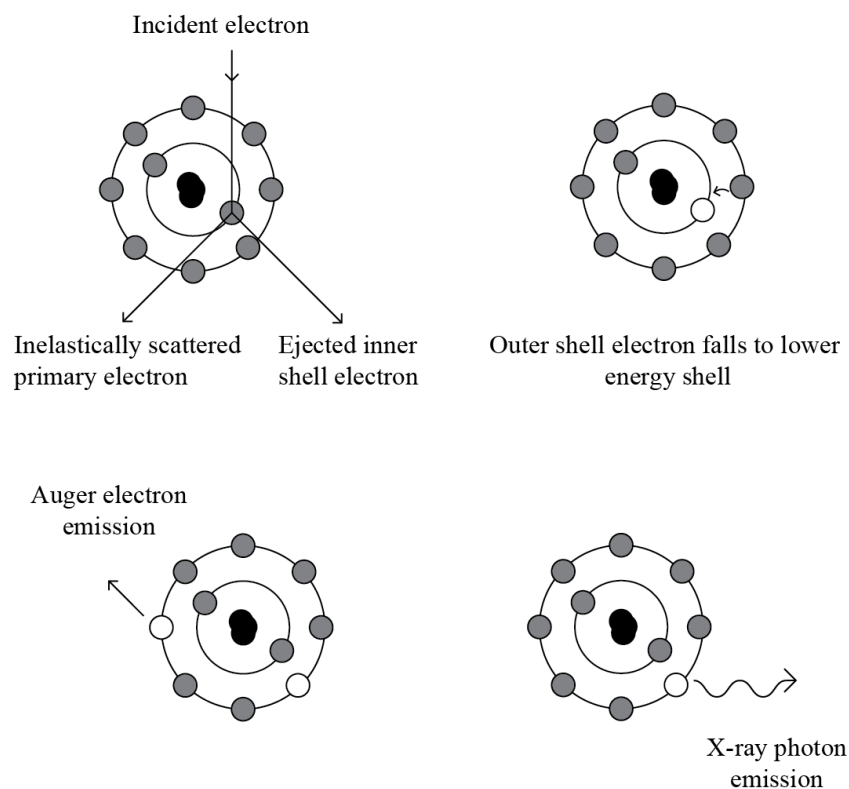


Figure 3-8: Mechanisms of Energy Dispersive X-ray Analysis

3.8. X-Ray Photoelectron Spectroscopy

X-Ray Photon Spectroscopy (XPS) is used to determine the elemental composition of a material. Of particular interest to this study, the uniformity of the elemental composition across the surface can be determined. Hydrogen and Helium lie outside of the detection range for XPS, which is most sensitive to elements with an atomic number greater than 3.

Monochromatic Al or Mg K α x-rays are generated and the sample is irradiated by these. Photoelectrons are emitted upon interaction with the x-rays, upon the detection of these, the energy spectrum is determined.

The X-rays interact with electrons lying in the K shell of an atom, this results in the emission of a 1s photoelectron, thus ionising the atom. The vacancy is filled by an electron from a higher shell due to relaxation. This can lead to either X-ray fluorescence or Auger emission. The binding energy of the emitted electron is calculated using:

$$KE = h\nu - BE \quad 3.3$$

Where $h\nu$ is the energy of the photon and BE is the binding energy.

The process takes place in ultra-high vacuum $\sim 10^{-10}$ Torr so as to avoid any contamination. The unique binding energy of the atom is determined (as kinetic energy is measured by the instrument and photon energy is known) and the chemical composition is determined.

For this study, the chemical analysis of tribo-films was carried out using a VG ESCALAB 250 X-ray Photoelectron Spectrometer (XPS). This system uses high power monochromatized x-ray of aluminium K alpha source, high transmission electron optics and a multi-channel detector. An area of 500 μm x 500 μm was analysed in the wear scar area. A survey was carried out at a pass energy of 150 eV at first to determine which elements were present. Longer scans at 20 eV pass energy of the selected peaks were then obtained to gain a clearer picture of the chemical composition. CASAXPS software was used to analyse the data. The position of the C1s peak at 285 eV was used as the reference point for charge correction found in a handbook of XPS. The peak area ratio, full width at half maximum (FWHM) and difference between binding energies of the doublets were

constrained. The processed data within this study has taken into account a linear background approximation and is deemed appropriate for the comparison of the tribo-film formation between samples. The samples were rinsed for 10 seconds in n-heptane prior to experimentation to remove any residual oils or contaminating species.

3.9. TEM and EELS

Transmission Electron Microscopy (TEM) and EELS (Electron Energy Loss Spectroscopy) were used in order to determine the percentage of sp^2 bonded atoms within the surface of the coating.

Focused ion beam transmission electron microscope (FIBTEM) sections were prepared from the samples using an FEI Nova 200 Nanolab dual beam scanning electron microscope, fitted with a Kleindiek micromanipulator. The ion column was operated at 30 kV and 5 kV, at beam currents between 5 nA and 0.05 nA and the electron column at 5 kV and 29 pA. The site of interest was coated in a 200 nm platinum layer deposited using a gallium ion beam as demonstrated in Figure 3-9.

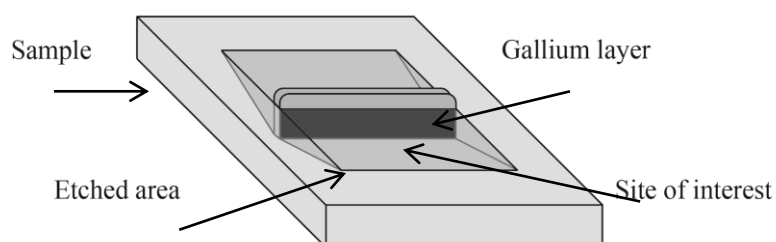


Figure 3-9: Diagram of sample prepared by focused ion beam etching

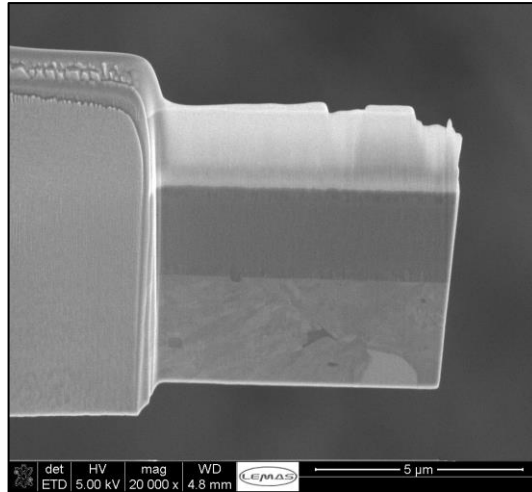


Figure 3-10: Focused ion beam etched sample ready for input into TEM

The surrounding material was removed using the gallium ion beam, and the finished section removed using a micromanipulator and attached to the TEM sample grid as can be seen in Figure 3-10. The section was thinned to < 100 nm in order to be useful within the TEM. The TEM and EELS were carried out using a Philips CM200 FEGTEM operated at 197 keV. The fitting of the EEL spectra was carried out according to Daniels and Brydson [179]

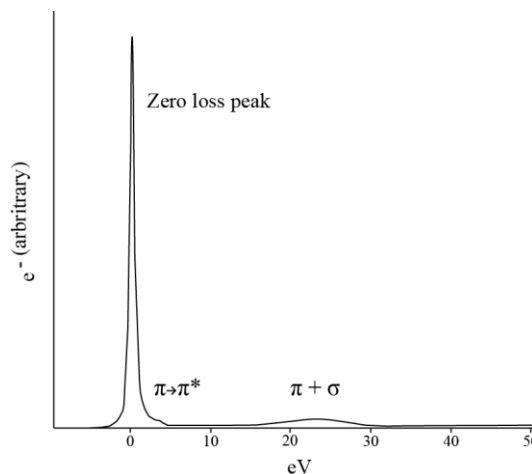


Figure 3-11: Low loss region of EELS spectrum of a-C:H

The relative intensity features of the EEL spectrum which arise from excitations of electrons to higher energy are representative of the amount of sp^2 bonding present since the presence of delocalised π type bonding is demonstrative only of the presence of sp^2 hybridised carbon atom [179]. The two features of the EEL spectrum that show this are the peak in the low loss region at 6.5 eV shown in Figure 3-11, which is representative of an interband transition between π^* bonding and anti-bonding orbitals. The peak within the core loss region at 285 eV representing the 1s to π^* feature is shown in Figure 3-12.

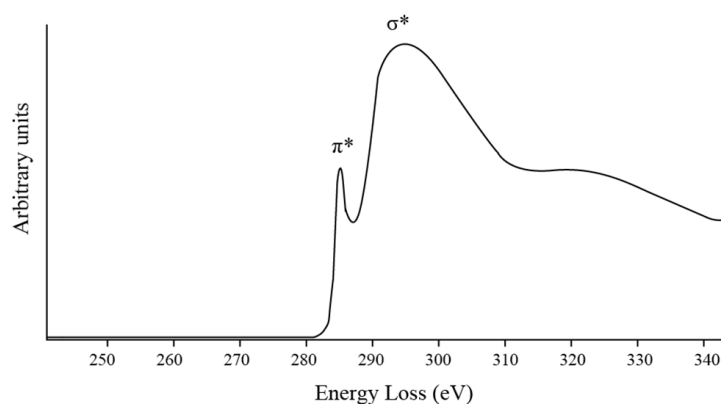


Figure 3-12: Core loss region of EEL spectrum of a-C:H

The ratio of the π^* peak at 285 eV in the core loss region and a 20 eV window about the σ^* peak is taken along with another 20 eV window representing the whole carbon signal, this ratio is normalised to the ratio of a 100% sp^2 graphite sample, the value for which was found in the literature [179] and verified using a sample of pure graphite.

3.10. Pin-on-Reciprocating Plate Tribometer

Friction and wear results were taken using a Biceri pin-on-reciprocating-plate tribometer (image presented in Figure 3-14, schematic shown in Figure 3-15). The

plate samples used were 30 mm discs previously deposited with DLC. The pins used for these experiments were cast iron, with a 40 mm radius of curvature on one end. The pressure exerted on the plate from the pin was calculated using Hertzian contact pressure equations using the normal load and weight hanging from the pivoted beam. The contact was taken as a sphere against a flat surface, and the pressure calculated using equation 3.4, although Hertzian contact pressure equations are usually used to model dry contact situations, it is reasonable to use these equations in boundary lubrication conditions. The stroke length was kept constant at 10 mm and frequency at 1 Hz. The effect of this is a constant load and a sinusoidal velocity profile of the counter-body.

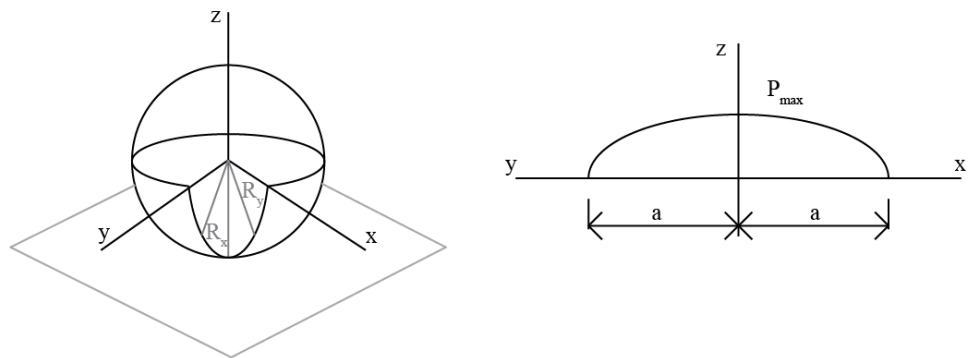


Figure 3-13: Spherical contact and semi-elliptical pressure distribution

$$P_{max} = \frac{2}{3} P_{mean} = \frac{1}{2\pi} \left(\frac{3wE'^2}{R^2} \right)^{\frac{1}{3}} \quad 3.4$$

p_{max} – Maximum Hertzian contact pressure

p_{mean} – Mean Hertzian contact pressure

R – Effective radius

$$\left(\frac{1}{R_x} + \frac{1}{R_y}\right)^{-1}$$

3.5

$R_{x/y}$ – Radius in x/y direction

$$\left(\frac{1}{R_a} + \frac{1}{R_b}\right)^{-1}$$

3.6

w – Load

E' – Effective elastic modulus

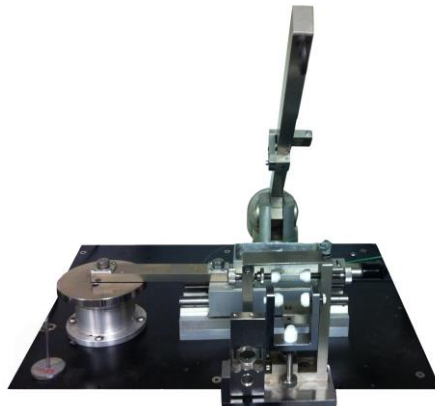


Figure 3-14: Pin on reciprocating plate tribometer

When the plate is in motion, the force experienced by the cantilever arm is absorbed by the load cell, measurement of the oscillary force against the load cell allowed for friction measurements to take place between the pin and reciprocating plate, which is then converted into a coefficient of friction by a labview program. A thermocouple is attached to the lubricant bath in order to regulate the temperature; for all experiments this was kept constant at 100 °C.

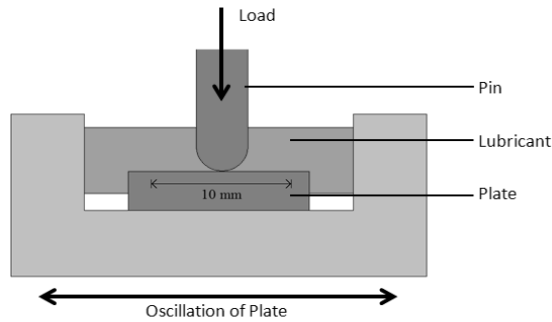


Figure 3-15: Biceri pin on reciprocating plate tribometer schematic

As the contact will be lubricated, care must be taken to ensure the correct lubrication regime is followed. Cam/follower components are lubricated by a boundary lubrication ($\lambda < 1$) mechanism as seen in Figure 3-16. During this phase, the surfaces are in asperity contact – the surfaces are not completely separated by the film formed by the lubricant and thus rely upon the anti-friction and load bearing capability of the lubricant. Within a hydrodynamic (full fluid film $\lambda = 3$) area, the surfaces are completely separated by the lubricant films. In elastohydrodynamic lubrication ($1 < \lambda < 3$), the surfaces are completely separated in some areas but may be deformed elastically by loading.

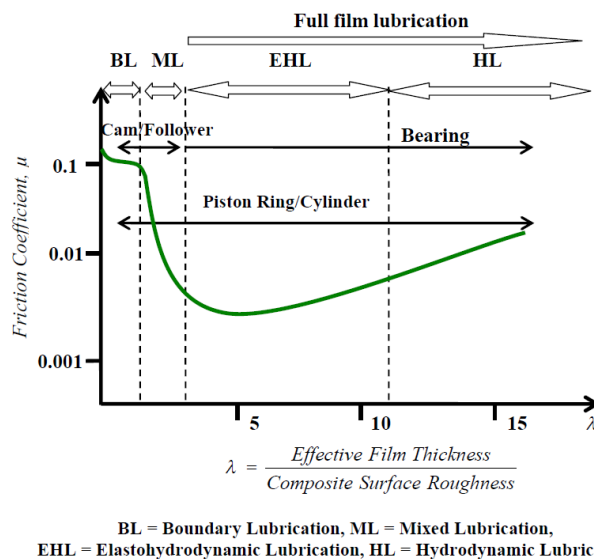


Figure 3-16: Modified Stribeck curve with lubrication regimes and their associated application. [32]

The lubrication regime can be calculated by determining the lambda ratio seen in equation 3.7.

$$\lambda = \frac{h_{min}}{\sqrt{R_{q1}^2 + R_{q2}^2}} \quad 3.7$$

Where R_{q1} and R_{q2} are the RMS of the two solid surfaces and h_{min} is the minimum lubricant thickness which can be calculated using equation 3.8.

$$h_{min} = 3.63 \times R \times U_{\Sigma}^{0.68} \times G_{\Sigma}^{0.49} \times W_{\Sigma}^{-0.073} (1 - e^{-0.68k_e}) \quad 3.8$$

Where $U_{\Sigma} = \frac{\eta_0 U}{E^* R}$; $G_{\Sigma} = \alpha_p E^*$; $W_{\Sigma} = \frac{W}{E^* R^2}$; U is the sliding velocity, η_0 is the viscosity at ambient pressure, E^* is the effective modulus of elasticity, R is the radius of the pin, α_p is the viscosity pressure coefficient, W is the normal load and k_e is the elliptical parameter which is equal to 1.0339 for a sphere on a flat contact [32, 87, 118, 180].

3.11. White light Interferometry

In order to determine the surface roughness of the samples pre and post deposition, a white light interferometer (WYKO) manufactured by Veeco will be used. The white light interferometer works using a beam of white light; this is then split into two separate beams. One is used as a reference beam and is reflected from a reference mirror while the other beam is reflected from the surface of the sample under observation. The beams then recombine to create an interferogram which is processed by computer software which generates information relating to the

topography of the sample. Sub-nanometre resolution is available. Lasers are often used to generate the light needed – this is more accurate for samples that are very smooth. The WYKO is a non-contact surface profilometer and can be used where surface contact is an issue.

3.12. Atomic Force Microscopy

The atomic force microscope (AFM) was used in order to gain topographical information of the surfaces examined. The AFM is a high resolution scanning probe microscope with three different modes of operation: contact mode, non-contact mode and tapping mode. This study will use the AFM in contact mode. A schematic of the AFM is shown in Figure 3-17, and an example of an AFM image of diamond-like carbon is shown in Figure 3-18.

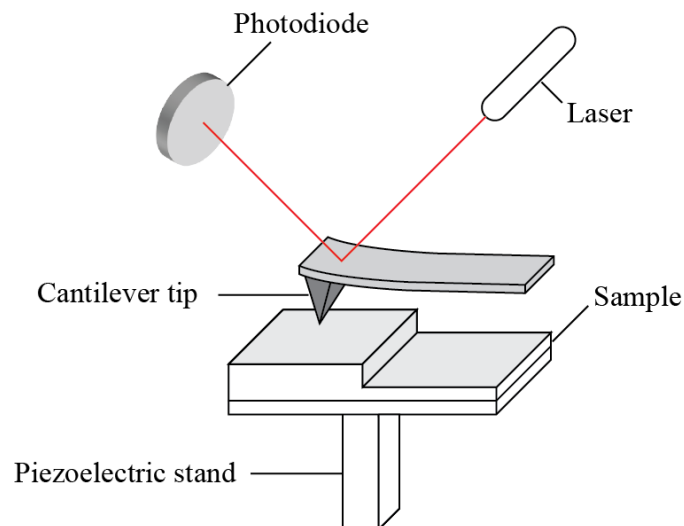


Figure 3-17: Schematic of the AFM showing the basic mechanisms within the equipment

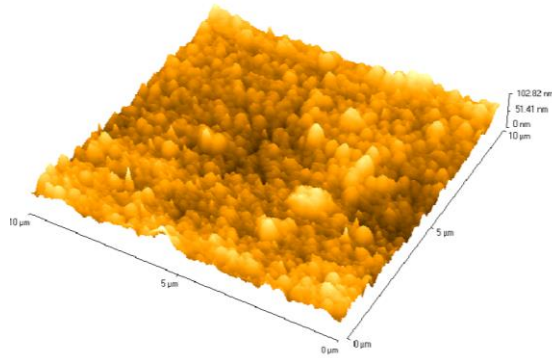


Figure 3-18: Typical AFM image of diamond-like carbon

The cantilever is a silicon nitride tip with a radius of an order of nanometres. The cantilever contains piezoelectric elements which allow it to raster scan across the surface of the sample within a pre-defined area and detects the deflection of the tip due repulsive van der waals forces experienced from the sample surface. This is calculated by measuring the vertical deflection of the probe using a laser and an array of photo detectors as shown in Figure 3-17, and using Hooke's Law shown in equation 3-1.

$$F = Kx$$

3-1

Chapter 4

Results: Tribological Performance of a-C:H, Si-DLC and W-DLC

4.1. Introduction

In this chapter, three Diamond-like Carbon (DLC) coatings are analysed. The coatings were created using PECVD, detailed in section 2.7.4. The coatings are amorphous hydrogenated Diamond-Like Carbon (a-C:H), silicon doped amorphous hydrogenated DLC (Si-DLC), both of these produced at the University of Leeds. PVD was used to create a Cr + Cr/WC + W:C:H interlayer and PECVD using acetylene gas and argon. A tungsten doped DLC (W-DLC) acquired from Oerlikon Balzers (brand name Balinit C*) was used as the third DLC system. The coatings were characterised; thickness, hardness and elastic modulus were analysed using a calo-tester and nano indentation platform respectively. They were chemically analysed to establish the bond types, using TEM and EELS. The coatings were tribologically evaluated using a pin-on-reciprocating-plate tribometer in two different oils (a group three base oil, and a group three base oil containing zinc dialkyldithiophosphate (ZDDP)) to investigate tribo-film formation on the surfaces of the coatings. The Si-DLC and a-C:H were analysed using atomic force microscopy, and only the a-C:H sample was then examined using an XPS to determine whether or not a tribo-film formed when using oils containing ZDDP. This coating was the only one to be evaluated because this being the only sample

which did not delaminate during the tribo-testing and so the tribochemistry of the DLC surface could be evaluated with confidence. These tests are relevant to the application of these coatings to a valve train in a passenger car engine. The coatings must be durable enough to withstand the high pressures and temperatures whilst providing a low coefficient of friction and also must exhibit a low wear rate relative to that found in these types of coatings found in the literature, presented in Table 2-6, Table 2-7 and Table 2-8, in order for them to exist within this environment.

4.1.1. Substrate and Lubricant Types

The substrates used for the deposition of the different types of DLC throughout this thesis were an M2 grade high speed steel, hardened to 62 – 64 HRC. The surface roughness of the substrates was 0.02 $\mu\text{m Ra}$. The cast iron counter body used was a cast iron pin, hardened to 62 – 64 HRC with a 40 mm radius of curvature on one side, polished to a roughness of 0.02 $\mu\text{m Ra}$. The lubricants used were a group III base oil which is commonly employed within the automotive industry, and a fully formulated oil which consists of a group III base oil plus zinc dialkyldithiophosphate, in addition to other commonly found detergents and dispersants.

4.1.2. Coating Recipe

The two coatings tested in this section made at the University of Leeds using the Hauzer Flexicoat 850 system were the a-C:H and Si-DLC. The recipes for both of these coatings were developed by Hauzer. These are detailed in Table 4-1. The recipe for the interlayers of both of the coatings was the same. A schematic of the coatings and interlayers can be seen in Figure 4-1.

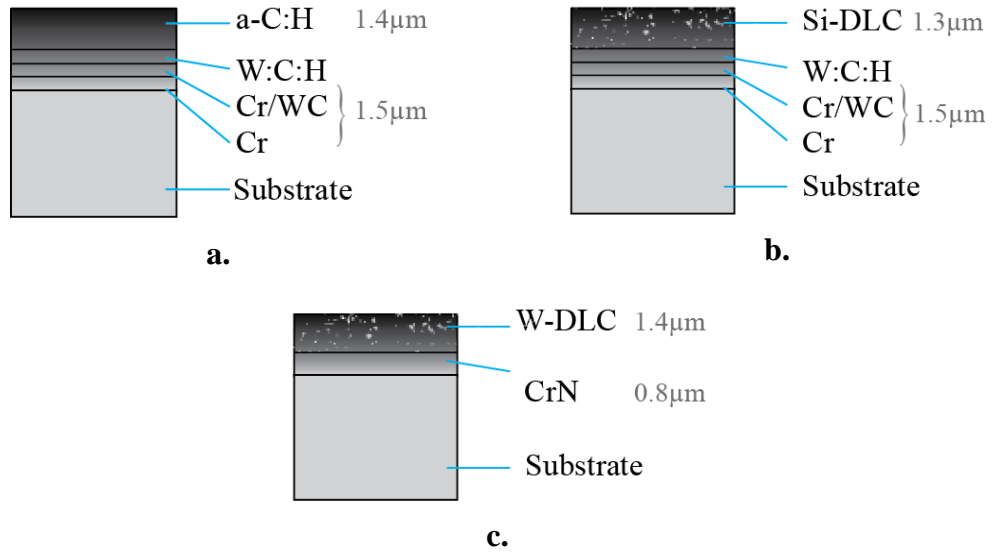


Figure 4-1: Schematic of the composition of a. a-C:H, b. Si-DLC and c. W-DLC coatings

Table 4-1: Recipe for a-C:H and Si-DLC. (Pre-deposition cleaning and processes, interlayer deposition and final DLC layer)

Step	Time (mins)	Gas Flow (sccm)		Bias (V)	Coil Current (A)	Cr Cathode (kW)	WC Cathode (kW)
		Ar	C ₂ H ₂				
Pumping	60	-	-	-	-	-	-
Target Clean	20	130	-	-500	1 – 4	1 – 6	1 – 3
Plasma etch	45	50	-	-200	-	-	-
Cr	25	130	-	-	4	3	-
Cr + WC	30	110	-	-	4	3 – 0.5	0.5 – 3
W-C:H	75	90	8 – 30 /30 min	-	2	-	3
a-C:H	150	-	270	-740	4	-	-
Si-DLC	150	HMDSO C ₂ H ₂		-740	4	-	-
		24 – 18 /8 mins	240 – 180 /8 mins				

4.2. a-C:H, Si-DLC and W-DLC Coatings: Mechanical Results

4.2.1. Thickness

The thickness of each of the samples was determined using a calo tester which is further detailed in 3.4. A 25 mm diameter stainless steel ball was rotated at 200 rpm against the surface of the coatings for two minutes. A drop of 1 μm diamond suspension was used to lubricate the interface and to provide an abrasive medium. The results are presented in Table 4-2. The thicknesses of the coatings are typical of other DLC coatings as can be seen in the literature in Table 2-2.

Table 4-2: Thickness of a-C:H, Si-DLC and W-DLC

Sample	Thickness μm	DLC Thickness μm
a-C:H	2.9 ± 0.07	1.4 ± 0.07
Si-DLC	2.8 ± 0.01	1.3 ± 0.01
W-DLC	2.06 ± 0.05	1.4 ± 0.07

4.2.2. Hardness and Elastic Modulus

A MicroMaterials nano platform described in 3.5 was used to determine the hardness and elastic modulus of the coatings. A Berkovich indenter was used and the maximum load reached was 1 mN, to ensure that the maximum penetration depth of the indentation was no more than 10% of the coating [178], with a loading/unloading rate of 2 mN/min. A minimum of ten indentations was carried out on each sample and the hardness and reduced modulus were calculated using a

power law fit dictated by the Oliver and Pharr method [181]. The hardness and elastic modulus for the coatings tested in this section are presented in Table 4-3. The H/E ratio is hypothesised to be an indication of the wear rate of the coating, described as the deformation relative to yielding [182]. The higher the H/E ratio of a coating, the higher the maximum tensile elastic stress is said to be [183], and thus can be said to correspond to a higher wear resistance. The H/E ratios for the a-C:H, a-C:H:Si and W-DLC samples are presented in Table 4-3. The H/E ratio is compared with the wear rate of the samples in Figure 7-3. These again correspond with hard a-C:H results found in the literature shown in Table 2-2. The incorporation of silicon into the DLC structure lowers the hardness and elastic modulus, as does tungsten [105, 107]. The addition of tungsten significantly lowers the hardness in relation to the a-C:H. This corresponds to the values of hardness claimed on the Oerlikon Balzers data sheet for this coating.

Table 4-3: Tabulated hardness and Young's modulus of a-C:H, Si-DLC and W-DLC

Sample	Hardness (GPa)	Young's Modulus (GPa)	H/E
a-C:H	31.1 ± 1.5	262.4 ± 24.8	0.12
Si-DLC	27.8 ± 1	188.6 ± 7.4	0.15
W-DLC	16.8 ± 2.7	161.4 ± 23.3	0.1

The hardness and elastic modulus of the a-C:H and Si-DLC coating are of typical – high hardness and elastic module end of those found in the literature (presented in Table 2-5 and Table 2-8, respectively), the W-DLC coating shown here is of average hardness and elastic modulus compared to those in the literature, as seen in Table 2-7.

4.2.3. TEM and EELS

TEM samples were prepared from each of the coatings. Figure 4-3 shows an example of curve fitting of an EELS spectrum of a-C:H. Three peaks are fitted in accordance with [179]. The percentage of sp^2 bonding is determined by comparing the ratio of the π^* peak to the total area, to the value of this found from pure graphite. This was done for each of the samples, a-C:H, a-C:H:Si and W-DLC and the results of which are shown in Figure 4-4. TEM images of the samples are shown in Figure 4-2.

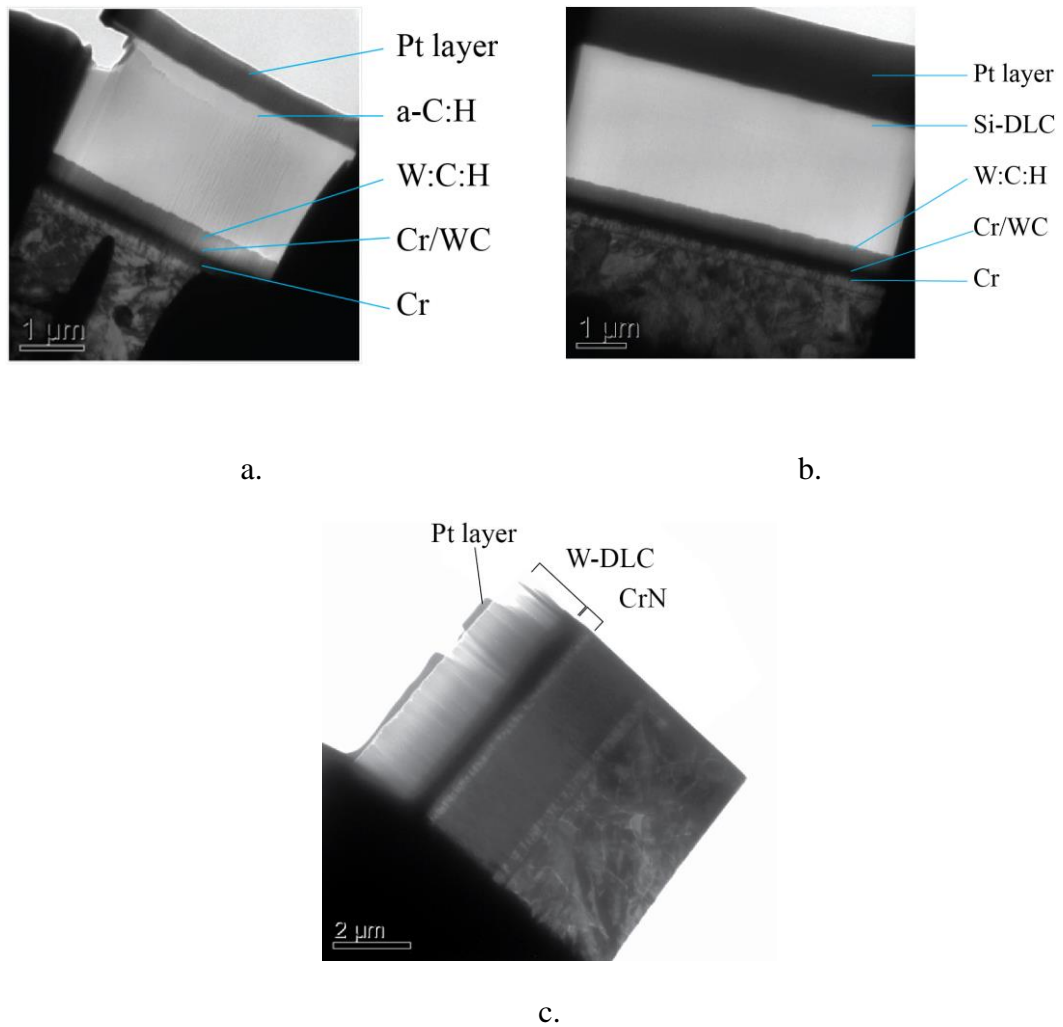


Figure 4-2 TEM images of a. a-C:H, b. Si-DLC and W-DLC

Figure 4-4 shows that the highest percentage of sp^2 bonding occurs in the a-C:H, with a decreasing amount in Si-DLC and a further decrease in W-DLC. This could be due to the different types of bonding present in the doped samples due to the introduction of other elements. Hydrogenated carbon films often have quite a high percentage of sp^3 bonds, despite being typically softer than their ta-C counterparts (which have higher sp^3 bonded areas and higher hardness) due to the sp^3 C-H bond, the inclusion of silicon increases this value further, whilst decreasing in hardness [11].

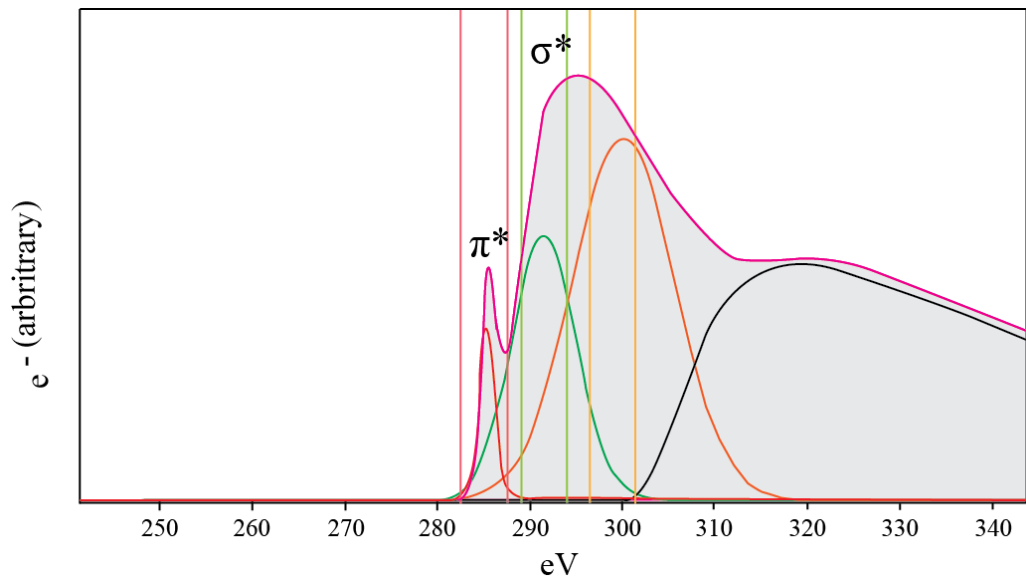


Figure 4-3: Fitted EELS spectra for a-C:H

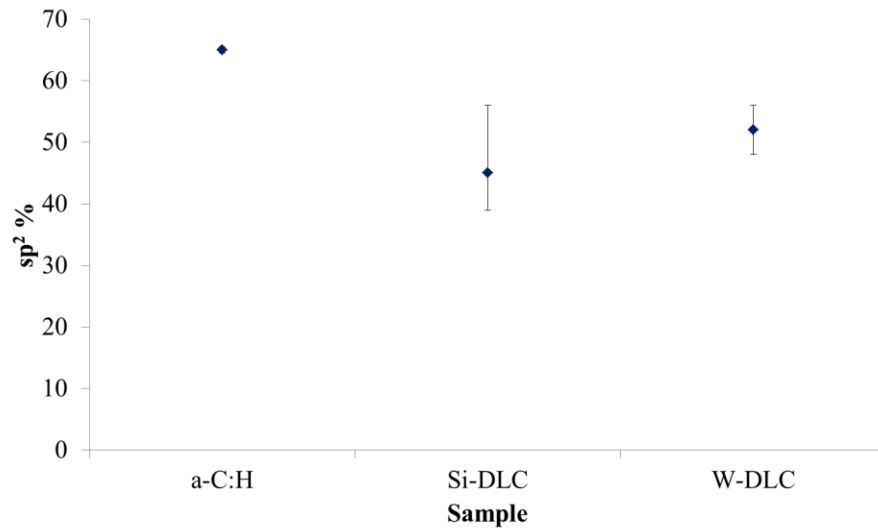
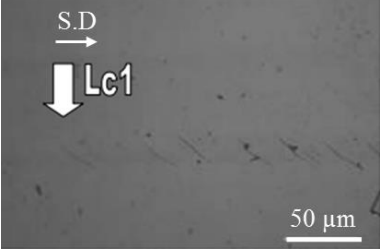
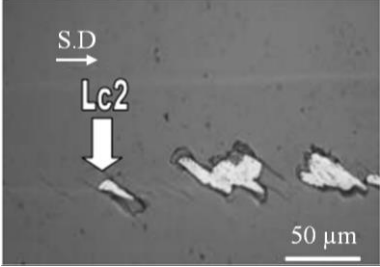
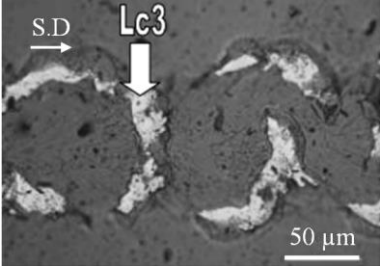


Figure 4-4: sp² % of a-C:H, Si-DLC and W-DLC

4.2.4. Scratch Testing

Scratch testing was carried out on the samples in order to determine the adhesion of the DLC coatings on the M2 steel substrates. The tests were carried out using a CSM micro scratch tester, using a progressive load, initially from 1 – 60 N at a loading rate of 98.33 N/min and a speed of 10 mm/min as a standard test incorporated in the machine and used by Hauzer Techno Coating. The length of the scratch was 6 mm. A Rockwell diamond indenter was used with a tip radius of 50 μm. The critical load was taken at Lc₂ which is classified using Table 4-4 [184].

Table 4-4: Classification of scratch test results [184]

Description of failure events	Micrograph (S.D. = sliding direction)
<p>Lc1 Forward chevron cracks at the borders of the scratch track.</p> <p><i>Lc₁ shall be taken at the closest end of the event to the scratch track start.</i></p>	
<p>Lc2 Forward chevron cracks at the borders of the scratch track, with local interfacial spallation or with gross interfacial spallation</p> <p><i>Lc₂ shall be taken at the failure event that occurs first and at the closest end of the event to the scratch track start.</i></p>	
<p>Lc3 Gross interfacial shell-shaped spallation</p> <p><i>Lc₃ shall be taken at the first point where the substrate can be seen at the centre of the track in a crescent that goes completely through the track.</i></p>	

Lc₁ is the point at which cohesive failure occurs, this is the minimum load at which crack initiation occurs within the coating. The Lc₂ value is the load at which adhesive failure occurs i.e. the point at which the crack reaches the coating/substrate interface which causes delamination and detachment of the coating. This is the point which is taken to determine the critical load value for coatings [185]. Figure 4-5 shows images of the scratch testing carried out on a. a-C:H, b. Si-DLC and c. W-DLC, arrows on the images show where the LC₂ value lies.

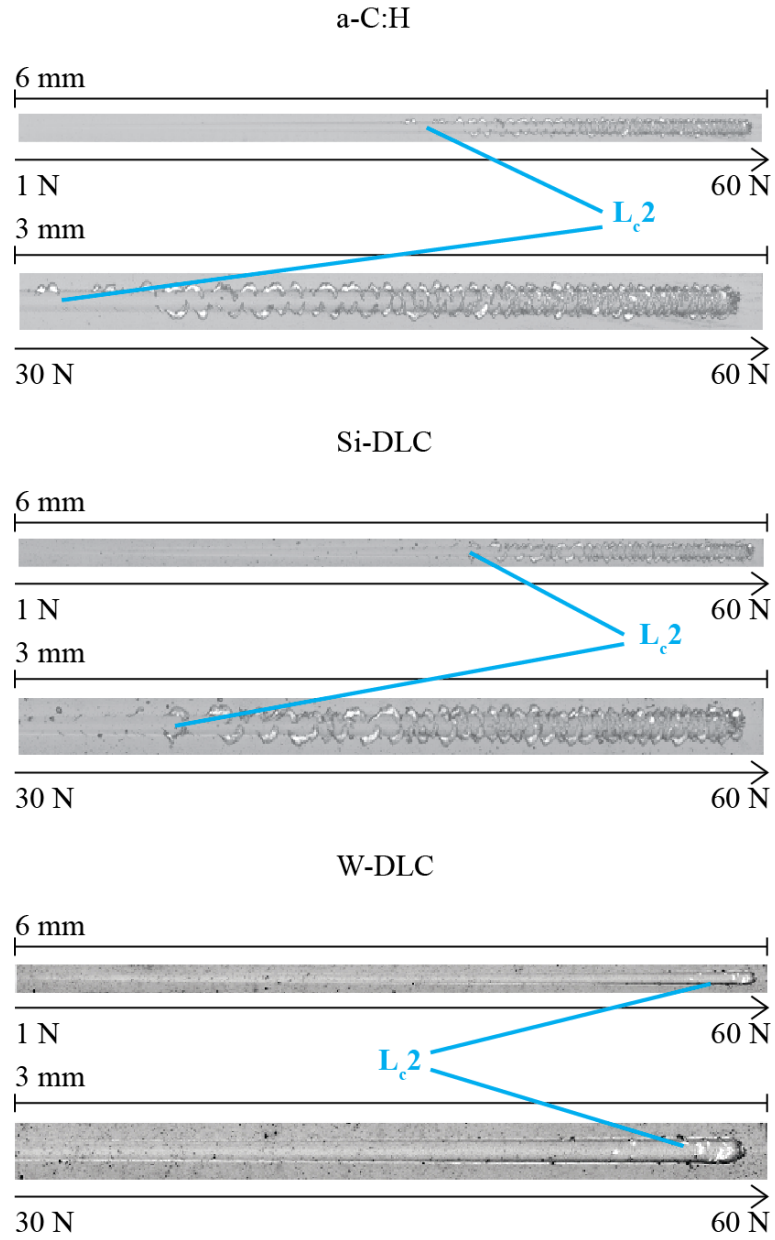


Figure 4-5: Scratch test images of a. a-C:H, b. Si-DLC, c. W-DLC with L_{c2} value indicated with arrows.

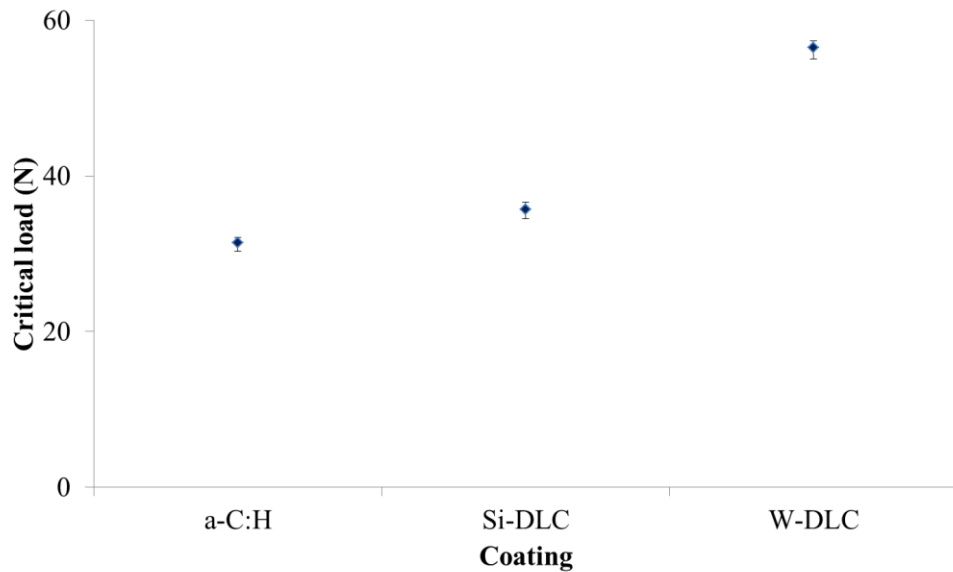


Figure 4-6: Critical loads from scratch test of a-C:H, Si-DLC and W-DLC

Figure 4-6 shows the critical load values for the a-C:H, Si-DLC and W-DLC. The critical load achieved by the a-C:H (31.4 N) and Si-DLC (35.7 N) were similar in value, the Si-DLC achieved a 10% higher critical load than the a-C:H. The W-DLC however, provided a much higher critical load. This suggests that the coating was more adherent to the surface of the substrate, but in tribo-testing the sample delaminated heavily and performed poorly when compared to the a-C:H and the Si-DLC (see Figure 4-13 for a-C:H wear rate, Figure 4-21 for Si-DLC wear rate and Figure 4-29 for W-DLC wear rate).

4.2.5. Tribological Tests

Tribological testing was carried out on all of the samples using a pin-on-reciprocating-plate tribometer described earlier. The tests were carried out using a group three base oil and a fully formulated oil containing zinc dialkyldithiophosphate (and anti-oxidant additives commonly found in fully formulated oils). The tests were conducted at 100 °C, with a Hertzian contact

pressure of 750 MPa which corresponded to 281 N normal load and 11.5 kg hanging weight, and to the pressure experienced in the cam tappet environment [24]. The average entrainment speed was 2 cm/s. The tests were carried out for durations of six, twelve and twenty hours. A cast iron pin was used as a counter-body with a 40 mm radius of curvature in all of the tests. Each experiment was repeated three times to ensure reliability and repeatability of results.

4.2.6. a-C:H

4.2.6.1. a-C:H Friction Results

The friction results as a function of time for a-C:H are given in Figure 4-8 (six hour test), Figure 4-9 (twelve hour test) and Figure 4-10 (twenty hour test). The coefficient of friction is seen to evolve from an apparent ‘running in’ stage after six hours as seen in Figure 4-8, to the final ‘steady state’ after 20 hours in Figure 4-10. The coefficient of friction of the a-C:H in base oil is not consistent and fluctuates excessively with relation to the steady friction performance seen in the fully formulated oil. This was expected due to the lack of performance enhancing additives in the base oil. The fully formulated oil provides a smooth coefficient of friction throughout all of the testing. Figure 4-7 gives an example of three tests conducted for a-C:H in fully formulated oil for six hours. The repeatability is seen to be good. Each experiment conducted on the pin-on-reciprocating-plate tribometer was repeated three times but only one example of the coefficient of friction trace will be shown for each test in base oil and fully formulated oil from this point.

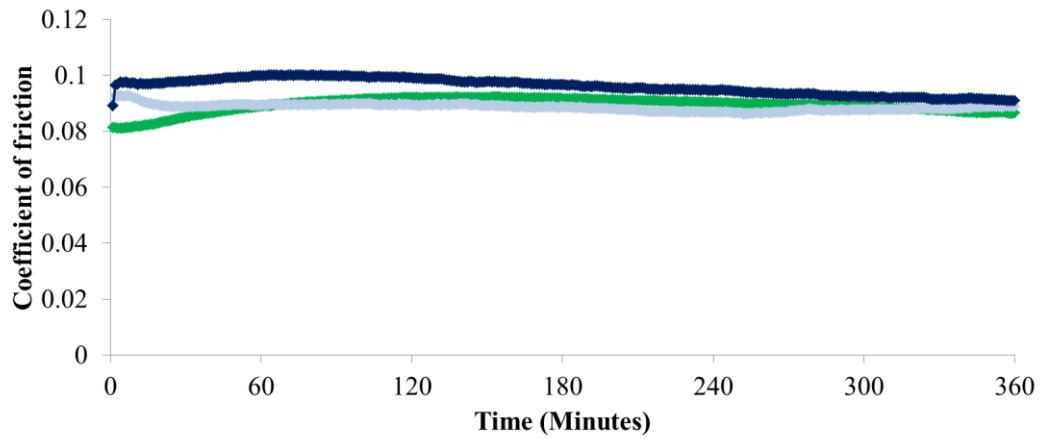


Figure 4-7: Example of error bars for friction plot of a-C:H after six hours testing in fully formulated oil

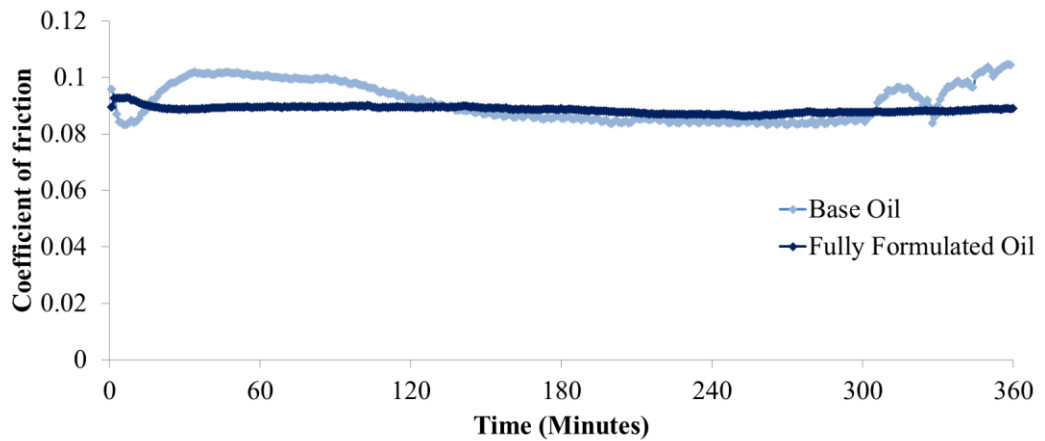


Figure 4-8: Coefficient of friction of a-C:H in base oil (BO) and fully formulated oil + ZDDP (FF) tested for six hours on pin on reciprocating plate tribometer

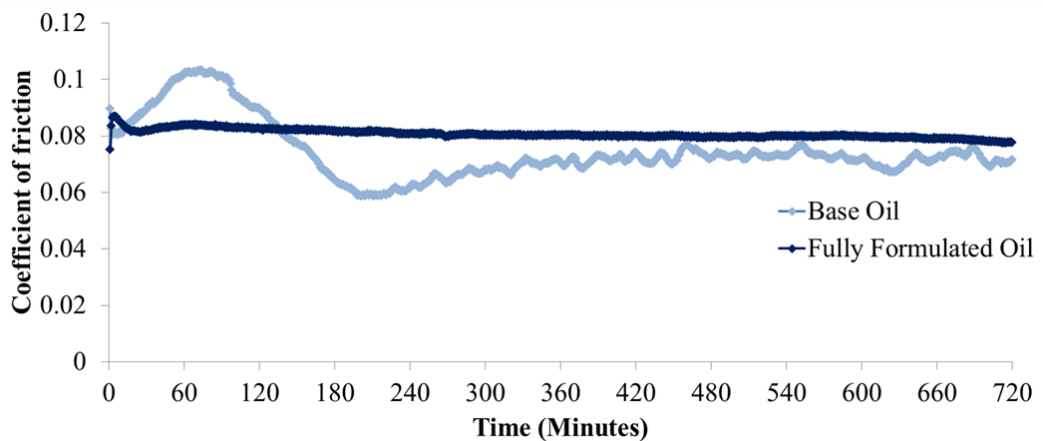


Figure 4-9: Coefficient of friction of a-C:H in base oil and fully formulated oil tested for twelve hours on pin on reciprocating plate tribometer

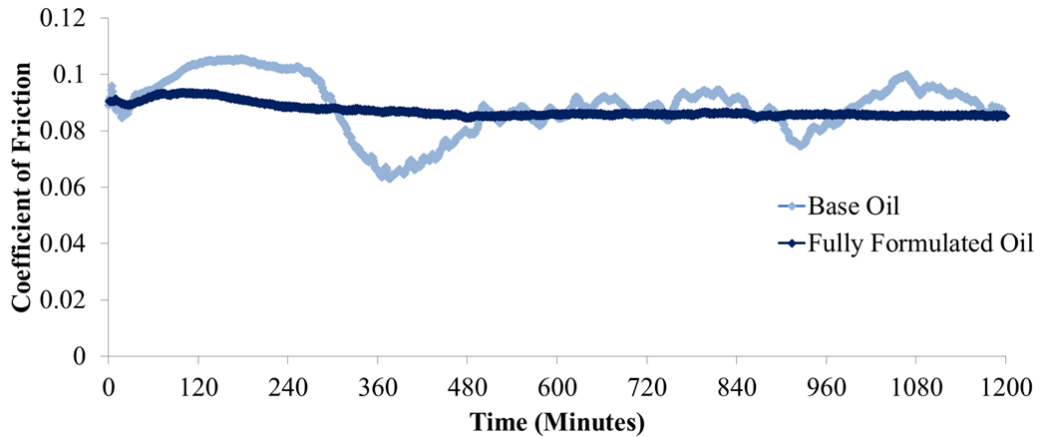


Figure 4-10: Coefficient of friction of a-C:H in base oil and fully formulated oil tested for twenty hours on pin on reciprocating plate tribometer

4.2.6.2. Steady State Friction for a-C:H

The steady state friction results for the a-C:H are presented in Figure 4-11. This was calculated by taking the average friction value for the last hour of each of the tests, and incorporating the error over the three tests conducted. The coefficient of friction of the a-C:H in the base oil is 31% and 33% less than the fully formulated oil in six hour and twelve hour tests respectively. The steady state friction in base oil at twenty hours is 3% higher than in fully formulated oil. However, the base oil provides the system with a much less stable friction coefficient overall throughout the tests. This is evidenced by the large error bars seen on the base oil results, relative to the fully formulated oil tests, which are quite consistent. The friction presented throughout the results is adequate in the oils tested, due to there being no friction modifier present. In the fully formulated oil there is only an anti-wear additive (ZDDP).

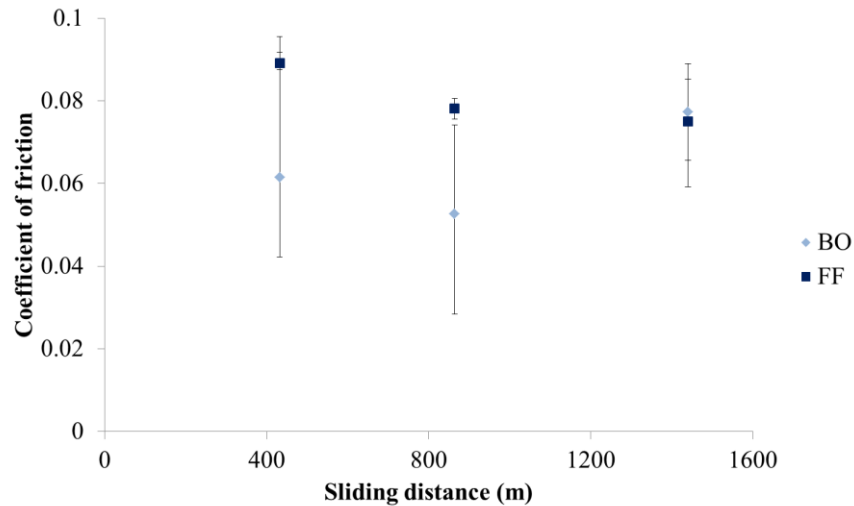


Figure 4-11: Steady state friction results for a-C:H. (BO = base oil, FF = fully formulated oil + ZDDP)

4.2.6.3. a-C:H Wear Volume and Wear Rate

The wear volume values for a-C:H in six, twelve and twenty hour tests are presented in Figure 4-12. The wear volume is lower in the tests using the fully formulated oil with the anti wear additive ZDDP as expected; in the six hour, twelve hour and twenty hour tests, the wear volume was 43%, 68% and 89% less respectively in the fully formulated oil. This is significantly less, and shows that the wear additive has a clear protective quality on the surface of the a-C:H, which is also evidenced by the decrease in wear rate over time as shown in Figure 4-13. There is much debate surrounding the formation of a phosphate containing tribo-film on Diamond-Like Carbon surfaces. This chapter hopes to investigate this formation, the increasing wear rate experienced by the a-C:H in base oil and the decreasing wear rate in fully formulated oil supports this claim of tribo-film formation at the a-C:H surface. The error values are quite large in the base oil experiments. This is due to the unrepeatability and instability of the system in this lubricant, whereas the fully formulated oil performs much more consistently.

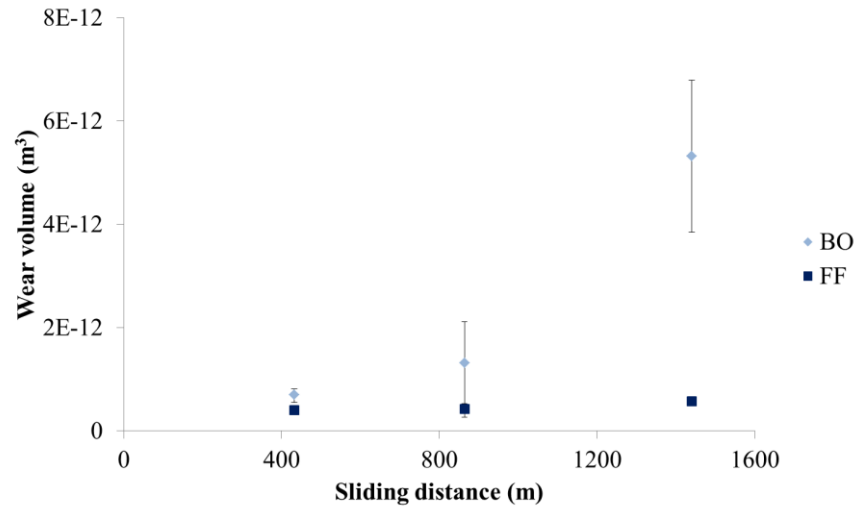


Figure 4-12: Wear volume of a-C:H plate after tribological testing in base oil (BO) and fully formulated oil + ZDDP (FF)

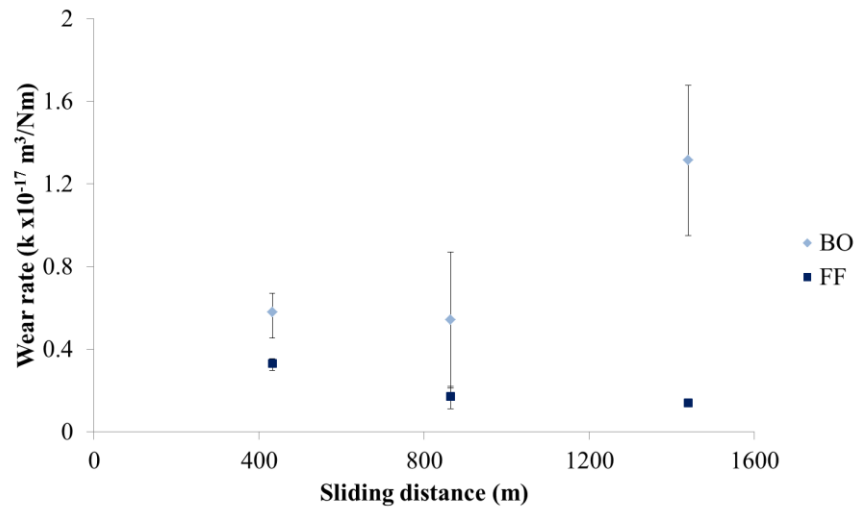


Figure 4-13: a-C:H Wear rate after tribological testing in base oil (BO) and fully formulated oil + ZDDP (FF)

The wear rate of the cast iron pins (shown in Figure 4-33) and the a-C:H coated plates (shown in Figure 4-13) tested in fully formulated oil + ZDDP show a similar trend; they both decrease as sliding distance increases. In the case of the testing conducted in base oil, the coefficient of wear increases over the larger distance for the a-C:H coating, but decreases for the cast iron pin. This has also been found by other authors, notably Haque [32].

4.2.7. Microscope Images of a-C:H Coating Wear

Microscope images of the wear experienced by the a-C:H coating in base oil after six and twenty hours, and in fully formulated oil + ZDDP after six and twenty hours are presented in Figure 4-14, a, b, c and d respectively. It can be seen from the images that the sample wear increased in severity from six to twenty hours in base oil, and remained the same after the longer duration in fully formulated oil + ZDDP.

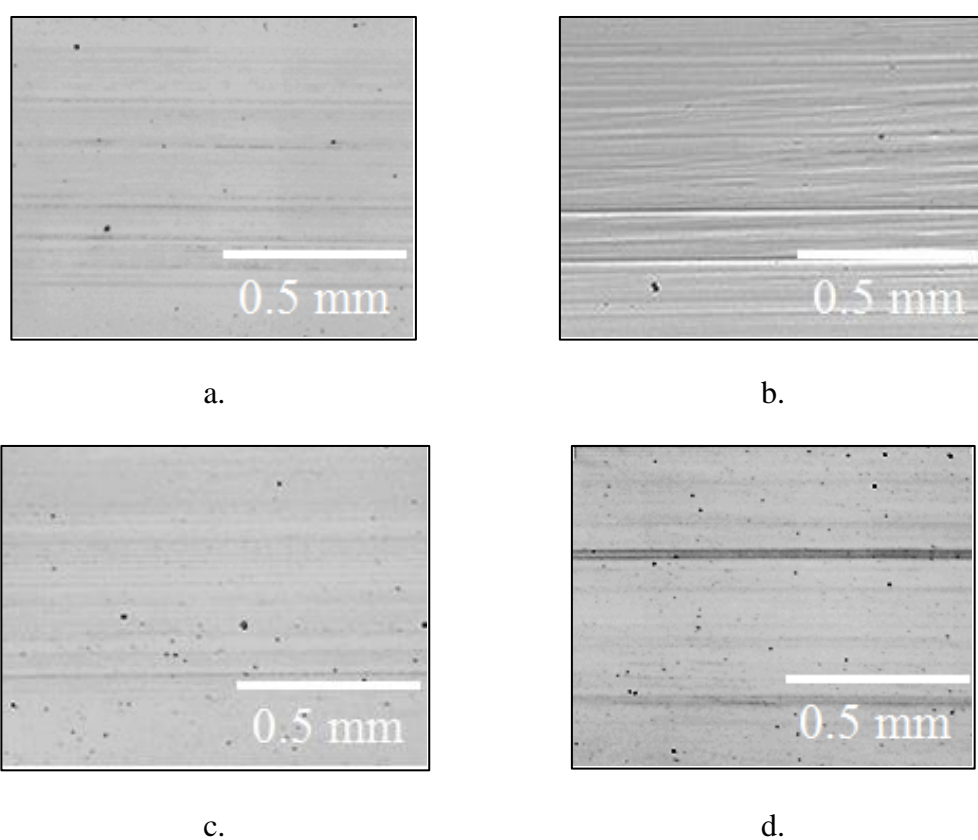
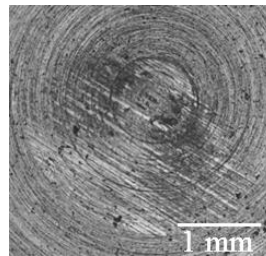


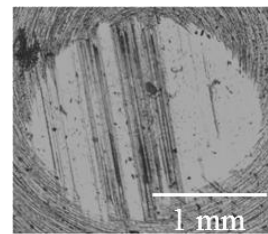
Figure 4-14: Wear images of a-C:H after tribo-testing in the pin-on-reciprocating plate rig: a. in base oil after six hours, b. in base oil after 20 hours, c. in fully formulated oil + ZDDP after six hours and d. in fully formulated oil +ZDDP after 20 hours.

4.2.8. Microscope Images of Counter-body Wear for a-C:H

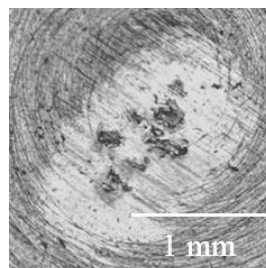
The cast iron counter-body images after tribometer tests against a-C:H for base oil for six and twenty hours and in fully formulated oil + ZDDP for six and twenty hours are presented in Figure 4-15, a, b, c, and d respectively. The images show for base oil that primarily polishing wear is taking place at the surface of the counter-body. The surface of the counter bodies in the fully formulated oil + ZDDP show less wear, but there is evidence of the DLC coating present on the surface of these samples.



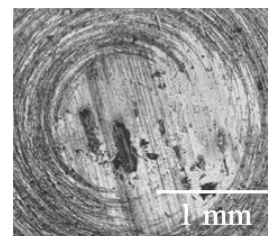
Base oil – six hours



Base oil – twenty hours



Fully formulated oil + ZDDP – six hours



Fully formulated oil + ZDDP – twenty hours

Figure 4-15: Microscope images of counter-body after tribometer testing against a-C:H

The pin wear for all of the coatings is quantified in section 4.2.15.

The following key points can be made about the friction and wear results obtained using base oil and fully formulated oil + ZDDP on a-C:H:

- The coefficient of friction was more stable in the tests performed in fully formulated oil.
- The friction performance in fully formulated oil was at a reasonable level (since the oil contained no friction modifier) at a coefficient of friction of 0.07 – 0.09.
- It appears that the ZDDP additive has a positive effect on tribological system, this is evidenced by both the volume lost through wear and the wear rate of the a-C:H tested in fully formulated oil compared to those tested in base oil.

4.2.9. Si-DLC

4.2.9.1. Si-DLC Friction Results

The Si-DLC was tested using the same conditions as the a-C:H. The friction results are presented as a function of time for six, twelve and twenty hours in Figure 4-16, Figure 4-17, and Figure 4-18, respectively. The experiments were repeated three times. The experimental methodology, oils and test parameters can be seen in 4.2.5 . It can be seen that the coefficient of friction for each of the time spans tested is very stable. However it must be noted that partial delamination occurred in each of the tribometer experiments; heavily in base oil and less so in the fully formulated oil. This was noticed after the experiments were conducted and is not indicated in the friction graphs.

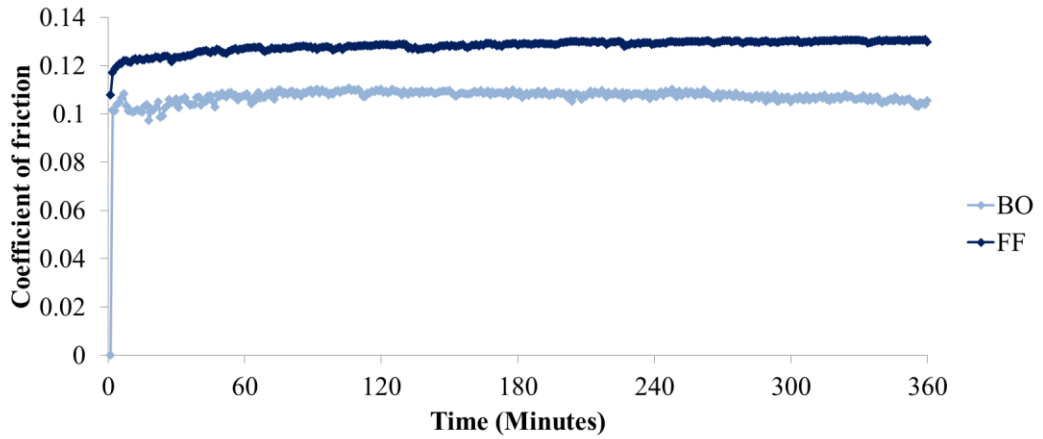


Figure 4-16: Coefficient of friction of Si-DLC in base oil and fully formulated oil tested for six hours on pin on reciprocating plate tribometer

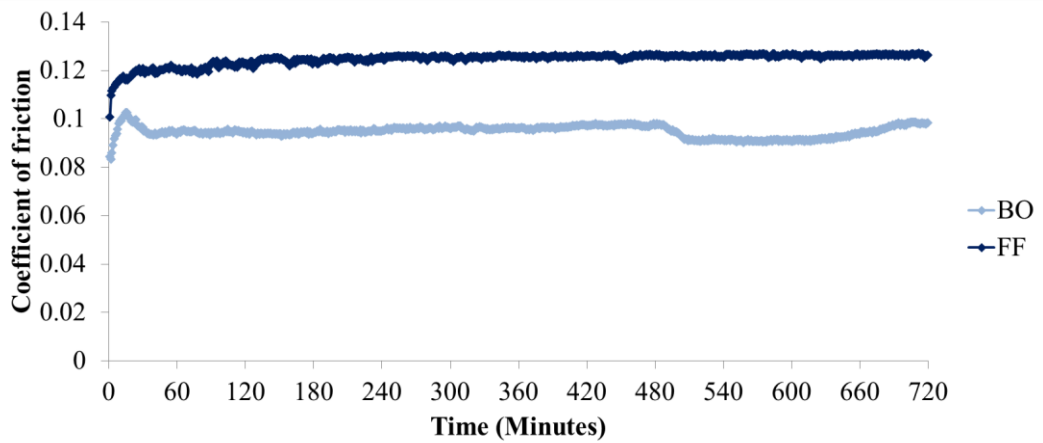


Figure 4-17: Coefficient of friction of Si-DLC in base oil and fully formulated oil tested for twelve hours on pin on reciprocating plate tribometer

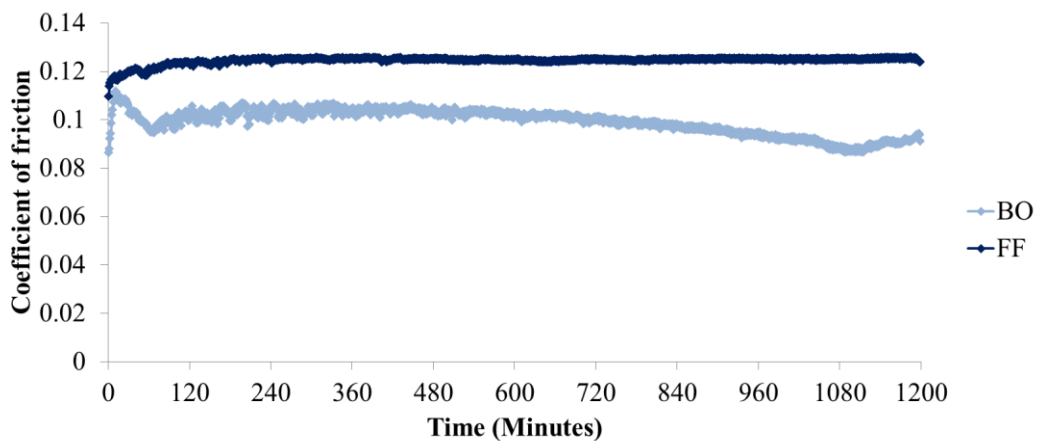


Figure 4-18: Coefficient of friction of Si-DLC in base oil and fully formulated oil tested for twenty hours on pin on reciprocating plate tribometer

4.2.9.2. Steady State Friction for Si-DLC

In each of the tribometer experiments, the Si-DLC seemed to perform better in base oil than in the fully formulated oil in terms of friction. Figure 4-19 shows that in six, twelve and twenty hour tests the steady state friction was 18%, 27% and 40% less in base oil than those conducted in fully formulated oil, it must be noted that despite the drop in friction, the samples had delaminated. The steady state friction values are very consistent for the testing in fully formulated oil from six to twenty hours testing, whereas in the base oil the steady state friction decreases over time. This seems to go against the results seen in a-C:H. However the wear volume and rate for the base oil is considerably higher than in the fully formulated oil as is presented in Figure 4-20 and in Figure 4-21 respectively.

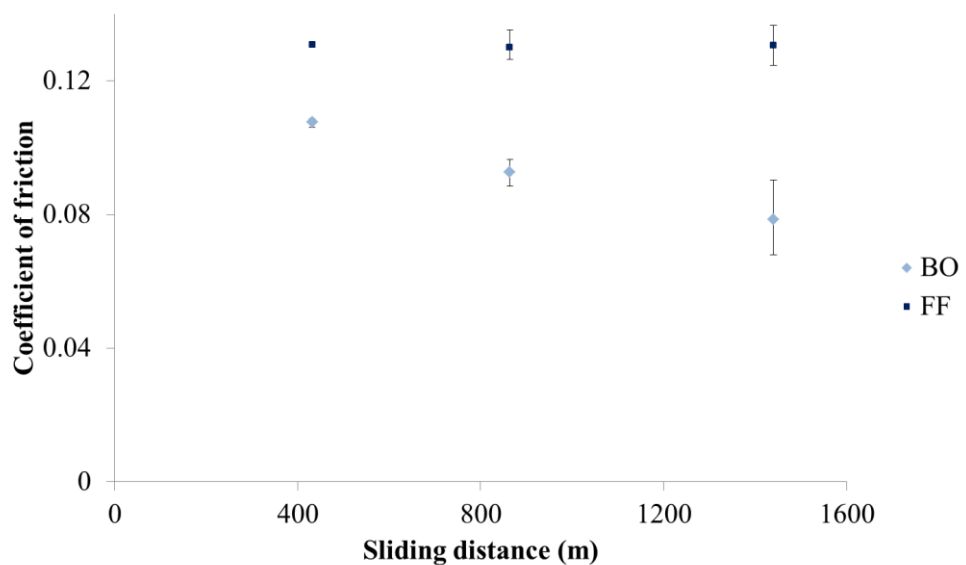


Figure 4-19: Steady state friction results for Si-DLC after tribological testing in base oil (BO) and fully formulated oil + ZDDP (FF)

4.2.9.3. Si-DLC Wear Volume and Wear Rate

Despite lower steady state friction coefficients in base oil than in fully formulated oil + ZDDP, the wear volume, shown in Figure 4-20 is higher. It is generally an order of magnitude higher than the wear volume seen in a-C:H Figure 4-12. When subjected to a twenty hour test in base oil, the friction is at its lowest value, 0.079, but the wear volume is at a maximum $1.33 \times 10^{-11} \text{ m}^3$, this shows that while the coating exhibiting low levels of friction, it is experiencing a high volume of wear, and that removal of the coating has taken place. The removal of the coating is not always apparent in the graphs depicting the friction coefficient of the coating. In the case of the Si-DLC coating, which only partially delaminated, this may be due to the wear area not being large enough to influence the friction.

The samples tested in fully formulated oil experience a higher steady state friction value (0.12 – 0.13) whilst similarly experiencing a high wear volume ($1.05 \times 10^{-11} \text{ m}^3$ after twenty hours testing). The fully formulated oil tests experienced much more consistency with regards to friction, whereas the opposite occurred in the tests conducted in base oil. The wear volume of the tests conducted in fully formulated oil is lower by 47% and 21% in six hour and twenty hour tests respectively, and higher by 18% in twelve hour tests, than those conducted in base oil.

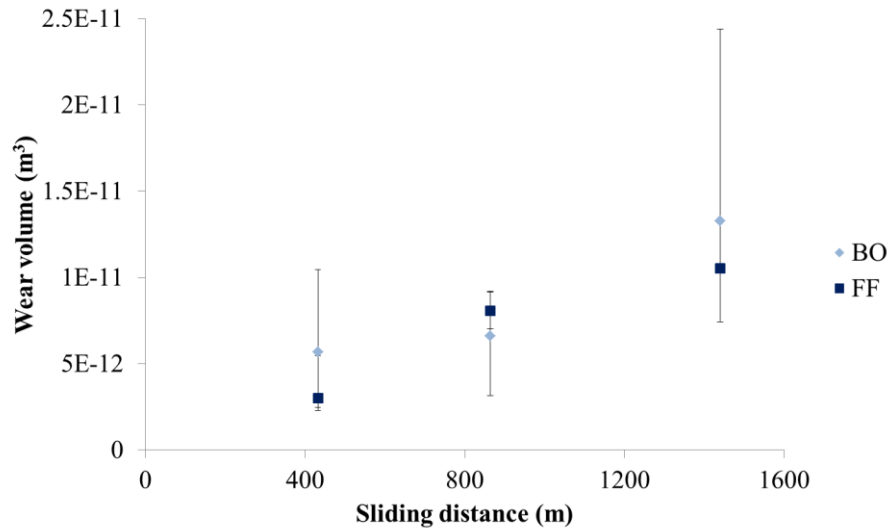


Figure 4-20: Wear volume of Si-DLC after tribological testing in base oil (BO) and fully formulated oil + ZDDP (FF)

The wear rate for Si-DLC as a function of time and lubricant can be seen in Figure 4-21. The wear rate fluctuates considerably when the sample is tested in base oil, whereas the values taken in fully formulated oil + ZDDP are relatively stable. The wear rate initially increases in the fully formulated oil testing, but decreases when the test reaches twenty hours, suggesting that protection is present on the surface of the Si-DLC. The wear rate for the Si-DLC coating is different to that seen in the a-C:H coating. The wear rate is seen to increase as the sliding distance increases, this is due to the partial delamination of the coating causing an increased wear volume, this does not occur in the case of a-C:H due to lower wear volumes. Other authors have also noted the delamination of Si-DLC in sliding systems in the presence of both base oil and fully formulated oil [186].

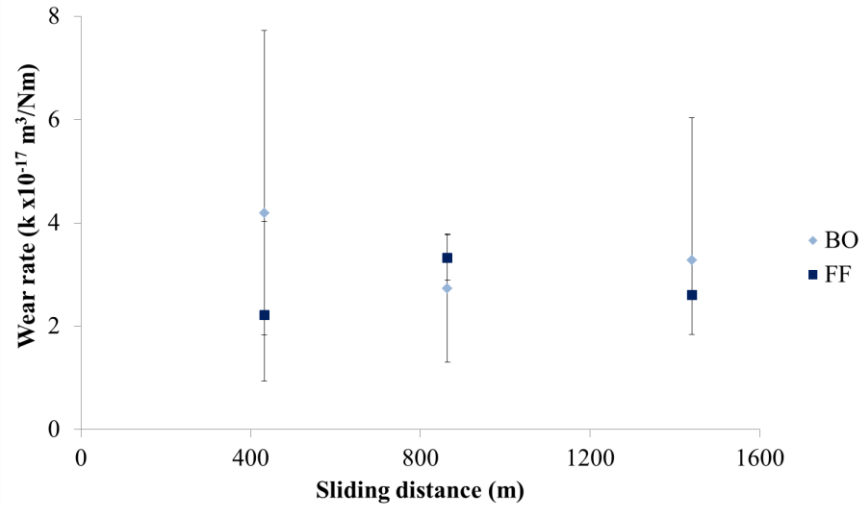
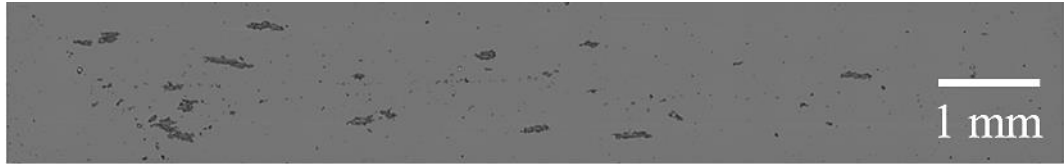


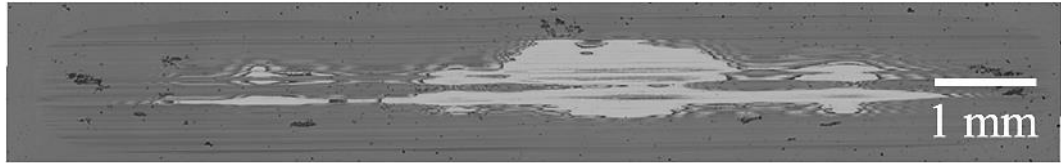
Figure 4-21: Wear rate of Si-DLC after tribological testing in base oil (BO) and fully formulated oil (FF)

4.2.10. Microscope Images of Si-DLC Coating Wear

Microscope images of the Si-DLC samples tested on the tribometer in base oil for six and twenty hours, and in fully formulated oil for six and twenty hours are presented in Figure 4-22, respectively. It is seen here that the severity of wear increased over time, exposing the interlayers and in some cases the substrate material. From these images and the wear rate data, it can be said that the addition of ZDDP into the sliding contact between the cast iron pin and the Si-DLC does not seem to have as great an effect as it does on the a-C:H coating, if at all. Some signs of improvement are shown in the wear of the Si-DLC when the ZDDP additive is used, but these are minimal.



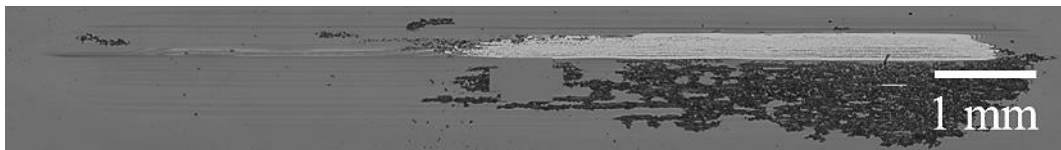
Si-DLC in base oil after six hours



Si-DLC in base oil after twenty hours



Si-DLC in fully formulated oil + ZDDP after six hours

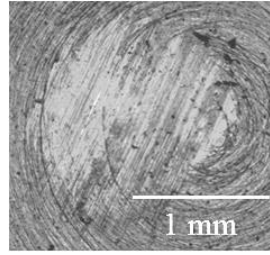


Si-DLC in fully formulated oil + ZDDP after twenty hours

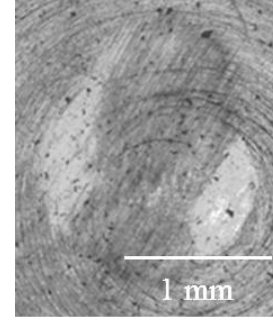
Figure 4-22: Wear images of Si-DLC plate

4.2.11. Microscope Images of Counter-body Wear for Si-DLC

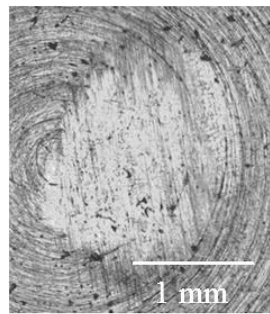
The cast iron counter-body images after tribometer tests against Si-DLC for base oil for six and twenty hours and in fully formulated oil + ZDDP for six and twenty hours are presented in Figure 4-23, a, b, c, and d respectively.



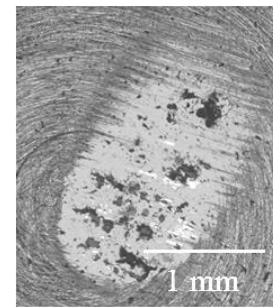
Base oil – six hours



Base oil – twenty hours



Fully formulated oil + ZDDP – six hours



Fully formulated oil + ZDDP – twenty hours

Figure 4-23: Microscope images of counter-body after tribometer testing against Si-DLC

The following key points can be made about the friction and wear results obtained using base oil and fully formulated oil + ZDDP:

- The coefficient of friction is consistently lower in base oil than in fully formulated oil + ZDDP.
- Despite lower coefficient of friction, a higher wear volume was noticed in base oil, due to the ZDDP additive in the fully formulated oil.
- The wear rate is lower for the tests performed in fully formulated oil due to the protective nature of ZDDP; the rates are also much more stable than those performed in base oil.

The Si-DLC did not perform as well as the a-C:H in the tribometer tests with regards to wear rate, shown in Figure 4-21, and wear volume, shown in Figure 4-20. The

microscope images of the worn samples tested in base oil, Figure 4-22, show signs of delamination from six hours, and the coating was completely removed in some areas after twenty hours of testing. In the fully formulated oil a similar trend was also seen. After six hours, some signs of delamination were present; however, this was less severe than in the tests conducted in base oil. In the twenty hour microscope image it can be seen that some areas of the coating were completely removed, with some areas surrounding this that show signs of coating removal, but not wholly. In the areas where the coating remained, some protection may have been present - a possible tribo-film perhaps, seen in the AFM images taken for this sample, Figure 4-39, but not enough to prevent the removal of the coating.

4.2.12. W-DLC

4.2.12.1. W-DLC Friction Results

The W-DLC was subject to the same testing as the a-C:H and Si-DLC. The friction results for W-doped DLC are presented as a function of time for six, twelve and twenty hours in Figure 4-24, Figure 4-25 and Figure 4-26, respectively. In each of the experiments, the coating delaminated fully in each of the durations tested.

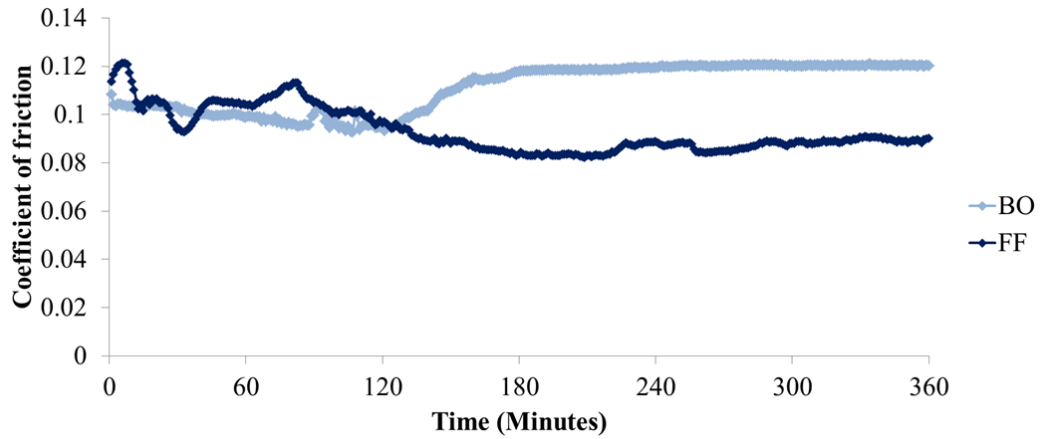


Figure 4-24: Coefficient of friction of W-DLC in base oil and fully formulated oil tested for six hours on pin on reciprocating plate tribometer

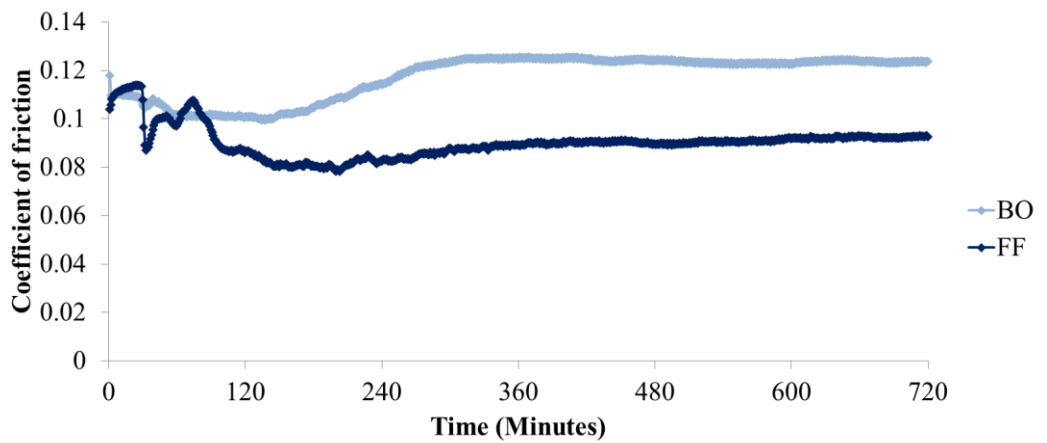


Figure 4-25: Coefficient of friction of W-DLC in base oil and fully formulated oil tested for twelve hours on pin on reciprocating plate tribometer

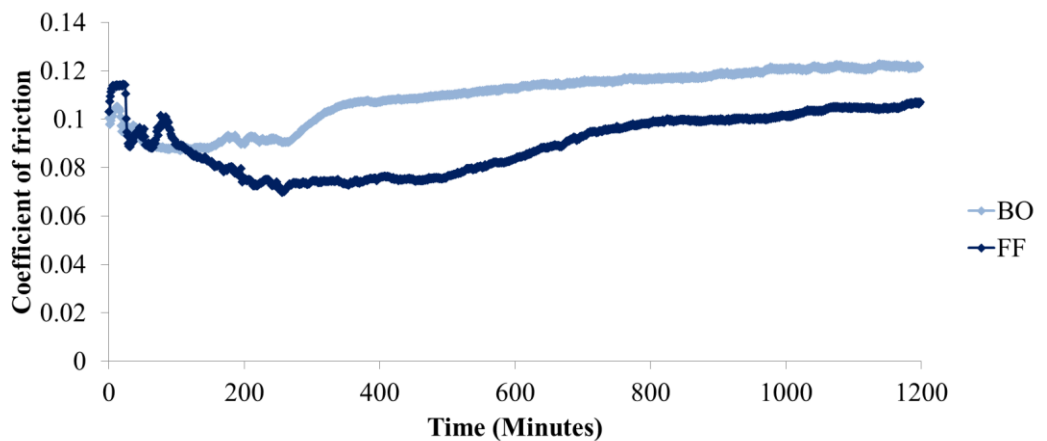


Figure 4-26: Coefficient of friction of W-DLC in base oil and fully formulated oil tested for twenty hours on pin on reciprocating plate tribometer

4.2.12.2. Steady State Friction W-DLC

The steady state friction results for W-DLC are shown in Figure 4-27. Since the coating delaminated fully almost instantaneously, the steady state friction results for these coatings are unrepresentative of the coating itself.

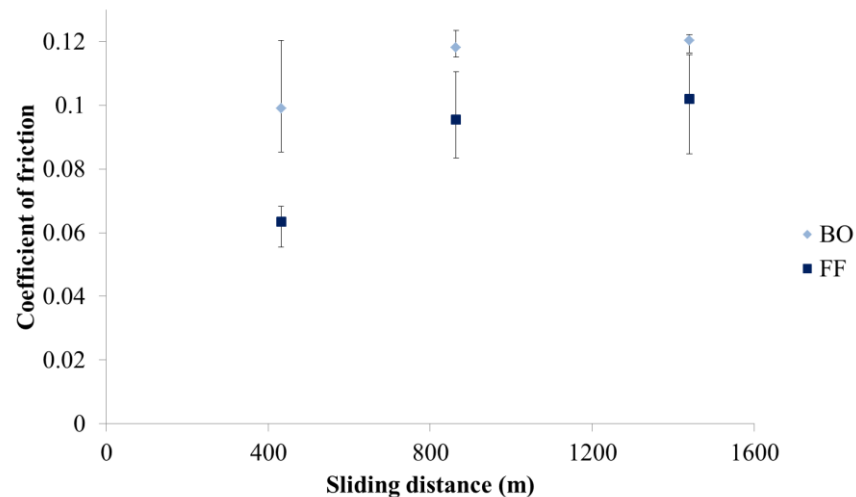


Figure 4-27: Steady state friction of W-DLC after tribological testing in base oil (BO) and fully formulated oil (FF)

4.2.12.3. W-DLC Wear Volume and Wear Rate

The wear rate for W-DLC is shown in Figure 4-29. The wear rate is high for the first six hours of the base oil and fully formulated oil tests; this is due to the coating fully delaminating. Since a factor of the wear rate is time, the rate here is seen to go down, since there is no coating left on the surface of the sample, whilst the wear volume (shown in Figure 4-28) remains quite similar throughout each duration – since all of the coating has been lost, and only the substrate is left to be worn.

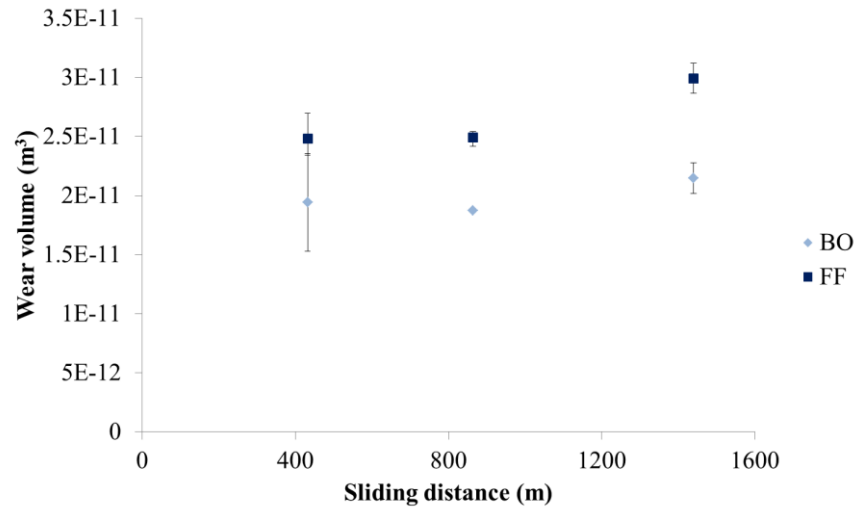


Figure 4-28: Wear Volume of W-DLC after tribological tests in base oil (BO) and fully formulated oil + ZDDP (FF)

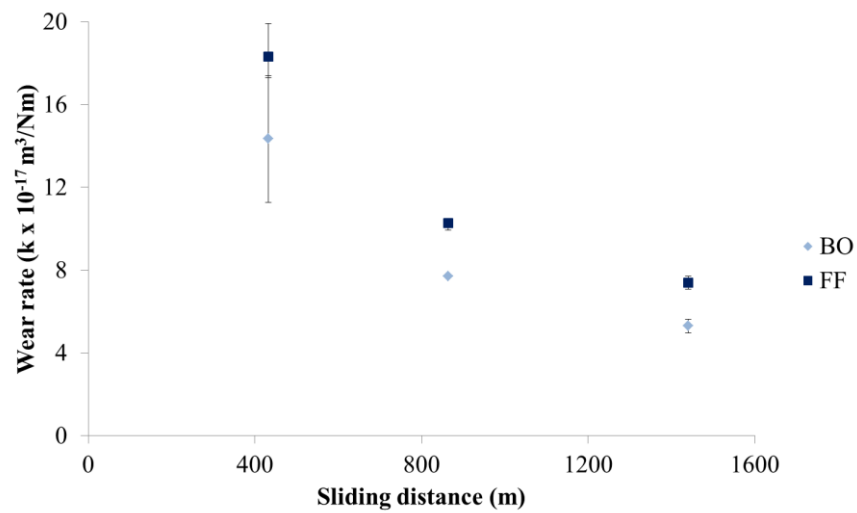
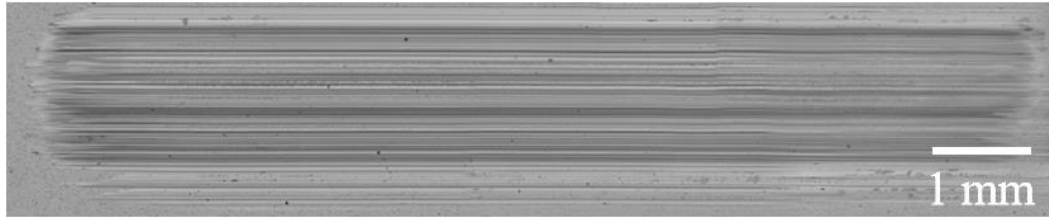


Figure 4-29: Wear Rate for W-DLC after tribological tests in base oil (BO) and fully formulated oil + ZDDP (FF)

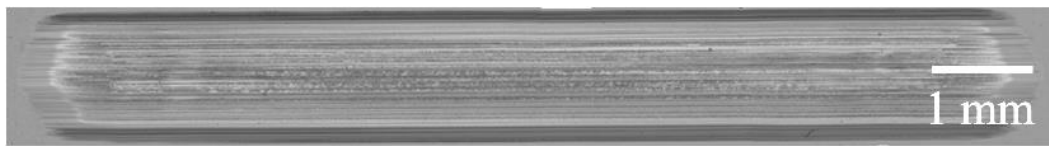
4.2.13. Microscope Images of W-DLC Coating Wear

Microscope images of the W-DLC samples tested on the tribometer in base oil for six and twenty hours, and in fully formulated oil + ZDDP for six and twenty hours are presented in Figure 4-30, respectively. The severity of wear increases over time

in the tests conducted in base oil, but as can be seen from the wear volume, only slightly as most of the material has been removed.



W-DLC in base oil after six hours



W-DLC in base oil after twenty hours



W-DLC in fully formulated oil + ZDDP after six hours



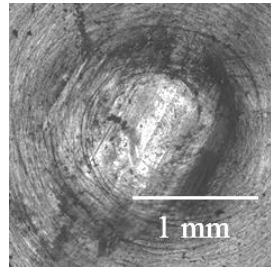
W-DLC in fully formulated oil + ZDDP after twenty hours

Figure 4-30: Wear images of W-DLC plate

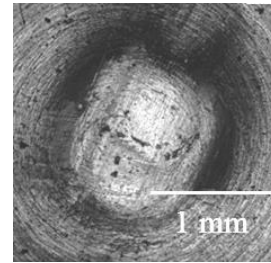
4.2.14. Microscope Images of Counter-body Wear for W-DLC

The cast iron counter bodies used in the tribometer tests against W-DLC in base oil for six and twenty hours and in fully formulated oil for six and twenty hours are presented in Figure 4-31, a, b, c and d respectively. It is apparent on each of the

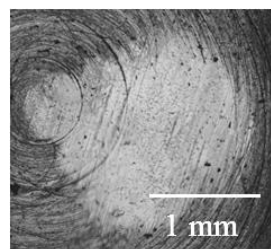
images that some of the W-DLC has transferred onto the pin. This appears to be worse in the samples tested in base oil than in fully formulated oil + ZDDP.



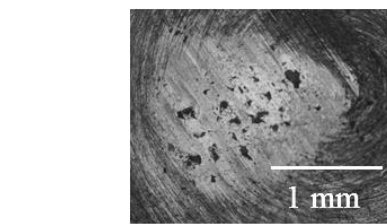
Base oil – six hours



Base oil – twenty hours



Fully formulated oil + ZDDP – six hours



Fully formulated oil + ZDDP – twenty hours

Figure 4-31: Microscope images of counter-body after tribometer testing against W-DLC

The following key points can be made about the W-DLC sample relating to the friction and wear results obtained using base oil and fully formulated oil + ZDDP:

- The W-DLC performed poorly and delaminated in all of the tests conducted in base oil and fully formulated oil + ZDDP

The W-DLC coating performed catastrophically in each of the tribometer tests. It can be seen from the wear volume this sample experienced after the tribometer testing, seen in Figure 4-28 that the values are an order of magnitude higher than those experienced by the a-C:H coating in both base oil and fully formulated oil + ZDDP. This increase in wear occurs in the literature, Kalin et al. [187] discovered

recently that W-DLC did not perform well within a sliding environment in base oil or in a fully formulated oil with anti-wear and extreme pressure additives. The W-DLC failure is attributed to severe adhesive wear and mutual transfer of coating and counter-body species, as is evidenced by the coating residue seen in Figure 4-31, causing an alteration in coating structure and the decomposition of the W-DLC, forming complex carbides (η -phase $W_{6-x}Fe_xC$). The drop in wear rate of the W-DLC seen in Figure 4-29, at first glance seems promising, however when compared to the wear volume it was clear that the wear rate had decreased due to the coating fully delaminating, and there being no material left to wear through. It has been suggested by Vengudusamy et al. [105] that wear induced graphitisation can inhibit the formation of the distinctive phosphate pad like structure, which is typically formed by the ZDDP additive, this mechanism could be inhibiting tribo-film formation within this study as seen in both the W-DLC and Si-DLC samples.

It is apparent from the microscope images of this sample shown in Figure 4-30, that after six hours testing in base oil, the coating is less severely damaged (although still heavily damaged relative to that seen in the a-C:H coating in Figure 4-14). The microscope images reinforce the wear volume data, showing that the coating has fully delaminated, with evidence of the interlayer structure seen at the ends of each wear scar. It is proposed here that a mechanism similar to that presented in section 7.1.3 is taking place; an adhesive wear mechanism which is evidenced by the transfer of DLC material to the cast iron counter-body surface (image presented in Figure 4-31). This occurred in all instances of testing; in base oil and fully formulated oil + ZDDP. The adhesion experienced during the wear testing has led to the complete removal of the coating, this has also been noted by other researchers

[188]. From the results presented here, it is apparent that this particular W-DLC coating (Balinit C*) is not suitable for this application; however other formulations may be more compatible, depending on the coating.

4.2.15. Counter-body Wear for a-C:H, Si-DLC and W-DLC

The wear for the cast iron counter-body from the six and twenty hour experiments in base oil and fully formulated oil is seen in Figure 4-32. As can be seen from the graph, the counter-body against the a-C:H showed a lower wear area in the tests using fully formulated oil, whereas the Si-DLC and W-DLC counter bodies had a higher wear area in the fully formulated oil compared with the base oil. Figure 4-33 shows the wear rate for the cast iron counterparts.

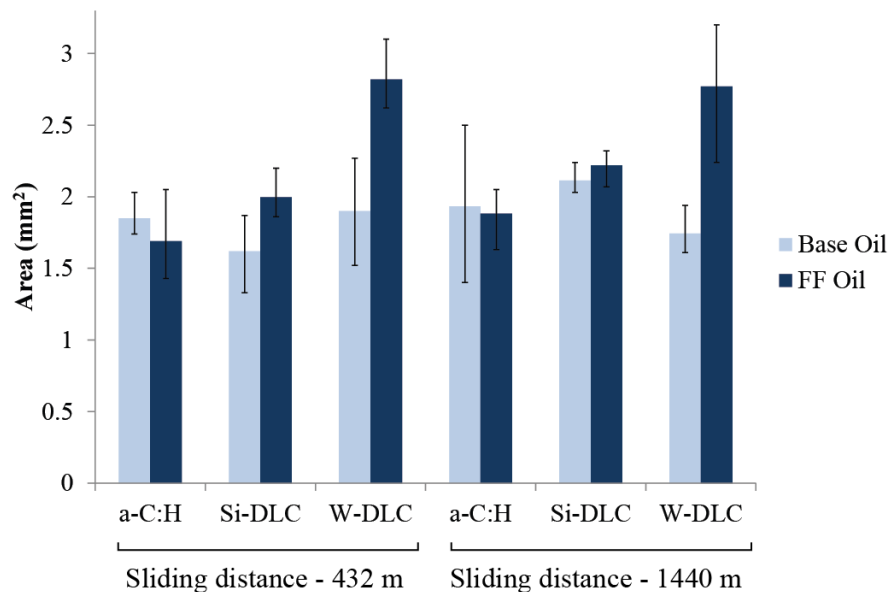


Figure 4-32: Pin wear of a-C:H, Si-DLC and W-DLC after tribo-testing against DLC

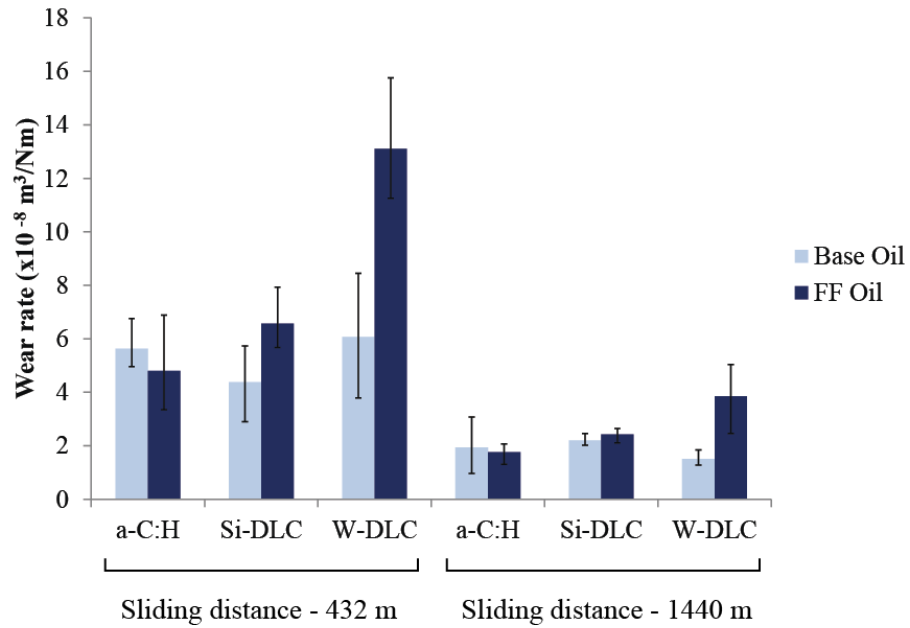


Figure 4-33: Wear rate for cast iron counter-body for a-C:H, Si-DLC and W-DLC after six and 20 hours sliding in base oil and fully formulated oil + ZDDP (FF oil)

From the wear rate, it is clear that that counter-body sliding against the a-C:H had a lower wear rate in fully formulated oil + ZDDP than in base oil, this was not the case where the counter-body was sliding against Si-DLC and W-DLC, where after 432 m of sliding, the wear rates are considerably greater in base oil. After 1440 m sliding, the wear rates of the counter bodies against the Si-DLC show a much lower discrepancy, whereas the W-DLC presents a much larger difference.

Table 4-5: Summary of wear tests of a-C:H, Si-DLC, W-DLC and counter-body

Sample	Lubricant	Distance	Delaminated	Wear Rate counterbody ($\times 10^{-8}$ m^3/Nm)	Wear rate plate ($\times 10^{-17}$ m^3/Nm)
a-C:H	Base oil	432		5.64	0.58
		1440		1.94	1.31
	Fully formulated oil + ZDDP	432		4.79	0.33
		1440		1.76	0.14
Si-DLC	Base oil	432		4.38	4.19
		1440		2.20	3.28
	Fully formulated oil + ZDDP	432		6.57	2.22
		1440		2.43	2.60
W-DLC	Base oil	432		6.07	14.35
		1440		1.50	5.30
	Fully formulated oil + ZDDP	432		13.10	10.27
		1440		3.85	7.40

4.2.16. Scanning Electron Microscopy and Energy Dispersive X-ray

Analysis

In order to further gauge the severity of wear, any potential tribochemical reactions and mechanisms, the samples were taken to be examined under SEM, EDX and white light interferometry, these techniques are described in 3.6, 3.7 and 3.11, respectively.

SEM and EDX analysis was carried out in the wear scars of the a-C:H, Si-DLC and W-DLC sample in order to determine the severity of the wear experienced by the samples. This was done using EDX point and mapping to detect which elemental species were present. The samples were thoroughly cleaned in an ultrasonic bath in acetone for 15 minutes to ensure that no tribo-film or lubricant species were present on the surface of the samples prior to observation. The SEM and EDX images are given in Figure 4-34, Figure 4-35 and Figure 4-36 for a. a-C:H, b. Si-DLC and c. W-DLC, respectively, after pin on reciprocating plate tests in fully formulated oil for twenty hours.

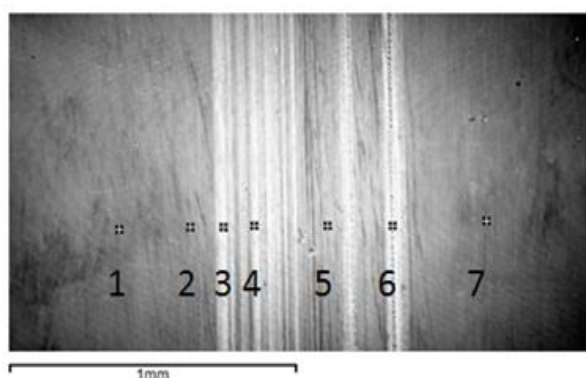


Figure 4-34: SEM image and EDX analysis for a-C:H after pin on reciprocating plate test in fully formulated oil + ZDDP for twenty hours

From the SEM images it can be seen that different mechanisms of wear are taking place. The a-C:H shows micro grooves on the surface whereas the Si-DLC shows little evidence of this, just delamination.

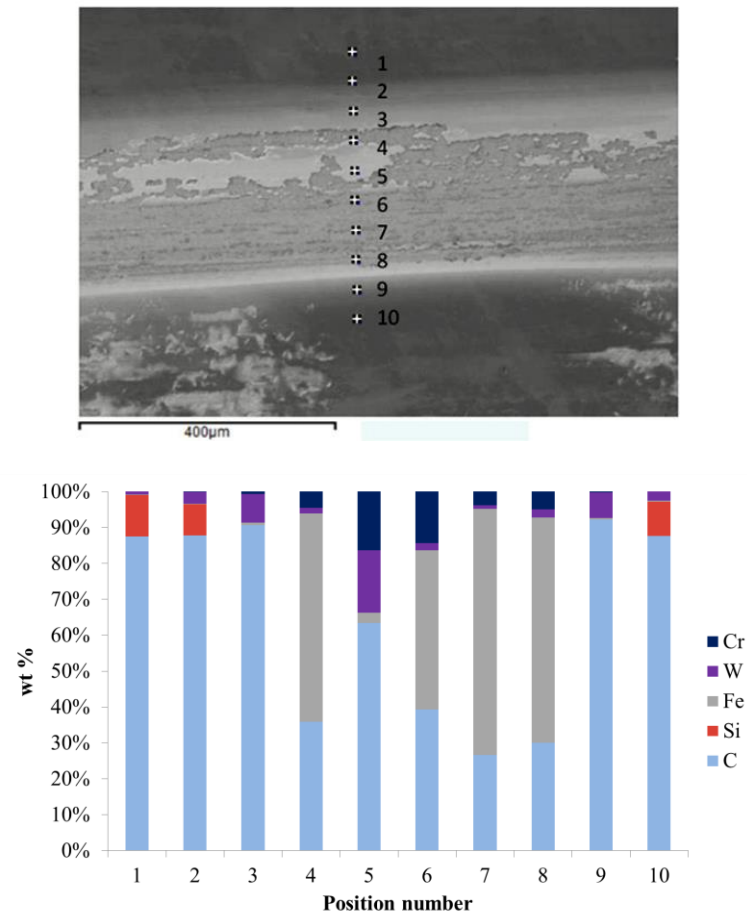
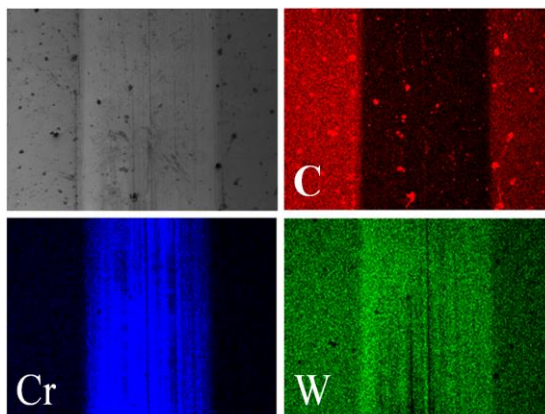


Figure 4-35: SEM image and EDX analysis for Si-DLC after pin on reciprocating plate test in fully formulated oil + ZDDP for twenty hours

The W-DLC was completely delaminated. The EDX scans for these samples show that the a-C:H was not removed. The Si-DLC shows large amounts of interlayer and substrate species, Cr, WC and Fe. A different approach to the EDX was taken with the W-DLC in order to present the severity of delamination. Only a small amount of carbon is present in the wear scar, with a majority of Cr and WC interlayer species, demonstrating that the coating has fully delaminated.



c. W-DLC

Figure 4-36: SEM image and EDX analysis for W-DLC after pin on reciprocating plate test in fully formulated oil + ZDDP for twenty hours

4.2.17. White Light Interferometry

The samples that were tested on the pin-on-reciprocating-plate tribometer for twenty hours in fully formulated oil were examined (along with all of the other samples from this chapter) under a white light interferometer detailed further in 3.11. The white light interferometer gave values for wear volume which are presented earlier in this chapter. The images gained from the twenty hour tests are presented in Figure 4-37, which show the depth of the wear scars. It can be seen that very little of the a-C:H was worn, whereas in the Si-DLC and the W-DLC much more of the coating has been removed.

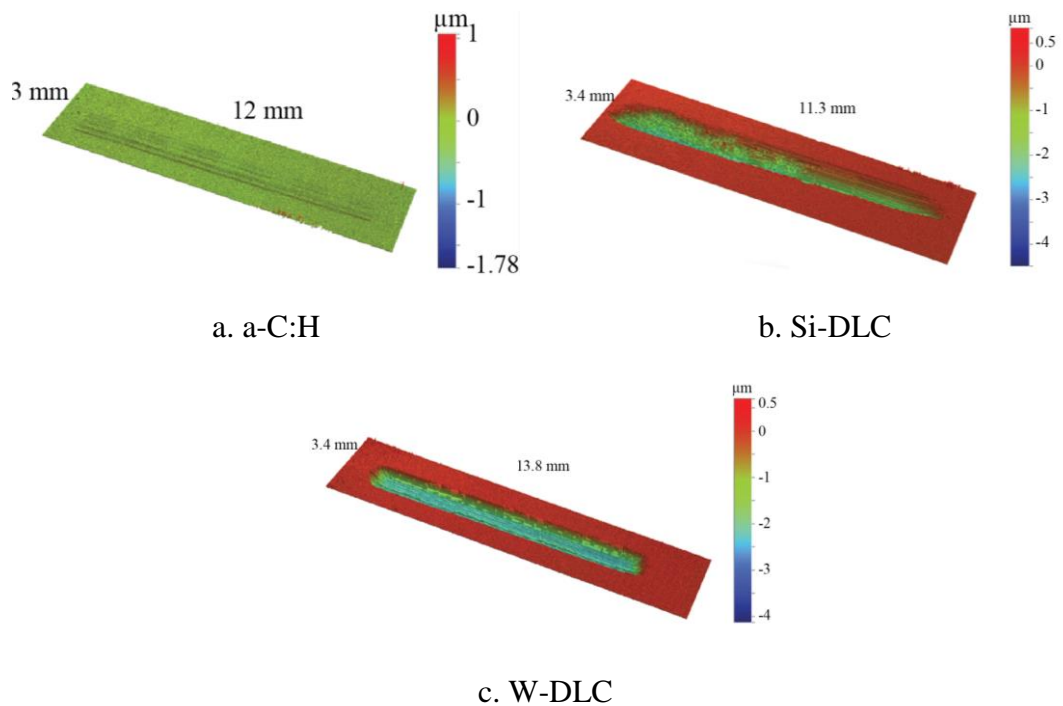
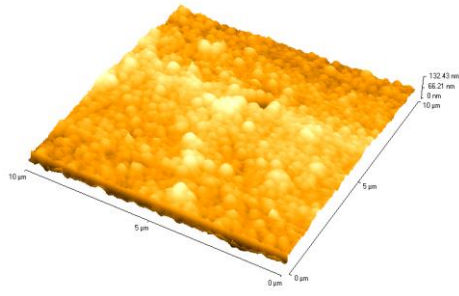


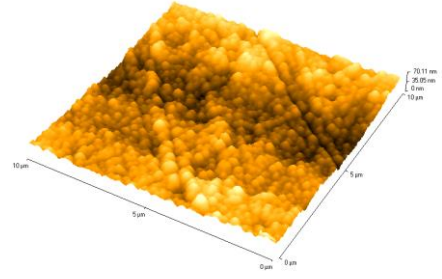
Figure 4-37: White light interferometry images for a. a-C:H, b. Si-DLC and c. W-DLC after testing on pin on reciprocating plate tribometer for twenty hours in fully formulated oil + ZDDP showing the wear tracks of three selected samples

4.2.18. Atomic Force Microscopy

After the wear testing was completed, it was apparent that the tungsten doped DLC did not function well within the tribometer tests after delaminating completely and no trace of DLC being left on the substrate within the wear scar, and as such was discontinued from further testing. The wear rates of DLC and Si-DLC were significantly lower in the tribological testing using fully formulated oil. This oil contained the anti-wear additive which is effective in steel/iron systems and is well documented in the literature [33, 189]. However there is a debate as to whether this additive has an effect on DLC coatings [115]. The a-C:H and Si-DLC samples were inspected using a VEECO AFM before and after tribological testing, these images can be seen in Figure 4-38 and Figure 4-39 respectively. The experimental details are outlined in 3.12.

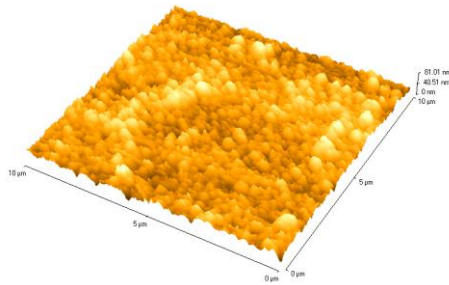


a. a-C:H

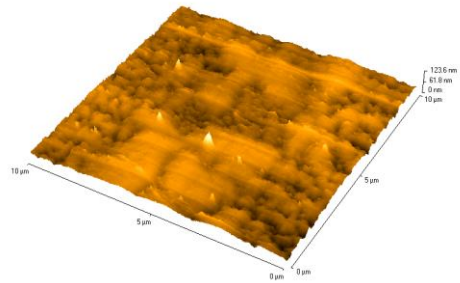


b. Si-DLC

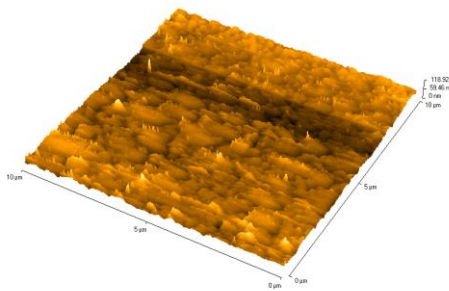
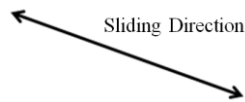
Figure 4-38: AFM images of a. a-C:H and b. Si-DLC prior to tribological testing



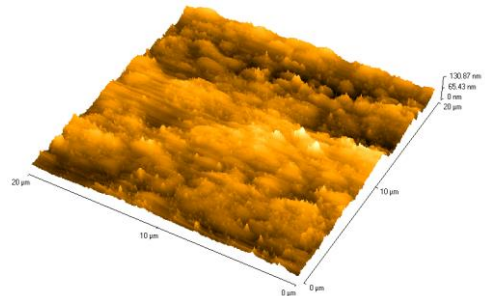
a. a-C:H Six Hours



b. a-C:H Twenty Hours



c. Si-DLC Six Hours



d. Si-DLC Twenty Hours

Figure 4-39: AFM Images of a-C:H and Si-DLC after six and twenty hours on the tribometer using fully formulated oil + ZDDP

It can be seen in Figure 4-39 a. that the a-C:H tested in six hours is relatively unaffected by the sliding, whereas the Si-DLC in Figure 4-39 c. tested for six hours

begins to show signs of wear, as can be seen by the directionality of the wear track beginning to form.

The images shown for the testing conducted for twenty hours are shown for a-C:H and Si-DLC in Figure 4-39 b. and d. respectively. Each of the images shows evidence of a tribo-film, though the patchy like structure is more evident in the a-C:H image. The images show evidence of wear mechanisms, the Si-DLC shows signs of polishing wear and some directional wear, also delamination as is evidenced by the wear volume loss and SEM images of the coating. The a-C:H was protected by what appears in the AFM images to be a tribo-film, the Si-DLC appears to have a similar structure, but since the tribo-testing showed severe delamination of this coating, it was not continued to the further X-Ray Photoelectron Spectroscopy (XPS) testing.

4.2.19.XPS

X-ray Photoelectron Spectroscopy was used in this project in order to determine whether or not a tribo-film was present on the surface of DLC.

XPS was carried out on the a-C:H sample alone using the method described in 3.8. Since the Si-DLC sample had delaminated partially during the tribometer testing and showed little signs of a tribo-film in the AFM analysis, it was not included. The W-DLC sample was not included due to the severe delamination experienced by this coating during tribo-testing.

XPS analysis was carried out on the cast iron counter-body and the a-C:H sample after tribo-testing on a pin on reciprocating plate tribometer for six and twenty hours

in fully formulated oil containing ZDDP. The survey scans for these samples can be found in Figure 4-40.

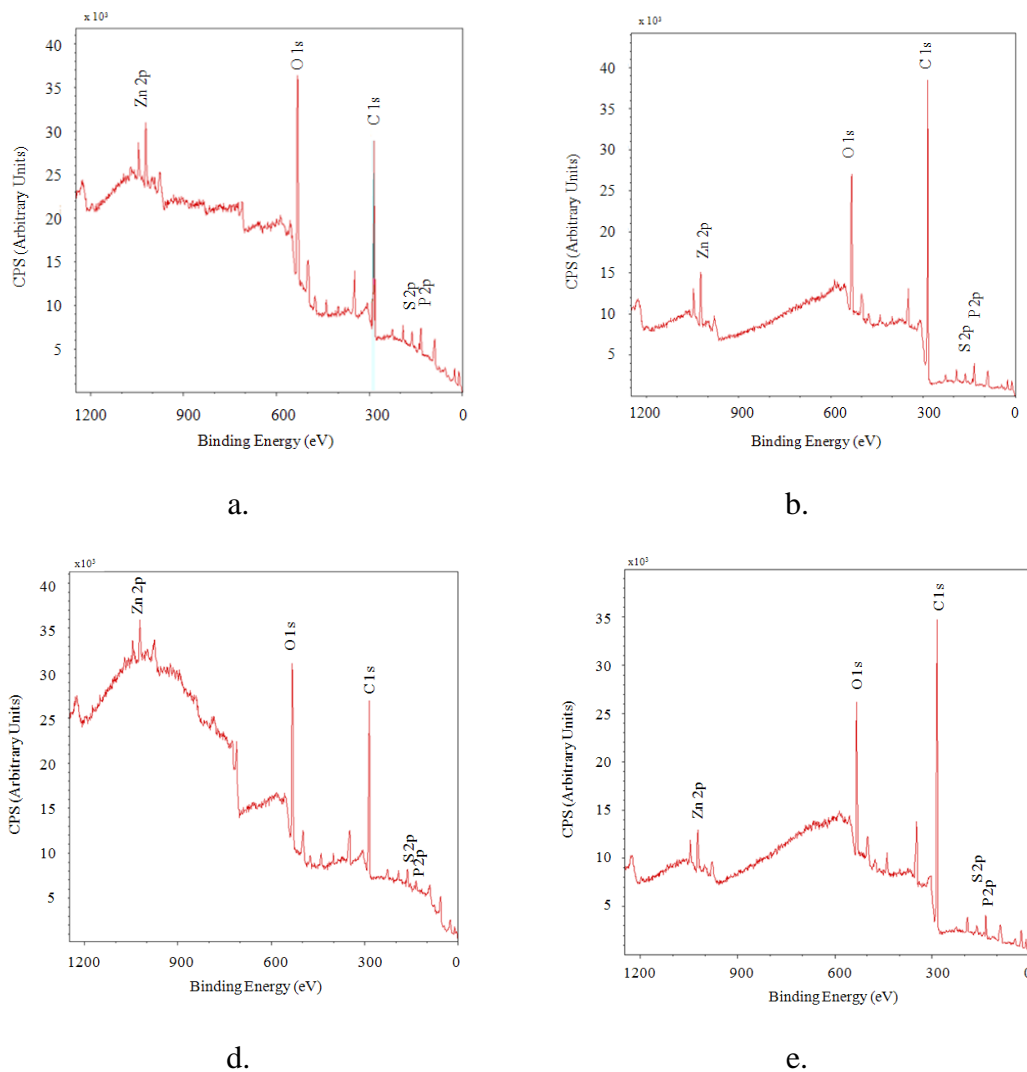


Figure 4-40: XPS survey scan of a. cast iron pin and b. a-C:H after six hours and c. Cast iron pin and d. a-C:H after twenty hours on tribometer in fully formulated oil.

Each element present was quantified and the atomic percentage present for the a-C:H coating and the cast iron counter-body is given in Table 4-6.

Table 4-6: XPS elemental quantifications of cast iron counter-body and a-C:H in fully formulated oil + ZDDP after twenty hours.

Element	Cast Iron Counter-body	a-C:H
C 1s	61.2%	77.2%
Ca 2p	3.5%	3.6%
Fe 2p	2.4%	0.1%
K 2p 3/2	0.2%	0%
N 1s	0%	0%
Na 1s	0.2%	0%
P 2p	2.6%	3.9%
S 2p	3.9%	1%
Zn 2p 3/2	0.7%	0.5%

The most common element for both samples was carbon, this was expected due to the high content of carbon in both samples. Species known to be present in the lubricant were also found at the surface such as dispersants and antioxidants, Ca, Na, P, Zn. Contaminants such as Na and K were also found at the surfaces. In order to gain a more in depth view of the chemical species present, the XPS curves were fitted using Casa XPS software so as to gain a quantitative analysis of the binding energies, corresponding chemical compounds and their atomic concentration in the tribo-film. This information is presented for both the cast iron pin and the a-C:H surface for six and twenty hours testing in Table 4-7 and Table 4-8 respectively. An example of the curve fitting for these elements is shown for the cast iron pin in Figure 4-41 and for the a-C:H in Figure 4-42.

Table 4-7: Binding energies, chemical composition and concentration of the XPS analysis carried out on a-C:H and the cast iron counter-body after six hours testing

Sample	Element	Binding Energy	Chemical Species and concentration
a-C:H after six hour tribometer test	O 1s	531.9	Phosphate/Sulphate (41%)
		532.9	Phosphate (59%)
	S 2p	163	Sulphide (100%)
		P 2p	133.5
	134.5		Metaphosphate (59%)
Zn 2p	1022.9	ZnS/ZnO/Zn-Phosphate (100%)	
Cast Iron Counter- body After six hour tribometer test	O 1s	531.4	Phosphate/Sulphate (88%)
		533.2	C-O Compound (12%)
	S 2p	160.8	Sulphide (21%)
		161.9	Sulphide (79%)
	P 2p	132.9	Pyrophosphate (51%)
133.8		Pyrophosphate (49%)	
Zn 2p	1022	ZnS/ZnO/Zn-Phosphate (100%)	

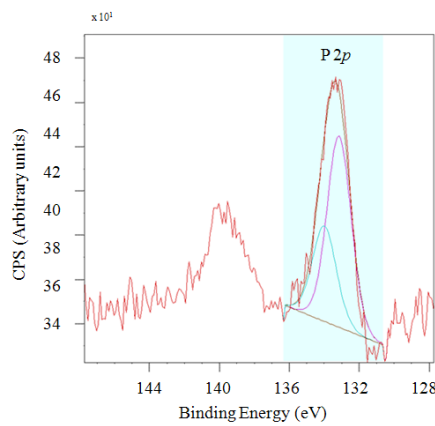
Table 4-8: Binding energies, chemical composition and concentration of the XPS analysis carried out on a-C:H and the cast iron counter-body after twenty hours testing

Sample	Element	Binding Energy	Chemical Species and concentration
a-C:H after twenty hours tribometer test	O 1s	532.1	Phosphate/Sulphate (100%)
	S 2p	160.9	Sulphide (11%)
		162.3	Sulphide (91%)
	P 2p	133.6	Pyrophosphate (67%)
		134.4	Metaphosphate (33%)
Zn 2p	1022.6	ZnS/ZnO/Zn-Phosphate (100%)	
Cast Iron Counter- body After twenty hours tribometer test	O 1s	529.9	Fe ₂ O ₃ (10%)
		531.7	Phosphate/Sulphate (90%)
	S 2p	161.1	Sulphide (21%)
		162.2	Sulphide (79%)
	P 2p	133.1	Pyrophosphate (67%)
133.9		Pyrophosphate (33%)	
Zn 2p	1022.1	ZnS/ZnO/Zn-Phosphate (100%)	

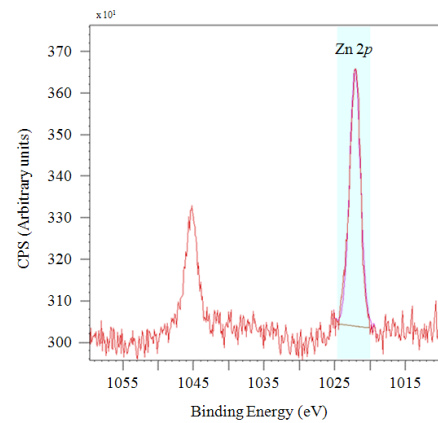
It is apparent that tribo-film species are present on both the pin and plate as early as six hours, as is evidenced by the presence of zinc, phosphorus and oxygen phosphate components detected on the surface by the XPS, shown in Table 4-7. The phosphorus peak at 133.7 eV, present on the a-C:H plate after six hours testing is typically associated with a glassy phosphate; this is the typical structure for a ZDDP tribo-film.

In the twenty hours XPS results, the O1s peak shows a binding energy of 532.1 eV on the a-C:H surface, and 531.9 eV on the cast iron counter-body surface, which is

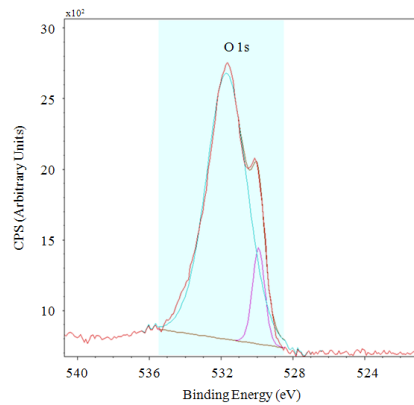
typically associated with phosphates and sulphates. After curve fitting the S 2p peak in both samples, it was discovered that this element exists in both samples as a sulphide, rendering the O bonding to be that of a phosphate, which can be attributed to the phosphate tribo-film theorised to form. The O 1s peak corresponds to Fe₂O₃ in the cast iron counter-body; this is known to react with the ZDDP in the lubricant to form a glassy phosphate tribo-film.



a. P2p Peak on cast iron counter-body



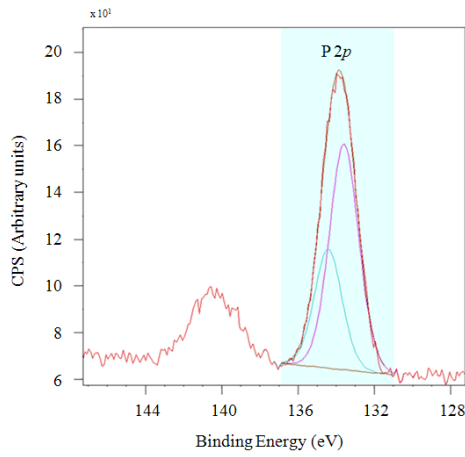
b. Zn2p Peak on cast iron counter-body



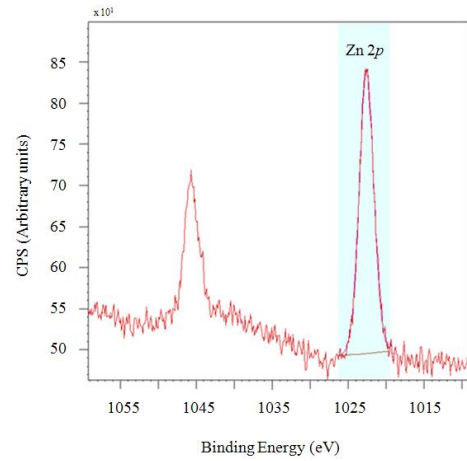
c. O 1s Peak on cast iron counter-body

Figure 4-41: Chemical species present at the cast iron counter-body surface after twenty hours tribometer testing

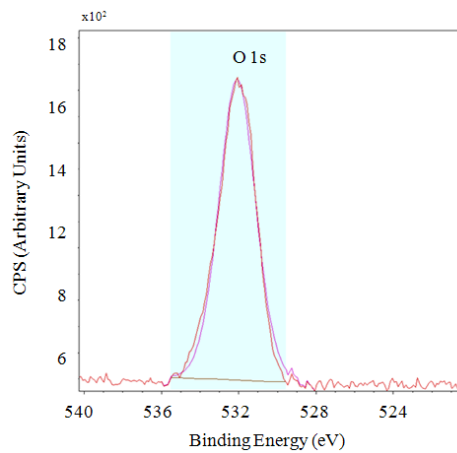
Figure 4-42 a and b show phosphate and zinc peaks, showing that there is a P based tribo-film present at the surface of the DLC.



a. P2p Peak on a-C:H surface



Zn2p Peak on a-C:H surface



c. O 1s peak on a-C:H surface

Figure 4-42: Chemical species present at DLC surface after twenty hours tribometer testing

Figure 4-41 shows the P 2p and Zn 2p species present at the cast iron counter-body surface after twenty hours tribometer testing. This was expected since ZDDP reacts with the iron within the pin. These species are also found on the a-C:H surface as can be seen in Figure 4-42, proving that a tribo-film exists on the DLC surface.

These species have also been proven to be present at the surfaces of both the cast iron counter-body and the a-C:H surface after six hours tribometer testing. Due to the wear rate decreasing with an increasing tribometer testing time as shown in Figure 4-13 and the obvious presence of the tribo-film on the twenty hour test sample when imaged using AFM, but lack of any being seen on the AFM (Figure 4-39) of the sample tested for six hours, it is clear that this builds up over time. It is theorised here that the tribo-film first forms on the cast iron counter-body and is transferred to the DLC surface during the tribometer testing.

The following key information can be noted following the XPS results

- The ZDDP lubricant additive has formed on the cast iron counter-body and the a-C:H surface, forming a protective layer after durations of six and twenty hours tribometer testing.
- The phosphate layer has developed over time on the a-C:H surface, providing protection from wear.

4.3. Summary

The results presented in this chapter show the mechanical (thickness, hardness, elastic modulus, critical load (scratch test) and sp^2 content) and tribological properties (friction, wear, tribo-film formation) of three different types of DLC. Their tribological ability was tested in two different oils. Friction and coating durability was found to be heavily reliant on the type of oil used in the a-C:H case, performing better in the fully formulated oil tests, also the presence of a ZDDP based tribo-film was found on the coating, which is shown to protect the surface from wear. The Si-DLC coating was found to delaminate under the test conditions

used, the W-DLC delaminated completely under testing, and both of these coatings are shown here to be unsuitable for this application.

Chapter 5

Results: Microwave Plasma Enhanced Chemical Vapour Deposition Using One Microwave Source

5.1. Introduction

In this chapter, Diamond-Like Carbon coatings created using microwave PECVD are assessed. Their mechanical and tribological properties are evaluated using a range of techniques. The focus of this chapter is how the deposition parameters of the coating process affect the mechanical (and eventually) tribological properties of the coatings. All of the tests were carried out using a half load on the substrate table. This enabled the user to physically see if plasma was present in the chamber, as no in-situ detection is present within the deposition system. The order of testing was as follows:

In the first part of this chapter, only one microwave source was used to deposit the coatings. This was to determine the effect that only one source had on the coatings, which would be compared with two microwave sources later in the chapter.

- The effect that the gas ratio ($C_2H_2:Ar$) within the chamber was assessed using only one microwave source. The samples were placed in two positions; one just above the microwave source and one directly in front of the source.
- The correct position was further defined using more samples spanning the length of the dummy.

- The DLC deposition time was refined in order to ensure stability of the microwave process and the optimum thickness of the coatings for testing.
- In the last stage of the testing using only one source a full factorial matrix was designed in order to test the combined effect that altering the gas ratio and the bias voltage simultaneously had on the DLC coatings.

In the second part of this chapter, two sources were used. The main focus of this chapter was to determine the optimum hardness of the samples by varying the bias voltage as it was seen in the literature to have a large impact on the hardness of the coatings [18, 56, 103]. The order of testing for two microwave sources was as follows:

- The optimum position of the samples in the chamber had to be determined, and so a positional test was carried out which was similar to that conducted using one source in the first part of this chapter.
- Following this, it was evident that the microwave sources were stable and a higher power was proposed to be used within the next series of experiments, the power was tested at 1000 W and 1200 W.
- An experiment which varied the bias voltage only was conducted next. The bias voltage was varied from 50 – 300 V in increments of 50 V. The maximum of 300 V was chosen, as above this value has a detrimental effect on the coating properties, such as hardness and elastic modulus [190, 191]
- After the bias scan series of experiments it was found that the highest hardness lies between two points of the bias voltage, 200 and 250 V, a further series of experiments were conducted between these points at smaller increments of 10 V.

5.2. Gas Ratio Tests

The first tests conducted using the microwave PECVD system were the gas ratio tests. These experiments served two purposes; to determine the stability of the source when different amounts of acetylene are used (the source is initially ignited in a pure argon atmosphere and acetylene is introduced gradually in order to ensure stability), and to gauge the effect that this had on the final coatings. Conservative values based on previous experiences of Hauzer Technocoating were used for the constant parameters as it was the initial test. The negative bias voltage was - 100 V as this was found to be a stable bias to use as seen in the literature [103, 191], the microwave power at 800 W and the test duration was set at 33 minutes. The 33 minutes duration allowed for a two minute microwave ignition in pure argon atmosphere to initially stabilise the plasma, the acetylene was then introduced gradually for two minutes. The interlayer used was a simple Cr adhesion layer. This allowed for adequate adhesion of the DLC coating and a shorter overall coating time, the recipe for which can be found in Table 4-1.

5.2.1. Recipe

The tests were performed using one source only; the full processing parameters can be seen in Table 5-1. The samples were placed in the chamber at three different positions as shown in Figure 5-1.

Table 5-1: Processing parameters for gas ratio experiments

Step	Time (mins)	Gas Flow (sccm)		Bias (V)	Coil Current (A)	Cr Cathode (kW)	WC Cathode (kW)	μ wave source 6.2 (kW)
		Ar	C ₂ H ₂					
Pumping	20	-	-	-	-	-	-	-
Plasma source etch	15	50	-	- 200	-	-	-	-
Cr	15	110	-	- 25	4	5	-	-
μ wave DLC	33	Variable	-	- 100	3	-	-	0.8

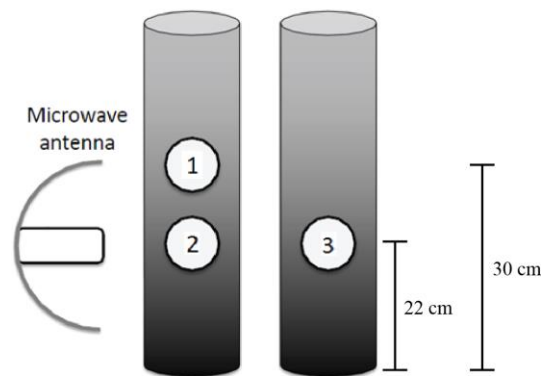


Figure 5-1: Position of the samples on the substrate holders in the deposition chamber for microwave gas ratio experiments.

The bias current trends for the gas ratio matrix are presented in Figure 5-2. This is useful in determining the stability of the process as it monitors the current across the isolated substrate table, which indicates when there is plasma present (due to the charged nature of the plasma). If the bias current drops to zero, it means that the process has halted and no coating deposition is taking place. The process ran smoothly until around 25 minutes for most of the processes as can be seen in Figure 5-2, where the bias current was very low. An exception to this is in the experiment

using 30% C₂H₂ where the bias current remains quite high relative to the other ratios. From the thickness of the DLC formed on the samples (shown in Table 4-2 it is clear that this steady bias current is due to a lower deposition rate of DLC coating on the substrate table. The lowest current is in the process which ran with 80% acetylene. It is obvious that the high deposition rate of DLC is detrimental to the long running duration of the process; this is due to the DLC coating building up and insulating the substrate table and therefore the bias voltage. This can be seen in the decline in bias current over time in Figure 5-2. When the bias current is 0, the plasma is unable to be sustained and thus is extinguished. The duration of the tests will be optimised in future experiments presented in this thesis.

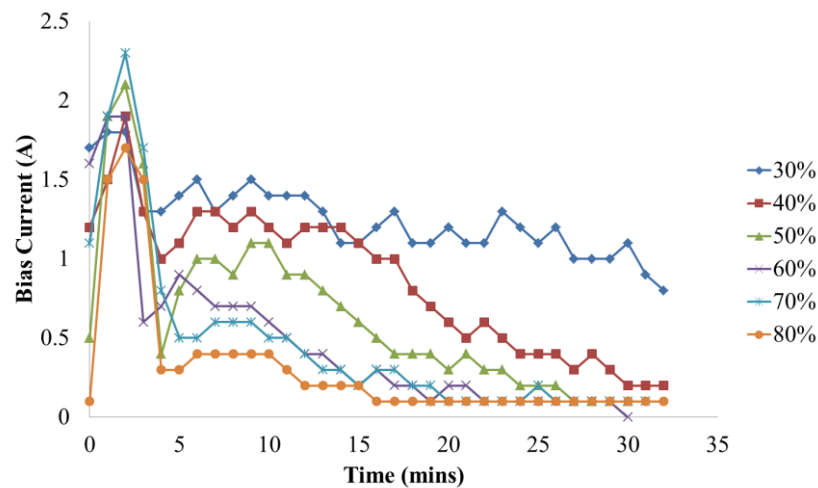


Figure 5-2: Trend showing the bias current for samples in the DLC deposition process in the gas ratio matrix tested at 100 V bias voltage for 33 minutes

As can be seen in Figure 5-3, the temperature of the processes did not exceed 100 °C, and all followed the same upward trend.

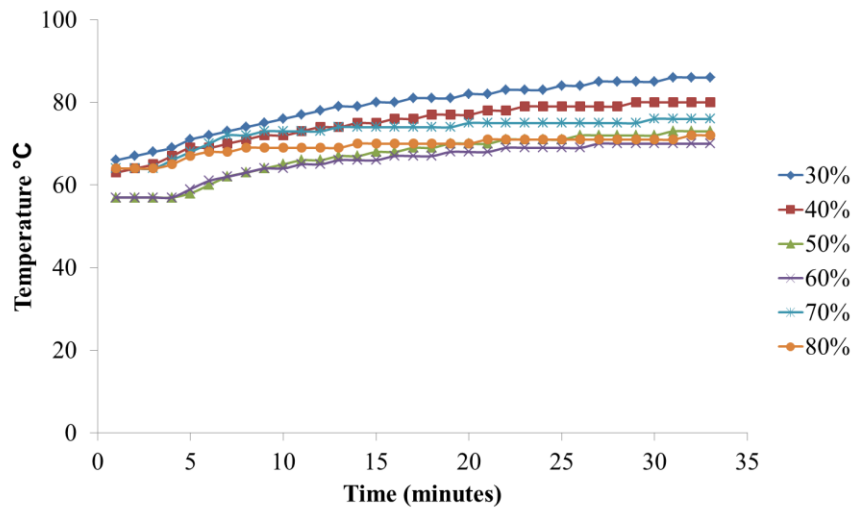


Figure 5-3: Temperature of the substrate table during the microwave deposition process of the gas ratio samples

5.2.2. Thickness

The thickness of the coatings was determined using a calo tester. The thicknesses of the coatings for this experimental matrix are presented in Figure 5-4, with images of these presented in Figure 5-5. The thickness of the samples placed directly in front of the microwave antenna (position two and three) was higher than those placed at the top of the reflector (position one), as expected. The samples placed in positions two and three also experienced more delamination and much more instability, possibly due to the higher thickness of the DLC.

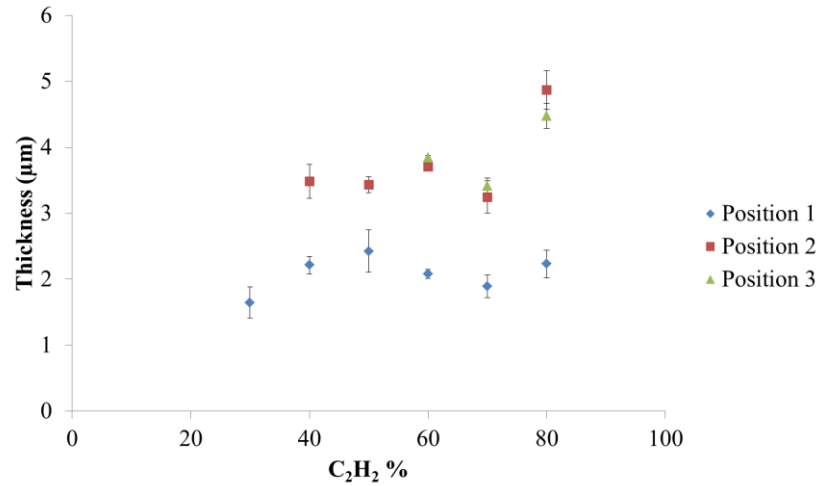


Figure 5-4: Thickness of gas ratio experiments – whole coating including interlayers

The samples placed in position one varied slightly in thickness but only by ± 0.5 μm , with the highest thickness recorded at 40% acetylene, and the lowest at 30%. These results differed from those in positions two and three, in these positions the thickness increased with the acetylene percentage which was expected, with the thickest DLC deposited at 80% acetylene at 4.8 μm , which is very thick for a coating of this nature. The samples displaying zero thickness had delaminated after being removed from the chamber. The thickness of the DLC generally increases as the acetylene flow is increased, however at values between 40 – 60% the thickness appears to remain stable.

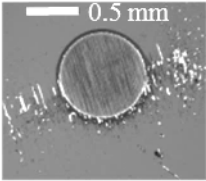
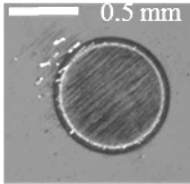
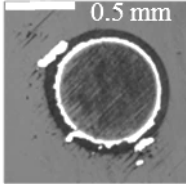
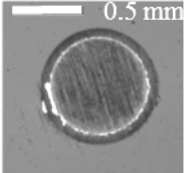
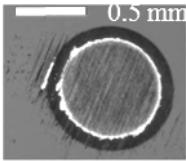
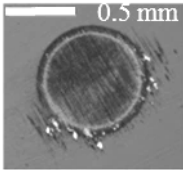
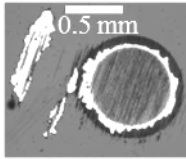
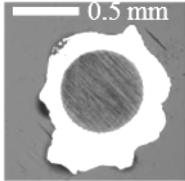
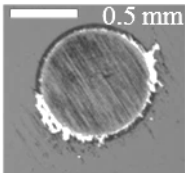
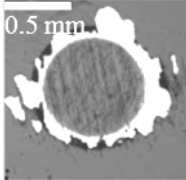
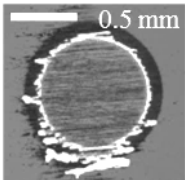
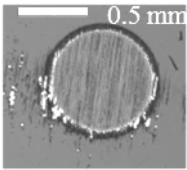
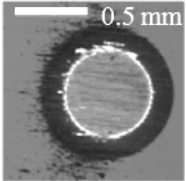
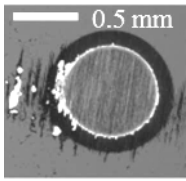
C ₂ H ₂ %	Position		
	1	2	3
30		x	x
40			x
50			x
60			
70			
80			

Figure 5-5: Images of the coatings made in the gas ratio series of experiments after calo testing to measure the thickness. (Where there is an x in place of an image, no coating was deposited onto the substrate and no calo test was done).

Figure 5-5 presents the microscope images of the samples after thickness tests were conducted. It was difficult to determine the thickness in some samples, such as 60% acetylene in position three, and 70% acetylene in position two due to the delamination of the coating about the abrasive wear scar. This shows that the coatings contain internal stresses and quite readily delaminate.

5.2.3. Hardness and Elastic Modulus

The hardness of the samples can be seen in Table 5-2. Only samples placed in position one were tested for hardness, this is due to the samples in positions two and three being thicker than was necessary and not useful for the application chosen for the coatings. The hardness of the samples is low, at a maximum of ~10 GPa at 60% C₂H₂. These are comparable to soft a-C:H samples seen in the table created from the literature in Table 2-2, which is below the range expected of these coatings (>15 GPa). Due to the preliminary nature of the coatings, the microwave power was 800 W; in the next series of experiments the power was increased to 1000 W to determine whether this has an effect on the coating properties.

Table 5-2: Hardness of samples tested in gas ratio experiments

C ₂ H ₂ %	Hardness (GPa)	±
40	8.03	1.36
60	10.42	0.33
70	8.22	0.83
80	8.62	1.47

5.2.4. Scratch Test Results

The critical loads achieved by the samples were comparable to other DLC coatings in the literature 15 – 25 N [192]. The sample created at 30% acetylene gas was not examined due to its delamination before the testing could begin. The sample produced using 80% acetylene has the highest critical load at 39.94 ± 3.42 GPa. The images taken from the scratch tests can be seen in Figure 5-7. It is seen that the 80% acetylene sample fares much better, this cannot be attributed to thickness alone (as the samples at 40% and 50% have similar thicknesses), nor hardness (as the values of hardness for 40% and 70% are similar).

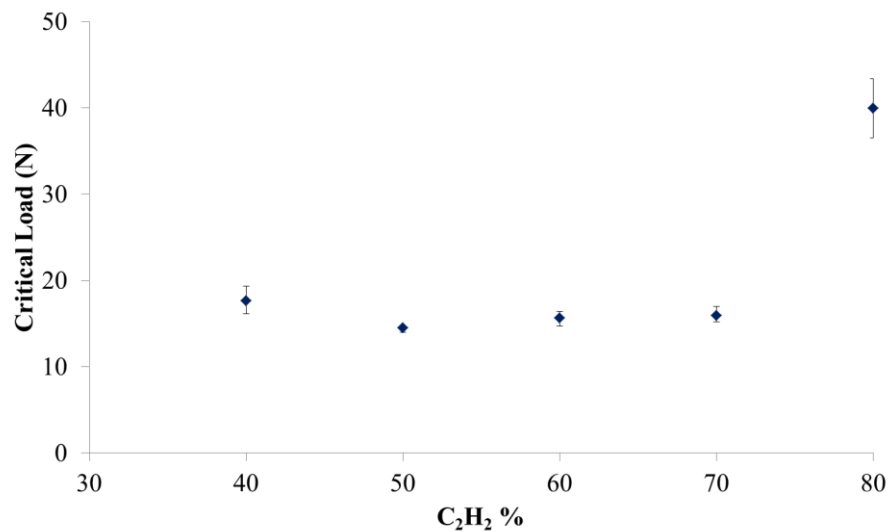


Figure 5-6: Critical load values from scratch testing of the DLC coatings produced in the gas ratio matrix

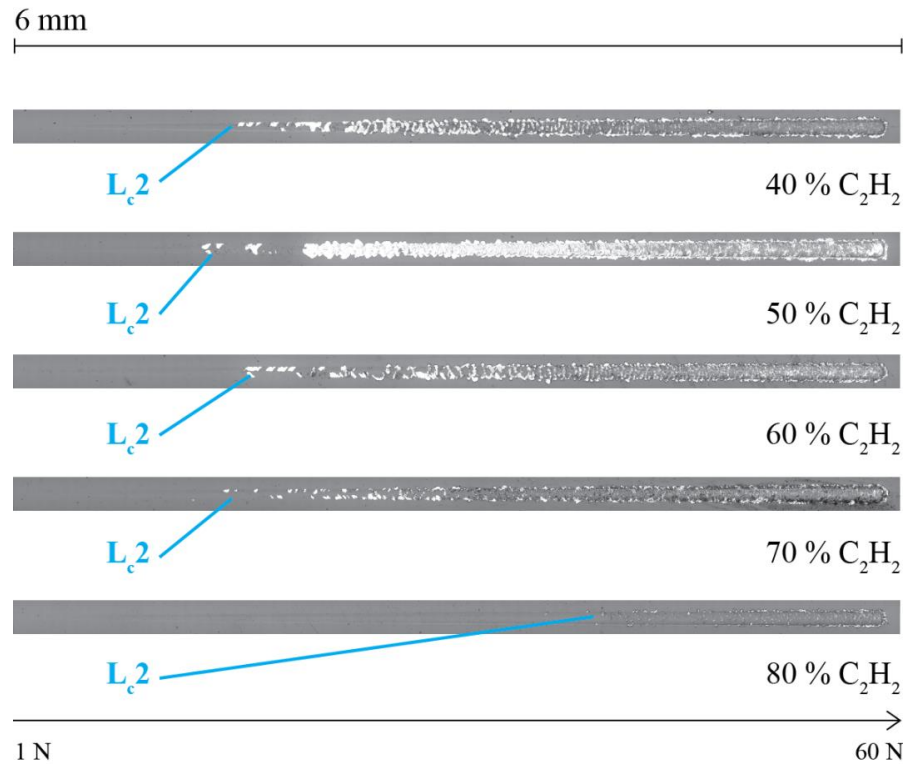


Figure 5-7: Scratch test imaged taken from critical load experiments using 0 – 60 N gradual loading on DLC coatings produced in the gas ratio matrix

5.2.5. Summary

The following key points can be made about the gas ratio experiments using microwave PECVD:

- Thickness is high for a short deposition process (~ 33 minutes rather than 150 minutes for PECVD). However the deposition time is deemed too long due to instability of the sources.
- Low hardness is attributed to low microwave power and bias voltages. These are to be refined later in this chapter.
- Critical load is below expected range (< 30 N) this is attributed to poor adhesion layer of only Cr deposited for 15 minutes.

5.3. Optimum Time Tests Using One Microwave Source

The correct amount of time needed for the optimum thickness for the final microwave DLC step had to be determined as 33 minutes was seen to be too long. These tests were performed using two different interlayers; one chromium and one chromium/tungsten carbide interlayer in order to compare the effect these had on the durability of the final coating after the delamination seen in the gas ratio tests. The tests were performed for durations of 10, 15, 20 and 30 minutes

5.3.1. Recipe

Table 5-3: Recipe for thickness versus time tests for DLC deposited with a Cr interlayer

Step	Time (mins)	Gas Flow (sccm)		Bias (V)	Coil Current (A)	Cr Cathode (kW)	WC Cathode (kW)	μ wave source 6.2 (kW)
		Ar	C ₂ H ₂					
Pumping	20	-	-	-	-	-	-	-
Plasma source etch	15	50	-	-200	-	-	-	-
Cr	15	110	-	-25	-	5	-	-
μ wave DLC	10, 15, 20, 30	~50%	~50%	- 100	3	-	-	1

Table 5-3 shows the recipe for the sample containing only the Cr interlayer, and Table 5-4 shows the recipe for the sample containing Cr + WC interlayer. These recipes were again based on a standard a-C:H and microwave DLC recipe, with the interlayer deposition duration shortened due to the preliminary nature of the experiments. The microwave DLC step was again based on a standard Hauzer

recipe, with the time as the variable to determine the thickness and stability of the sources. The stability of the sources was a very important factor when determining the success of the recipe; this can be affected by duration, power and bias voltage, gas ratio, pressure etc. The duration of the experiments is important as the build-up of insulating DLC on the substrate table (where the bias is present) will extinguish the plasma.

Table 5-4: Recipe for thickness versus time test for DLC deposited with a Cr + WC interlayer.

Step	Time (mins)	Gas Flow (sccm)		Bias (V)	Coil Current (A)	Cr Cathode (kW)	WC Cathode (kW)	μ wave source 6.2 (kW)
		Ar	C ₂ H ₂					
Pumping	20	-	-	-	-	-	-	-
Plasma source etch	15	50	-	-200	-	-	-	-
Cr	15	110	-	-25	4	5	-	-
Cr/WC	30	110	-	-	4	3 – 0.5	0.5 - 3	-
μ wave DLC	10, 15, 20, 30	~50%	~50%	-100	3	-	-	1

The bias current for each of the time tests with chromium and chromium and tungsten carbide interlayers are shown in Figure 5-8 and in Figure 5-9 respectively. The processes are generally quite stable, with the 30 minute processes (samples d and h) being the exception in both interlayer cases. This suggests that a duration of over 25 minutes is in excess of what the process is capable of, becoming unstable at this time.

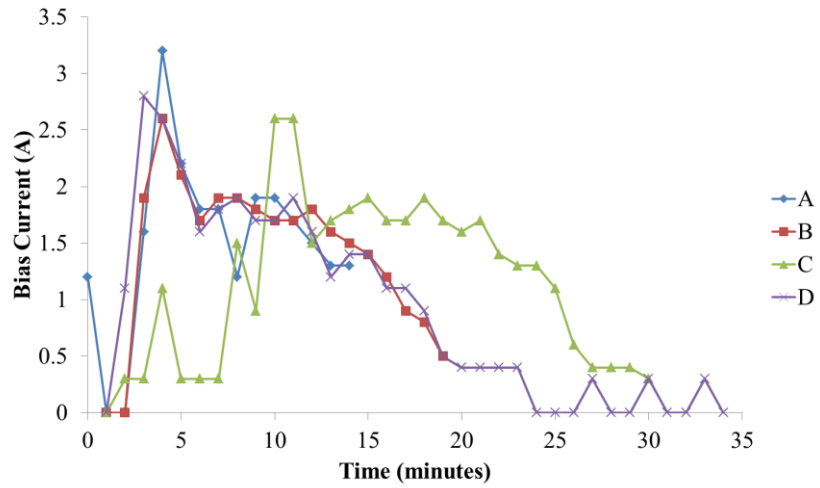


Figure 5-8: Bias current for optimum time tests with Cr interlayer

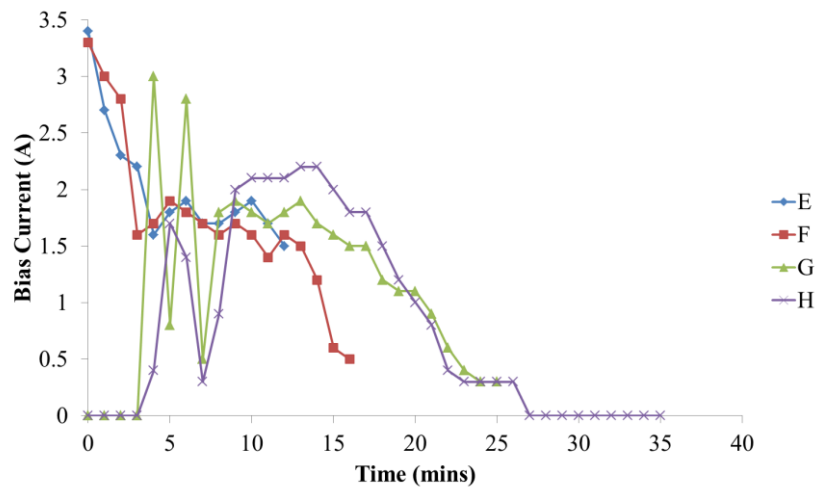


Figure 5-9: Bias current for optimum time tests with Cr + WC interlayer

Since the bias current is reliant on the stability of the process, it can be seen from the trends shown in Figure 5-7 and in Figure 5-8 that this can be somewhat unpredictable at times. Several steps were taken in order to ensure that the process was controlled. The plasma was monitored closely visually (as no remote detection system was in place) and the bias current was monitored closely also. If the process began to become unstable then the stub tuner positions were altered until stability

was achieved. Again, this was not an automated process and had to be undertaken by hand. Care was taken to ensure that if the process was interrupted by instability that this time was made up later in the process.

5.3.2. Thickness

The thickness of the entire coating from both sets of experiments can be seen in Table 5-5, the thickness varies as expected, i.e. increasing with time. One exception of this is the experiments performed with a 30 minute duration. This is due to the microwave sources becoming unstable at this length of time due to the coating build up around the chamber, which insulates the substrate table, resulting in the process only lasting for 22 minutes for the Cr + DLC sample and 23 minutes for the Cr + WC + DLC samples. The samples were not tested for hardness due to the preliminary nature of the experiments, the critical load was tested, however in order to determine the adhesion of the coating with different interlayers.

Table 5-5: Thickness of the DLC samples created with a Cr and Cr + W-DLC interlayers determined using a calo-tester.

Cr + DLC				Cr + WC + DLC			
Sample	Time	Thickness (μm)	DLC Thickness (μm)	Sample	Time	Thickness (μm)	DLC Thickness (μm)
A	10	1.25	0.74	E	10	1.54	0.8
B	15	1.28	0.77	F	15	1.76	1
C	20	1.68	1.17	G	20	2	1.3
D	30	1.48	0.97	H	30	2.15	1.4

5.3.3. Scratch Test Results

Scratch testing was carried out on the samples to determine the effect the different interlayers had on the adhesion of the coating. The results obtained from the scratch tests on these samples can be seen in Figure 5-10. The samples all performed well, and mostly above the critical load achieved by the standard a-C:H (31.4 N). It is clear that the samples with the Cr + WC interlayer performed better than those with just a Cr interlayer overall, but only marginally. The samples in the 30 minute process time were not tested; this was due to the process stopping short of this duration.

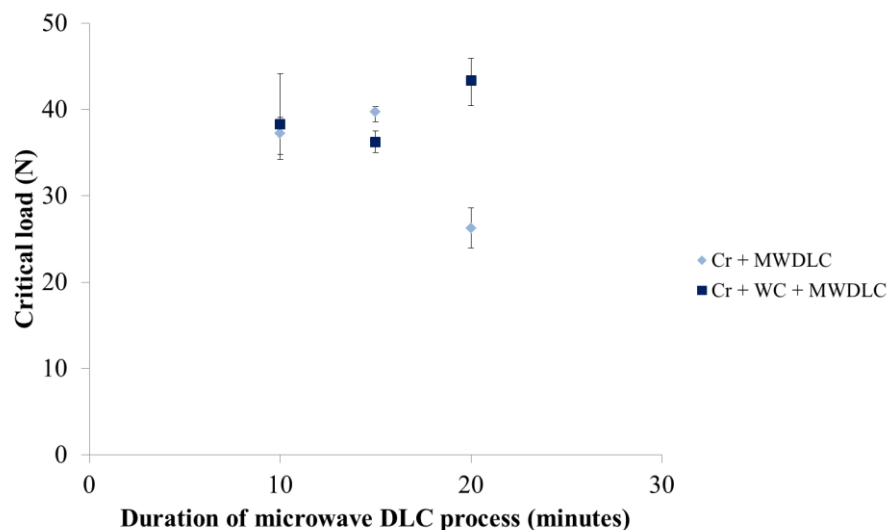


Figure 5-10: Scratch test results of the samples tested to determine correct duration in the microwave step

5.3.4. Summary

The following key points can be made about the optimum time tests using one source experiments:

- The process became unstable after ~ 20 minutes, rendering this the upper limit for processing duration in the microwave PECVD DLC stage. This is due to coating build up on the substrate table which also serves as a bias voltage. An insulating coating build up on this table will extinguish the microwave sources as there is no bias voltage to sustain it.
- The thickness of coatings produced after this time tended to remain similar to or less than those at 20 minutes. This indicates that re-sputtering has taken place or the process has ended prematurely due to the plasma being extinguished by the instability of the sources.
- The different interlayers did not have a significant impact on the scratch resistance of the coatings; the test conducted at 20 minutes with only a Cr interlayer is the same as in the gas ratio, which indicates further that this test duration is too long; a lower duration will be carried forward in the testing.
- A test time of 10 minutes + 3 minutes is proposed for future experiments. The three additional minutes will allow for stabilization of the microwave plasma, after two minutes the acetylene gas will be introduced gradually over a further two minutes, allowing for a solid 10 minute deposition time.

5.4. Tests to Determine the Optimal Position of Samples Using One Microwave Source

After the optimal time was established for the DLC stage of the process, the correct position for the samples on the substrate holder had to be determined; this is due to the non-uniform nature of the technique as shown in Figure 6-1. Samples were

placed along the length of the dummy and the calo-tester was used to determine the thickness at 1 cm intervals on the samples.

5.4.1. Recipe

For these tests, the recipe was a simple Cr + Cr/WC + Microwave DLC coating, as shown in Table 5-6. A WC layer was added due to the Cr only layer due to the Cr/WC interlayer DLC coating having a higher critical load at longer durations in the previous experiments. The interlayer duration was shorter than is commonly used in DLC processes, in order to shorten the process time for the preliminary experiments, and still achieve sufficient adhesion.

Table 5-6: Recipe for the tests to determine optimum position of samples in the deposition chamber using one microwave source

Step	Time (mins)	Gas Flow (sccm)		Bias (V)	Coil Current (A)	Cr Cathode (kW)	WC Cathode (kW)	μ wave source 6.2 (kW)
		Ar	C ₂ H ₂					
Pumping	20	-	-	-	-	-	-	-
Plasma source etch	15	50	-	- 200	-	-	-	-
Cr	10	110	-	- 25	4	5	-	-
Cr/WC	30	110	-	0	4	3 – 0.5	0.5 – 3	-
μ wave DLC	13	50%	50%	- 100	3	-	-	1

The recipe was based on a standard PECVD a-C:H and Microwave DLC recipe. The DLC step was 13 minutes in duration; this includes a two minute delay time on the C₂H₂ and a two minute ramping time up to 50% C₂H₂. The ramping time is added so

as to introduce the hydrocarbon gas to the chamber slowly after initial microwave ignition in an argon atmosphere. The argon atmosphere serves to rid the chamber of impurities that may then be incorporated into the coating. The parameters are monitored on the deposition system and are a useful tool to determine the stability of each process and to improve future experiments. The trend shown in Figure 5-11 shows the microwave DLC process began at zero minutes and ended at fourteen minutes, with a two minute delay time before the C₂H₂ was introduced into the system and with a two minute ramp time up to full C₂H₂ flow. It can be seen that the process was very stable, with only a small amount of reflected microwave power (at two minutes, 80 W) but this was dispelled quickly using the impedance stubs. The microwave power was very stable throughout the duration of the experiment.

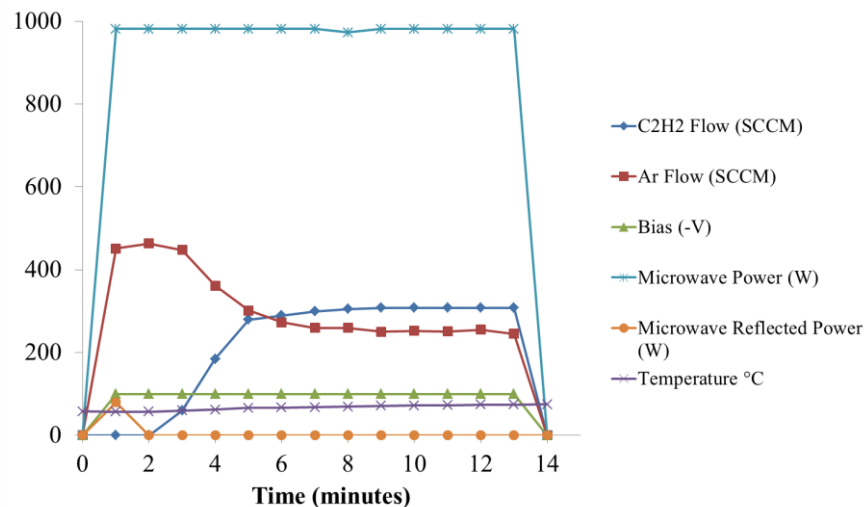


Figure 5-11: Trend of the C₂H₂ flow, Ar flow, bias voltage, microwave power and reflected power of the tests to determine the optimum position of the substrates using one microwave source.

The bias current in Figure 5-12 shows the values for the final microwave stage of the process. It is important to monitor the bias current throughout the process in order to determine whether a plasma is present in the system alongside physically

seeing the plasma and therefore if coating deposition is taking place. As the process continues, the bias current can be seen to decrease; this is due to the loss in conductivity the substrate table experiences due to a build-up of insulating DLC coating on the surface. The bias current for this process is seen to remain stable.

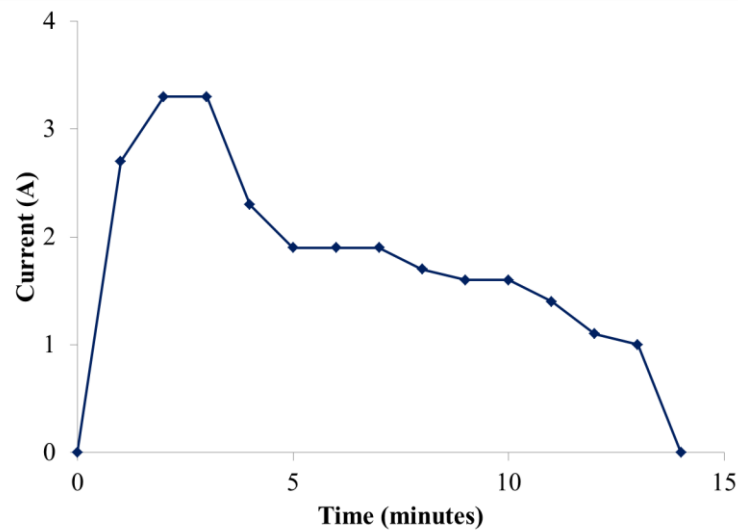


Figure 5-12: Bias current trend of the tests conducted to determine the optimum position of the substrates using one microwave source

5.4.2. Thickness

Table 5-7 shows microwave images and thickness of the position tests using one microwave source after thickness testing on the calo tester. It is seen that the quality of the coating deteriorates close to the extremities of the microwave source. No pictures are included for the upper and lower bounds; this is due to no coating being present upon removal from the substrate chamber. This is potentially due to high stresses present internally in the DLC, resulting in the instant delamination of the coating.

Table 5-7: Positional thickness test results including microscope images, one microwave source – entire coating thickness

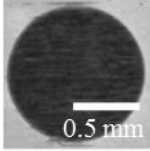
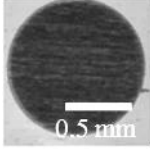
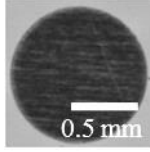
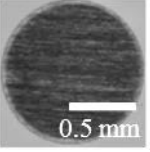
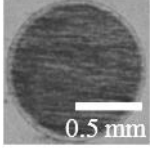
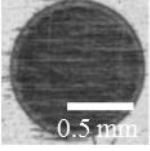
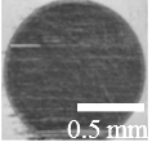
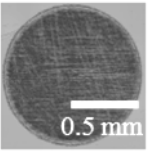
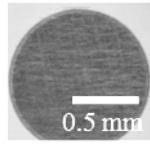
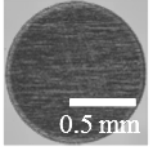
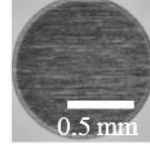
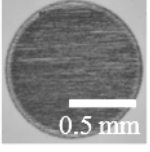
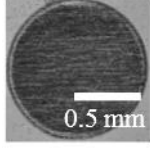
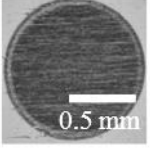
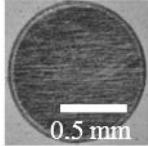
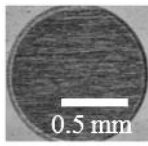
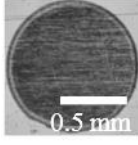
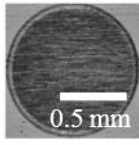
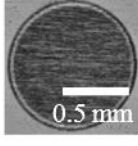
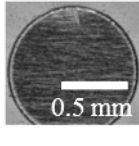
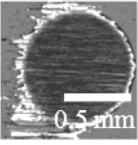
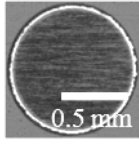
cm from bottom of dummy	Thickness (μm)	Microscope image	cm from bottom of dummy	Thickness (μm)	Microscope image
36	0.62		35	0.6	
34	0.6		33	0.61	
32	0.63		31	0.66	
30	0.62		29	0.68	
28	0.76		27	0.81	
26	0.87		25	0.80	
24	1.01		23	1.02	

Table 5-7 continued.

cm from bottom of dummy	Thickness (μm)	Microscope image	cm from bottom of dummy	Thickness (μm)	Microscope image
22	1.24		21	1.21	
20	1.30		19	1.27	
18	1.18		17	1.25	
16	1.04		15	1.03	

No hardness or scratch testing was carried out on these samples due to the preliminary nature of the experiments, and the main focus being of the position in which to place the samples for optimum thickness ($\sim 1 \mu\text{m}$). As can be seen from the thickness measurements in Table 5-7, the thickness of the coating fluctuated depending on the position relative to the microwave antenna. Figure 5-13 shows the thickness of the DLC deposited excluding the interlayers. It can be seen that in front of the microwave source produces the thickest DLC layer which was expected and also noticed in the gas ratio experiments. The position chosen in which to place the samples for future testing using one source was at 20 cm from the bottom of the

dummy, to achieve optimal thickness. The centre of the (circular) samples will be placed at this value.

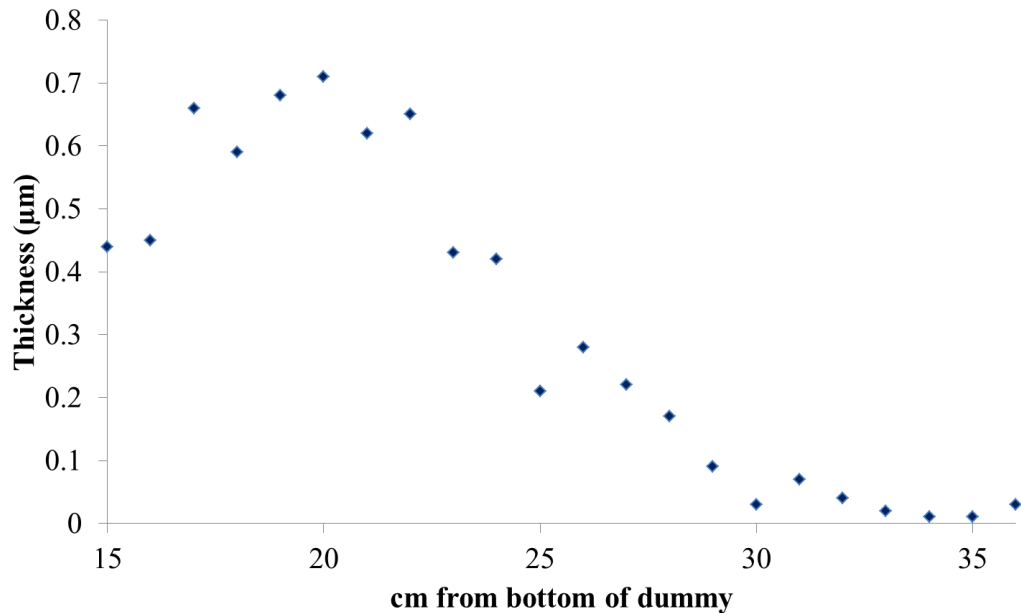


Figure 5-13: Thickness of the DLC layer produced when determining the optimal position for the substrates when using one microwave source

5.4.3. Summary

The following key points can be made about the positional testing conducted using one microwave source:

- This series of testing has shown that the 10 minute deposition time + 3 minute ignition time is sufficient time to achieve a coating of desirable thickness and that the buildup of the coating on the substrate table is not enough to inhibit the stability of the sources.
- In future, the samples will be positioned 20 cm, from their centre to the bottom of the dummy. At this position the highest thickness was observed at 1.3 µm.

5.5. Microwave PECVD Two Variable Matrix Using One

Microwave Source

After the preliminary experiments were completed, a matrix was designed to enable the combined effect of the gas ratio and the bias voltage on the end performance of the coatings to be determined. An empirical equation would be formulated to enable users of the deposition system at the University of Leeds to accurately predict the mechanical properties of the coating using the parameter values before deposition takes place. The series of experiments to determine the effect that the gas ratio had on the coating hardness showed only a minor difference from 40% to 80% acetylene, whereas the bias voltage was seen to have a large effect in both the experiments carried out later in this thesis and within the literature [193]. It is hypothesised here that the bias voltage and the gas ratio will have a combined effect to create a peak hardness.

5.5.1. Test Matrix

The test matrix was designed as a full-factorial matrix as shown in Table 5-8 which combined a high, medium and low value for each of the gas ratio and bias voltage. The high, medium and low values were chosen as 80%, 55%, 30% for C₂H₂ percentage, and -300 V, -200 V and -100 V for the bias voltage, respectively. The value for the actual percentage of C₂H₂ in the system is given in the table, since the amount of C₂H₂ in the system had to be calculated and entered in manually. This deviated slightly from the desired amount in some cases.

Table 5-8: Test matrix

Test number	C ₂ H ₂ %	Actual % C ₂ H ₂	Bias Voltage
1	30	30	-100
2	55	55	-100
3	80	78	-100
4	30	30	-200
5	55	55	-200
6	80	79	-200
7	30	30	-300
8	55	54	-300
9	80	80	-300

5.5.2. Recipe

The recipe for testing within this matrix is presented in Table 5-9. Within this matrix only one source was used. The interlayer used was based on those used in the a-C:H samples as outlined in Table 4-1, however it was condensed in order to shorten the experimental time frame. A solid interlayer was still used, incorporating chromium as the first adhesion layer and then tungsten carbide as the secondary layer as was confirmed to be sufficient in previous experiments. The final microwave DLC layer had a 13 minute duration as was found to be the optimum time as found in section 5.3. The first two minutes were to allow the microwave source to ignite in a pure argon atmosphere, after which the acetylene gas was inlet at a gradual rate over two minutes. This allows for a reliable 10 minute deposition period.

Table 5-9: Recipe for microwave two variable matrix using one source

Step	Time (min)	Gas Flow (SCCM)		Bias (V)	Coil Current (A)	Cr Cathode (kW)	WC Cathode (kW)	μ wave 6.1 (kW)	μ wave 6.2 (kW)
		Ar	C ₂ H ₂						
Heating 200°C	60	Heating the chamber to 200C is necessary to optimise the performance of the plasma source.							
Plasma Etch	10	50	-	-200	4	-	-	-	-
Cr	15	110	-	-	4	5	-	-	-
Cr/WC	30	110	-	-	4	3 – 0.5	0.5 – 3	-	-
Pumping Standby	This step is necessary to reduce the pump speed before the microwave step.								
μ wave DLC	13		30%	-100					1000
			55%	-200					
			80%	-300					

The stability of the processes involved in this matrix is shown using the bias current in Figure 5-14. This shows that some of the processes were less stable than desired. Where the bias current is 0, no plasma is present in the system, this time lost was added on to the end of the process once it had been stabilised.

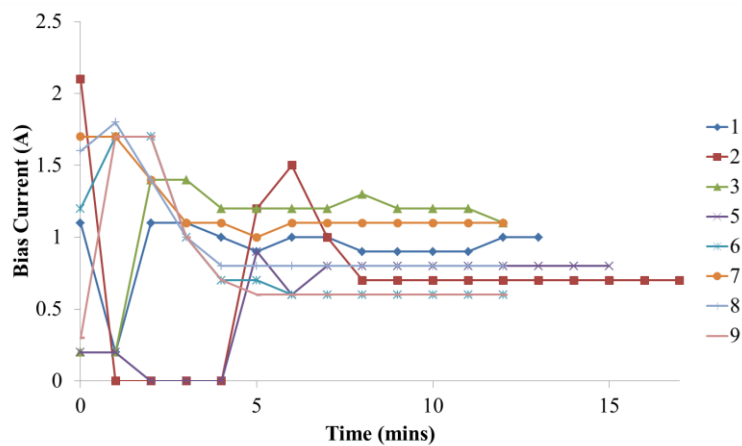


Figure 5-14: Bias currents of the tests conducted in the two variable matrix

As can be seen in Figure 5-14, the bias current for test number two and five is zero for the first few minutes, this is because the microwave sources did not ignite initially, the duration was corrected for this and the time lost was added onto the end of the process. The temperatures experienced during these processes are shown in Figure 5-15.

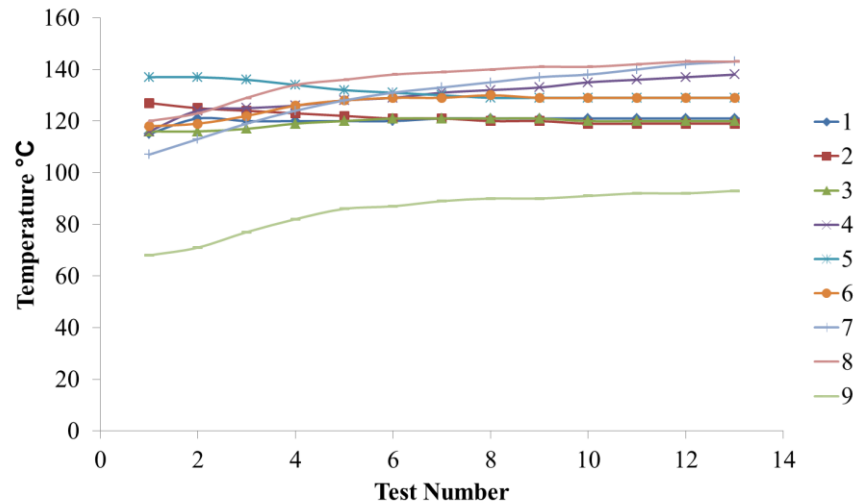


Figure 5-15: Temperature of the microwave deposition process for tests conducted in the two variable matrix

5.5.3. Thickness

The thickness of each DLC sample was calculated using the calo tester as previously described. These results are presented in a contour graph shown in Figure 5-16. The thickness is highest at 55% C_2H_2 and -100 V bias, with the thickness decreasing with increasing C_2H_2 ratio and with both extremities of bias voltage.

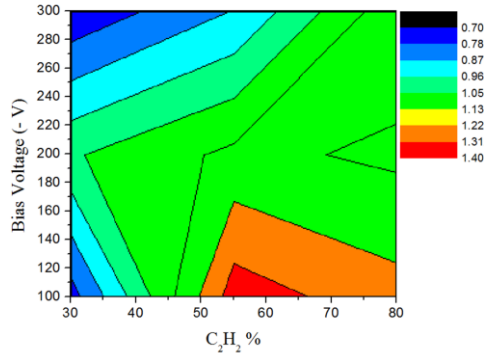


Figure 5-16: Thickness contour graph of two variable test matrix (entire coating)

5.5.4. Hardness and Elastic Modulus

The procedure for determining the hardness and elastic modulus was the same as has been previously described and is further detailed in 3.5. The hardness and elastic modulus were measured for each of the samples in this matrix. The results are tabulated in Table 5-10 and shown in graphs in Figure 5-17 for hardness and in Figure 5-18 for elastic modulus.

Table 5-10: Microwave two variable matrix using one source, hardness and elastic modulus

Test	C ₂ H ₂ %	Bias Voltage	Hardness (GPa)	Elastic Modulus (GPa)
1	30	-100	16 ± 1.4	141.4 ± 9.9
2	55	-100	10 ± 0.5	98.2 ± 12
3	80	-100	8.2 ± 1	78.6 ± 4.1
4	30	-200	18.2 ± 1.4	168.2 ± 12.8
5	55	-200	16.5 ± 1.5	135.8 ± 15.1
6	80	-200	7.8 ± 1.2	87.9 ± 5.9
7	30	-300	22.7 ± 1.8	185.5 ± 14.3
8	55	-300	14.6 ± 1	142.9 ± 15.2
9	80	-300	10.1 ± 0.8	101.7 ± 11.1

The hardness and elastic modulus of the samples are higher when combined than when tested individually. This shows that the variables have a synergistic effect on the coating properties. The highest hardness was seen at 30% C_2H_2 and at a -300 V bias; this was ~ 22.7 GPa which is desirable for this type of coating.

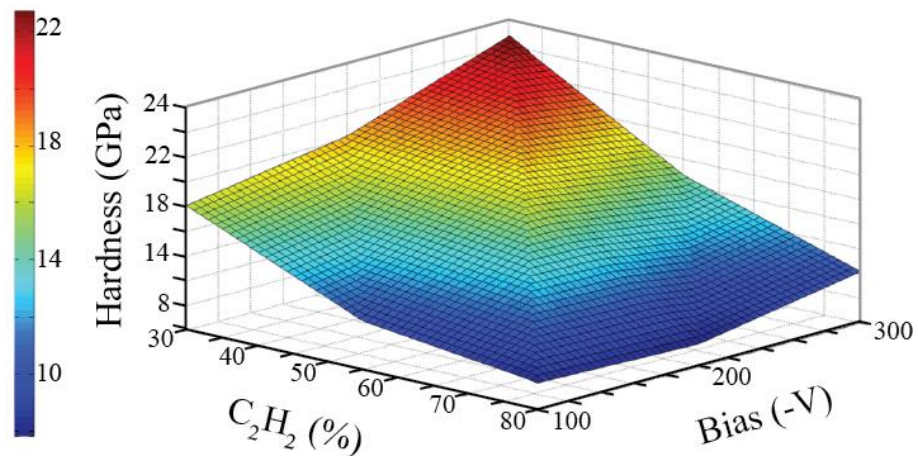


Figure 5-17: Hardness of the microwave DLC coatings as a function of gas ratio and bias voltage

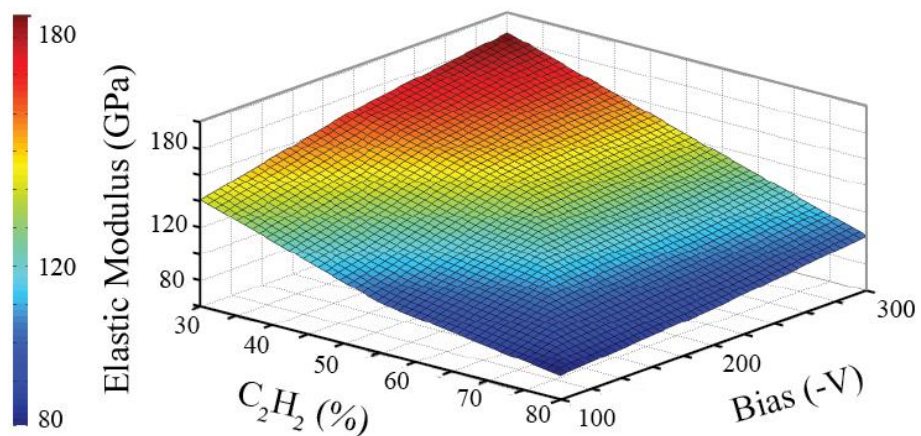


Figure 5-18: Elastic Modulus of the microwave DLC coatings as a function of gas ratio and bias voltage

5.5.5. Semi-Empirical Equations Relating Bias Voltage and Gas Ratio to Hardness and Elastic Modulus

A least squares regression was performed in order to determine the coefficients in the equation 5-1 and 5-2 which are third order based polynomials (2^3). This gives a semi-empirical equation which will allow further users to determine the hardness of the coating by inputting bias voltage and gas ratio values before the testing has begun. The resulting equation for hardness is presented in equation 5-1, and for elastic modulus in equation 5-2. The graphs showing the fit for hardness and elastic modulus are presented in Figure 5-19 and Figure 5-20 respectively.

$$h = A_1b + A_2g^2 + A_3b^2 + A_4bg + A_5g^3 + A_6b^3 + A_7g^2b + A_8b^2g \quad 5-1$$

Table 5-11: Constant values for equation 5-1

Constant	Value (Unit)	Constant	Value (Unit)
A_1	$2.931 \times 10^{-1} (GPa/V)$	A_5	$2.275 \times 10^{-5} (GPa)$
A_2	$-2.935 \times 10^{-3} (GPa)$	A_6	$2.043 \times 10^{-6} (GPa/V^3)$
A_3	$-1.296 \times 10^{-3} (GPa/V^2)$	A_7	$-2.960 \times 10^{-6} (GPa/V)$
A_4	$-2.504 \times 10^{-4} (GPa/V)$	A_8	$2.600 \times 10^{-7} (GPa/V^2)$

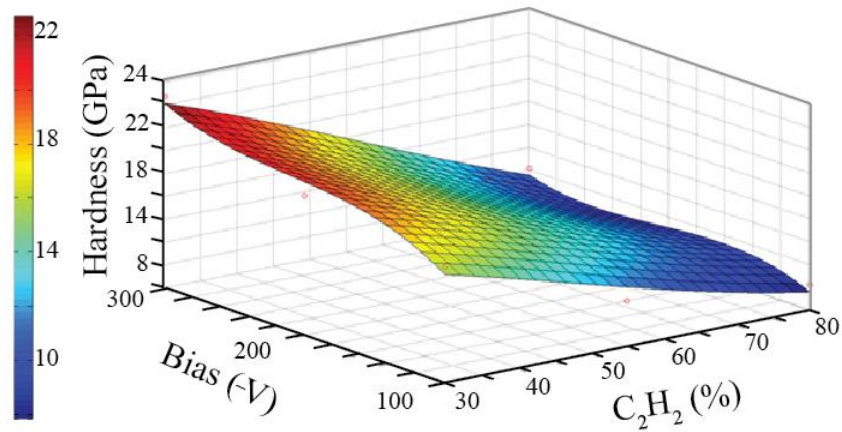


Figure 5-19: Least squares regression fit to hardness data for Matrix

Below is an equation to determine elastic modulus from bias voltage and gas ratio values which is derived from the experimental data:

$$E = B_1b + B_2g^2 + B_3b^2 + B_4bg + B_5g^3 + B_6b^3 + B_7g^2b + B_8b^2g \quad 5-2$$

Table 5-12: Constant values for equation 5-2

Constant	Value (Unit)	Constant	Value (Unit)
B_1	2.674 (GPa/V)	B_5	3.375×10^{-4} (GPa)
B_2	-3.542×10^{-2} (GPa)	B_6	1.869×10^{-5} (GPa/V ³)
B_3	-1.258×10^2 (GPa/V ²)	B_7	-8.857×10^{-5} (GPa/V)
B_4	-2.011×10^3 (GPa/V)	B_8	1.407×10^{-5} (GPa/V ²)

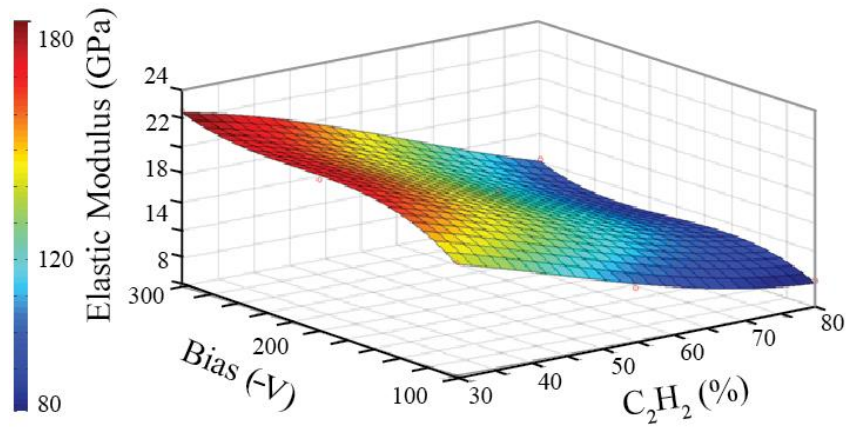


Figure 5-20: Least squares regression fit to elastic modulus data for the two variable matrix series of experiments

For each of the equations given by the empirical results, the accuracy is given in Table 5-13. It can be seen that there is little error, and the equations can be relied upon to give a fairly accurate estimate of coating hardness with respect to deposition parameters of C₂H₂ ratio and bias voltage.

5.5.5.1. Accuracy

Table 5-13: Accuracy values for the hardness and elastic modulus fit determined from least squares regression data fit to empirical data.

C ₂ H ₂ %	Bias voltage	Hardness Error (GPa)	Elastic Modulus Error (GPa)
30	-100	-0.038	-0.011
55	-100	0.123	0.031
80	-100	-0.075	-0.02
30	-200	0.067	0.018
55	-200	-0.148	-0.045
80	-200	0.156	0.035
30	-300	-0.027	-0.008
55	-300	0.084	0.022
80	-300	-0.06	-0.015

5.5.6. Summary

The following key points can be made about the microwave matrix experiments using one source:

- A thicker interlayer was used after the results produced in the time testing suggesting that this would result in slightly better adhesion. These samples performed well in scratch testing.
- The hardness varied depending on the parameters, the lowest hardness was found in the samples which were subject to low bias voltage and high gas acetylene percentages.
- The highest hardness was found in samples experiencing low to medium acetylene concentrations and at medium to high bias voltages.

- An equation was generated using these results which will enable users on the machine to decide parameters based on desired properties of the coating. The error margins on this equation are acceptable.

Chapter 6

Results: Microwave Plasma Enhanced Chemical Vapour Deposition Using Two Microwave Sources

6.1. Introduction

After the series of experiments using just one microwave source, the testing began with two sources. The microwave sources are vertically spaced equally within the chamber wall. It is hypothesised that using two sources the deposition rate will increase. Alongside this, due to the increased energy the extra source will bring to the system, other properties such as hardness and elastic modulus may increase. The primary goal of this series of experiments is to determine the highest value of hardness that may be achieved using this method of deposition.

6.2. Tests to Determine the Optimal Position of Samples Using Two Microwave Sources

As in section 5.4, the ideal position for the sample substrates had to be determined before any testing could commence, due to the non-uniform deposition nature of the microwave PECVD process and using two sources instead of just one will change the energy distribution across the chamber, shown in Figure 6-1. Samples were positioned along the length of the dummy and thickness values were taken for a 13 minute deposition period. As previously, the microwave sources ignited in a pure

argon atmosphere for two minutes, to allow stabilisation of the process. Following this, C₂H₂ is introduced gradually over a further two minutes until the value of 50% is achieved.

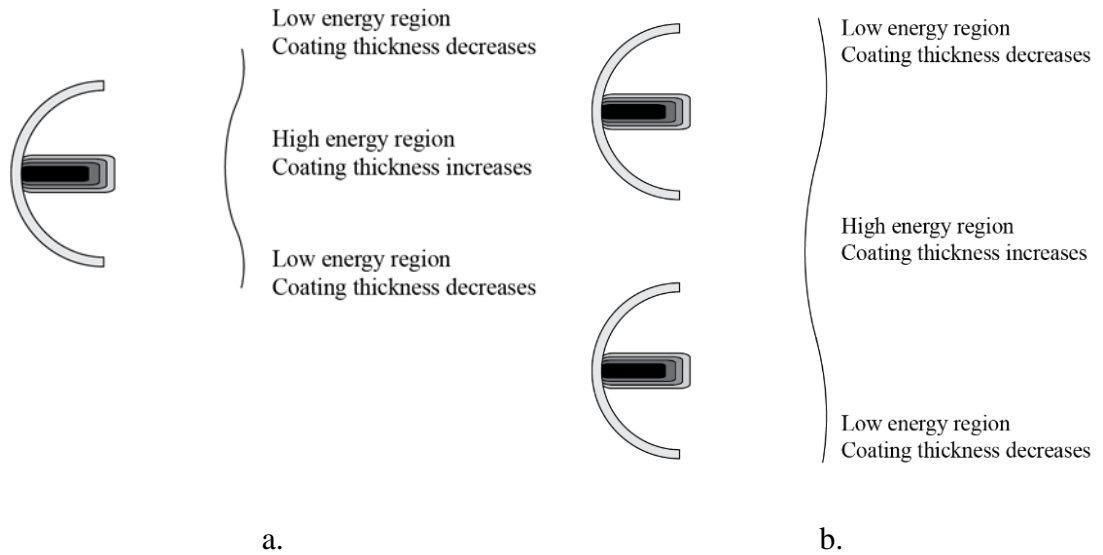


Figure 6-1: Energy distribution of a. one and b. two microwave sources

6.2.1. Test Recipe for the Optimal Sample Position Test Using Two Microwave Sources

The recipe used for the two microwave source position test is shown in Table 6-1. This was the same recipe used for the position testing using one microwave source shown in Table 5-7, but with an added microwave source.

Figure 6-2 shows the trend generated by the system for the position tests using two microwave sources. The trend shows that a stable process was achieved as can be seen in Figure 6-3. There appears to be more reflected power using two microwave sources relative to when only one source is used, this is dispelled by manually adjusting the impedance stubs incorporated into the microwave sources as described earlier. The reflected power did not affect the overall power.

Table 6-1: Recipe for position test using two microwave sources

Step	Time (mins)	Gas Flow (sccm)		Bias (V)	Coil Current (A)	Cr Cathode (kW)	WC Cathode (kW)	μwave 6.1 (kW)	μwave 6.2 (kW)
		Ar	C ₂ H ₂						
Pumping	20	-	-	-	-	-	-	-	-
Plasma source etch	20	50	-	- 200	-	-	-	-	-
Cr	15	110	-	- 25	4	5 kW	-	-	-
Cr + WC	30	110	-	-	4	3 – 0.5	0.5 – 3	-	-
μwave DLC	13	50%	50%	- 100	3	-	-	1	1

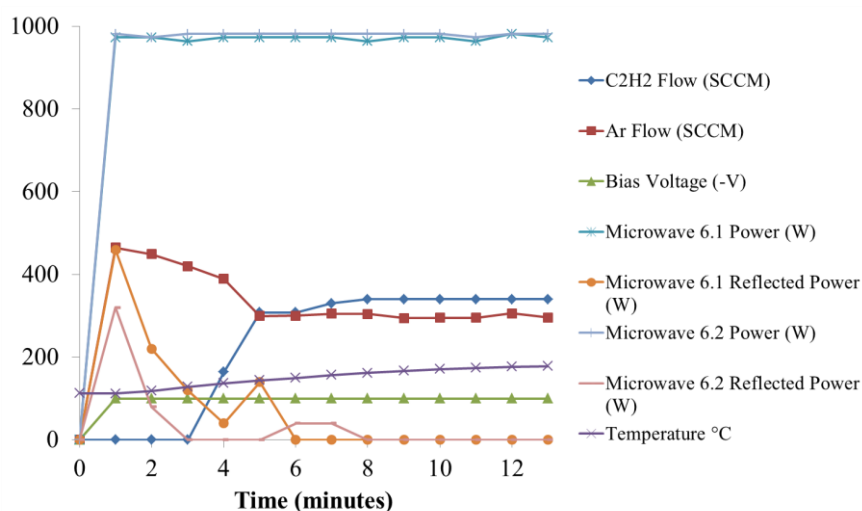


Figure 6-2: Trend of the deposition parameters: C₂H₂ flow, Ar flow, bias voltage, microwave power and reflected power for the position test using two microwave sources experiments

The trend generated for the bias current as a function of time is shown in Figure 6-3.

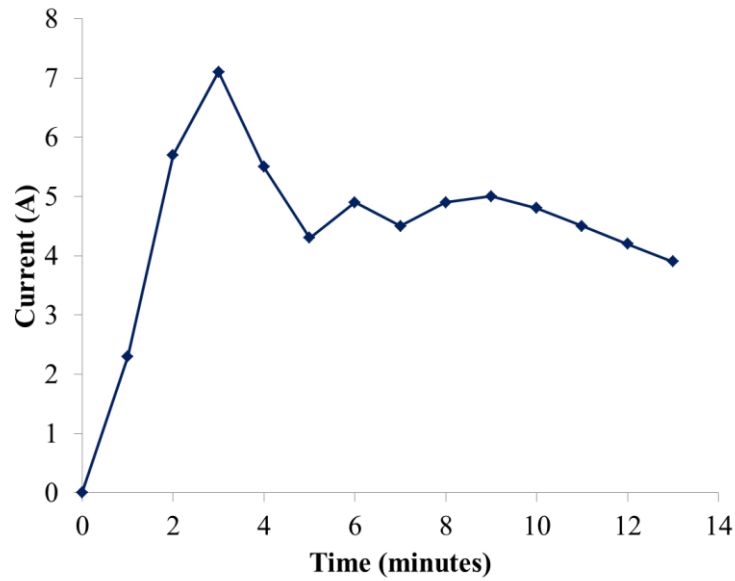


Figure 6-3: Position test using two sources bias current versus time

The bias current for two microwave sources follows the same trend as for one microwave source (which can be seen in Figure 5-12), but with a much larger current. This is due to both sources providing a higher power to the chamber (2 kW combined, as opposed to 1 kW from only one source).

6.2.2. Thickness of the samples prepared in the position test using two microwave sources

Thickness results for the two source position test are presented in Table 6-2. The duration of the test was 13 minutes, the same as the position testing using one microwave source, this was due to longer periods of time resulting in the microwave sources extinguishing due to a build-up of insulating DLC on the substrate bias table. It can be seen that the thickness is similar, with higher thickness in those seen in Table 5-7.

Table 6-2: Position test using two microwave sources – entire coating

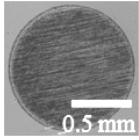
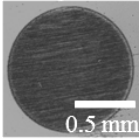
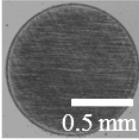
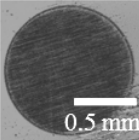
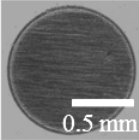
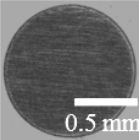
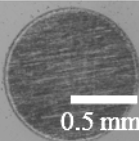
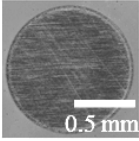
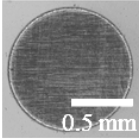
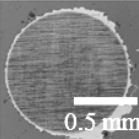
Cm from bottom of dummy	Thickness (μm)	Microscope image	Cm from bottom of dummy	Thickness (μm)	Microscope image
37.3	0.81		35.8	0.93	
32.4	0.86		30.7	0.85	
27.3	0.90		25.8	0.91	
22.3	0.94		20.8	0.91	
17.3	0.91		15.8	1.11	

Table 6-3: Position test using two microwave sources – DLC coating only

Cm from bottom of dummy	Thickness (μm)	Cm from bottom of dummy	Thickness (μm)
37.3	0.11	25.8	0.21
35.8	0.23	22.3	0.24
32.4	0.16	20.8	0.21
30.7	0.15	17.3	0.21
27.3	0.2	15.8	0.41

The results show a more even distribution across the centre of the dummy than in the testing with only one source. However, the samples at the far extremities of the dummy were of non-measurable thickness due to delamination of the coating after taking the samples out of the chamber.

6.2.3. Summary

The following key points can be made about the position testing using two sources:

- The position chosen to place the samples in for the two source testing was in the centre (30 cm from bottom and top of dummy) of the dummy, and of the two sources.

6.3. Microwave Power Experiments 1000 W versus 1200 W

After the position testing, the ideal power value also had to be determined for the two sources in order to also eliminate this variable from the ongoing testing, since it was now realised that the microwave sources operate in a stable manner at 1 kW. The microwave sources operate optimally in a power range from 800 – 1200 W. Since all preliminary tests prior to this had been conducted in 1000 W or 800 W power, a test was carried out in order to see the effect the power value had on the end coating and which was best to take forward. The processing parameters can be seen in Table 6-4.

An important part of this particular experiment was to determine the stability of the sources at these higher values of microwave power Figure 6-5 and Figure 6-7 show the trends and bias current respectively, in the processes carried out with 1000 W and 1200 W microwave power, these show how stable the processes were. The

processes ran smoothly with only a small amount of reflected microwave power occurring. The bias current behaves as expected, being quite stable at around 2 A.

Table 6-4: Processing parameters of 1000 and 1200 W power variables

Step	Time (mins)	Gas Flow (sccm)		Bias (V)	Coil Current (A)	Cr Cathode (kW)	WC Cathode (kW)	μ wave 6.1 (kW)	μ wave 6.2 (kW)
		Ar	C ₂ H ₂						
Pumping	20	-	-	-	-	-	-	-	-
Plasma source etch	20	50	-	200	-	-	-	-	-
Cr	25	13 0	-	-	4	3	-	-	-
Cr + WC	30	11 0	-	-	4	3 – 0.5	0.5 – 3	-	-
W-C:H	75	90	8 - 30	-	2	-	3	-	-
μ wave DLC	15	45 %	55%	200	3	-	-	1 & 1.2	

6.3.1. Microwave Power experiments conducted at 1000 W

The processing trend for the tests conducted using two microwave sources at 100 W is shown in Figure 6-4 and the bias current is shown in Figure 6-5. These trends show that the microwave power was stable, the reflected power was minimal and the bias current trend shows that a good process was achieved as this was consistent throughout the process.

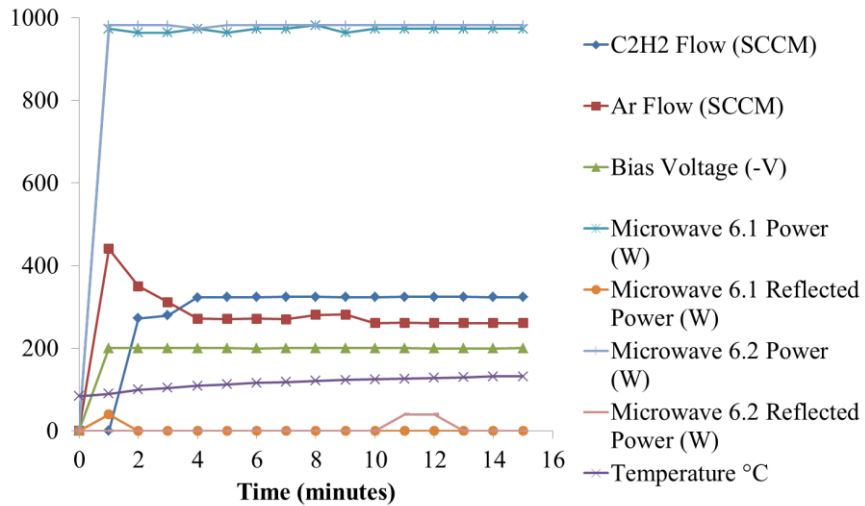


Figure 6-4: Microwave power 1000 W power trend

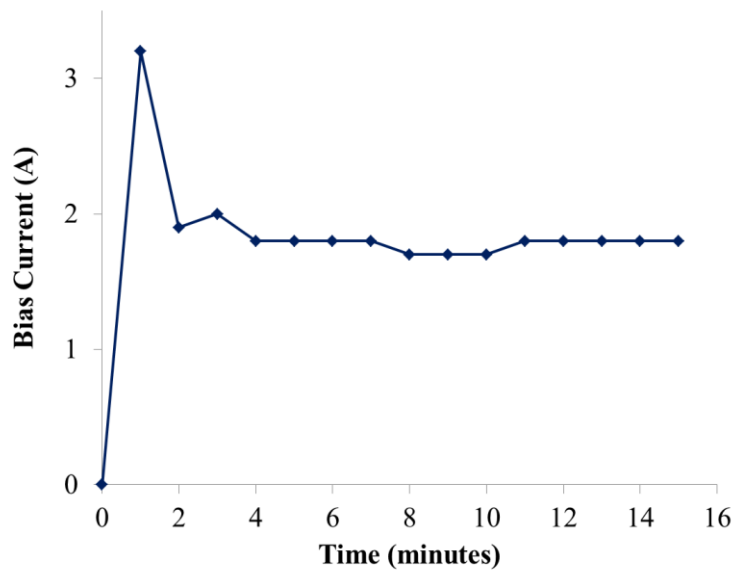


Figure 6-5: Microwave power 1000 W power bias current

6.3.2. Microwave Power experiments conducted at 1200 W

The overall trend and bias current for the testing conducted at 1200 W are found in Figure 6-6 and Figure 6-7, respectively. The process ran smoothly with only minimal reflected microwave power, and the bias current was also smooth, giving a higher value than that for 1000 W microwave power.

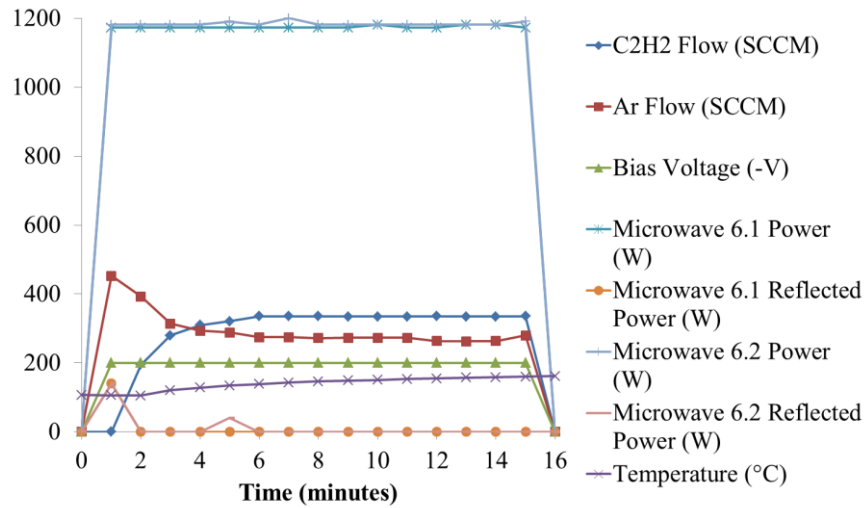


Figure 6-6: Microwave power 1200 W power trend

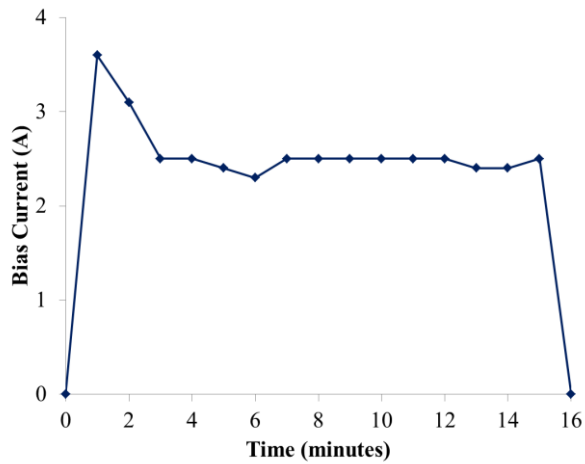


Figure 6-7: Microwave power 1200 W power bias current trend

6.3.3. Thickness

The thickness of the samples tested with 1000 and 1200 W power is shown in Table 6-5. The samples tested with 1200 W power are $\sim 0.2 \mu\text{m}$ thicker than the ones tested using 1000 W power.

Table 6-5: Thickness of samples tested with 1000 and 1200 W microwave power

Power (W)	Thickness (μm)	DLC Thickness (μm)
1000	2.11	0.61
1200	2.32	0.82

6.3.4. Summary

The following key points can be made about the microwave power experiments:

- A significant increase in thickness was seen from 1000 W to 1200 W, thus reducing the amount of time that these sources would need to be operational for which is of benefit due to stability of the sources being an issue. Thus it was decided to continue the processing at the higher power.

6.4. Bias Scan

It is well known from the literature that in standard PECVD processes the bias voltage plays a large role in the properties of the coating. It is also known that this is similar for microwave PECVD coatings. It was suggested by the manufacturer (Karlsruhe Institute of Technology) of the microwave sources that over 20 GPa hardness DLC coatings could be produced. This section investigates that claim, and intends to find the optimum value for DLC hardness using this technique. Table 6-6 shows the deposition recipe for the bias scan matrix. The interlayer recipe (from pumping to W-C:H layer) was based on a standard PECVD coating from Hauzer. For the microwave step, 1200 W power was used, 55% C_2H_2 and varied bias voltage at -50, -100, -150, -200, -250, -300 V. These bias voltages are within the range currently used within PECVD and Microwave PECVD processes. The intention of

this matrix is to determine where the hardest coating lies with regards to bias voltage; the next stage within these experiments will be to further refine accuracy of this to within 10 V.

6.4.1. Recipe

Table 6-6: Deposition recipe for Microwave DLC: Bias Matrix

Step	Time (mins)	Gas Flow (SCCM)		Bias (V)	Coil Current (A)	Cr Cathode (kW)	WC Cathode (kW)	μwave source 6.1 (kW)	μwave source 6.2 (kW)
		Ar	C ₂ H ₂						
Heating 200°C	60	Heating the chamber to 200C is necessary to optimise the performance of the plasma source.							
Target Cleaning	15	-	-	-500	1 - 5	1 - 5	1 - 3	-	-
Plasma Etch	15	50	-	200	-	-	-	-	-
Cr	25	130	-	-	4	3	-	-	-
Cr/WC	30	110	-	-	4	3 - 0.5	0.5 - 3	-	-
W-C:H	75	90	0 - 30 sccm (over 30 mins)		2	-	3	-	-
Pumping Standby	This step is necessary to reduce the pump speed before the microwave step.								
μwave DLC	15	45%	55%	50 - 300	-	-	-	1200	1200

As previously discussed, the stability of the process can be measured by the bias current. Figure 6-8 shows the bias currents for the bias scan matrix from -50 V to -300 V. The current shown for these are all stable, with the higher bias voltages having a higher current, this is expected due to the higher energy on the bias. The

trend for -50 V declines more rapidly than the others, this is due to the voltage being too small to sustain the plasma and this is reflected in further testing. The test conducted at -200 V was unstable at around 3 minutes in where the discharge failed. This was rectified and the sources were up and running within one minute, because of this fault the process in this instance was extended for a further minute to allow for this.

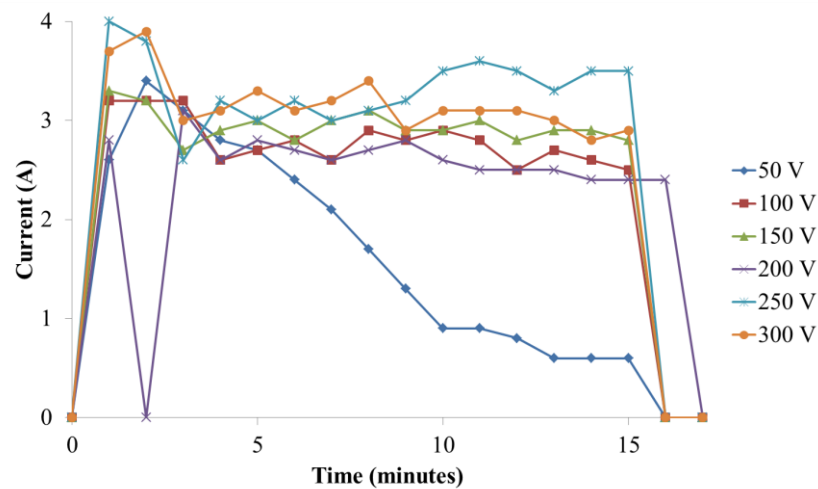


Figure 6-8: Bias current trends for the experiments conducted for bias scan matrix

Figure 6-9 shows the maximum temperatures reached during the microwave stage of each of the deposition processes undertaken in the bias scan matrix. It can be seen that no temperature exceeds 200 °C, and thus the processing temperature is considerably below the graphitisation temperature of > 400 °C.

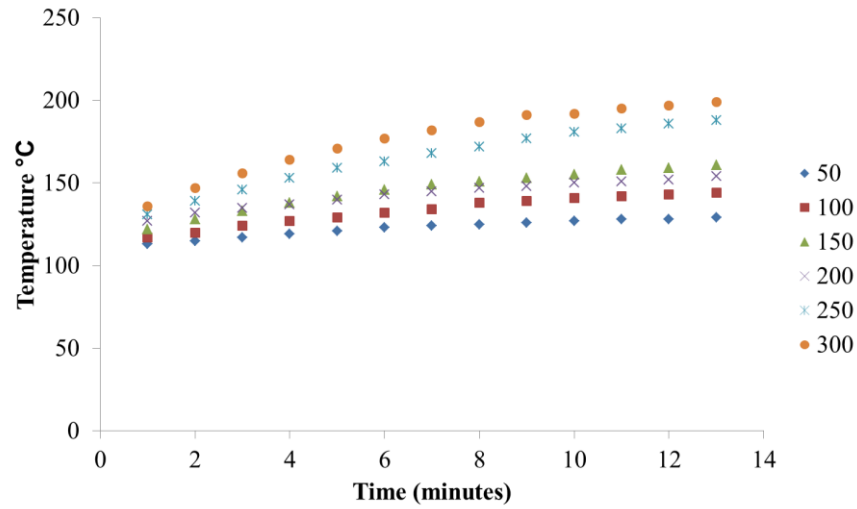


Figure 6-9: Maximum temperature reached during the final microwave step in each process within the bias scan variable matrix

The thickness of the DLC coatings made using this matrix are shown in Figure 6-10.

The thickness experiences a minimum of 2.1 μm at -200 V bias and a maximum of 2.6 μm at -50 V, but only varies by $\pm 0.3 \mu\text{m}$ from the average at any point.

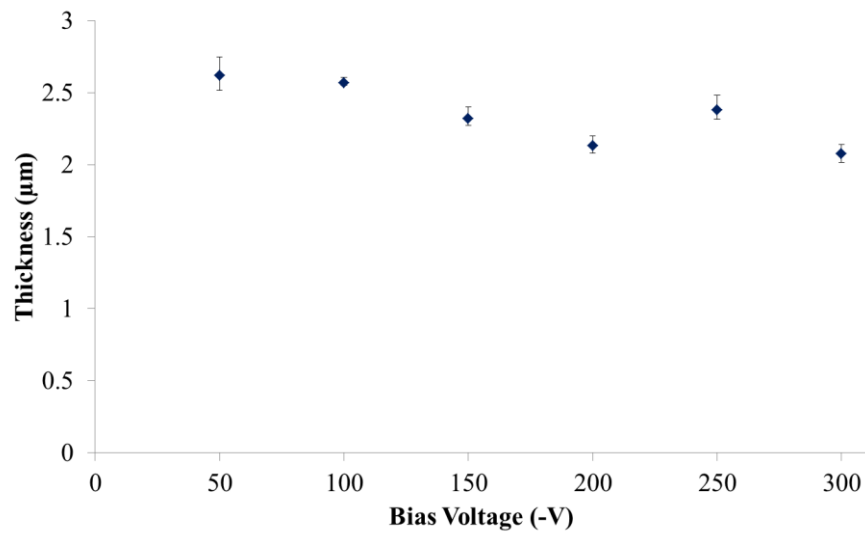


Figure 6-10: Thickness of the DLC made in the bias scan matrix of experiments

6.4.2. Hardness and Elastic Modulus

The mechanical properties of the coating were determined as in previous experiments, using a Micro Materials nano platform which is further detailed in 3.5. The nano hardness results for the bias scan matrix are shown Figure 6-11. The hardness increases initially with the bias voltage, and a maximum is reached as expected. The hardness is within the expected range for standard PECVD at -200 – -300 V (16.21 – 20.53 GPa) and peaks at a maximum of 20.53 GPa at – 250 V. This peak is characteristic of bias variation within the traditionally deposited PECVD DLC samples and can be seen in literature. The range chosen to look more closely at was -200 to -250 V in increments of 10 V. The hardness of the samples tested from -50 V to -300 V in this matrix can be seen in Figure 6-11. The elastic modulus can be seen in Figure 6-12.

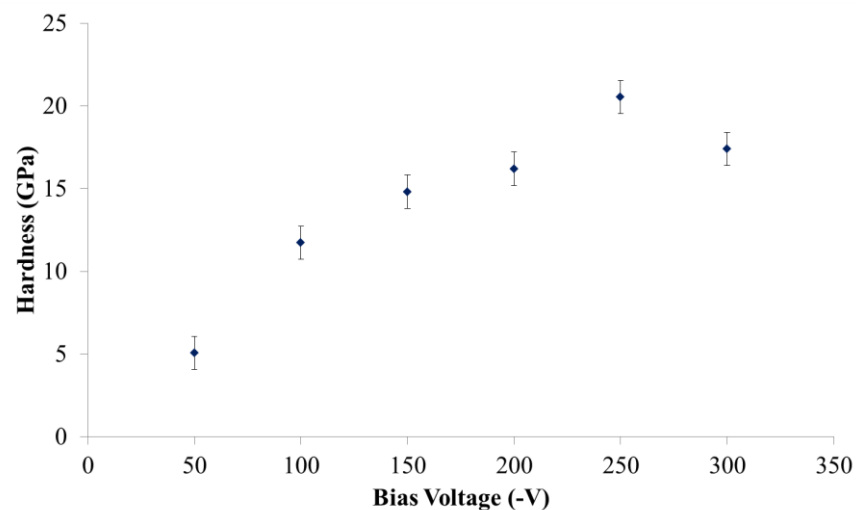


Figure 6-11: Hardness for microwave DLC deposited from -50 - -300 bias voltage

The elastic modulus follows a similar trend to the hardness, as can be seen in Figure 6-12 and falls within the expected range for this type of coating. There is a peak in the elastic modulus which is 164 GPa at -250 V.

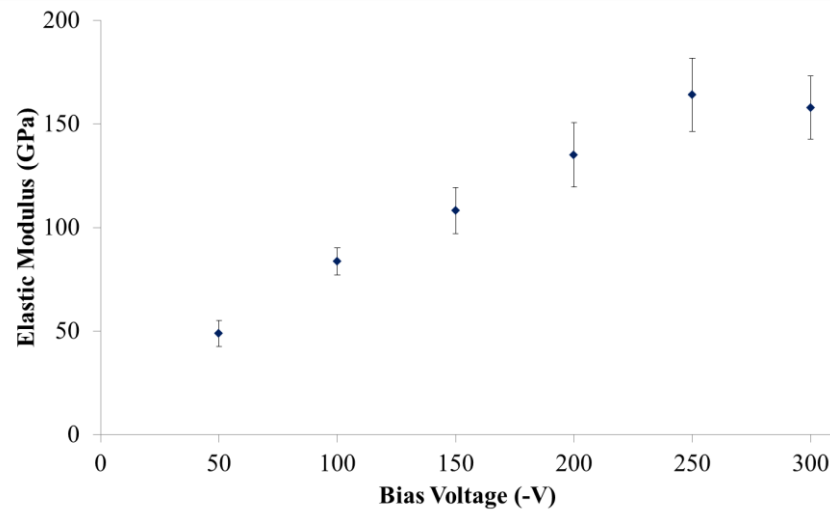


Figure 6-12: Elastic modulus for samples created in bias scan matrix

6.4.3. Summary

The following key points can be made about the bias scan series of experiments:

- The hardness and elastic modulus peak at -250 V and -100 V respectively.
- Microwave PECVD follows the same trend with regards to bias voltage and hardness as more traditionally deposited PECVD coatings.
- The highest hardness recorded during this experiment a maximum hardness of ~ 20 GPa at -250 V.

6.5. Bias Scan – Smaller Increments

The purpose of this matrix of experiments was to find the highest value of hardness that could be found by varying the bias voltage in increments of 10 V between -200

and -250 V, as between these values was hypothesised to lie the highest value of hardness, taken from the previous results in the bias scan, shown in Figure 6-11. The recipe for the tests conducted in the next set of experiments was the same as that seen in Table 6-6, except with the bias voltage at -210, -220, -230 and -240 V. Hardness and elastic modulus values for these experiments can be seen in Table 6-7 and graphed in Figure 6-13. As was seen previously in the hardness results for the bias scan matrix in Figure 6-11, the hardness peaks within this matrix also. Within this matrix the hardness is at a maximum at 26.8 GPa at -230 V which is above what was expected for this deposition technique as given by the manufacturers of the sources (KIT) at 20 GPa.

6.5.1. Hardness and Elastic Modulus

Table 6-7: Hardness and elastic modulus of samples deposited with bias voltages from -210 - -240 V

Bias	Hardness (GPa)	±	Elastic Modulus (GPa)	±
-210	18.5	2.1	151.5	11.6
-220	21.4	1.9	166.7	12.0
-230	26.7	1.2	287.0	30.5
-240	25.5	2.4	259.3	34.7

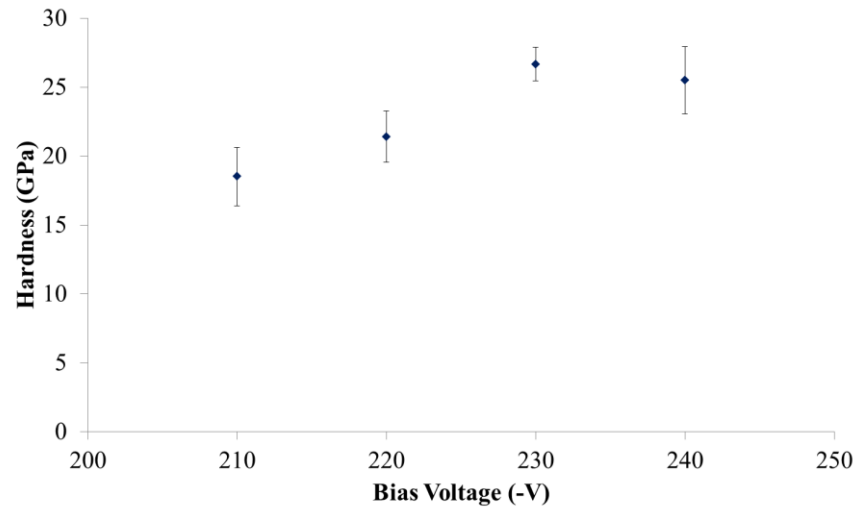


Figure 6-13: Hardness of DLC coatings from the matrix: bias scan, smaller increments

The elastic modulus follows a similar trend to the hardness and peaks at -230 V at ~250 GPa, this is comparable to the PECVD a-C:H which had an elastic modulus of ~262 GPa, but high when compared to Si-DLC and W-DLC which had elastic moduli of ~188 and 161 GPa, respectively.

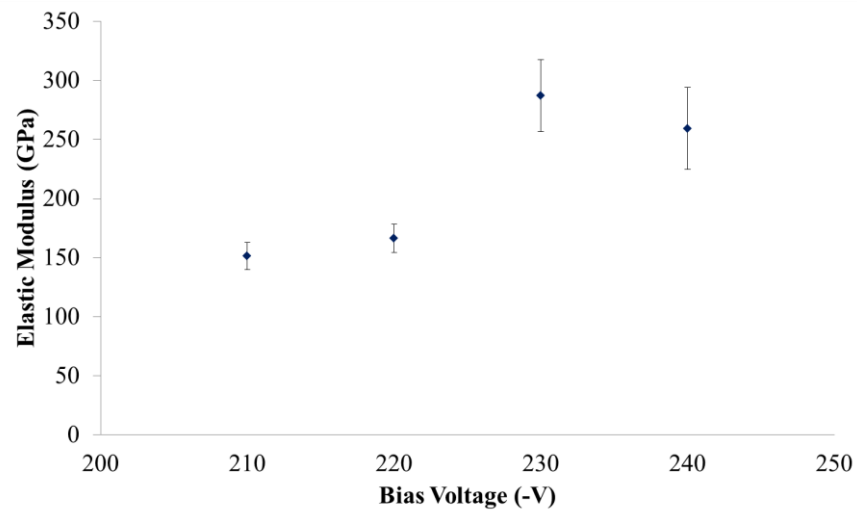


Figure 6-14: Elastic modulus of DLC coatings from the matrix: bias scan, smaller increments

6.5.2. Scratch Testing

Scratch testing was carried out for the samples made using two microwave sources. The results differed to those deposited using only one microwave source. No cracks or indication of an Lc_2 point was apparent on the surface. Figure 6-15 shows the scratch for the sample created using -250 V in the bias voltage series of experiments, this was at a progressive load of 1 – 60 N and the scratch for the sample created at -220 V which had a progressive load of 60 – 120 N. No Lc_2 value was present on either of the scratches. The scratches were deep enough to expose the substrate on each of the samples, however.

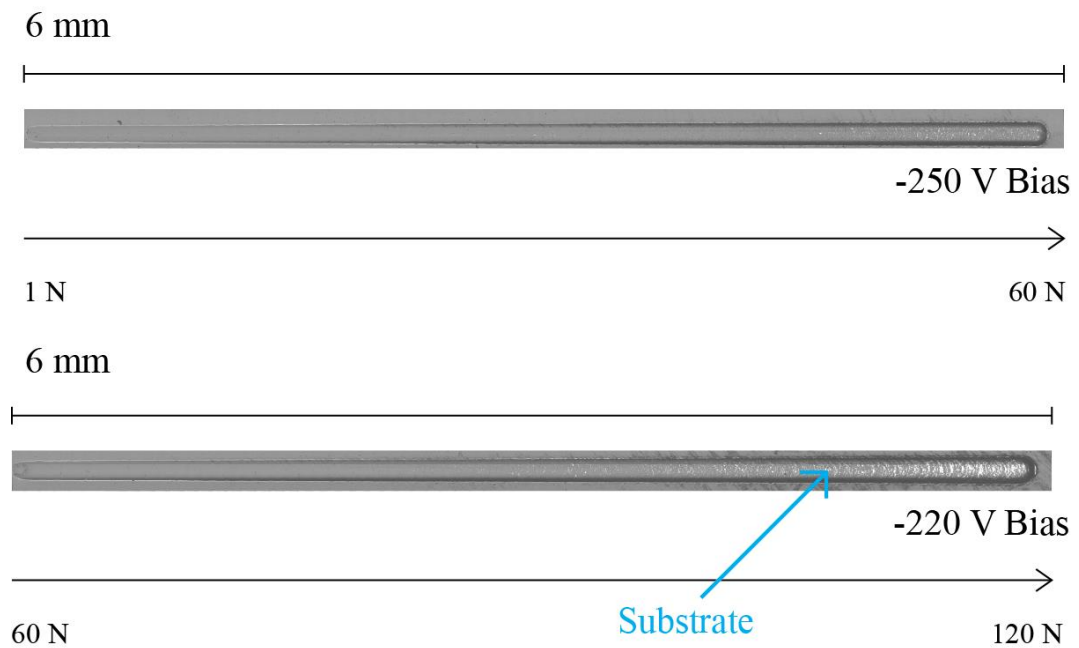


Figure 6-15: Scratch test images of samples produced using -250 V and -220 V bias, scratch tested using a maximum load of 60 and 120 N respectively.

6.5.3. Current Densities of the Diamond-Like Carbon Deposition Process

The current density of the process gives insight into the ionisation density of the system. This was calculated by taking the average bias current over the DLC deposition period and dividing this by the surface area of the negatively biased substrate table. The results can be seen in Figure 6-16.

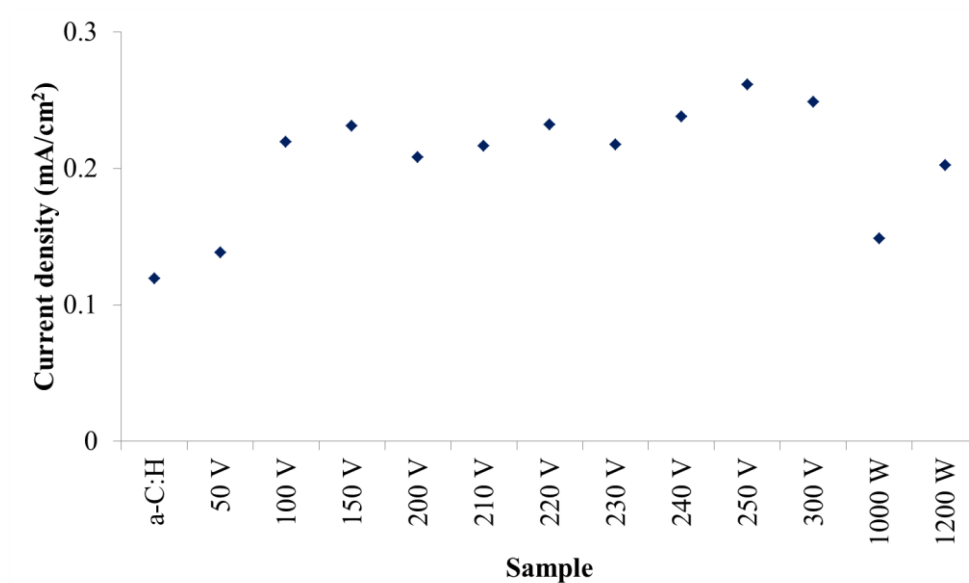


Figure 6-16: Current densities of the Diamond-Like Carbon deposition process across a selection of samples

It can be seen that those samples deposited using the microwave deposition process have a higher current density than those deposited using more traditional PECVD methods (the a-C:H). This is due to the extra energy donated to the system by the microwave sources. This can especially be seen in the samples that were deposited at 1000 W and 1200 W, where the sample prepared using a 1200 W microwave power had a higher current density.

6.5.4. Summary

- The hardness is higher than those tests conducted in the previous bias scan matrix at around 25 GPa.
- It is clear from these experiments that even by varying the bias by as little as 10 V an effect is seen on the mechanical properties of the coatings.
- With the high hardness comes very high elastic modulus at almost 300 GPa. This is extremely high and could potentially have a negative effect on the coatings mechanical and tribological properties.
- No critical load values were able to be obtained due to no classic signs of spalling or cracking of the surface within these coatings.
- There are differences seen when using only one microwave source when compared to two:
 - The coatings created using two sources are thicker. This was expected due to there being more energy within the deposition stage of the process when two microwaves are present and thus more ionisation of the source gas leading to a thicker deposit on the substrate.
 - The scratch test analysis shows that the resistance of the coatings using one microwave source was different to those deposited using two. The coatings deposited using two microwave sources proved difficult to analyse; no L_{c2} value was seen where these coatings were concerned and they appear to be resistant to cracking. This could be due to the higher energy in the system when two microwave sources are present and possibly creating a more dense coating.

Discussion

Discussion	
PECVD	Microwave PECVD
Tribochemical Interactions	<i>Effect of Number of Sources on Thickness of DLC Coatings</i>
<i>a-C:H</i>	<i>Si-DLC</i>
Tribological Interactions	<i>Comparison of Coatings Created at the University of Leeds to Those in the Literature</i>
<i>Friction</i>	
<i>Friction and Wear</i>	
<i>Critical Load and Wear</i>	

7.1. Plasma Enhanced Chemical Vapour Deposition Diamond-Like Carbon Coatings, Including Tungsten and Silicon Dopants

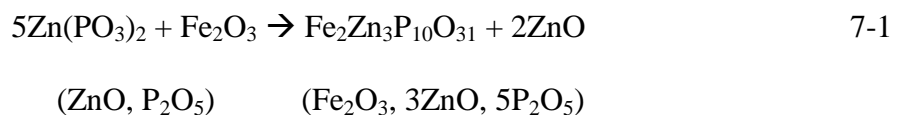
The mechanical properties of three Diamond-Like Carbon coatings deposited using Plasma Enhanced Chemical Vapour Deposition (a-C:H, Si-DLC and W-DLC) have been determined and evaluated in Chapter 4, alongside their tribological performance in two different oils; a group III base oil, and a fully formulated oil

with a group III base stock containing the anti-wear additive ZDDP. The coatings will be compared with those in the literature, and the mechanisms of formation of a phosphate tribo-film will be discussed.

7.1.1. Tribochemical Interactions

ZDDP is commonly used as an anti-wear additive in boundary lubrication conditions. The protection mechanisms for ZDDP in a ferrous environment are well documented. Nascent iron and iron oxide wear debris generated during sliding form an integral part of phosphate film formation as described by some authors [194], [115], whereas others describe the formation as a purely thermally induced process [195].

The formation of a phosphate film is based in the HSAB (hard and soft (Lewis) acid base theory). Phosphates (in this case PO_4^{3-}) derived from ZDDP are defined as ‘hard base’ and will react strongly with the hard acid (Fe^{3+}) from the cast iron pins.



Equation 7-1 shows the cation exchange process between Fe_2O_3 and ZnO (as described by [115]). The digestion of the iron oxide in the phosphate glass protects the surface from wear; this process requires friction to generate the iron oxide particles. As the wear protection of the surface becomes more prevalent and Fe is no longer being worn from the surface of the cast iron pin, more negative charges are needed to balance the exchange of Zn^{2+} with Fe^{3+} . Thus the chain length of the long metaphosphates is shortened into pyrophosphates in order to provide the negative

charges. This phosphate tribo-film is dynamic in that once the iron oxide particles are provided, the protection is sufficient to no longer need them, in which case the tribo-film has formed short pyrophosphates which protect the surface further; acting as 'molten' glass and allowing localised EHL sites to occur on the surface of the sample.

7.1.2. a-C:H

Within this study, it is apparent that a glassy phosphate film has been discovered on the surface of both the a-C:H DLC sample and the cast iron counter-body after six and twenty hours of testing on the tribometer. It is proposed here that the phosphate present in the additive has reacted with the Fe_2O_3 in the cast iron counter-body as described above. It is then seen to transfer to the DLC surface during sliding, since this surface is inert and does not react with the ZDDP [118, 196]. The XPS results of the quantified chemical species shown after tribo-testing for six and twenty hours in Figure 4-41 and Figure 4-42, respectively, show that the phosphate present after six hours is mostly long chained metaphosphate (59%), after twenty hours of testing, the shorter pyrophosphate chains dominate at a concentration of 67%. In the cast iron counter-body a different picture is seen, the phosphate occurs as short chained pyrophosphate (100%) after both six and twenty hours testing. It is seen in the literature that short chained pyrophosphate derived from the ZDDP anti-wear additive is more effective in protecting the surfaces than the long chained metaphosphates [197]. This suggests that the film transferred to the DLC surface changes from long chained metaphosphates to short chained pyrophosphates at a slower rate, or that it is transferred gradually from the cast iron pin to the DLC. On the cast iron pin, the metaphosphate was not detected by XPS; the change to

pyrophosphate here is much faster and thus protects the surface from an earlier stage.

The gradual transfer of the phosphate tribo-film to the surface of DLC is supported by other results; the wear rate of the a-C:H coating decreases over time, as is shown in Figure 4-13. The wear volume remains at a steady state after six hours of tribometer testing as seen in Figure 4-12, suggesting this gradual build up. The AFM images presented in Figure 4-39 show a clear tribo-film present on the a-C:H surface after twenty hours. However this cannot be seen on the six hour sample image. This could be due to the tribo-film being too thin for the AFM to detect on the sample tested for six hours, since the XPS results presented in Figure 4-40 show species on the surface of both samples tested at six and twenty hours that are present in the classic ZDDP tribo-film, this shows that a tribo-film of this nature is indeed present after both six and twenty hours.

A much thicker tribo layer is seen in the AFM images for the a-C:H after twenty hours, and none is visible after six. It is suggested that due to the presence of the tribo-film as proven by the XPS data, the wear rate decreasing and wear volume remaining static, that the tribo-film is formed initially on the cast iron counter-body surface and is gradually transferred to the a-C:H surface during sliding. This eventually provides protection of this surface, a schematic of this process can be seen in Figure 7-1.

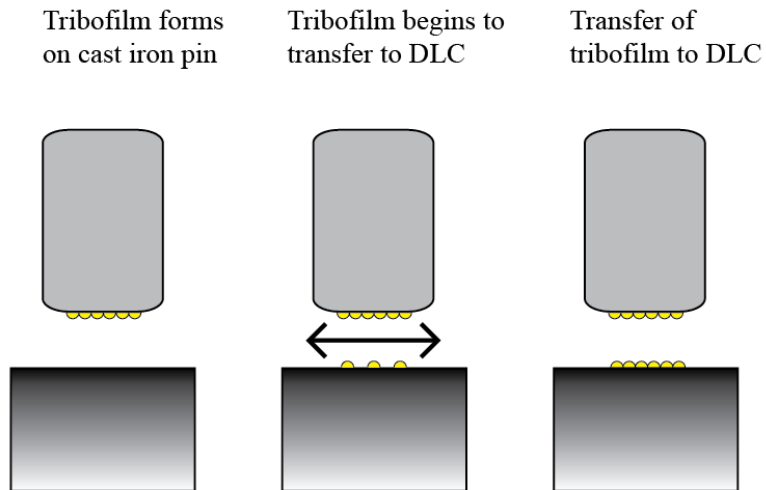


Figure 7-1: Transfer of tribo-film from cast iron pin to DLC surface

It can be seen from the microscope images of the a-C:H after the tribometer testing in Figure 4-14 that those in base oil suffered more wear than those tested in fully formulated oil + ZDDP in both six and twenty hour tests, though this was relatively mild wear when compared to that of the Si-DLC (Figure 4-22) and W-DLC (Figure 4-30). It can also be seen from the counter-body microscope images in Figure 4-15 that some trace of the coating can be found on this surface, an adhesive wear mechanism is proposed here, though only slight, whereby the tribo-film formed on the cast iron counter-body is transferred to the DLC, and particulates of the DLC are transferred to the counter-body, creating protective layers on each surface. This allows the wear volume to remain static, and the wear rate to decrease.

The a-C:H was the hardest of the three coatings tested in this series, a property that is often attributed to wear resistance [18, 64]. The H/E ratio of the a-C:H coating was in-between that of the Si-DLC (0.15) and W-DLC (0.1), at 0.11. However, as will be discussed later in this chapter, the H/E ratio does not necessarily correlate with wear resistance in lubricated contacts.

7.1.3. Si-DLC

The wear rate of the Si-DLC coating tested in fully formulated oil + ZDDP increased from six hours to twelve hours but then experienced a decrease at twenty hours. This could be due to the build-up of a tribo-film, as was potentially detected in the AFM images (Figure 4-39). However by this time the coating had partially worn away and the protection offered by the film had been negated. The wear mechanism is suggested to originally be that of adhesion, but after the coating begins to wear away, a third body interaction appears to be taking place which exacerbates the problem and causes further removal of the coating.

7.1.4. Friction

The steady state friction for a-C:H and Si-DLC are presented in base oil in Figure 4-11 and Figure 4-19, respectively. Friction was seen to be affected by the ZDDP additive, although minimally. Primarily an anti-wear additive, ZDDP was not expected to affect the friction in a large way. However, it was noticed in the a-C:H coating that friction indeed decreased over time, whereas the Si-DLC stayed fairly consistent.

The experiments conducted in base oil in both a-C:H and SI-DLC show the friction to be unstable and quite unrepeatable, giving large error bars and in the case of Si-DLC, removal of the coating, shown in Figure 4-22. The results in fully formulated oil + ZDDP are similar to those found by Vengudusamy et al. [105], showing that friction is minimally affected by the ZDDP additive. The Si-doped DLC tested in base oil had a decreasing steady state friction over time (despite higher wear volume over the same time), whereas in the fully formulated oil + ZDDP, the steady state

friction increased over time. In both instances of lubrication, the coating had been removed at twenty hours testing; the presence of the ZDDP in the lubricant appears to increase the friction once delamination has occurred, whereas in base oil this is being reduced. The W-DLC experienced an increase in friction coefficient in both the base oil and the fully formulated oil + ZDDP, which again agrees with the results of Vengudusamy et al. [105]. However, unlike the results in this study, the coating had been completely removed by this time and therefore the friction measured was largely that between the substrate and the counter-body, rather than the coating and the counter-body.

7.1.5. Friction and Wear

The coefficient of friction as a function of wear rate is presented in Figure 7-2. W-DLC was again excluded due to its complete removal, therefore the friction value given being unrepresentative of that between the coating and the counter-body. It is apparent that the combination of a-C:H and the fully formulated oil + ZDDP was the most successful in terms of the lowest wear rate and friction coefficient. The samples tested in base oil were very unstable with regards to friction and show high error due to this. The a-C:H sample performed better in both base oil and fully formulated oil + ZDDP, showing less friction and wear than the Si-DLC tested in fully formulated oil. This could be due to the a-C:H being harder than the Si-DLC, this property of the a-C:H could afford it higher wear resistance and lower friction. Also the synergy of the coating and the counter-body with the ZDDP additive is clearly contributing to both the friction and wear resistance. The best coating and lubricant combination for these tests are indicated in Figure 7-2 with regards to low friction and wear.

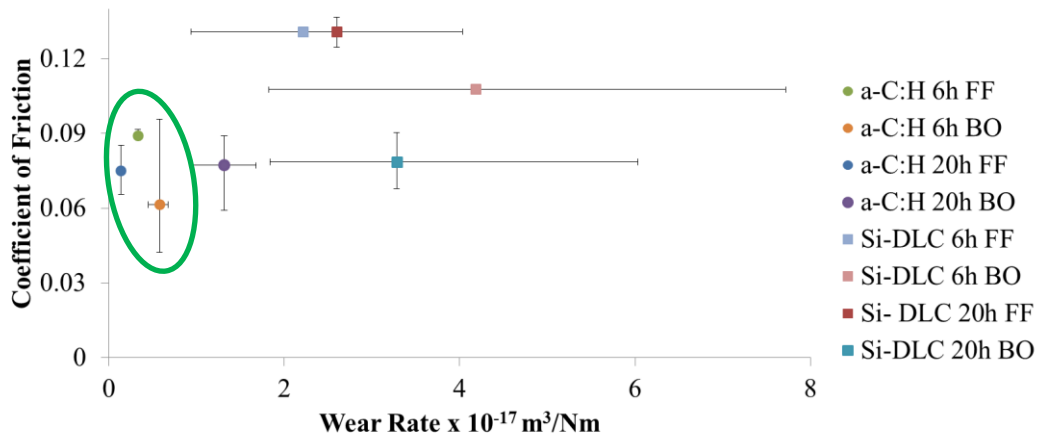


Figure 7-2: Coefficient of friction as a function of wear rate for a-C:H and Si-DLC after six and twenty hours testing. BO = Base oil, FF = fully formulated oil + ZDDP

Due to the effect of hardness on the a-C:H wear resistance, the wear rate of the samples is shown as a function of the coating hardness in Figure 7-3. It is clear from this graph that the a-C:H samples performed better, in both base oil and fully formulated oil. The sample was measured to be ~ 3 GPa harder than the Si-DLC. Hardness is a property often attributed to increased wear resistance [64] and it is clear that this property has an impact in this instance, since even in the samples tribo-tested in base oil, the wear rate is lower in the harder sample (a-C:H) than of the Si-DLC, which is of lower hardness as indicated in Figure 7-3. Other values for similar coatings presented in the literature by de Barros’Bouchet *et al.*[97] and Vengudusamy *et al.* [95] to provide a comparison. It can be seen from the graph that harder coatings do not necessarily equate to better wear resistance. The wear rate appears to not be entirely reliant on the hardness. Another factor that influences the wear rate is the ratio of the hardness and elastic modulus as has been widely noted by Leyland and Matthews [70, 71].

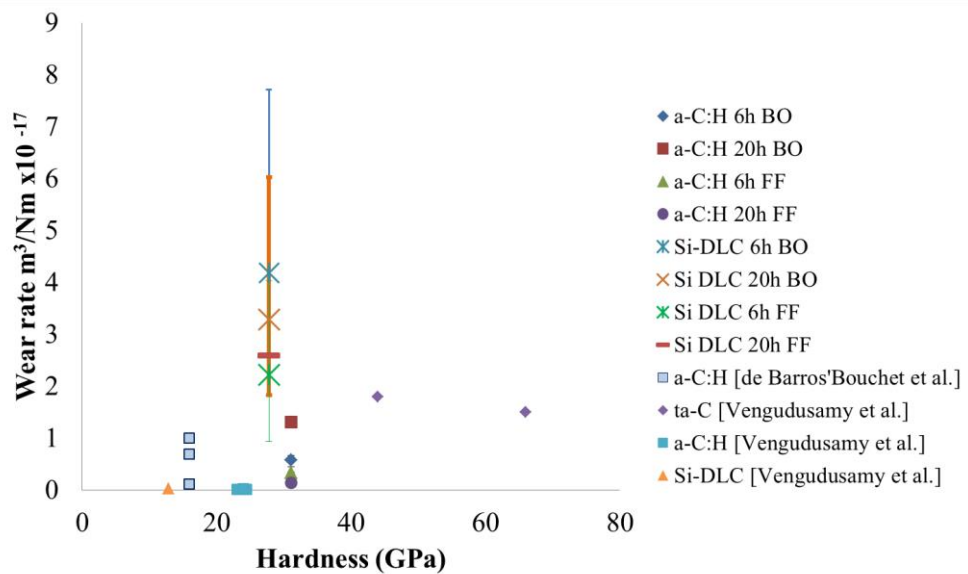


Figure 7-3: Wear rate as a function of coating hardness of a-C:H and Si-DLC. BO = base oil. FF = fully formulated oil + ZDDP. Including literature values from Vengudusamy *et al.* [95] and de Barros' Bouchet [97]

7.1.6. Critical Load and Wear

There is much debate in the literature surrounding the prediction of a coatings wear lifetime using varying means. Figure 7-5 presents the wear rate (after twenty hours of testing in base oil (BO) and fully formulated (FF) oil) as a function of the critical load taken from scratch tests for a-C:H, Si-DLC and W-DLC. This shows some surprising results, namely that as the critical load increases, as does the wear rate of the sample. This was surprising due to the critical load being a measure of a materials scratch resistance, but as is evidenced by Figure 7-5, a higher scratch resistance does not necessarily equate to a higher wear resistance, in fact, the opposite appears to be true. The scratch testing takes place at room temperature and involves no lubrication, thus the softer coating (W-DLC) will have the opportunity to deform elastically, whereas the other, harder samples (with higher elastic modulus) do not.

Figure 7-4 shows the critical load versus the H/E ratio of the DLC samples created during the course of this thesis. As can be seen here, as the critical load that the sample is able to withstand (where the L_{c2} value is found) increases, the H/E ratio decreases. However, it is noted within the literature that an H/E ratio with high hardness and a low elastic modulus is desirable for wear resistance [73], this is not the case for some of the coatings presented here. The coatings created within the gas ratio series of experiments tended to have low hardness (8 – 10 GPa) and low elastic modulus (56 – 63 GPa) and show the lowest L_{c2} values of the range of coatings tested. The coatings created within the two variable matrix have a slightly higher range of hardness (from 7 – 18 GPa) but also a much higher elastic modulus than those created in the gas ratio series of experiments (up to 185 GPa) but show much higher L_{c2} values. From this graph it can be said that a H/E ratio of ~ 0.1 is optimal for adhesion within dry scratch testing.

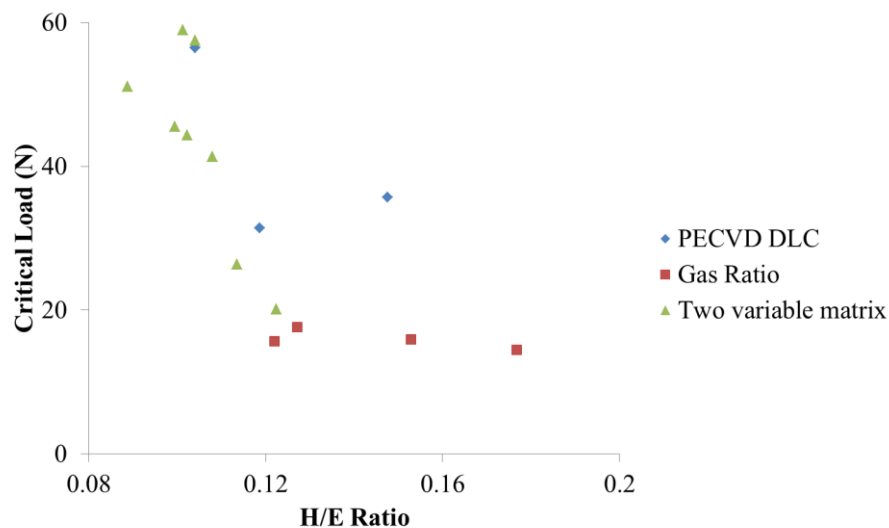


Figure 7-4: Critical load versus H/E ratio for the samples created during the course of this thesis.

The H/E ratio of each of the samples is presented in Table 4-3, the H/E ratio is sometimes used by authors as a tool to predict wear performance of coatings and other materials [70] which is said to indicate the materials elastic strain to failure, with a higher value of H/E being more conducive to a lower wear resistance. Of the three samples tested in this study, the W-DLC had the highest H/E ratio, signifying that it should have the best wear resistance. This was untrue for the samples tested in lubricant on the tribometer, however, the W-DLC sample outperformed both the a-C:H and Si-DLC on the scratch tests, reaching a critical load of 56.5 N, as opposed to that reached by a-C:H and Si-DLC of 31.4 N and 35.72 N respectively.

It would seem that the wear resistance indicated by the H/E ratio was true for the dry scratch tests, but both of these values were not useful in predicting wear resistance on the lubricated tribometer tests, which have a more complicated tribochemistry, as can be seen from Figure 7-5. It is important to recognise the limitations of the critical load value as an indicator for wear resistance in lubricated contacts, as this is a mechanical and chemical process, whereas scratch testing is purely mechanical and does not take into account the chemical factors.

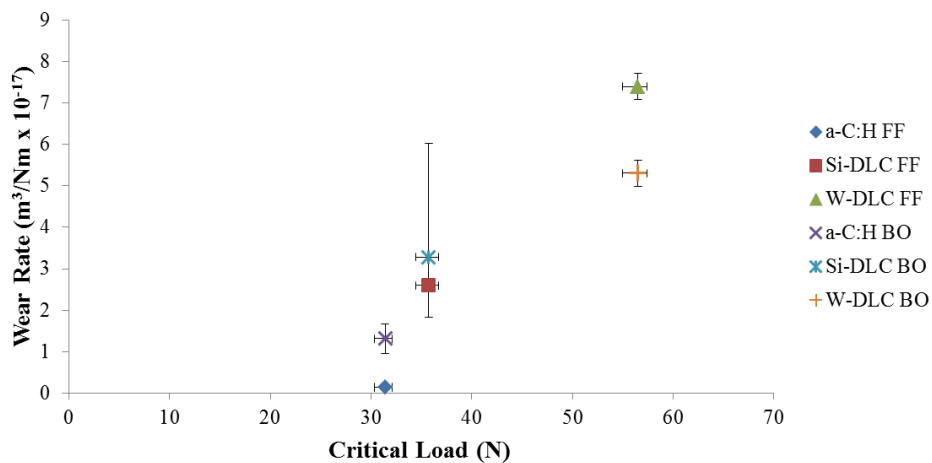


Figure 7-5: Wear rate as a function of critical load for a-C:H, Si-DLC and W-DLC after twenty hours testing

7.2. Microwave Plasma Enhanced Chemical Vapour Deposition

Diamond-Like Carbon Coatings

The novel microwave plasma enhanced chemical vapour deposited Diamond-Like Carbon coatings have been assessed for their mechanical properties and the relationship between these and the deposition parameters. This has been presented using one microwave source in Chapter 5 and two microwave sources in Chapter 6. The results of the mechanical and tribological properties, where relevant, will be compared with coatings presented in the literature. The effect that the deposition parameters have on the mechanical properties of the coatings will be discussed.

7.2.1. Thickness of Microwave PECVD Coatings with Variation in

Position on Substrate Holder Created with One and Two Microwave Sources

In the positional and thickness tests for one source and two source testing, the thickness of the DLC coating varied. The DLC was much thicker when just one source was used for 13 minutes than when two sources were used; the results are compared in Figure 7-6. The same bias voltage, interlayer and gas ratio was used. It would seem that using two sources lowers the thickness of the coatings despite delivering more power to the system. The results absent from either extremity of the substrate holder (dummy) are due to these coatings ‘pinging’ from the substrate and a measurement was unable to be taken. It is clear that there is a maximum thickness of the coatings produced using one microwave source; this is the area at which the centre of the antenna lies. No such maximum is found when two sources are used to deposit the coatings.

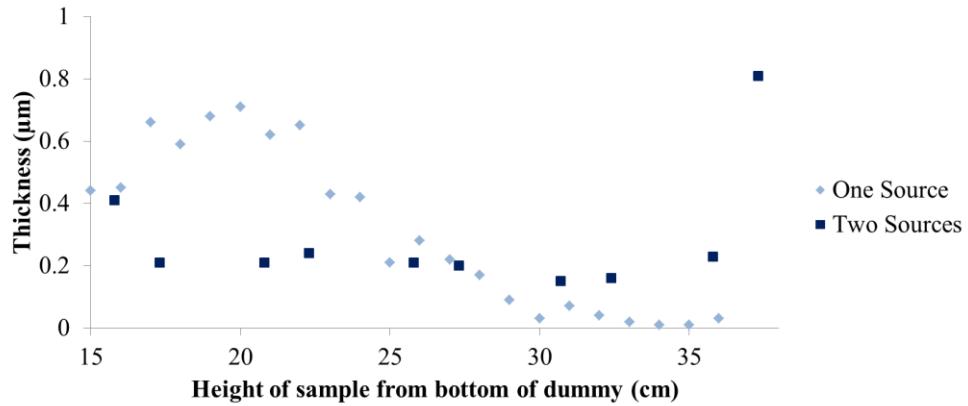


Figure 7-6: Thickness of DLC made using one and two microwave sources in different positions along the substrate holder.

The thickness where two sources have been used is greatest at the outer extremities of the sample holder, after which the coatings no longer adhere to the substrate. From the results it is apparent that a more even power distribution is achieved when two sources are used. From a commercial point of view this is a useful result as it allows a fairly uniform distribution of the coating over a large surface area, enabling a higher volume of products to be coated with the same thickness of material. Using only one source would not achieve this and would be impractical from this perspective, giving an uneven distribution across the span of the sample holder.

7.2.2. The Effect of Bias Voltage on Thickness, Hardness and Elastic Modulus of DLC Coatings Made with One and Two Microwave Sources

All of the samples compared within this section have been produced with a microwave DLC recipe using 55% acetylene and 45% argon. The difference in processing parameters are: The power in the process using two sources was 1.2 kW and duration was 15 minutes (with acetylene for 13 minutes of the process) whereas

in the process using one microwave source this was 1 kW, and a 13 minute duration (with acetylene for 11 minutes). Despite these differences in processing parameters the coatings can still be compared with respect to trends seen in the thickness, hardness, and elastic modulus.

The thickness of the DLC in experiments that varied the bias voltage show opposite results to those previously seen in section 7.2, however the DLC coatings deposited using two microwave sources had a duration of two minutes longer than the coatings using one source, which accounts for this discrepancy. Nevertheless, the samples created using one source and two sources follow a similar trend of decreasing thickness with increasing bias voltage as can be seen in Figure 7-7.

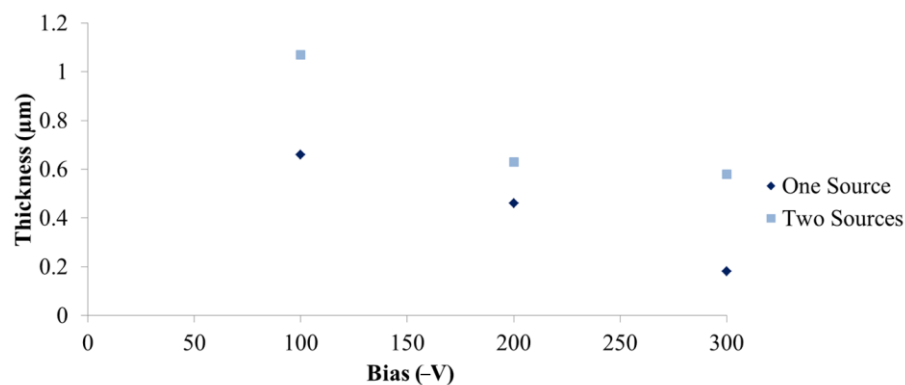


Figure 7-7: Variation of the thickness of microwave DLC coatings produced using one and two microwave sources with respect to bias voltage

As the coating thickness decreases with increasing bias voltage, the hardness increases in both the samples created using one microwave source and with two microwave sources as presented in Figure 7-8. This could be due to the higher ion energy induced by the increased bias voltage, which encourages a higher sp^3 percentage in the atomic matrix. The sp^3 bonded carbon is more densely packed than sp^2 bonded carbon and could account for the lower thickness of the coating [11].

This is supported by the increase in elastic modulus with respect to the bias, results of which are compared in Figure 7-9, which indicates that higher internal stresses are present. The hardness and elastic modulus vary only slightly with the difference in number of sources, and the results are all within error of one another. The results of the previous section (7.2) show that the variation in thickness relies heavily upon the position of the samples in the chamber, in these experiments the position in the chamber was fixed at the optimum points as previously discussed for one source in section 5.4 and for two sources in section 6.2.

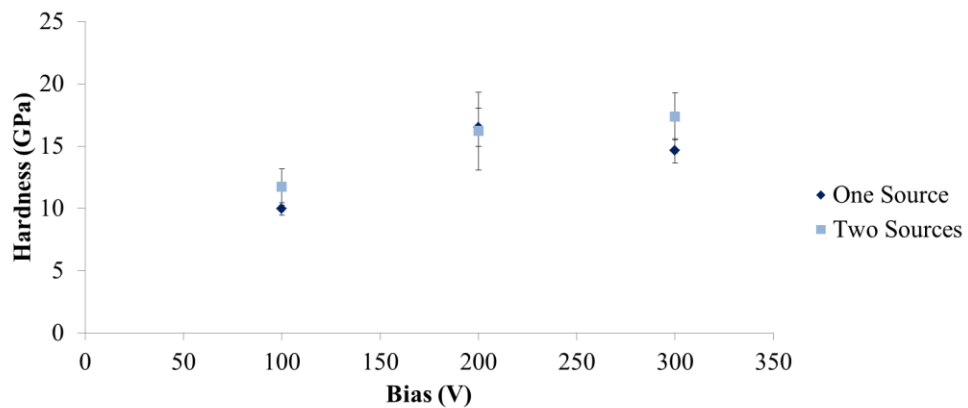


Figure 7-8: Variation of the hardness of microwave DLC coatings produced using one and two microwave sources with respect to bias voltage

With the substrates in a fixed position, the number of sources used for coating deposition does not affect the hardness or elastic modulus of the coatings, neither does the difference in power (one source: 1 kW, two sources: 1.2 kW). This property of the coating seem to rely mostly on the bias voltage, which interestingly, as it is increases, also increases the hardness and elastic modulus of the coating, but decreases the thickness.

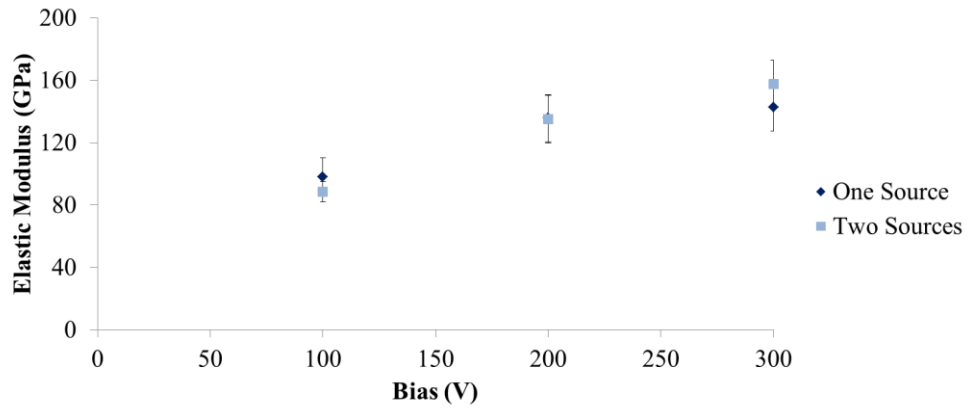


Figure 7-9: Variation of the elastic modulus of microwave DLC coatings produced using one and two microwave sources with respect to bias voltage

7.2.3. Comparison of the Coatings Created at the University of Leeds to Those Found in the Literature

The coatings created using the deposition system at the University of Leeds will be compared with existing industrial coatings.

As can be seen from Table 7-1, a wide variation in mechanical properties can be achieved by using different deposition techniques, and parameters (more clearly seen in section 2.5.5). The a-C:H coating falls amongst the ‘hard’ a-C:H coatings noted in Table 2-2. The microwave coatings exceed that found using similar methods (no two deposition chambers are exactly alike – producing different results for different set ups) in hardness, which a result much welcomed by the sponsors of this project.

Table 7-1: A selection of coating properties from the literature

Coating Type	Deposition Method	Hardness (GPa)	Elastic Modulus (GPa)	H/E	Reference
a-C:H	Magnetron	8.8	110	0.08	69
a-C:H	PECVD	16	130	0.12	71
a-C:H	Microwave	16	180	0.089	72
a-C:H	Microwave	15	180	0.083	75
a-C:H	Microwave	16	146	0.11	77

The microwave coating hardness varied throughout the testing from a very low hardness (5 GPa in the 50 V bias scan experiment using two sources seen in section 6.4.2) to the maximum hardness found of ~ 26 GPa (also in the bias scan series of experiments using two sources shown in section 6.5.1). This shows that the deposition parameters can be varied by small amounts to achieve vastly different results. The graphs and equations generated from this empirical data (presented in section 5.5.5) will serve to provide future users of this particular deposition system with a means by which to produce coatings of known hardness or elastic modulus (within a reasonable margin of accuracy).

Chapter 8

Conclusions

This study has provided insight to the tribological interactions of a-C:H, Si-DLC and W-DLC and the anti-wear additive ZDDP with the support of physical and chemical analysis. Of note are the interactions between ZDDP and a-C:H (sliding against a cast iron counter-body). Also microwave PECVD DLC coatings were produced and their mechanical properties were defined. A diverse range of deposition parameters were explored which gave many varied results. Conclusions for both PECVD and Microwave PECVD elements of this thesis are provided here, along with recommendations for future work.

8.1. Conclusions

- It has been shown that ZDDP has an effect on the wear resistance of a-C:H coating surfaces when reciprocating against a cast iron counter-body
- A phosphate based tribo-film has been produced on the a-C:H surfaces
- The phosphate tribo-film on the a-C:H surface has been shown to consist mainly of long chained metaphosphates after six hours sliding against a cast iron pin, devolving into short chained pyrophosphates after twelve hours.
- It has been shown that the short chained pyrophosphates enhance the protection of the a-C:H surface more so than the long chained metaphosphates.

- The phosphate film is transferred from the cast iron pin to the a-C:H surface over time.
- ZDDP was seen to lower the friction minimally in the case of a-C:H
- The Si-DLC used within this study was not adequate for the application due to coating removal during testing.
- A tribo-film was seen to begin to form, but the removal of the coating preceded this, negating any protection it could potentially offer.
- The W-DLC (Balanit C*) proved completely unsuitable for this application, being completely removed from the substrate after six hours of testing.
- The H/E ratio is seen to be a helpful indicator of the scratch resistance of the DLC coated samples, however, as the tribochemistry of a contact changes i.e. if lubricant is present, this is not the case.
- Using two microwave sources allows more uniformity across the deposition area, using only one source creates an 'energy profile' and is undesirable in commercial application
- The thickness of the DLC deposited using the microwave sources are heavily dependent on the bias voltage and less so on the number of microwave sources used. This could be attributed to the higher amount of sp³ bonding present which is evidenced by the high elastic modulus.
- Hardness and Elastic modulus are not affected by the number of sources present but are heavily affected by the bias voltage, tending to increase as the bias is increased.

- The highest hardness achieved using two microwave sources was ~25 GPa, which was harder than the DLC produced using PECVD on the same deposition system
- Empirical equations have been produced which will allow future users of the deposition system to decide upon the hardness and elastic modulus properties they wish to have. The equations will give the optimum bias voltage and gas ratio to achieve this, within a maximum of 15% error.

The a-C:H performed the best of the three coatings in the tribometer tests, providing a wear resistance an order of magnitude lower than the DLC containing tungsten, and for most tests performed with the Si-DLC.

8.2. Future work

There is great potential to extend the current study and build upon the knowledge within this area. Such points are discussed below.

- Durability of tribo-films.

Once the tribo-films have formed on the coating surface, mechanical measurements of them would be useful in determining the useful lifetime of the films.

- Effective addition of additives into the DLC coating.

The successful levels of dopants should be explored in order to achieve a better unison between coating and existing lubricant additives

- Microwave PECVD.

More variables should be considered when making the coatings. This would help to determine the exact effect each parameter has on the end properties of the coating

The tribological properties of these coatings should be investigated and compared to the existing PECVD coatings.

The level of Sp^2 bonding should be investigated in order to determine the compositional nature of the coatings, and the effect that the deposition parameters have on this.

References

- [1] A. M. Merlo, "The contribution of surface engineering to the product performance in the automotive industry," *Surface and Coatings Technology*, vol. 174–175, pp. 21-26, 2003.
- [2] J. T. Houghton, "Global warming," *Reports on Progress in Physics*, vol. 68, p. 1343, 2005.
- [3] J. T. Houghton, Y. Ding, D. J. Griggs, M. Noguer, P. J. van der Linden, X. Dai, *et al.*, "Climate Change 2001, The Scientific Basis," in *IPCC 2001 Third Assessment Report*, Cambridge, 2001.
- [4] "Greenhouse gas emission trends and projections in Europe 2009," ed. Copenhagen: EEA, 2009.
- [5] *On type approval of motor vehicles with respect to emissions from light passenger and commercial vehicles (Euro 5 and Euro 6) and on access to vehicle repair and maintenance information*, E. Parliament 715/2007, 2007.
- [6] J. Ahn, G. Jeong, and Y. Kim, "A forecast of household ownership and use of alternative fuel vehicles: A multiple discrete-continuous choice approach," *Energy Economics*, vol. 30, pp. 2091-2104, 2008.
- [7] K. Holmberg, P. Andersson, and A. Erdemir, "Global energy consumption due to friction in passenger cars," *Tribology International*, vol. 47, pp. 221-234, 2012.
- [8] S. C. Tung and M. L. McMillan, "Automotive tribology overview of current advances and challenges for the future," *Tribology International*, vol. 37, pp. 517-536, 2004.
- [9] B. Bhushan, *Modern tribology handbook*: CRC Press, 2001.
- [10] J. A. Williams, *Engineering tribology*: Cambridge University Press, 2005.
- [11] C. Donnet and E. Erdemir, *Tribology of Diamond-Like Carbon Films. Fundamentals and Applications*. New York: Springer Science, 2008.
- [12] D. A. Gurnett and A. Bhattacharjee, *Introduction to Plasma Physics With Space and Laboratory Applications*. Cambridge, UK: Cambridge University Press, 2005.
- [13] R. Fitzpatrick. (2008, January 2012). *The Physics of Plasmas*. Available: <http://farside.ph.utexas.edu/teaching/plasma/380.pdf>

- [14] A. Bogaerts, E. Neyts, R. Gijbels, and J. van der Mullen, "Gas discharge plasmas and their applications," *Spectrochimica Acta Part B: Atomic Spectroscopy*, vol. 57, pp. 609-658, 2002.
- [15] D. Lundin, "The HiPIMS Process," PhD, Linkoping University, 2010.
- [16] B. Chapman, *Glow discharge Processes Sputtering and Plasma Etching*. Canada: John Wiley and Sons Inc., 1980.
- [17] J. R. Roth, R. Jozef, D. Xin, and M. S. Daniel, "The physics and phenomenology of One Atmosphere Uniform Glow Discharge Plasma (OAUGDP) reactors for surface treatment applications," *Journal of Physics D: Applied Physics*, vol. 38, p. 555, 2005.
- [18] J. Robertson, "Diamond-like amorphous carbon," *Materials Science and Engineering: R: Reports*, vol. 37, pp. 129-281, 2002.
- [19] S. V. Hainsworth and N. J. Uhure, "Diamond like carbon coatings for tribology: production techniques, characterisation methods and applications," *International Materials Reviews*, vol. 52, pp. 153-174, 2007.
- [20] Y. Enomoto and T. Yamamoto, "New materials in automotive tribology," *Tribology Letters*, vol. 5, pp. 13-24, 1998.
- [21] Y. Yasuda, M. Kano, Y. Mabuchi, and S. Abou, "Research on Diamond-Like Carbon Coatings for Low-Friction Valve Lifter," *SAE Technical Paper*, vol. 01, 2003.
- [22] S. D. A. Lawes, M. E. Fitzpatrick, and S. E. Hainsworth, "Evaluation of the tribological properties of DLC for engine applications," *Journal of Physics D: Applied Physics*, vol. 40, p. 5427, 2007.
- [23] Nissan. (2014, 25 May). *Ultra low friction using diamond-like carbon (DLC)*.
- [24] M. Priest and C. M. Taylor, "Automobile engine tribology -- approaching the surface," *Wear*, vol. 241, pp. 193-203, 2000.
- [25] E. P. Becker, "Trends in tribological materials and engine technology," *Tribology International*, vol. 37, pp. 569-575, 2004.
- [26] T. S. Eyre and B. Crawley, "Camshaft and cam follower materials," *Tribology International*, vol. 13, pp. 147-152, 1980.
- [27] S. Fukuoka, N. Hara, A. Mori, and K. Ohtsubo, "Friction loss reduction by new lighter valve train system," *JSAE Review*, vol. 18, pp. 107-111, 1997.
- [28] M. Kano, "Super low friction of DLC applied to engine cam follower lubricated with ester-containing oil," *Tribology International*, vol. 39, pp. 1682-1685, 2006.

- [29] M. Kano, Y. Yasuda, Y. Okamoto, Y. Mabuchi, T. Hamada, T. Ueno, *et al.*, "Ultralow friction of DLC in presence of glycerol mono-oleate (GMO)," *Tribology Letters*, vol. 18, pp. 245-251, 2005.
- [30] M. Kano and K. Yoshida, "Ultra Low Friction of DLC Coating with Lubricant," *Journal of Physics: Conference Series*, vol. 258, p. 012009, 2009.
- [31] S. Miyake, T. Saito, Y. Yasuda, Y. Okamoto, and M. Kano, "Improvement of boundary lubrication properties of diamond-like carbon (DLC) films due to metal addition," *Tribology International*, vol. 37, pp. 751-761, 2004.
- [32] T. Haque, "Tribochemistry of Lubricant Additives on Non-Ferrous Coatings for Reduced Friction, Improved Durability and Wear in Internal Combustion Engines," Ph.D Thesis, School of Mechanical Engineering, University of Leeds, Leeds, 2007.
- [33] A. Neville, A. Morina, T. Haque, and M. Voong, "Compatibility between tribological surfaces and lubricant additives--How friction and wear reduction can be controlled by surface/lube synergies," *Tribology International*, vol. 40, pp. 1680-1695, 2007.
- [34] S. Aisenberg and R. Chabot, "Ion-Beam Deposition of Thin Films of Diamondlike Carbon," *Journal of Applied Physics*, vol. 42, pp. 2953-2958, 1971.
- [35] P. J. Martin, S. W. Filipczuk, R. P. Netterfield, J. S. Field, D. F. Whitnall, and D. R. McKenzie, "Structure and hardness of diamond-like carbon films prepared by arc evaporation," *Journal of Materials Science Letters*, vol. 7, pp. 410-412, 1988.
- [36] R. Messier, A. R. Badzian, T. Badzian, K. E. Spear, P. Bachmann, and R. Roy, "From diamond-like carbon to diamond coatings," *Thin Solid Films*, vol. 153, pp. 1-9, 1987.
- [37] T. C. Arnoldussen and E. Rossi, "Materials for Magnetic Recording," *Annual Review of Materials Science*, vol. 15, pp. 379-409, 1985.
- [38] F. King, "Datapoint thin film media," *Magnetics, IEEE Transactions on*, vol. 17, pp. 1376-1379, 1981.
- [39] J. Robertson, "Amorphous carbon," *Advances in Physics*, vol. 35, pp. 317-374, 2013/08/12 1986.
- [40] A. Grill, V. Patel, and B. Meyerson, "Tribological behavior of diamond-like carbon: effects of preparation conditions and annealing," *Surface and Coatings Technology*, vol. 49, pp. 530-536, 1991.
- [41] H. Ronkainen, J. Koskinen, A. Anttila, K. Holmberg, and J. P. Hirvonen, "Tribological characterisation of hard carbon films produced by the pulsed

- vacuum arc discharge method," *Diamond and Related Materials*, vol. 1, pp. 639-643, 1992.
- [42] K. Miyoshi, R. L. C. Wu, and A. Garscadden, "Friction and wear of diamond and diamondlike carbon coatings," *Surface and Coatings Technology*, vol. 54-55, Part 2, pp. 428-434, 1992.
- [43] A. Erdemir, M. Switala, R. Wei, and P. Wilbur, "A tribological investigation of the graphite-to-diamond-like behavior of amorphous carbon films ion beam deposited on ceramic substrates," *Surface and Coatings Technology*, vol. 50, pp. 17-23, 1991.
- [44] C. Donnet, M. Belin, J. C. Auge, J. M. Martin, A. Grill, and V. Patel, "Tribochemistry of diamond-like carbon coatings in various environments," *Surface and Coatings Technology*, vol. 68-69, pp. 626-631, 1994.
- [45] V. F. Dorfman, "Diamond-like nanocomposites (DLN)," *Thin Solid Films*, vol. 212, pp. 267-273, 1992.
- [46] C. Donnet, "Recent progress on the tribology of doped diamond-like and carbon alloy coatings: a review," *Surface and Coatings Technology*, vol. 100 - 101, pp. 180-186, 1998.
- [47] A. Grill, "Review of the tribology of diamond-like carbon," *Wear*, vol. 168, pp. 143-153, 1993.
- [48] A. Grill, "Tribology of diamondlike carbon and related materials: an updated review," *Surface and Coatings Technology*, vol. 94-95, pp. 507-513, 1997.
- [49] A. Erdemir, "Friction and wear of diamond and diamond-like carbon films," *Proceedings of the Institution of Mechanical Engineers, Part J: Journal of Engineering Tribology*, vol. 216, pp. 387-400, 2002.
- [50] A. Erdemir and C. Donnet, "Tribology of diamond-like carbon films: recent progress and future prospects," *Journal of Physics D: Applied Physics*, vol. 39, p. R311, 2006.
- [51] G. Dearnaley and J. H. Arps, "Biomedical applications of diamond-like carbon (DLC) coatings: A review," *Surface and Coatings Technology*, vol. 200, pp. 2518-2524, 2005.
- [52] R. Hauert, "A review of modified DLC coatings for biological applications," *Diamond and Related Materials*, vol. 12, pp. 583-589, 2003.
- [53] J. P. Sullivan, T. A. Friedmann, M. P. de Boer, R. J. Hohlfelder, C. I. H. Ashby, M. T. Dugger, *et al.*, "Developing a New Material for MEMS: Amorphous Diamond," *Materials Research Society Symposium Proceedings*, vol. 657, pp. EE7.1.1 - EE7.1.9, 2001.
- [54] J. Robertson and E. P. O'Reilly, "Electronic and atomic structure of amorphous carbon," *Physical Review B*, vol. 35, pp. 2946-2957, 02/15/ 1987.

- [55] Y. Lifshitz, "Hydrogen-free amorphous carbon films: correlation between growth conditions and properties," *Diamond and Related Materials*, vol. 5, pp. 388-400, 1996.
- [56] D. Sheeja, B. K. Tay, S. P. Lau, and X. Shi, "Tribological properties and adhesive strength of DLC coatings prepared under different substrate bias voltages," *Wear*, vol. 249, pp. 433-439, 2001.
- [57] E. Liu, L. Li, B. Blanpain, and J. P. Celis, "Residual stresses of diamond and diamondlike carbon films," *Journal of Applied Physics*, vol. 98, pp. 073515-5, 2005.
- [58] J. Robertson, "Deposition mechanisms for promoting sp³ bonding in diamond-like carbon," *Diamond and Related Materials*, vol. 2, pp. 984-989, 1993.
- [59] M. Weber, K. Bewilogua, H. Thomsen, and R. Wittorf, "Influence of different interlayers and bias voltage on the properties of a-C:H and a-C:H:Me coatings prepared by reactive d.c. magnetron sputtering," *Surface and Coatings Technology*, vol. 201, pp. 1576-1582, 2006.
- [60] J. Choi, S. Nakao, M. Ikeyama, and T. Kato, "Effect of deposition pressure on the properties of DLC coatings deposited by bipolar-type PBII&D," *Surface and Interface Analysis*, vol. 40, pp. 806 - 809, 2007.
- [61] Y. Umehara, S. Murai, Y. Koide, and M. Murakami, "Effects of sp²/sp³ bonding ratios on field emission properties of diamond-like carbon films grown by microwave plasma chemical vapor deposition," *Diamond and Related Materials*, vol. 11, pp. 1429-1435, 2002.
- [62] K.-L. Choy and E. Felix, "Functionally graded diamond-like carbon coatings on metallic substrates," *Materials Science and Engineering A*, vol. 278, pp. 162-169, 1999.
- [63] J. S. Wang, Y. Sugimura, A. G. Evans, and W. K. Tredway, "The mechanical performance of DLC films on steel substrates," *Thin Solid Films*, vol. 325, pp. 163-174, 1998.
- [64] R. C. D. Richardson, "The wear of metals by relatively soft abrasives," *Wear*, vol. 11, pp. 245-275, 1968.
- [65] J. Guo, H. Wang, F. Meng, X. Liu, and F. Huang, "Tuning the H/E* ratio and E* of AlN coatings by copper addition," *Surface and Coatings Technology*, vol. 228, pp. 68-75, 2013.
- [66] T. Y. Tsui, G. M. Pharr, W. C. Oliver, Y. W. Chung, E. C. Cutiongco, C. S. Bhatia, *et al.*, "Nanoindentation and nanoscratching of hard coating materials for magnetic disks," *Materials Research Society Symposium - Proceedings*, vol. 356, pp. 767-772, 1995.

- [67] C. Rebholz, H. Ziegele, A. Leyland, and A. Matthews, "Structure, mechanical and tribological properties of Ti-B-N and Ti-Al-B-N multiphase thin films produced by electron-beam evaporation," *Journal of Vacuum Science and Technology A: Vacuum, Surfaces and Films*, vol. 16, pp. 2851-2857, 1998.
- [68] W. Ni, Y. T. Cheng, M. J. Lukitsch, A. M. Weiner, L. C. Lev, and D. S. Grummon, "Effects of the ratio of hardness to Young's modulus on the friction and wear behavior of bilayer coatings," *Applied Physics Letters*, vol. 85, pp. 4028-4030, 2004.
- [69] Y. T. Pei, P. Huizenga, D. Galvan, and J. T. M. De Hosson, "Breakdown of the Coulomb friction law in TiC/a-C:H nanocomposite coatings," *Journal of Applied Physics*, vol. 100, pp. -, 2006.
- [70] A. Leyland and A. Matthews, "On the significance of the H/E ratio in wear control: a nanocomposite coating approach to optimised tribological behaviour," *Wear*, vol. 246, pp. 1-11, 2000.
- [71] A. Leyland and A. Matthews, "Design criteria for wear-resistant nanostructured and glassy-metal coatings," *Surface and Coatings Technology*, vol. 177-178, pp. 317-324, 2004.
- [72] J. Halling, "The tribology of surface films," *Thin Solid Films*, vol. 108, pp. 103-115, 1983.
- [73] J. Musil, P. Novák, R. Čerstvý, and Z. Soukup, "Tribological and mechanical properties of nanocrystalline-TiC/a-C nanocomposite thin films," *Journal of Vacuum Science & Technology A*, vol. 28, pp. 244-249, 2010.
- [74] J. Musil, "Hard nanocomposite coatings: Thermal stability, oxidation resistance and toughness," *Surface and Coatings Technology*, vol. 207, pp. 50-65, 2012.
- [75] A. Erdemir, O. L. Eryilmaz, and G. Fenske, "Synthesis of diamondlike carbon films with superlow friction and wear properties," *Journal of Vacuum Science & Technology A*, vol. 18, pp. 1987-1992, 2000.
- [76] S. Sundararajan and B. Bhushan, "Micro/nanotribology of ultra-thin hard amorphous carbon coatings using atomic force/friction force microscopy," *Wear*, vol. 225-229, Part 1, pp. 678-689, 1999.
- [77] T. Haque, A. Morina, A. Neville, R. Kapadia, and S. Arrowsmith, "Effect of oil additives on the durability of hydrogenated DLC coating under boundary lubrication conditions," *Wear*, vol. 266, pp. 147-157, 2009.
- [78] J. Musil, R. Jílek, M. Meissner, T. Tölg, and R. Čerstvý, "Two-phase single layer Al-O-N nanocomposite films with enhanced resistance to cracking," *Surface and Coatings Technology*, vol. 206, pp. 4230-4234, 2012.

- [79] X. L. Peng and T. W. Clyne, "Residual stress and debonding of DLC films on metallic substrates," *Diamond and Related Materials*, vol. 7, pp. 944-950, 1998.
- [80] C. Wei and C.-H. Chen, "The effect of thermal and plastic mismatch on stress distribution in diamond like carbon film under different interlayer/substrate system," *Diamond and Related Materials*, vol. 17, pp. 1534-1540, 2008.
- [81] T. A. Friedmann, J. P. Sullivan, J. A. Knapp, D. R. Tallant, D. M. Follstaedt, D. L. Medlin, *et al.*, "Thick stress-free amorphous-tetrahedral carbon films with hardness near that of diamond," *Applied Physics Letters*, vol. 71, pp. 3820-3822, 1997.
- [82] B. Podgornik, D. Hren, and J. Vizintin, "Low-friction behaviour of boundary-lubricated diamond-like carbon coatings containing tungsten," *Thin Solid Films*, vol. 476, pp. 92-100, 2005.
- [83] J.-W. Lee, S.-K. Tien, Y.-C. Kuo, and C.-M. Chen, "The mechanical properties evaluation of the CrN coatings deposited by the pulsed DC reactive magnetron sputtering," *Surface and Coatings Technology*, vol. 200, pp. 3330-3335, 2006.
- [84] T. Mori, S. Fukuda, and Y. Takemura, "Improvement of mechanical properties of Ti/TiN multilayer film deposited by sputtering," *Surface and Coatings Technology*, vol. 140, pp. 122-127, 2001.
- [85] M. Kalin, J. Vižintin, J. Barriga, K. Vercammen, K. v. Acker, and A. Arnšek, "The Effect of Doping Elements and Oil Additives on the Tribological Performance of Boundary-Lubricated DLC/DLC Contacts," *Tribology Letters*, vol. 17, pp. 679-688, 2004.
- [86] R. Gåhlin, M. Larsson, and P. Hedenqvist, "ME-C:H coatings in motor vehicles," *Wear*, vol. 249, pp. 302-309, 2001.
- [87] K. Holmberg and A. Matthews, *Coatings tribology: properties, mechanisms, techniques and applications in surface engineering*: Elsevier Science, 2009.
- [88] J. Robertson, "Comparison of diamond-like carbon to diamond for applications," *Physica Status Solidi (a)*, vol. 205, pp. 2233-2244, 2008.
- [89] A. Grill, "Diamond-like carbon: state of the art," *Diamond and Related Materials*, vol. 8, pp. 428-434, 1999.
- [90] R. Hauert, "An overview on the tribological behavior of diamond-like carbon in technical and medical applications," *Tribology International*, vol. 37, pp. 991-1003, 2004.
- [91] S. D. A. Lawes, S. V. Hainsworth, and M. E. Fitzpatrick, "Impact wear testing of diamond-like carbon films for engine valve-tappet surfaces," *Wear*, vol. 268, pp. 1303-1308, 2010.

- [92] P. A. Dearnley, "Coatings tribology drivers for high density plasma technologies," *Surface Engineering*, vol. 26, pp. 80-96, 2010.
- [93] J. C. Pivin, M. Allouard, and G. Rotureau, "Determination of the optimal energy range for obtaining diamond-like films by ion implantation," *Surface and Coatings Technology*, vol. 47, pp. 433-444, 1991.
- [94] G. M. Pharr, D. L. Callahan, S. D. McAdams, T. Y. Tsui, S. Anders, A. Anders, *et al.*, "Hardness, elastic modulus, and structure of very hard carbon films produced by cathodic-arc deposition with substrate pulse biasing," *Applied Physics Letters*, vol. 68, pp. 779-781, 1996.
- [95] B. Vengudusamy, R. A. Mufti, G. D. Lamb, J. H. Green, and H. A. Spikes, "Friction properties of DLC/DLC contacts in base oil," *Tribology International*, vol. 44, pp. 922-932, 2011.
- [96] L. A. Donohue, A. Torosyan, P. May, D. E. Wolfe, J. Kulik, and T. J. Eden, "Investigation of PVD-DLC Thin Films Manufactured Using HIPIMS Etch / Unbalanced Magnetron Sputter (UBM) Deposition and Secondary Mechano-Chemical Modification," *Plating and Surface Finishing*, pp. 38 - 42, 2009.
- [97] M. I. de Barros'Bouchet, J. M. Martin, T. Le-Mogne, and B. Vacher, "Boundary lubrication mechanisms of carbon coatings by MoDTC and ZDDP additives," *Tribology International*, vol. 38, pp. 257-264, 2005.
- [98] S. Sahoo, S. S. Pradhan, V. Bhavanasi, and S. K. Pradhan, "Structural and mechanical characterization of diamond like carbon films grown by microwave plasma CVD," *Surface and Coatings Technology*, vol. 204, pp. 2817-2821, 2010.
- [99] D. S. Patil, K. Ramachandran, N. Venkatramani, M. Pandey, S. Venkateswaran, and R. D'Cunha, "Microwave plasma chemical vapour deposition of diamond like carbon thin films," *Journal of Alloys and Compounds*, vol. 278, pp. 130-134, 1998.
- [100] M. Günther, I. Bialuch, S. Peter, K. Bewilogua, and F. Richter, "High rate deposition of hard a-C:H films using microwave excited plasma enhanced CVD," *Surface and Coatings Technology*, vol. In Press, Corrected Proof, 2010.
- [101] W. S. Choi, I. Chung, Y.-Z. Lee, and B. Hong, "Characterization of diamond-like carbon thin films prepared by a microwave plasma enhanced chemical vapor deposition method," *Surface and Coatings Technology*, vol. 180-181, pp. 254-258, 2004.
- [102] T. Sharda, T. Soga, T. Jimbo, and M. Umeno, "Biased enhanced growth of nanocrystalline diamond films by microwave plasma chemical vapor deposition," *Diamond and Related Materials*, vol. 9, pp. 1331-1335, 2000.

- [103] R. M. Dey, S. B. Singh, A. Biswas, R. B. Tokas, N. Chand, S. Venkateshwaran, *et al.*, "Substrate bias effects during diamond like carbon film deposition by microwave ECR plasma CVD," *Current Applied Physics*, vol. 8, pp. 6-12, 2008.
- [104] L. Niederberger, H. Holleck, H. Leiste, M. Stüber, S. Ulrich, and H. Baumann, "Alloyed and hydrogenated diamond-like carbon thin films deposited by a new high performance microwave low pressure plasma source," *Surface and Coatings Technology*, vol. 174-175, pp. 708-712, 2003.
- [105] B. Vengudusamy, J. H. Green, G. D. Lamb, and H. A. Spikes, "Influence of hydrogen and tungsten concentration on the tribological properties of DLC/DLC contacts with ZDDP," *Wear*, vol. 298-299, pp. 109-119, 2013.
- [106] A. Varma, V. Palshin, and E. I. Meletis, "Structure - property relationship of Si-DLC films," *Surface and Coatings Technology*, vol. 148, pp. 305-314, 2001.
- [107] D. Hofmann, S. Kunkel, K. Bewilogua, and R. Wittorf, "From DLC to Si-DLC based layer systems with optimized properties for tribological applications," *Surface and Coatings Technology*, vol. 215, pp. 357-363, 2013.
- [108] M.-G. Kim, K.-R. Lee, and K. Y. Eun, "Tribological behavior of silicon-incorporated diamond-like carbon films," *Surface and Coatings Technology*, vol. 112, pp. 204-209, 1999.
- [109] H. Spikes, "The History and Mechanisms of ZDDP," *Tribology Letters*, vol. 17, pp. 469-489, 2004.
- [110] C.H. Bovington and A. Hubbard, "Lubricant additive effects on valve train friction and wear," *SAE 894021*, 1989.
- [111] Y. C. Lin and H. So, "Limitations on use of ZDDP as an antiwear additive in boundary lubrication," *Tribology International*, vol. 37, pp. 25-33, 2004.
- [112] H. So and R. C. Lin, "The combined effects of ZDDP, surface texture and hardness on the running-in of ferrous metals," *Tribology International*, vol. 32, pp. 243-253, 1999.
- [113] J. C. Bell, K. M. Delargy, and A. M. Seeney, "Paper IX (ii) The Removal of Substrate Material through Thick Zinc Dithiophosphate Anti-Wear Films," in *Tribology Series*. vol. Volume 21, C. M. T. T. H. C. C. M. G. D. Dowson and G. Dalmaz, Eds., ed: Elsevier, 1992, pp. 387-396.
- [114] Z. Yin, M. Kasrai, M. Fuller, G. M. Bancroft, K. Fyfe, and K. H. Tan, "Application of soft X-ray absorption spectroscopy in chemical characterization of antiwear films generated by ZDDP Part I: the effects of physical parameters," *Wear*, vol. 202, pp. 172-191, 1// 1997.

- [115] J. Martin, "Antiwear mechanisms of zinc dithiophosphate: a chemical hardness approach," *Tribology Letters*, vol. 6, pp. 1-8, 1999.
- [116] M. Kano, Y. Yasuda, and J. Ye, "The Effect of ZDDP and MODTC Additives on Friction Properties of DLC and Steel Cam Follower in Engine Oil," in *Papers from 2nd World Tribology Congress*, 2001, p. 342.
- [117] S. Equey, S. Roos, U. Mueller, R. Hauert, N. D. Spencer, and R. Crockett, "Tribofilm formation from ZnDTP on diamond-like carbon," *Wear*, vol. 264, pp. 316-321, 2008.
- [118] T. Haque, A. Morina, A. Neville, R. Kapadia, and S. Arrowsmith, "Non-ferrous coating/lubricant interactions in tribological contacts: Assessment of tribofilms," *Tribology International*, vol. 40, pp. 1603-1612, 2007 2007.
- [119] T. Haque, A. Morina, and A. Neville, "Influence of friction modifier and antiwear additives on the tribological performance of a non-hydrogenated DLC coating," *Surface and Coatings Technology*, vol. 204, pp. 4001-4011, 2010.
- [120] K. K. Mistry, A. Morina, and A. Neville, "A tribochemical evaluation of a WC a DLC coating in EP lubrication conditions," *Wear*, vol. 271, pp. 1739-1744, 2011.
- [121] T. Ohana, M. Suzuki, T. Nakamura, A. Tanaka, and Y. Koga, "Tribological properties of DLC films deposited on steel substrate with various surface roughness," *Diamond and Related Materials*, vol. 13, pp. 2211-2215, 2004.
- [122] J. Jiang and R. D. Arnell, "The effect of substrate surface roughness on the wear of DLC coatings," *Wear*, vol. 239, pp. 1-9, 2000.
- [123] B. Yeldose and B. Ramamoorthy, "Characterization of DC magnetron sputtered diamond-like carbon (DLC) nano coating," *The International Journal of Advanced Manufacturing Technology*, vol. 38, pp. 705-717, 2008.
- [124] R. Kohli and K. Mittal, *Developments in Surface Contamination and Cleaning* vol. 2. Oxford, UK: Elsevier, 2010.
- [125] B. Podgornik and J. Vižintin, "Influence of substrate treatment on the tribological properties of DLC coatings," *Diamond and Related Materials*, vol. 10, pp. 2232-2237, 2001.
- [126] M. M. Morshed, B. P. McNamara, D. C. Cameron, and M. S. J. Hashmi, "Effect of surface treatment on the adhesion of DLC film on 316L stainless steel," *Surface and Coatings Technology*, vol. 163-164, pp. 541-545, 2003.
- [127] J. C. Arnault, L. Demuynck, C. Speisser, and F. Normand, "Mechanisms of CVD diamond nucleation and growth on mechanically scratched Si(100) surfaces," *The European Physical Journal B - Condensed Matter and Complex Systems*, vol. 11, pp. 327-343, 1999.

- [128] S. J. Bull and A. Matthews, "Diamond for wear and corrosion applications," *Diamond and Related Materials*, vol. 1, pp. 1049-1064, 1992.
- [129] D. M. Mattox, "Handbook of Physical Vapor Deposition (PVD) Processing," ed: William Andrew Publishing/Noyes, 1998.
- [130] K. S. S. Harsha, *Principles of Physical Vapor Deposition of Thin Films*. Oxford, UK: Elsevier, 2006.
- [131] T. Putner, "Methods of cleaning glass by vapour degreasing and ultrasonically agitated solvents," *British Journal of Applied Physics*, vol. 10, p. 332, 1959.
- [132] P. W. May, "The Energies of Ions, Electrons and Neutrals in Reactive Ion Etching Plasmas," PhD, Department of Physical Chemistry, University of Bristol, Bristol, 1991.
- [133] S. Anders, A. Anders, and I. Brown, "Macroparticle free thin films produced by an efficient vacuum arc deposition technique," *Journal of Applied Physics*, vol. 74, pp. 4239-4241, 1993.
- [134] H. Takikawa and H. Tanoue, "Review of Cathodic Arc Deposition for Preparing Droplet-Free Thin Films," *Plasma Science, IEEE Transactions on*, vol. 35, pp. 992-999, 2007.
- [135] M. Kamiya, T. Yanagita, H. Tanoue, S. Oke, Y. Suda, H. Takikawa, *et al.*, "T-shape filtered arc deposition system with built-in electrostatic macro-particle trap for DLC film preparation," *Thin Solid Films*, vol. 518, pp. 1498-1502, 2009.
- [136] H. Takikawa, K. Izumi, R. Miyano, and T. Sakakibara, "DLC thin film preparation by cathodic arc deposition with a super droplet-free system," *Surface and Coatings Technology*, vol. 163-164, pp. 368-373, 2003.
- [137] K. Yukimura, M. Kumagai, M. Kumagai, H. Saito, M. Kohata, and K. Takaki, "Deposition of amorphous carbon using a shunting arc discharge," *Surface and Coatings Technology*, vol. 174-175, pp. 1187-1190, 2003.
- [138] P. J. Martin, A. Bendavid, and H. Takikawa, "Ionized plasma vapor deposition and filtered arc deposition; processes, properties and applications," *Papers from the 45th National Symposium of the American Vacuum Society*, vol. 17, pp. 2351-2359, 1999.
- [139] P. Siemroth, J. Berthold, B. Petereit, H. H. Schneider, and H. Hilgers, "A new generation of filtered arc sources for ultrathin top coats on magnetic hard disks," *Surface and Coatings Technology*, vol. 188-189, pp. 684-690, 2004.
- [140] V. Kouznetsov, K. Macák, J. M. Schneider, U. Helmersson, and I. Petrov, "A novel pulsed magnetron sputter technique utilizing very high target power densities," *Surface and Coatings Technology*, vol. 122, pp. 290-293, 1999.

- [141] S. P. Bugaev, N. N. Koval, N. S. Sochugov, and A. N. Zakharov, "Investigation of a high-current pulsed magnetron discharge initiated in the low-pressure diffuse arc plasma," *Discharges and Electrical Insulation in Vacuum, 1996. Proceedings. ISDEIV., XVIIth International Symposium on*, vol. 2, pp. 1074-1076 vol.2, 21-26 Jul 1996 1996.
- [142] I. K. Fetisov, A. A. Filippov, G. V. Khodachenko, D. V. Mozgrin, and A. A. Pisarev, "Impulse irradiation plasma technology for film deposition," *Vacuum*, vol. 53, pp. 133-136, 1999.
- [143] A. P. Ehiasarian, "High Power Impulse Magnetron Sputtering and its Applications," *Pure and applied chemistry*, vol. 82, pp. 1247 - 1258, 2010.
- [144] A. P. Ehiasarian, W. D. Münz, L. Hultman, U. Helmersson, and I. Petrov, "High power pulsed magnetron sputtered CrNx films," *Surface and Coatings Technology*, vol. 163–164, pp. 267-272, 2003.
- [145] Y. Purandare, A. Ehiasarian, A. Santana, and P. Hovsepian, "ZrN coatings deposited by high power impulse magnetron sputtering and cathodic arc techniques," *Journal of Vacuum Science & Technology A*, vol. 32, 2014.
- [146] M. Samuelsson, D. Lundin, J. Jensen, M. A. Raadu, J. T. Gudmundsson, and U. Helmersson, "On the film density using high power impulse magnetron sputtering," *Surface and Coatings Technology*, vol. 205, pp. 591-596, 2010.
- [147] D. Lundin, "Transition between the discharge regimes of high power impulse magnetron sputtering and conventional direct current magnetron sputtering," *Plasma Sources Science and Technology*, vol. 18, 2009.
- [148] A. P. Ehiasarian, W.-D. Munz, L. Hultman, and U. Helmersson, "SVC - 45th Annual Technical Conference Proceedings," pp. 328-334, 2002.
- [149] W. D. Münz, "HIPIMS: The New PVD Technology," vol. 20, pp. 27-32, 2008.
- [150] U. Helmersson, M. Lättemann, J. Bohlmark, A. P. Ehiasarian, and J. T. Gudmundsson, "Ionized physical vapor deposition (IPVD): A review of technology and applications," *Thin Solid Films*, vol. 513, pp. 1-24, 2006.
- [151] H. O. Pierson, *Handbook of Chemical Vapor Deposition (CVD)*, Second ed.: Noyes Publications, 1999.
- [152] D. B. Graves, "Plasma processing," *Plasma Science, IEEE Transactions on*, vol. 22, pp. 31-42, 1994.
- [153] S. Rossnagel, J. Cuomo, and W. Westwood, *Handbook of Plasma Processing Technology: Fundamentals, Etching, Deposition and Surface Interactions*. New York: Noyes Publications, 1990.

- [154] A. Aanesland, J. Bredin, P. Chabert, and V. Godyak, "Electron energy distribution function and plasma parameters across magnetic filters," *Applied Physics Letters*, vol. 100, pp. 044102-3, 2012.
- [155] L. Martinu and D. Poitras, "Plasma deposition of optical films and coatings: A review," *Journal of Vacuum Science & Technology A: Vacuum, Surfaces, and Films*, vol. 18, pp. 2619-2645, 2000.
- [156] M. Gunther, I. Bialuch, S. Peter, K. Bewilogua, and F. Richter, "High rate deposition of hard a-C:H films using microwave excited plasma enhanced CVD," *Surface and Coatings Technology*, vol. 205, Supplement 2, pp. S94-S98, 2011.
- [157] M. Umeno and S. Adhikary, "Diamond-like carbon thin films by microwave surface-wave plasma CVD aimed for the application of photovoltaic solar cells," *Diamond and Related Materials*, vol. 14, pp. 1973-1979, 2005.
- [158] S. Silver, *Microwave Antenna Theory and Design*. London: Peter Peregrinus Inc. , 1984.
- [159] P. Lemoine, J. P. Quinn, P. Maguire, and J. A. McLaughlin, "Comparing hardness and wear data for tetrahedral amorphous carbon and hydrogenated amorphous carbon thin films," *Wear*, vol. 257, pp. 509-522, 2004.
- [160] A. A. Voevodin, J. G. Jones, T. C. Back, J. S. Zabinski, V. E. Strel'nitzki, and I. I. Aksenov, "Comparative study of wear-resistant DLC and fullerene-like CN_x coatings produced by pulsed laser and filtered cathodic arc depositions," *Surface and Coatings Technology*, vol. 197, pp. 116-125, 2005.
- [161] R. Lossy, D. L. Pappas, R. A. Roy, J. J. Cuomo, and V. M. Sura, "Filtered arc deposition of amorphous diamond," *Applied Physics Letters*, vol. 61, pp. 171-173, 1992.
- [162] A. C. Ferrari, J. Robertson, M. G. Beghi, C. E. Bottani, R. Ferulano, and R. Pastorelli, "Elastic constants of tetrahedral amorphous carbon films by surface Brillouin scattering," *Applied Physics Letters*, vol. 75, pp. 1893-1895, 1999.
- [163] N. Miyakawa, S. Minamisawa, H. Takikawa, and T. Sakakibara, "Physical-chemical hybrid deposition of DLC film on rubber by T-shape filtered-arc-deposition," *Vacuum*, vol. 73, pp. 611-617, 2004.
- [164] J. Robertson, "Properties of diamond-like carbon," *Surface and Coatings Technology*, vol. 50, pp. 185-203, 1992.
- [165] K. J. Clay, S. P. Speakman, N. A. Morrison, N. Tomozeiu, W. I. Milne, and A. Kapoor, "Material properties and tribological performance of rf-PECVD deposited DLC coatings," *Diamond and Related Materials*, vol. 7, pp. 1100-1107, 1998.

- [166] S. J. Bull, "Tribology of carbon coatings: DLC, diamond and beyond," *Diamond and Related Materials*, vol. 4, pp. 827-836, 1995.
- [167] H. W. Choi, D. M. Gage, R. H. Dauskardt, K.-R. Lee, and K. H. Oh, "Effects of thermal annealing and Si incorporation on bonding structure and fracture properties of diamond-like carbon films," *Diamond and Related Materials*, vol. 18, pp. 615-619, 2009.
- [168] E. H. A. Dekempeneer, R. Jacobs, J. Smeets, J. Meneve, L. Eersels, B. Blanpain, *et al.*, "R.f. plasma-assisted chemical vapour deposition of diamond-like carbon: physical and mechanical properties," *Thin Solid Films*, vol. 217, pp. 56-61, 1992.
- [169] K. T. Wojciechowski, R. Zybala, R. Mania, and J. Morgiel, "DLC layers prepared by the PVD magnetron sputtering technique," *Achievements in Materials and Manufacturing Engineering*, vol. 37, pp. 726 - 729, 2009.
- [170] C. A. Charitidis, "Nanomechanical and nanotribological properties of carbon-based thin films: A review," *International Journal of Refractory Metals and Hard Materials*, vol. 28, pp. 51-70, 2010.
- [171] M. Keunecke, K. Weigel, K. Bewilogua, R. Cremer, and H. G. Fuss, "Preparation and comparison of a-C:H coatings using reactive sputter techniques," *Thin Solid Films*, vol. 518, pp. 1465-1469, 2009.
- [172] S. Kumar, C. M. S. Rauthan, P. N. Dixit, K. M. K. Srivatsa, M. Y. Khan, and R. Bhattacharyya, "Versatile microwave PECVD technique for deposition of DLC and other ordered carbon nanostructures," *Vacuum*, vol. 63, pp. 433-439, 2001.
- [173] X. T. Zhou, S. T. Lee, I. Bello, A. C. Cheung, D. S. Chiu, Y. W. Lam, *et al.*, "Physical properties of a-C:H films prepared by electron cyclotron resonance microwave plasma chemical vapor deposition," *Materials Science and Engineering B*, vol. 77, pp. 229-234, 2000.
- [174] A. Kromka, O. Babchenko, T. Izak, K. Hruska, and B. Rezek, "Linear antenna microwave plasma CVD deposition of diamond films over large areas," *Vacuum*, vol. 86, pp. 776-779, 2012.
- [175] C. Corbella, I. Bialuch, M. Kleinschmidt, and K. Bewilogua, "Modified DLC coatings prepared in a large-scale reactor by dual microwave/pulsed-DC plasma-activated chemical vapour deposition," *Thin Solid Films*, vol. 517, pp. 1125-1130, 2008.
- [176] S. Kumar, P. N. Dixit, D. Sarangi, and R. Bhattacharyya, "Diamond-like carbon films grown by very high frequency (100 MHz) plasma enhanced chemical vapor deposition technique," *Applied Physics Letters*, vol. 69, pp. 49-51, 1996.

- [177] L. Qian, M. Li, Z. Zhou, H. Yang, and X. Shi, "Comparison of nano-indentation hardness to microhardness," *Surface and Coatings Technology*, vol. 195, pp. 264-271, 2005.
- [178] S. Bec, A. Tonck, J. M. Georges, E. Georges, and J. L. Loubet, "Improvements in the indentation method with a surface force apparatus," *Philosophical Magazine A*, vol. 74, pp. 1061-1072, 1996.
- [179] H. Daniels, R. Brydson, B. Rand, and A. Brown, "Investigating carbonization and graphitization using electron energy loss spectroscopy (EELS) in the transmission electron microscope (TEM)," *Philosophical Magazine*, vol. 87, pp. 4073-4092, 2007.
- [180] B. J. Hamrock and D. Dowson, *Ball bearing lubrication: the elastohydrodynamics of elliptical contacts*: Wiley, 1981.
- [181] W. C. Oliver and G. M. Pharr, "An improved technique for determining hardness and elastic modulus using load and displacement sensing indentation experiments," *Journal of Materials Research*, vol. 7, pp. 1564-1583, 1992.
- [182] G. Pintaude, *Tribology - Fundamentals and Advancements*: InTech, 2013.
- [183] X. Jiang, K. Reichelt, and B. Stritzker, "The hardness and Young's modulus of amorphous hydrogenated carbon and silicon films measured with an ultralow load indenter," *Journal of Applied Physics*, vol. 66, pp. 5805-5808, 1989.
- [184] E. C. D. G. J. R. Centre, "The certification of critical coating failure loads: a reference material for scratch testing according to ENV 1071-3: 1994 BCR-692," 2004.
- [185] K. L. Mittal, *Adhesion Measurement of Films and Coatings*. Utrecht: VSP BV, 1992.
- [186] J. Lanigan, H. Zhao, A. Morina, and A. Neville, "Tribocchemistry of silicon and oxygen doped, hydrogenated Diamond-like Carbon in fully-formulated oil against low additive oil," *Tribology International*, vol. Article in press, 2014.
- [187] M. Kalin and J. Vižintin, "Differences in the tribological mechanisms when using non-doped, metal-doped (Ti, WC), and non-metal-doped (Si) diamond-like carbon against steel under boundary lubrication, with and without oil additives," *Thin Solid Films*, vol. 515, pp. 2734-2747, 2006.
- [188] J. Veverkova and S. V. Hainsworth, "Effect of temperature and counterface on the tribological performance of W-DLC on a steel substrate," *Wear*, vol. 264, pp. 518-525, 2008.
- [189] A. Morina and A. Neville, "Tribofilms: aspects of formation, stability and removal," *Journal of Physics D: Applied Physics*, vol. 40, p. 5476, 2007.

- [190] M. A. Tamor, W. C. Vassell, and K. R. Carduner, "Atomic constraint in hydrogenated "diamond-like" carbon," *Applied Physics Letters*, vol. 58, pp. 592-594, 1991.
- [191] J. Robertson, "The deposition mechanism of diamond-like a-C and a-C: H," *Diamond and Related Materials*, vol. 3, pp. 361-368, 1994.
- [192] N. X. Randall, G. Favaro, and C. H. Frankel, "The effect of intrinsic parameters on the critical load as measured with the scratch test method," *Surface and Coatings Technology*, vol. 137, pp. 146-151, 2001.
- [193] K. Yamamoto and K. Matsukado, "Effect of hydrogenated DLC coating hardness on the tribological properties under water lubrication," *Tribology International*, vol. 39, pp. 1609-1614, 2006.
- [194] G. W. Stachowiak, *Wear: Materials, Mechanisms and Practice*: John Wiley and Sons, 2005.
- [195] M. L. S. Fuller, M. Kasrai, G. M. Bancroft, K. Fyfe, and K. H. Tan, "Solution decomposition of zinc dialkyl dithiophosphate and its effect on antiwear and thermal film formation studied by X-ray absorption spectroscopy," *Tribology International*, vol. 31, pp. 627-644, 1998.
- [196] H. Renondeau, R. I. Taylor, G. C. Smith, and A. A. Torrance, "Friction and wear performance of diamond-like carbon and Cr-doped diamond-like carbon coatings in contact with steel surfaces," *Proceedings of the Institution of Mechanical Engineers, Part J: Journal of Engineering Tribology*, vol. 222, pp. 231-240, 2008.
- [197] M. Crobu, A. Rossi, and N. Spencer, "Effect of Chain-Length and Countersurface on the Tribochemistry of Bulk Zinc Polyphosphate Glasses," *Tribology Letters*, vol. 48, pp. 393-406, 2012.